Hydrogeological drivers and fate of spring discharge in a semi-arid and remote setting

By

Robin Keegan-Treloar

Thesis
Submitted to Flinders University
for the degree of

Doctor of Philosophy
College of Science and Engineering
21st of March 2023

DECLARATION

I certify that this thesis does not incorporate without acknowledgment any material previously submitted for a degree or diploma in any university; and that to the best of my knowledge and belief it does not contain any material previously published or written by another person except where due reference is made in the text.

Robin Keegan-Treloar

21^{st} of March 2023

CO-AUTHORSHIP STATEMENT

This PhD thesis was produced as a series of journal publications submitted in peer-reviewed international scientific journals. Chapters 2, 3, 4 and 5 were written as independent journal papers. At the time this thesis was completed, Chapters 2, 3 and 4 were published, and Chapter 5 was being finalised for submission. I am the first author on all journal publications and was responsible for leading and conducting the research contained in them, writing original draft, including the methodology, data analyses, review and editing and publication of the research.

The first draft of the modelling section of Chapter 2 was written by Dr S. Cristina Solorzano-Rivas. The first draft of the management section of Chapter 2 was written by Professor Matthew Currell. Additionally, the papers in this thesis have benefitted from ongoing advice and input from my supervisors and co-authors who provided intellectual supervision and editorial comment. Feedback from external reviewers as part of the journal peer-review process was also of great benefit to the published papers and I acknowledge their valuable advice and important contributions.

ACKNOWLEDGMENTS

Firstly, I would like to thank my supervisors, Dylan Irvine, Adrian Werner and Eddie Banks. The thesis would not have been possible without your unwavering support, dedication and insightful feedback. Dylan, thank you for your ongoing mentorship, guidance and support. Adrian, your incredible attention to detail and excellent analytical skills are much appreciated. Eddie, your field skills and hydrochemical knowledge were instrumental in the success of this project. I see this not as the end of our collaboration but as just the beginning.

I would like to thank Cristina Solorzano-Rivas for her expertise and for writing the first draft of the numerical modelling section of Chapter 2. Matthew Currell for his management advice and for writing the first draft of the management section of Chapter 2. Ian Cartwright for his incredible hydrochemistry knowledge and generous assistance with the guidance of Chapter 5.

I am grateful for the financial support provided by the Australian Government through the Research Training Program Scholarship.

A special thanks to my friends and family for their unwavering support.

I thank my internal examiners, John Hutson, David Bruce and Howard Fallowfield for their insightful feedback and support. I also acknowledge the valued feedback from the anonymous reviewers for the published versions of Chapters 2, 3 and 4.

This research was conducted as part of an ARC Linkage Project (LP190100713), of which the Business Services of Coast and Country Inc. was the industry partner. I would like to acknowledge Derec Davies from Coast and Country for his involvement in the research included in this thesis, including (but not limited to) support during field campaigns, identifying data sources, providing funding and sharing his extensive knowledge of the study area.

I would like to thank Professor Kristine Walraevens and Professor Philippe Renard for their detailed and constructive reviews of the thesis.

CONTENTS

SUMMARY

Globally, springs are a critical source of water to wetland ecosystems and often hold high ecological and cultural significance (Bogan et al., 2014; Silcock et al., 2020). Springs often occur due to geological features (such as faults) that provide a pathway or barrier to groundwater flow, leading to discharge to the surface. There is a need for further research of these systems including the relationships between aquifer hydraulic head and spring discharge, and the regional hydraulic and hydrochemical flow systems.

This thesis addresses these limitations through the presentation of a detailed literature review, and three research chapters on a hydrogeological system that includes faults and springs. The research chapters utilise the Doongmabulla Springs Complex (DSC) and surrounding area in Queensland, Australia as a case study. The DSC are an important system to study given the high ecological and cultural values and the potential for impacts from a nearby mining development.

Chapter 2 reviews fault-controlled springs to synthesise the knowledge of faults and springs. The review highlights the knowledge gaps in the current understanding of fault-controlled

spring systems, including the selection of methods to identify spring-source aquifers and the relationships between aquifer hydraulic head and spring flow rates. Additionally, the relationships between spring discharge properties (e.g., flow rates, temperature, chemistry) and ecological functioning requires further investigation to understand how the change in spring discharge properties may impact receiving ecosystems. These findings emphasise the need for the management of fault-controlled springs to adopt a structured management approach that considers both the surface (and associated ecosystems) and subterranean regimes as a single interconnected system.

Chapter 3 identified the hydraulic head threshold required to support spring flow and used this threshold to assess alternative conceptual models for the DSC source aquifer. Ordinary Indicator Co-Kriging was used to construct cumulative distribution functions (CCDFs), from sparsely distributed hydraulic head data. The CCDFs informed the likelihood of the alternative source aquifers having adequate hydraulic head to meet a threshold required to sustain spring discharge. These results suggest that the Triassic-aged Formations (the shallower aquifer units) have a higher likelihood of sufficient hydraulic head to support the springs than the Permian-aged Formations (the deeper aquifer units) and the hydraulic head in both aquifer groups are likely only slightly greater than the spring geomorphic thresholds. These findings suggest that even a small change in the aquifer hydraulic head may lead to the cessation of spring flow, which has important implications given the nearby Carmichael Coal Mine.

In Chapter 4 a novel geostatistical technique was developed to probabilistically map extrema (i.e., minima and maxima) and concavity (i.e., concave up or concave down) of the hydraulic head surface. Likely recharge and discharge areas in Triassic-aged aquifers of the Galilee Basin (Queensland, Australia) were identified by comparing maps of concavity and extrema in the hydraulic head surface with known surface features such as geological outcrops, rivers, and lakes. Results suggested recharge predominantly occurs in the north-east and south-east where the Triassic-aged Formations outcrop, while discharge is apparent near several rivers, lakes and the DSC. These observations demonstrate the importance of the Triassic Formations as a source of water to surface features, likely including the DSC, which emphasises potential widespread impacts from dewatering at the Carmichael Coal Mine. The demonstrated approach is broadly applicable to studies aiming to identify recharge and discharge areas on a regional scale and further use of the approach is facilitated by a worked example provided online (DOI:10.5281/zenodo.6655359).

Chapter 5 examines hydrochemistry and isotope data from the Triassic-aged aquifers of the Galilee Basin to assess recharge and discharge areas and characterise the key hydrochemical processes occurring along flow paths. There was good agreement between recharge and discharge areas identified in Chapter 4 and those suggested from the interpretation of hydrochemical data. The main hydrochemical processes controlling total dissolved solids variations were silicate weathering in the Clematis Formation and Dunda Beds (the deeper units of the Triassic aquifers) and evapotranspiration in the shallower Moolayember Formation. Additionally, analysis of Na/Cl ratios and total dissolved solids in a transect near the DSC suggested that the springs may receive water from a mixture of a shallower, local flow path and a deeper regional scale flow path, which have differing salinities.

The outcomes of this thesis help to improve the understanding of fault-controlled spring systems through a global review and three research chapters examining the DSC and the surrounding region. The three research chapters helped in reducing the uncertainty in the conceptualisation of the DSC and the surrounding hydrogeological system. Chapter 3 found that the Triassic aquifers were more likely than the Permian aquifers to have adequate hydraulic head to support spring flow from the DSC. Similarly, Chapter 4 showed likely discharge features in the hydraulic head surface of the Triassic aquifers near the several rivers, lakes and the DSC. Chapter 5 found differing salinities within the separate units of the Triassic aquifers suggesting that the springs may receive a mixture of water from local and more regional scale flow paths. These observations have important implications for the DSC, as changes to groundwater flow paths due to mine-induced drawdown may impact the contribution of the local and regional flow paths, potentially reducing the rate of spring discharge and impacting the water quality. Given the sensitivities of spring-dependent ecosystems to changes in flow and salinity, further investigation is merited.

LIST OF FIGURES

LIST OF TABLES

CHAPTER 1

INTRODUCTION

1.1 The Research Problem

Globally, springs are commonly associated with faults. A global review of hot springs by Curewitz and Karson (1997) showed that 78% of the 822 springs inventoried were associated with faults. Springs often occur where faults or fractures provide a preferential flow path or barrier for groundwater flow (Bryan, 1919; Curewitz and Karson, 1997). Faults can behave as either barriers to flow, conduits to flow or both, depending on the fault composition and stage of evolution (Forster and Evans, 1991; Caine et al., 1996; Cook et al., 2022). Despite their prevalence, there are few detailed studies of fault-controlled springs systems, with existing knowledge primarily based on published case studies of faults or springs.

An essential condition for the occurrence of springs, including fault-controlled springs, is that the source aquifer(s) must have a sufficient hydraulic head for the water to discharge to the surface. The spring flow rate is proportional to the fault conductance and the aquifer hydraulic head (Love et al., 2013a). However, identifying the fault conductance can be challenging and previous studies have had difficulty developing an appropriate relationship between hydraulic head and spring flow rates (e.g., Love et al., 2013a). As a lower bound, the hydraulic head in the source aquifer to the spring must be greater than an elevation known as the spring geomorphic threshold, which is the elevation of the lip, mound, or surface of the spring vent at the ground surface (Currell et al., 2017; Toth et al., 2022). Assessing whether an aquifer has an adequate hydraulic head can be challenging, particularly in data-sparse areas where few hydraulic head measurements are available. As such, there is a clear need to develop effective methods to estimate the likelihood of spring source aquifers having adequate hydraulic head to support spring discharge.

In arid and semi-arid regions, springs provide the main source of water to wetland ecosystems (Bogan et al., 2014; Springer and Stevens, 2009). In cases where springs are spatially isolated, endemic plant and animal species can develop and evolve to the unique spring conditions (Davis et al., 2017). Springs often have high cultural values, and many culturally significant spring complexes have been altered over the last century (Silcock et al., 2020). These alterations are attributable mainly to human-induced changes (e.g., mining and agricultural activities) to surface water and groundwater systems (Davis et al., 2017; Silcock et al., 2020). Given their ecological and cultural values, understanding groundwater discharge from springs is vital to preserve spring ecosystems.

Springs are also an important component of the larger hydrogeological system. Recharge to the source aquifer(s) of springs can occur at a substantial distance from the spring expression, and thus, it may take millennia for this groundwater to travel to the spring and discharge to the surface. To further complicate the understanding of springs, springs may obtain water from a combination of localised and/or regional scale groundwater flow systems. For example, Criss (2010) found that water from Big Spring (Missouri, USA) represented the superposition of long-timescale regional groundwater flow and short-timescale pulse-type events following local precipitation. Understanding the regional groundwater flow system, including the evolution of hydrochemistry along flow paths, is critical for the effective management of springs.

Ecology and cultural significance are important factors for the Doongmabulla Springs Complex (DSC) and the surrounding region of the Galilee Basin (Australia) making it an ideal case study to examine fault-controlled springs and their role in the larger hydrogeological system (Currell et al., 2017). The DSC has received a lot of recent attention due to uncertainties in the regional hydrogeology and the approval of a large open cut coal mine, the Carmichael Coal Mine, in close proximity (8 km) to the DSC springs (Currell et al., 2020). The source aquifer to the springs has been subject of conjecture (e.g., Currell et al., 2017; Currell et al., 2020) and the regional hydrogeology (including flow directions, recharge/discharge areas and hydrochemical processes) remains poorly understood. Identifying the spring source aquifer(s) and the key regional hydrogeological processes is critical to understand the potential short- and long-term impacts of the mining development. Given the high conservation values and potential impacts from mining, the DSC and the surrounding region is used as a case study for the technical research chapters of this thesis (Chapters 3, 4, 5), and is discussed briefly in a review of fault-controlled spring systems (Chapter 2).

1.2 Background

1.2.1 Climate and regional geology of the Galilee Basin

The Galilee Basin is a large, late-Carboniferous and Triassic-aged intracratonic basin that acts as a recharge area to the Great Artesian Basin (GAB) (see Figure 1.1a) (Jiang, 2014; Moya et al., 2016). The climate is semi-arid to arid, with typical annual rainfall of 300 to 600 mm/yr and high evapotranspiration rates of 2200 to 2900 mm/yr (Lewis et al., 2018). The GAB aquifers are a crucial source of groundwater for industry and irrigation and are estimated to support 12.8 billion dollars in economic activity annually, with mining and coal seam gas activities accounting for almost two thirds of the total economic activity (Frontier Economics, 2016; Ordens et al., 2020). These resource developments, including in the Galilee Basin, potentially pose a risk to water levels and recharge in the GAB.

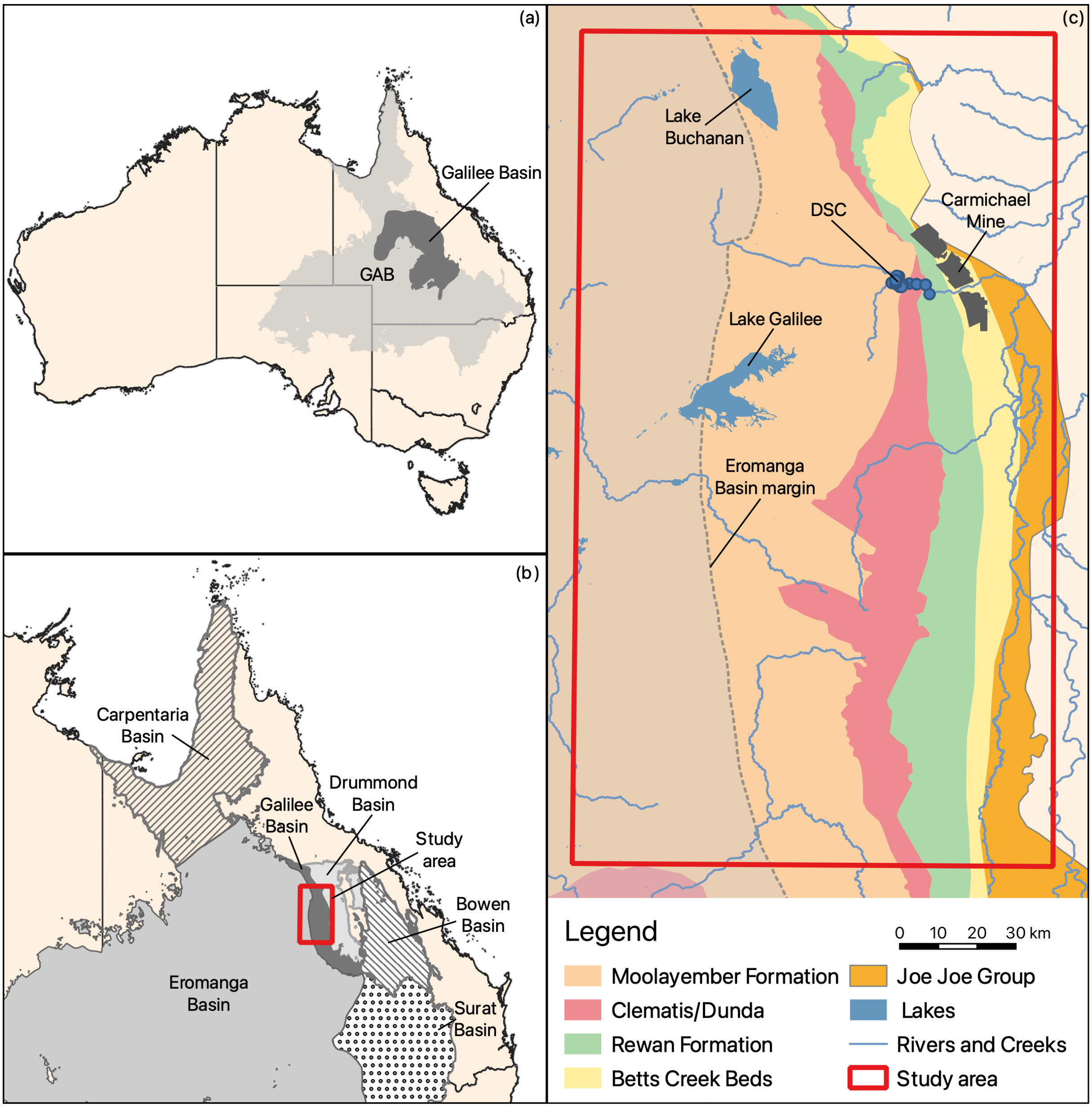

Figure 1.1: *(a) The Galilee Basin and the Great Artesian Basin (GAB) relative to Australia. (b) The major geological basins in the Galilee Basin region with the study area shown in the red rectangle. (c) The study area outlined in red, shown with the extent of the major geological formations, the major water courses, lakes, the Doongmabulla Springs Complex (DSC) and the Carmichael Mine site. Note the geological formations shown in c are shown in stratigraphic order and continue to the west beneath overlying units.*

The Galilee Basin outcrops to the east of the GAB and is overlain by the Jurassic–Cretaceous and Cenozoic-aged Eromanga Basin to the west (Allen and Fielding, 2007; Figure 1.1b). The eastern outcrop areas of the Galilee Basin are believed to be an important recharge area for the GAB, with the upper units of the Galilee and Eromanga Basins considered part of the GAB (Habermehl and Lau, 1997; Kellett, et al., 2003; Moya et al., 2016). To the east, the Galilee Basin is bounded by the Late Devonian to Early Carboniferous-aged Drummond Basin (Allen and Fielding, 2007).

The study area is situated in the eastern Galilee Basin (Figure 1.1b). The extent of the major stratigraphy and surface features of the study site are shown in Figure 1.1c. The stratigraphy is composed of the Moolayember Formation, the Clematis Formation, the Dunda Beds, the Rewan Formation, the Betts Creek Beds and the Joe Joe Group. The stratigraphy, age, lithology and thickness of these sediments are summarised in Figure 1.2 and are briefly discussed below in order from oldest to youngest.

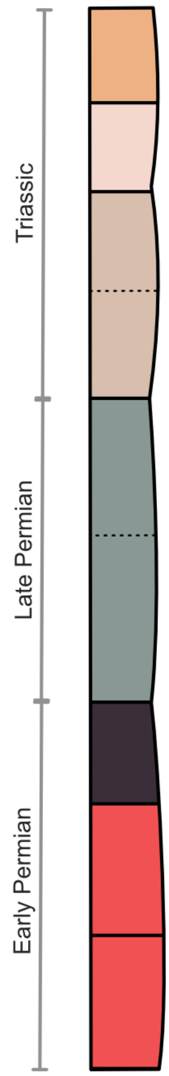

Stratigraphy	Lithology	Thickness mean, [min, max] in m	
Moolayember Formation	Siltstone, Mudstone	175, [8, 717]	
Clematis Formation	Sandstone, Siltstone	94, [13, 394]	
Dunda Beds	Sandstone, Siltstone, Mudstone	83, [12, 223]	Rewan Group
Rewan Formation	Mudstone, Sandstone, Siltstone	160, [9, 389]	Rewan Group
Bandanna Formation	Sandstone, Siltstone, Coal	58, [2, 161]	Betts Creek Beds
Colinlea Formation	Siltstone, Sandstone, Coal	49, [11, 123]	Betts Creek Beds
Aramac Coal Measures	Sandstone, Coal, Mudstone	106, [18, 272]	Joe Joe Group
Jochmus Formation	Sandstone, Siltstone	276, [17, 1028]]	Joe Joe Group
Jericho Formation	Mudstone, Siltstone	305, [53, 730]	Joe Joe Group

Figure 1.2: *Stratigraphy, lithology and thickness (mean, minimum and maximum) of the Galilee Basin sediments. Adapted from Allen and Fielding (2007), Jiang (2014), Moya et al. (2016) and Evans et al. (2017).*

The Joe Joe Group is composed of the Jericho Formation, the Jochmus Formation and the Aramac Coal Measures (Figure 1.2). The Jericho Formation was deposited in the early Permian in a lacustrine and braided fluvial system and is composed primarily of mudstones and siltstones (Jiang, 2014). Overlying the Jericho Formation is the Jochmus Formation that was deposited by fluvial processes in the Late Carboniferous to early Permian and is composed of sandstone and siltstone (Van Heeswijck, 2006; Jiang, 2014). The early Permian-aged Aramac Coal Measures overlie the Jochmus Formation and were deposited by peat swamps (Jiang, 2014). The Aramac Coal Measures contain coal deposits and sandstone (Van Heeswijck, 2006; Jiang, 2014). The Joe Joe Group is considered a low permeability unit (AECOM, 2021).

The late Permian-aged units that overlie the Aramac Coal Measures include the Colinlea Formation, which is overlain by the Bandanna Formation. The Colinlea and Bandanna Formations are often grouped together as the Betts Creek Beds. The Betts Creek Beds sediments were deposited after a period of non-deposition, when fluvial and paludal processes led to the deposition of sandstone, siltstone and low rank coal (Allen and Fielding, 2007). The distinction between the Colinlea Formation and Bandanna Formation can be identified by a marine transgression (Van Heeswijck, 2006). The Betts Creek Beds are important regional aquifers providing water suitable for domestic and stock usage (2000-3000 µS/cm) (Currell et al., 2017). The coal seams in the Betts Creek Beds are the target of major mining developments throughout the Galilee Basin (Currell et al., 2017; Currell et al., 2020), including the Carmichael Coal Mine shown in Figure 1.1c.

The Triassic-aged units overlie the Betts Creek Beds and comprise of the Rewan Formation aquitard, overlain by the Dunda Beds, the Clematis Formation and the Moolayember Formation. The Rewan Formation was deposited by fluvial processes and intermittent lacustrine processes during a dry period in the early Triassic (Jiang, 2014). The Rewan Formation is composed of green-grey mudstone, sandstone and siltstone, and is considered an aquitard (AECOM, 2021). The Rewan Formation grades into the Dunda Beds, which are composed of sandstone, siltstone and some mudstone, and represent a transitional unit between the Rewan and Clematis Formation (Van Heeswijck, 2006; AECOM, 2021). The Dunda Beds and Rewan Formation are often combined as the Rewan Group, although from a hydrogeological perspective, the Dunda Beds appear more similar to the Clematis Formation. Overlying the Rewan Group is the Clematis Formation that was deposited by braided fluvial processes and is composed of sandstones and siltstones (Jiang, 2014). The Dunda Beds and Clematis Formation are important regional aquifers. Overlying the Clematis Formation is the Moolayember Formation, which is composed of fluvial and lacustrine deposits of mudstone and siltstone (Jiang, 2014). The Moolayember Formation acts as an aquitard by confining the Clematis Formation and Dunda Beds (AECOM, 2021).

Regionally, faults have been mapped in the Galilee Basin and are believed to be an important cause of inter-aquifer connectivity between the Triassic and Permian-aged Formations. To the north of the Carmichael Coal Mine, a large fault was mapped in the now abandoned Chinastone Coal project site (Evans et al., 2017). The fault was at least 18 km long and had a displacement of 100 m, which caused the Rewan Formation to be offset into the Clematis Formation (Evans et al., 2017). In the southwest of the Galilee Basin is the Barcaldine Ridge, where the Joe Joe Group has been upthrown against the Triassic-aged units (Evans et al., 2018). The Barcaldine Ridge marks the subdivision between the northern and southern Galilee Basin and appears to form a regional groundwater flow divide in the Clematis Formation (Evans et al., 2018). In the north-eastern area of the Galilee Basin, there are a series of faults, monoclines, and ridges where the Galilee Basin interacts with the Drummond Basin (AECOM, 2021). Four smaller faults with displacements of up to 40 m have also been observed in the Permian-aged units in the vicinity of the Carmichael Coal Mine (AECOM, 2021). Regional hydrochemistry examined by Moya et al. (2016) suggested that there may be inter-aquifer connectivity, particularly in the west of the Galilee Basin, likely due to faulting.

1.2.2 Rivers, lakes and springs

Surface water flows in the Galilee Basin are highly seasonal and vary between no flow during periods of drought and episodic flooding (Evans et al., 2018). Groundwater is an important component of the surface water systems, providing baseflow to rivers, springs and lakes. In other areas, these surface water features recharge groundwater systems through infiltration. Key surface water features in the study area include the Carmichael River, Lake Galilee, Lake Buchannan and the DSC (Figure 1.1c). There are numerous rivers and creeks throughout the region that have complex (and often poorly understood) groundwater-surface water interactions. For example, the Carmichael River, which flows from west to east, is thought to be gaining in the east of the study area, where the river incises into the outcrops of the Moolayember and Clematis/Dunda Formations (Evans et al., 2018), and losing in the vicinity of the Carmichael Coal Mine (AECOM, 2021).

Lake Galilee and Lake Buchanan are large salt lakes located in the Galilee Basin (Figure 1.1c), which were formed by tectonic uplift in the Earth's crust (Rolfe et al., 1997). Lake Galilee is located in a basin bordered by the Great Dividing Range to the north and west, along the margin of the Eromanga Basin (Figure 1.1c). The lake covers an area of 257 km^2, has a catchment area of 2554 km^2 and is intermittent with brackish salinity (Rolfe et al., 1997). Lake Galilee provides an important breeding habitat for waterbirds including the freckled duck (Porter et al., 2006). To the north of Lake Galilee lies Lake Buchanan (Figure 1.1c). Located in the hills of the Great Dividing Range, Lake Buchanan covers an area of

117 km^2 with a surface catchment of 2712 km^2 (Chivas et al., 1986). The lake is mostly dry with a persistent deeper pool in the south-eastern corner (Chivas et al., 1986). Periodically, the lake will dry entirely. Under these conditions the south-eastern lake floor is coated in a halite crust (Chivas et al., 1986).

The DSC springs are located to the northeast of Lake Galilee (Figure 1.1c). Discharge from the DSC support >100 wetlands, many of which provide critical habitats for endemic species and are collectively of high cultural significance to the Wangan and Jagalingou people (Currell et al., 2017; Currell et al., 2020). Currently, there are three alternative conceptual models for the source of water to the DSC. The conceptualisation put forward by Bradley (2015) proposes that the springs obtain water from the Clematis Formation and/or Dunda Beds, which are isolated from the deeper Permian-aged Formations by the Rewan Formation aquitard. Under this conceptualisation, the drawdown in the Betts Creek Beds from the Carmichael Coal Mine dewatering will have minimal impact on the springs. However, two alternative conceptual models have been proposed by Webb (2015). In the first model, the springs source water from the Betts Creek Beds via a fault or leakage through the Rewan Formation aquitard. In the second model, the springs obtain water from the Clematis and/or Dunda Beds, but the Rewan Formation is leaky, or intersected by faulting or fracturing. Under these two conceptual models from Webb (2015), the mine-induced drawdown in the Betts Creek Beds have the potential to impact the DSC either by reduced hydraulic head to feed the springs from the Betts Creek Beds, or by drawdown in the Betts Creek Beds propagating across the Rewan Formation aquitard and reducing water levels in the Clematis Formation and/or Dunda Beds.

1.2.3 Mining developments in the Galilee Basin

Until recently, the Galilee Basin remained largely untouched by mining operations with groundwater extraction primarily for stock or domestic purposes (Peeters et al., 2018). Due to the remoteness and limited groundwater extraction, the groundwater monitoring network is sparse and comprises mostly of one-off measurements from landholder or exploration wells. Coal and coal seam gas operations are being developed where the coal-bearing Betts Creek Beds outcrop along the eastern margin of the Galilee Basin and denser monitoring networks are being developed, mostly within the prospective leases. The Carmichael Coal Mine (Figure 1.1c) is the first major mine approved in the area and will consist of an open cut and underground mine, covering an area of 280 km^2. Once constructed, the mine is expected to act as a large regional sink of groundwater as mining operations will dewater the Betts Creek Beds in the vicinity of the mine to access coal deposits during the active mining operation (Currell et al., 2017; Currell et al., 2020). The approval of the Carmichael Coal Mine has been the focus of much conjecture due to uncertainties in the potential impacts of mining operations on the regional hydrogeology, and the nearby DSC and Carmichael River (Currell et al., 2017; Currell et al., 2020). Further mines are expected throughout the region, with at least six additional coal and coal seam gas projects undergoing assessment (Peeters et al., 2018).

1.3 Research aims

This thesis aims to address the knowledge gaps for fault-controlled spring systems and demonstrate approaches to utilise available datasets to inform hydrogeological systems that contain important springs. The thesis consists of a global review of fault-controlled springs (Chapter 2) and three case studies of the DSC and the surrounding Galilee Basin (Chapters 3, 4, 5). Data scarcity in this remote region, and challenges with conducting field work during the COVID-19 pandemic necessitated an emphasis on the interpretation of largely pre-existing datasets. The research aims of the thesis are to address:

1. The relationships between faults and springs through a global review of the existing literature. The review was undertaken to synthesise the disparate knowledge of faults and springs and identify the knowledge gaps in the current understanding of these systems.

2. The hydraulic head threshold required to support spring discharge and the likelihood of alternative aquifers having adequate hydraulic head to meet this threshold. This was demonstrated using a geostatistical model and available hydraulic head data to assess the likelihood of the Triassic and Permian aquifers supporting the DSC.

3. The regional flow directions and locations of recharge/discharge areas. These were identified for the Triassic-aged aquifers in the Galilee Basin using a novel geostatistical technique.

4. The hydrochemical evidence of recharge and discharge areas and the evolution of waters along flow paths. This demonstrated how hydrochemistry datasets can be used to inform the conceptual model for the Triassic-aged aquifers in the Galilee Basin.

These aims are the focus of the four studies presented in Chapters 2-5.

1.4 Structure and contribution of this thesis

This PhD explores fault-controlled springs and their role in the larger hydrogeological system using the DSC and the surrounding Galilee Basin as a case study. The review of fault-controlled springs (Chapter 2) was required as it has been hypothesised the DSC may occur due to faulting across the Rewan Formation and although extensive reviews have been conducted of faults (e.g., Forster and Evans, 1991; Caine et al., 1996; Bense et al., 2013) and springs (e.g., Hynes, 1970; van der Kamp, 1995; Springer and Stevens, 2009), few studies have considered fault-controlled springs as a complete system. This review, for the first time, brings together disparate knowledge of faults and springs. The findings highlight the knowledge gaps in the current understanding of fault-controlled spring systems, including in the selection of methods to identify spring-source aquifers and the relationships between aquifer hydraulic head and spring flow rates.

Chapter 3 identifies the hydraulic head required to support spring flow and uses this to assess alternative conceptual models for the DSC source aquifer. As hydraulic head measurements were sparsely distributed and subject to varying uncertainty, a geostatistical method was utilised to assess the likelihood of alternative aquifers meeting the required hydraulic head thresholds to sustain spring flow. This approach fully utilises sparsely distributed hydraulic head data to inform the likelihood of hydraulic head exceeding set threshold values, which is broadly generalisable to threshold type problems throughout hydrogeology.

Chapter 4 extended the hydraulic head analyses to stochastically identify potential recharge and discharge features on a regional scale for the Triassic-aged aquifers of the Galilee Basin. A novel geostatistical method was developed that used sequential Gaussian simulation to jointly simulate hydraulic head and its first and second derivatives. The derivative values were subsequently used to identify regional groundwater flow directions, to locate extrema (i.e., minima and maxima), and to assess the concavity (i.e., concave up or concave down) of the hydraulic head surface. Mapped concavity and extrema were compared to the locations of surface features to attribute these areas to recharge and discharge from surface features of the system (e.g., rivers, lakes or geological outcrops), which was used to construct a probabilistic map of the likely recharge and discharge features. This research demonstrated how the geostatistical simulation can utilise sparse hydraulic head datasets to simulate the derivatives of the hydraulic head surface and map likely recharge and discharge areas.

The regional conceptual model was further refined in Chapter 5 by identifying the hydrochemical signatures of recharge, chemical weathering along flow paths and the properties of discharge waters. Chapter 5 used the regional hydrochemistry of the Galilee Basin to evaluate the recharge/discharge areas identified in Chapter 4 and to assess the evolution of water along flow paths. A conceptual model was developed to show the major hydrochemical reactions occurring along flow paths from recharge areas to likely discharge features. This demonstrated how even limited hydrochemical datasets can be used to reduce uncertainty of conceptual models.

Utilising the four research chapters, the conclusion chapter synthesises the key findings and further discusses contributions of this research.

CHAPTER 2

FAULT-CONTROLLED SPRINGS: A REVIEW

Published in Earth-Science Reviews: Keegan-Treloar, R., Irvine, D.J., Solórzano-Rivas, S.C., Werner, A.D., Banks, E.W., Currell, M.J., 2022. Fault-controlled springs: A review. Earth-Science Rev. 230, 104058.

Approximate contribution of co-authors: Robin Keegan-Treloar (65%), Dylan Irvine (10%), Cristina Solórzano-Rivas (10%), Adrian Werner (5%), Eddie Banks (5%) and Mathew Currell (5%).

Abstract

Springs sustain groundwater-dependent ecosystems and provide freshwater for human use. Springs often occur because faults modify groundwater flow pathways leading to discharge from aquifers with sufficiently high pressure. This study reviews the key characteristics and physical processes, field investigation techniques, modelling approaches and management strategies for fault-controlled spring systems. Field investigation techniques suitable for quantifying spring discharge and fault characteristics are often restricted by high values of spring ecosystems, requiring mainly non-invasive techniques. Numerical models of fault-controlled spring systems can be divided into local-scale, process-based models that allow the damage zone and fault core to be distinguished, and regional-scale models that usually adopt highly simplified representations of both the fault and the spring. Water resources management relating to fault-controlled spring systems often involves ad hoc applications of trigger levels, even though more sophisticated management strategies are available. Major gaps in the understanding of fault-controlled spring systems create substantial risks of degradation from human activities, arising from limited data and process understanding, and simplified representations in models. Thus, further studies are needed to improve the understanding of hydrogeological processes, including through detailed field studies, physics-based modelling, and by quantifying the effects of groundwater withdrawals on spring discharge.

2.1 Introduction

Springs often sustain highly productive and diverse aquatic and terrestrial ecosystems (Bogan et al., 2014; Davis et al., 2017). Where springs are spatially isolated, ‘ecological islands’ can form (Bogan et al., 2014), providing habitats for endemic species to develop and evolve to the unique spring conditions (Davis et al., 2017). In the case of arid and semi-arid regions, springs may provide the only permanent source of water for significant distances, allowing for the survival of rare plants and a broad range of animal species (Springer and Stevens, 2009). Many ecologically and culturally significant spring complexes have been altered over the last century, attributable mainly to human-induced changes to groundwater regimes (Davis et al., 2017).

Springs occur under a variety of hydrogeological conditions, commonly due to geological features that create transmissive pathways or barriers to flow (Bryan, 1919; Curewitz and Karson, 1997; Rowland et al., 2008). These geological features include faults, which are planar fractures or discontinuities in rock where displacement has occurred (Caine et al., 1996; Bense et al., 2013). Faults may impede and/or act as preferential pathways to groundwater flow (Forster and Evans, 1991; Caine et al., 1996; Bense et al., 2013). Bryan (1919) and Meinzer (1923) define five spring types based on their subsurface geology (contact springs, fissure/fault springs, depression springs, tubular or fracture springs and volcanic springs), of which, contact springs and fissure/fault springs often occur due to faults (see Figure 2.1). Springer and Stevens (2009) developed a revised inventory of 12 spring conceptual models, of which five include geological faults. Curewitz and Karson (1997) reviewed the structural settings of hot springs and found that 78% of the 822 hot springs inventoried were associated with faults. Although the review was specific to hot springs, there is evidence from case studies that other spring types (e.g., cooler 16-25 °C springs, acid sulphate springs, bubbling CO_2 springs) are commonly associated with faults (e.g., Bignall and Browne, 1994; Battani et al., 2010; Apollaro et al., 2012).

The properties of faults and the associated hydrogeological processes have been extensively reviewed (e.g., Forster and Evans, 1991; Caine et al., 1996; Bense et al., 2013;

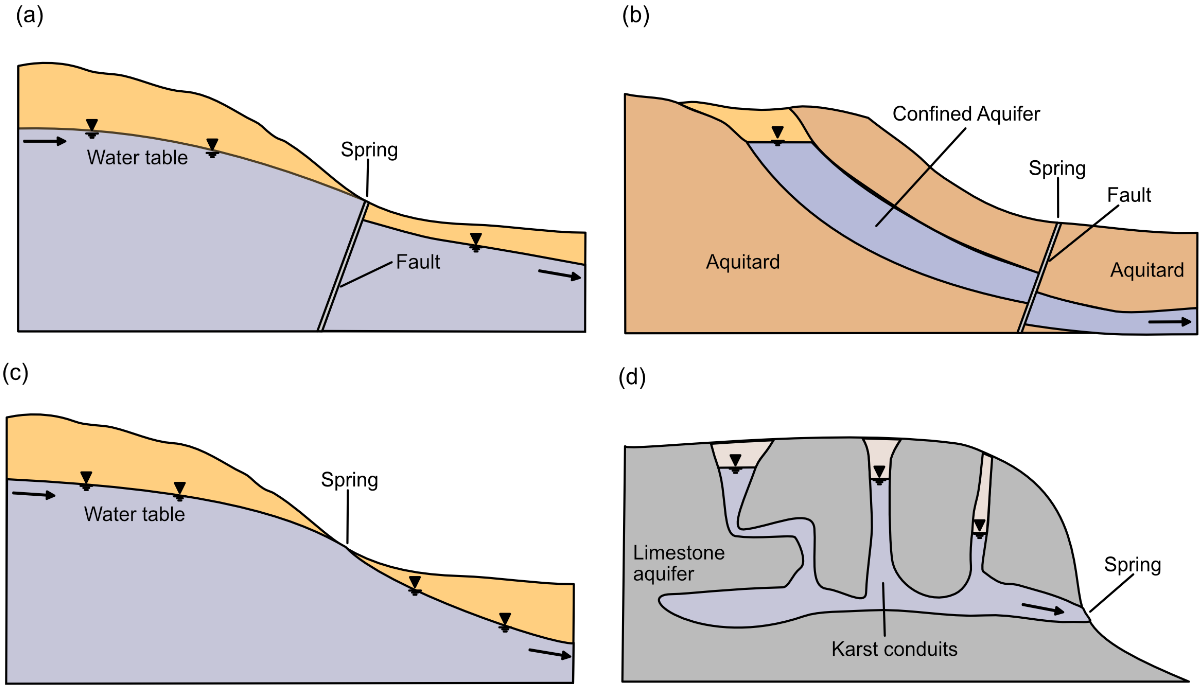

Figure 2.1: *Spring conceptual models for four of the spring types described by Meinzer (1923) showing: (a) a contact spring where the water table outcrops along a fault, (b) a fissure/fault spring where a fault provides a conduit for flow from a confined aquifer, (c) a depression spring where the water table intersects the surface and (d) a tubular or fracture spring where water flows through karst conduits and discharges through an orifice at lower elevation. Volcanic springs are not shown as these are typically associated with the formation of steam and have varying geological/hydraulic characteristics.*

Scibek et al., 2016), as has the hydrology of springs (e.g., Meinzer, 1923; Hynes, 1970; van der Kamp, 1995; Springer and Stevens, 2009; Kresic, 2010). While faults and springs have been reviewed independently, their hydrogeological interrelation has received little attention, and the current understanding of fault-controlled spring systems is based primarily on a review of the structural settings of hot springs by Curewitz and Karson (1997) and case studies (e.g., Jewell et al., 1994; Crossey et al., 2006; Rowland et al., 2008).

This review draws on existing literature on faults and springs to establish the current state of knowledge on fault-controlled spring systems. Although the review is based primarily on case studies of fault-controlled spring systems, some of the approaches discussed can be generalised to studies of faults or springs (e.g., the methods described to quantify spring discharge in Section 3.1 are similar for fault-controlled springs and other spring types). The following aspects of fault-controlled spring systems are reviewed: (1) hydrogeological processes; (2) field investigation techniques; (3) numerical modelling; and (4) management. Finally, we outline major knowledge gaps and future research directions required to improve the protection and reliable characterisation of fault-controlled spring systems, particularly those threatened by groundwater-affecting activities.

2.2 Hydrogeological processes

Here, the hydrogeological processes associated with the occurrence of springs that source water from groundwater flow through faults are subdivided into: (1) fault characteristics, (2) spring and aquifer hydraulics, and (3) surface conditions and spring environments.

2.2.1 Fault characteristics

Faults are classified based on their angle relative to the horizontal (i.e., dip) and the relative displacement of rock on either side of the fault plane (i.e., slip) (Bense et al., 2013).

There are three main classes of faults (Figure 2.2). Normal faults (Figure 2.2a) occur due to extensional stresses, generally leading to dips of 45-70° relative to the horizontal, although in some cases (e.g., when associated with metamorphic core complexes), normal faults can have dips at lower angles (e.g., Faulds and Varga, 1998; Faulds et al., 2008). Reverse (or thrust) faults (Figure 2.2b) occur due to compressional stresses, causing dips generally «45° (Bense et al., 2013). Both normal (Figure 2.2a) and reverse faults (Figure 2.2b) have near-vertical slips (displacement of rock on one side of the fault relative to the other). Strike-slip faults (Figure 2.2c and 2.2d) have vertical (or near-vertical) dips, with horizontal slips (Bense et al., 2013). They are classified as either left-lateral or right-lateral, based on whether the displacement is to the left (Figure 2.2c) or the right (Figure 2.2d) when viewed from either side. Additionally, faults can be a combination of the aforementioned four classes. For example, normal oblique-slip faults, which have been associated with hot springs (e.g., La Rosa et al., 2019), have components of both normal and strike-slip faults. The type of fault and its stress regime influence the fault permeability (e.g., extensional stresses can increase permeability). However, the fault permeability is also strongly influenced by the rock type and the fault architecture (Caine et al., 1996). This prevents the use of generic permeability models based only on the fault classification (Bense and Van Balen, 2004).

Conceptually, the fault architecture is represented using a three-component model comprising the fault core, the damage zone and the protolith (Caine et al., 1996; Mitchell and Faulkner, 2009) (Figure 2a). The fault core is where most of the displacement has occurred, comprising deformed materials such as gouge, cataclasite, breccia and/or smear (Caine et al., 1996; Torabi et al., 2019). The damage zone surrounds the fault core and features secondary structures such as micro- or macro-fractures arising from slip and/or deformation events (Caine et al., 1996). The protolith is the surrounding material that has not been

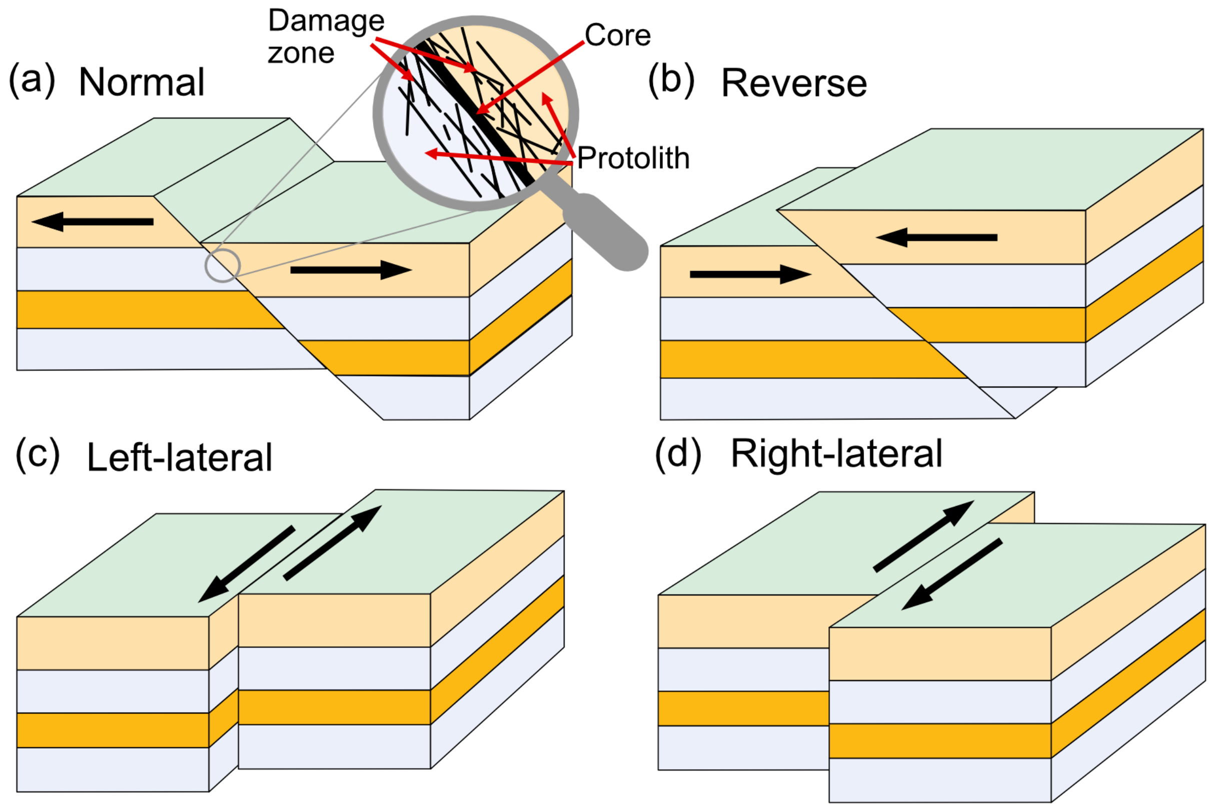

Figure 2.2: *Conceptual diagrams of fault classes showing: (a) normal, (b) reverse, (c) left-lateral strike-slip and (d) right-lateral strike-slip faults (stress directions indicated by black arrows). The inset shows the fault core, damage zone and protolith.*

substantially modified by faulting (Bense et al., 2013).

Whether the fault acts as a barrier and/or a conduit to flow depends on its composition and the stage of fault evolution (Caine et al., 1996). For example, the core may act as a conduit immediately following deformation and later as a barrier due to the precipitation of minerals (Caine et al., 1996). Fluid flow in the damage zone is typically higher than in the fault core or protolith, occurring predominantly through fractures (e.g., Bense and Person, 2006; Folch and Mas-Pla, 2008). For example, the dataset of fault permeabilities compiled by Scibek (2020) indicate that the permeability of the damage zone is on average two orders of magnitude greater than the fault core.

The hydrogeologic behaviour of faults has been characterised in terms of the fault architecture by Caine et al. (1996), who suggested three quantitative indices:

$$F_a = W_{dz}/(W_{dz} + W_{core}) \tag{2.1}$$

$$F_m = mean(Fa) \tag{2.2}$$

$$F_s = max(F_a) - min(F_a) \tag{2.3}$$

Where F_a represents the relative proportion of the damage zone present in the fault, with values that vary from zero to one, W_{dz} is the damage zone width (m), and W_{core} is the core width (m). F_m is the mean of spatial variations in F_a for a given fault, and F_s is the range in F_a values for a given fault. As the damage zone is typically considered of higher permeability relative to the fault core, Fa values close to one indicate that the fault is likely to behave as a conduit to flow, whereas F_a values close to zero indicate that the fault is likely to act as a barrier (Caine et al., 1996). F_a can be calculated parallel and/or perpendicular to the fault, wherever measurements are available, to assess the relative proportions of the spatial extent of the damage zone. As W_{dz} and W_{core} can vary spatially, F_m and F_s can be useful for classifying the larger-scale behaviour of the fault (Caine et al., 1996).

Understanding the relationship between fault and spring locations is a key area of research for fault-controlled springs. Curewitz and Karson (1997) conducted an extensive review of the geological settings of hot springs. They found that hot springs generally occurred in five structural settings along fault zones, including: (1) the fault tip where the breakdown area formed from intense fracturing gives rise to springs, (2) fault interaction areas where the breakdown areas from several fault tips interact or merge into a single breakdown area, (3) locked-in fault intersection areas where faults have opposing directions of slip leading to a breakdown area in the intersection between the faults, (4) slipping fault intersection areas where faults are slipping in the same direction, and there is limited breakdown area and (5) fault traces (i.e., surface disturbance where a fault intersects the ground surface) where localised fracturing may occur due to pressures during slip. Offsets between major faults, known as accommodation zones, are a form of interaction area that has been associated with high levels of geothermal activity and the occurrence of hot springs (e.g., Curewitz and Karson, 1997; Faulds et al., 2002). These studies suggest that fault-controlled springs, particularly fault-controlled hot springs, mostly occur where multiple fault traces interact (Curewitz and Karson, 1997; Faulds et al., 2002; Faulds et al., 2008).

2.2.2 Spring and aquifer hydraulics

An essential condition for the occurrence of springs is that the hydraulic head within the source aquifer (i.e., the aquifer providing water to the springs) must be sufficient for water to discharge to the surface. In confined aquifers, no major flow is expected through the confining unit unless preferential pathways (e.g., faults or fractures) are present (Brehme et al., 2016). The flow rate of a spring is directly related to the hydraulic head gradient between the aquifer and the surface (Woith et al., 2011; Brehme et al., 2016). As a lower bound, the hydraulic head in the source aquifer/s must be greater than the topographic elevation at the point of spring discharge, referred to as the spring geomorphic threshold (Currell et al., 2017; Keegan-Treloar et al., 2021). The spring geomorphic threshold is the topographical elevation of the lip, mound or surface of the spring vent that the hydraulic head must exceed for the spring to discharge. If the hydraulic head in the source aquifer drops beneath the spring geomorphic threshold, the spring will cease to flow (e.g., Currell et al., 2017).

Although the conceptual model of the spring geomorphic threshold and spring discharge is simple, spring discharge rates may be temporally variable, arising from complex external stresses. For example, Criss (2010) found that spring discharge rates may be influenced by events occurring over multiple timescales. They concluded that the flow from Big Spring (Missouri, USA) represented the superposition of long-timescale regional hydraulic head gradients and short-timescale pulse-type events due to aquifer head changes following local precipitation.

Conceptually, spring discharge rates are controlled by the source-aquifer hydraulic head and the fault conductance. Assuming Darcian flow in the fault, the conductance can be defined as:

$$C_f = \frac{KA}{\Delta z} = \frac{Q}{\Delta h} \tag{2.4}$$

Where, C_f is the fault conductance [L^2 T^{-1}], K is hydraulic conductivity of the fault zone

[L T-1], A is the fault zone cross-sectional area to flow (i.e., fault width · fault length) [L^2], Δz is the difference in elevation between the spring geomorphic threshold and the source aquifer [L], Q is the spring discharge [L^3 T^{-1}], and Δh is the difference in elevation between the source aquifer head and the water level at the spring outlet [L]. However, as is the case in hydrogeology more generally, there are challenges in accurately quantifying K and Δh (e.g., Durner, 1994; Post and von Asmuth, 2013; Rau et al., 2019), which translate to uncertainties in estimates of C_f.

In practice the fault conductance is a difficult parameter to measure, which can present problems in the translation of aquifer hydraulic head to spring discharge rates. For example, Love et al. (2013a) compared spring discharge rates to head differences between the source aquifer and the surface for mound springs of the Great Artesian Basin (Australia). They found no predictable relationships between the hydraulic head differences and the rate of spring discharge suggesting the fault conductance was highly variable between springs. As the fault conductance was unknown, they were unable to predict how spring discharge might vary in response to future changes in aquifer hydraulic head.

The fault conductance can undergo changes if the fault is seismically active (e.g., Gudmundsson, 2000), which can lead to temporal variations in discharge. Changes in fault conductance, aquifer permeability and other aquifer properties (e.g., storativity) have been observed following earthquake events, resulting in variations in the discharge and/or water quality of the spring (e.g., Curewitz and Karson, 1997; Cox et al., 2012). For example, Cox et al. (2012) observed the emergence of new springs and a large change in groundwater levels following the magnitude 7.1 Darfield earthquake in Canterbury, New Zealand. These changes were hypothesised to be due to increased aquifer permeability, new fracture pathways, and changes in the aquifer properties (e.g., storativity and/or transmissivity).

Changes in spring water temperature and hydrochemistry were also observed following the Darfield earthquake, suggesting modified contributions from shallow meteoric and deeper groundwater to spring discharge (Cox et al., 2015). As such, the impact of seismic activity on fault behaviour and spring discharge may be an important consideration in characterising and managing fault-controlled springs in tectonically active regions.

2.2.3 Surface conditions and spring environments

Travertine structures are a common surface expression of springs (e.g., De Filippis et al., 2012; Henchiri et al., 2017; Karaisaoglu and Orhan, 2018), typically occurring where spring discharge is high in CO2, leading to carbonate mineral precipitation due to differences between the partial pressures of CO2 in the ascending water and the atmosphere (Keppel et al., 2011). Travertine deposits may occur along fault traces, indicating fault locations (Hancock et al., 1999; Brogi and Capezzuoli, 2009). Travertine structures can lead to the modification of spring discharge rates by sealing flow pathways or forming impoundments around the spring vents. For example, Soda Dam is a large dam-like structure encompassing several springs in New Mexico (USA) that significantly alters discharge to the surrounding environment (Goff and Shevenell, 1987). In areas of travertine deposition, it is often necessary that faults are active to prevent the fault from sealing, which can lead to the cessation of spring discharge (Brogi and Capezzuoli, 2009). As such, the travertine deposits surrounding springs have been extensively used to provide a historic record of the fault and spring discharge activity (e.g., Hancock et al., 1999; Brogi and Capezzuoli, 2009; Priestley et al., 2018). For example, Brogi et al. (2012) used travertine deposits around thermal springs in the Sarteano area (Italy) to reconstruct the historical locations of the main discharge areas, the record of faulting events and the physicochemical properties of the discharge waters.

Spring discharge to surface water bodies can support extensive ecosystems and niche habitats for endemic species (e.g., Wolaver and Diehl, 2011; Carvalho Dill et al., 2014). Spring-dependent ecosystems include terrestrial ecosystems surrounding the water source and aquatic ecosystems within the water source itself (Springer and Stevens, 2009). The variability, permanence and physiochemical characteristics (e.g., salinity, pH, temperature, nitrate) of spring discharge are key controls on the composition of dependent ecosystems (van der Kamp, 1995). However, detecting these relationships may be difficult, as Boy-Roura et al. (2013) found that some physiochemical characteristics of spring discharge (i.e., nitrate concentrations) remained constant annually while other characteristics (i.e., spring flow rates and electrical conductivity) were variable.

Spring discharge that provides stream baseflow can support aquatic and terrestrial species during dry periods (Rossini et al., 2018; Bonada et al., 2007). These may include secondary ecosystems that rely on spring-fed streams and lakes (e.g., Bonada et al., 2007). For example, the Doongmabulla Springs Complex (Australia) provides baseflow to the nearby Carmichael River and supports a wide diversity of endemic species, which vary between individual spring vents (Fensham et al., 2016a; Currell et al., 2017). This variability indicates permanence of discharge and relative isolation of individual springs.

Differences have been observed in taxon number and composition between springs with permanent discharge or pooled water, and those with intermittent flow (Meyer and Meyer, 2000; Wood et al., 2005). Species often have lifecycles that have adapted to the specific spring discharge conditions. For example, springs with permanent discharge or pooled water have been shown to host unique species that require constant water availability. One such example are hydrobiids (a small snail species) found around springs in the Great Artesian Basin (Australia) that cannot undergo desiccation for more than a few minutes and require neutral to basic water in their habitat (Ponder and Colgan, 2002). Conversely, intermittent springs have been shown to host species capable of tolerating dry periods (Meyer and Meyer, 2000; Wood et al., 2005). For example, in a study of springs in the English Peak District (United Kingdom), Wood et al. (2005) found species adapted to dry periods through diapause, aestivation or extended flight periods. Meyer and Meyer (2000) propose that the unique adaptions of species present in springs may be used as a proxy to determine the flow conditions. This was demonstrated by Erman and Erman (1995), who found that caddisflies, calcium concentrations, moss, rooted plants, and temperature could be used as a proxy for spring discharge permanence.

In addition to the species in springs, the historical composition of wetland flora and fauna surrounding springs can provide information on how spring discharge conditions (e.g., flow rates and water chemistry) have changed over time (Smith et al., 2003). If spring conditions change, the composition of wetland flora and fauna may change to adapt to the new flow conditions (Ashley et al., 2004; Deane et al., 2017). For example, Ashley et al. (2004) used pollen and diatom records in soil cores to assess changes in the regional hydrology resultant from past climate change events.

2.3 Field investigation techniques

Field investigation techniques are vital for gathering hydrogeological information to characterise and assist in the management of fault-controlled springs. Field investigation techniques include approaches to: (1) quantify spring discharge rates (e.g., weir-based methods), (2) identify source aquifers and their contribution to spring discharge (e.g., using isotopes and hydrochemistry from water samples), and (3) use geophysical techniques to investigate fault structure and properties (Figure 2.3). Additionally, field campaigns routinely characterise spring ecosystem health and examine cultural and archaeological values of

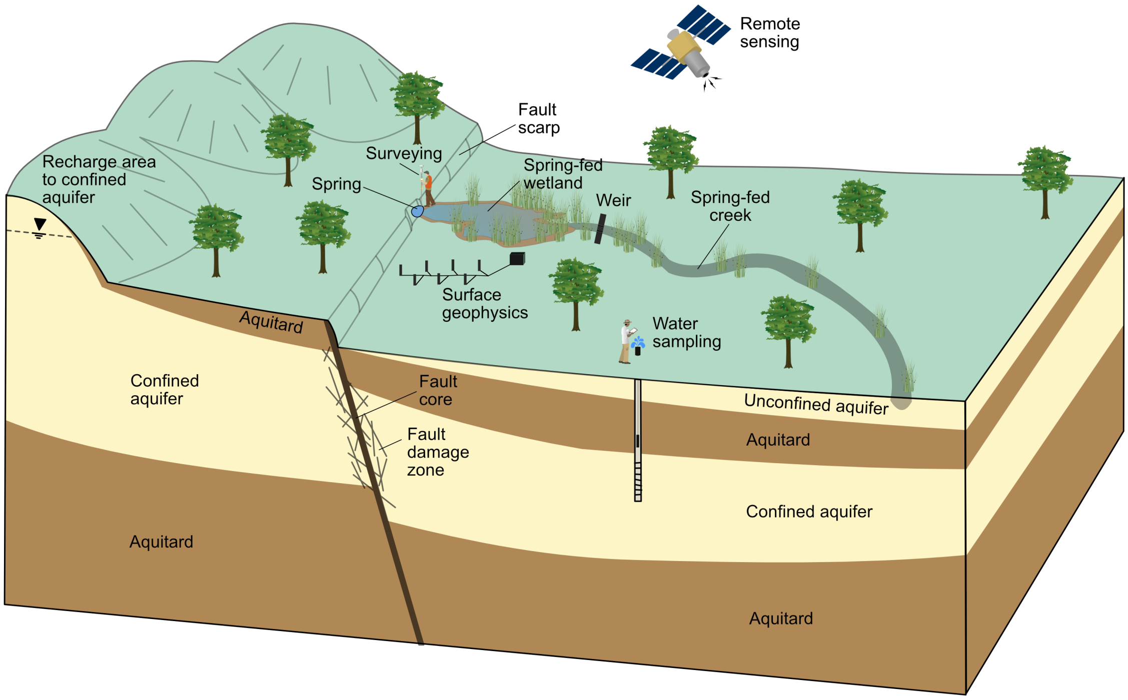

Figure 2.3: *Field investigation techniques for fault-controlled spring systems. Shown techniques include surface geophysics, water sampling for chemical and isotopic analysis, surveying of spring elevations, remote sensing, and a weir to measure spring discharge rates. The potentiometric surface from the recharge area to the right-hand side of the diagram is sufficient to provide flow to the spring.*

spring systems, although the related field techniques are not covered in the subsections that follow.

2.3.1 Methods for quantifying spring discharge

Quantifying spring discharge, particularly its temporal variations, provides valuable information on both ecological requirements and changes to driving factors that control spring flow. For example, spring discharge rates have been used to estimate groundwater recharge (e.g., Segadelli et al., 2021), the baseflow contribution of springs to streams (e.g., Fournier et al., 1976; Fournier, 1989; Friedman and Norton, 2007), geothermal heat flux (e.g., Fournier et al., 1976; Mariner et al., 1990), and lag times between recharge and changes in spring discharge (e.g., Manga, 1999; Celico et al., 2006). Additionally, knowledge of spring discharge rates provide insight into aquifer characteristics (e.g., permeabilities, vertical fluxes), which are useful for constraining hydrogeological models (e.g., Manga, 1997; Saar and Manga, 2004; Martínez-Santos et al., 2014). For example, Sato et al. (2000) found that spring discharge in Awaja Island (Japan) increased following an earthquake event (likely due to increased permeability), and gradually reduced following an approximately exponential trend. They used spring discharge observations to estimate the hydraulic diffusivity of the aquifer material between the spring and its recharge area using equations derived from Darcy's law.

Spring discharge rates have been quantified using a variety of techniques including direct flow measurements, Darcy's law-based approaches, physiochemical tracer methods and remote sensing techniques (see Table 2.1). The optimal method depends on the spring discharge rates being quantified, the physiochemical properties of water, the surrounding ecosystems, and the geomorphology of the spring vent. Details on the application of these techniques is provided below.

Direct measurements

The simplest form of direct flow measurements are timed volumetric measurements where the spring discharge is calculated from the time taken to fill a container of known volume (e.g., Gentry and Burbey, 2004; White et al., 2016; Segadelli et al., 2021). Despite the apparent simplicity of this technique, its application requires a localised discharge point, and can be problematic for springs with diffuse discharge. White et al. (2016) proposed that issues with diffuse discharge could be addressed by using flumes and sandbags to direct discharge to a measurement site. Although suitable for point in time measurements, caution is advised for the collection of long-term datasets as the modifications to the spring environment may degrade dependent ecosystems.

Weir-type approaches lead to volumetric spring discharge estimates by using either a pressure transducer or a ruler to measure the height of water that passes through a weir with a known cross-sectional area (e.g., Felton and Currens, 1994; Zhang et al., 2013; Mathon et al., 2015). The application of weir-type approaches requires discrete or directed spring discharge, as might occur within a channel or waterway (e.g., Heasler et al., 2009), or through geomorphic features or within the spring tail in the case of mound springs. Weir-type approaches have been applied to spring discharge rates of up to 1200 L/s (e.g., Celico et al., 2006; Falcone et al., 2012).

Where spring discharges to a stream or creek, differential gauging can be applied to estimate spring discharge as the difference in streamflow upstream and downstream of the spring. This technique was used by Manga (1999) to obtain spring discharge rates in the range of 3200 to 4800 L/s. Although, this requires that discharge can be accurately measured using a weir, which is not always possible (e.g., during high or low flows, or in areas of hyporheic exchange).

Darcy's law-based approaches

Approaches to calculate spring discharge based on Darcy's law use measured hydraulic gradients, flow cross-sectional areas, and hydraulic conductivity. Martínez-Santos et al. (2014) installed piezometers in springs to measure vertical head gradients, which were subsequently used, along with permeabilities obtained from slug tests, to estimate spring discharge based on Darcy's law. This was applied to the Fuentes Grandes springs (Spain), leading to an estimate of spring discharge of $\approx$0.5 L/s. Despite the relatively simple nature of Darcy's law-based methods, these approaches are rarely applied in the literature, likely due to the high uncertainty in measurements of hydraulic conductivity.

Chemical tracers

The most widely applied chemical tracer technique for the quantification of spring discharge to a stream is the chloride inventory technique (e.g., Ellis and Wilson, 1955; Fournier, 1989; Friedman and Norton, 2007). Discharge rates are quantified by sampling chloride concentrations in spring discharge and in a stream in the reaches above and below where the spring contributes to streamflow (Ellis and Wilson, 1955; Fournier et al., 1976). If differences in chloride concentrations are not detectable, a salt-dilution test can be used (e.g., White et al., 2016), where a known concentration of salt is released, and the concentration is monitored downstream. The chloride inventory method is not well suited to continuous automated monitoring as typically chloride concentrations cannot be easily measured in the field, although electrical conductivity has been used as a proportional surrogate for chloride (Norton and Friedman, 1985) allowing for the analysis of temporal changes. The chloride inventory method has been demonstrated for spring discharge rates between 0.39 and 3644 L/s (Ingebritsen et al., 2001).

Remote sensing

Remote sensing provides an attractive approach to quantify spring discharge, particularly for isolated data-sparse areas, as it relies on aerial- or satellite-derived products. Two main strategies have been applied, namely estimated wetland area (e.g., Williams and Holmes, 1978; White and Lewis, 2011; White et al., 2016), and aerial thermal imagery (e.g., Haselwimmer et al., 2013).

Wetland area approaches use a log-linear model to relate the spring wetland area to the spring discharge rate. Typically, a site-specific relationship is developed by measuring spring discharge rates (e.g., with a direct measurement technique) and using a log-linear regression model to develop a relationship between the wetland area and the observed spring discharge rates (e.g., Fatchen, 2001; White and Lewis, 2011). This relationship can then be used to monitor how the spring discharge rates change over time based on remotely sensed variations in the wetland area (e.g., Fatchen, 2001; White and Lewis, 2011). Generic relationships based on previous studies may be useful to provide approximate estimates of spring discharge rates. However, site-specific ecohydrological conditions will lead to different relationships between sites. Furthermore, Fatchen (2001) warned that extrapolating these relationships beyond the range of observed measurements (i.e., to extreme high or low discharge rates) can be problematic as the relationship may be valid for only a specific range of discharge rates. Wetland area-based approaches have been used to quantify spring discharge rates ranging from $\approx$0.01 L/s (Fatchen, 2001) to $\approx$200 L/s (Williams and Holmes, 1978).

Aerial thermal imagery can provide an alternative to wetland area-based remote sensing approaches, particularly for thermal springs. Haselwimmer et al. (2013) used remotely sensed thermal imagery (1 m pixels) to estimate spring discharge from the Pilgrim Hot Springs (Alaska). Their discharge estimates were obtained by first calculating a total heat flux from the springs and converting heat flux to a volumetric flux based on an assumed geothermal temperature for spring discharge and the thermal properties of water. This approach yielded estimates of spring discharge ranging between 1.1 L/s and 17 L/s, which was in reasonable agreement with field measurements of spring discharge. However, Haselwimmer et al. (2013) noted that discharge calculations were particularly sensitive to wind speeds.

Table 2.1: *Examples of spring discharge with the method and range of discharge values reported. NA (not available) denotes cases where discharge rates were not reported or were provided as a summation from multiple springs.*

Method	Examples	Spring discharge (L/s)
Chloride inventory method	Ellis and Wilson (1955)	NA
	Fournier et al. (1976)	NA
	Norton and Friedman (1985)	NA
	Fournier (1989)	NA
	Mariner et al. (1990)	0.4 to 120
	Ingebritsen et al. (2001)	0.39 to 3,644
	Friedman and Norton (2007)	$\approx$395 to $\approx$3,250
Wetland area as a proxy	Fatchen (2001)	0.01 to 10
	Fensham and Fairfax (2003)	NA
	White and Lewis (2011)	$\approx$5 to $\approx$170
	White et al. (2016)	$\approx$0.001 to $\approx$1,427
Weir-type methods	Felton and Currens (1994)	14 to 71
	Swanson and Bahr (2004)	3 to 30
	Celico et al. (2006)	0 (no flow) to 440
	Heasler et al. (2009)	NA
	Amoruso et al. (2011)	65 to 166
	White and Lewis (2011)	NA
	Falcone et al. (2012)	400 to 1,200
	Haselwimmer et al. (2013)	1.1 to 17
	Zhang et al. (2013)	0.1 to 6
	Mathon et al. (2015)	1 to 10
	White et al. (2016)	$\approx$0.005 to $\approx$300
Aerial thermal imagery	Haselwimmer et al. (2013)	1.1 to 17
Manual container measurements	King et al. (1994)	$\approx$0.15 to $\approx$0.6
	Gentry and Burbey (2004)	0.1 to 0.25
	White et al. (2016)	$<$0.15
	Segadelli et al. (2021)	NA
Salt dilution tests	White et al. (2016)	0.09 to 0.6
Darcy's law	Martínez-Santos et al. (2014)	$\approx$0.5
Differential stream gauging	Manga (1999)	3,200 to 4,800
Venturimeter	Amoruso et al. (2011)	65 to 166

2.3.2 Techniques to identify water origins

Hydrochemistry

Bivariate plots, ternary diagrams, and specialised plots are often used to classify water types as a first step in the hydrochemical analysis of spring systems. Widely applied approaches include bivariate plots (e.g., Grobe and Machel, 2002), Schoeller diagrams (e.g., Bajjali et al., 1997), Piper plots (e.g., Brugger et al., 2005; Crossey et al., 2009; Alçiçek et al., 2016), ternary diagrams (e.g., Duchi et al., 1995; Apollaro et al., 2012) and Langelier-Ludwig diagrams (e.g., Brombach et al., 2000; Frondini et al., 2009). Piper plots are a graphical procedure for visualising water chemistry and have been applied in studies of spring systems to identify contributing groundwater endmembers to spring discharge (e.g., Brugger et al., 2005; Crossey et al., 2009; Alçiçek et al., 2016). Duchi et al. (1995) used a ternary diagram with analytes of HCO_3, SO_4 and Cl to classify water samples as groundwater (high HCO_3), mature water (high Cl) or steam heated acidic waters (high SO_4). They found that the spring waters plotted towards the HCO_3 apex of the diagram, suggesting groundwater from a carbonate-source aquifer. Langelier-Ludwig diagrams (rectangular diagrams based on the percent of cations from Na + K and Mg + Ca, and the percent of anions from HCO_3 + CO_3 and SO_4 + Cl) have been used in spring source-water studies to identify endmember water-types, geochemical reactions, and mixing (e.g., Frondini et al., 2009; Brogi et al., 2012). For example, Frondini et al. (2009) used a Langelier-Ludwig diagram to analyse hydrochemistry from springs and geothermal carbonate and metamorphic formations, finding four distinct water groups reflecting the geology and geochemistry of the source aquifers. These groups were tightly clustered, suggesting the sources were hydraulically isolated, and there was minimal mixing between sources.

The minerals present in spring discharge have been extensively used to characterise the subsurface geology and potential source aquifers (e.g., Brombach et al., 2000; Brugger et al., 2005; Frondini et al., 2009). Mineral speciation and saturation indices can be calculated using geochemical modelling software (e.g., PHREEQC, SOLMINEQ-88, Geochemists Workbench) and as they are dependent on temperature, these geochemical processes and water-rock interactions have been used to estimate the temperature in the source aquifer (e.g., Gemici and Tarcan, 2002) using a variety of techniques referred to as geothermometry (see Section 2.3.3).

2.3.3 Isotopes and age tracers

The stable isotopes of water (^{18}O, ^{17}O, ^{16}O and ^{2}H, ^{1}H), have been used to trace the origin of spring water and provide information on the climatic and environmental conditions at the time of recharge (Alcicek et al., 2016). Comparing the stable isotopes of water with the local meteoric water line can provide insights into how evaporation and transpiration have influenced water composition and the seasonality of recharge (Appello and Postma, 2010). Stable isotopes of water have been used extensively to investigate the recharge elevation (e.g., Amoruso et al., 2011), the seasonality or age of spring source waters (e.g., Ingebritsen et al., 1992; Grobe and Machel, 2002; Alcicek et al., 2016) and evaporation and/or transpiration (e.g., Duchi et al., 1995; Brusca et al., 2001; Brugger et al., 2005; Della Porta, 2015).

Age tracer techniques utilise the known rates of radioactive decay of isotopes to determine groundwater age. By comparing the activity in a water sample with the initial activity (e.g., that in the atmosphere) it is possible to infer the age of the water (Kazemi et al., 2006; Bethke and Johnson, 2008). By examining age of spring discharge, it is possible to assess the vulnerability to impacts such as contamination and/or groundwater drawdown (Kazemi et al., 2006; Bethke and Johnson, 2008).

Tritium (^3H), a tracer that can be used to distinguish the presence of modern waters aged <50 years old, has been used in studies of fault-controlled springs (e.g., Heinicke and Koch, 2000; Demlie et al., 2008; Alcicek et al., 2016) to distinguish old deep-derived water from shallow younger waters. Radon-222 (^{222}Rn), is another short-lived (half-life of 3.82 days) radioactive tracer that has been used to indicate the rapid ascent of water from a deep reservoir in spring discharge (e.g., Brugger et al., 2005) and to identify the contribution of ^{222}Rn to water during flow through fractures or faults (Choubey et al., 2000). Changes in ^{222}Rn concentrations have also been observed due to stress regimes before earthquake events, which has been used to provide information on the stress regimes and activity of faults beneath springs (Kuo et al., 2006).

Other useful tracer techniques are based on isotopes of the carbon atom and their relative ratios in a water sample. The analysis of $\delta^{13}C$ can be applied to CO_2 gases (e.g., Cartwright et al., 2002; Battani et al., 2010), CH_4 gases and carbonate minerals such as travertine (e.g., Brogi et al., 2012; De Filippis and Billi, 2012; Alcicek et al., 2016). Battani et al. (2010) used the $\delta^{13}C$ of bubbling CO_2 in spring discharge to assess the source of water to the springs and they found $\delta^{13}C$ was similar to typical values for the mantle indicating a reasonable contribution (likely $\approx$40%) from a deeper source. Often the $\delta^{13}C$ values can vary within an aquifer unit, which makes it difficult to select a representative value for the aquifer. $\delta^{13}C$ signatures from biological sources have been found in spring discharge to assist in the determination of the source of spring water. For example, Brugger et al. (2005) found $\delta^{13}C$ in dissolved inorganic carbon ranged from -12.3 to -8.7 ‰ indicating a biological source, likely C-4 plants.

The $\delta^{13}C$ of CO_2 of travertine deposits surrounding springs has also been used to investigate the source of water contributing to spring discharge. For example, Brogi et al. (2012)

studied δ^{13}C values in travertine surrounding springs and found values of between 1.6 and -2.5 ‰, indicating a mix between hydrothermal fluids (δ^{13}C $\geq$ 0) and shallow waters (δ^{13}C < -4). The benefit of examining travertine deposits rather than water from the springs or aquifer directly, is that samples can be collected without the need to install invasive infrastructure (e.g., wells), and the deposits can potentially provide a historical record of δ^{13}C. Similarly, radiocarbon (^{14}C) has been used to calculate the age of old travertine deposits using an initial activity based on the ratio of the ^{14}C activity in recent travertine deposits and atmospheric CO_2 (Mas-Pla et al., 1992).

Noble gases are produced in the crust (e.g., ^{4}He, ^{4}0Ar), the mantle (e.g., ^{3}He) or the atmosphere (e.g., ^{20}Ne, ^{36}Ar) and have been used in studies of springs to assess the contributions to spring discharge from recent recharge and old deeper groundwater (Gilfillan et al., 2011). The ^{3}He/^{4}He ratio has been used widely in fault-controlled spring studies to assess the contributions of gases from the mantle and/or crust to spring source waters (e.g., Hoke et al., 2000; Haszeldine et al., 2005; Crossey et al., 2006; Crossey et al., 2009). In contrast to ^{3}He and ^{4}He, ^{20}Ne is primarily produced in the atmosphere and can be used to assess the atmospheric contribution to a sample (Gilfillan et al., 2011). For example, Chen et al. (2006) examined ^{4}He/^{20}Ne in spring water samples to assess the relative contribution of fluids containing crustal gases (^{4}He) and atmospheric gases (^{20}Ne). They observed high ratios in spring water relative to the atmosphere, indicating the addition of ^{4}He from a deep source, suggesting water may ascend via a fault.

^{40}Ar/^{36}Ar ratios have been measured in springs emanating from faults (e.g., Brauer et al., 2011; Gilfillan et al., 2011), to assess the contribution to spring water from gases from the mantle (^{40}Ar/^{36}Ar ratio $\approx$40,000; Marty and Dauphas (2003)) and the atmosphere (^{40}Ar/^{36}Ar ratio = 295.5; Marty (1995)). For example, Gilfillan et al. (2011) observed ^{40}Ar/^{36}Ar ratios from spring samples ranging from 1369 to 1687, indicating a contribution of ^{40}Ar from the mantle. Crossey et al. (2006, 2009) compared ^{40}Ar/^{36}Ar from spring samples with the concentrations of other noble gases (e.g., ^{3}He) as different noble gases have distinct sources (i.e., the mantle, the crust, the atmosphere, etc.).

Temperature and geothermometers

The rate of groundwater ascent and contribution from deep aquifers to spring discharge can be estimated from spring water temperatures (Apollaro et al., 2012; Held et al., 2018). Typically, the temperature of groundwater increases with depth at a rate of 1 °C per 20-40 m (Anderson, 2005). In cases where springs source water from deep geological units, the spring discharge temperature may be elevated relative to ambient temperatures (Kresic, 2010; Wolaver et al., 2020). The temperature of spring source-water is related to a variety of factors including the source depth, the rate of ascent, the thermal conductivity of the geological media and the ambient surface temperatures (Blackwell, 1978; Brugger et al., 2005). The temperatures of spring discharge and aquifers can be measured directly using temperature sensors (e.g., Fairley and Hinds, 2004) or estimated based on chemical or isotopic indicators, called 'geothermometers' (e.g., Sakai and Matsubaya, 1974; Fournier, 1981; Giggenbach, 1988; Kharaka and Mariner, 1989; Arnorrson, 2000).

Geothermometers reflect geochemical reactions that occurred under equilibrium conditions and the rate of these reactions can be slow relative to the rate of groundwater flow (Fournier, 1981; Giggenbach, 1988). The use of geothermometers may better capture the temperature in the spring source aquifer than direct temperature measurements, as discharging waters can quickly equilibrate to ambient groundwater or surface temperatures, especially where the rate of ascent is slow. Once spring discharge samples have been collected, chemicals or isotopes can be considered to assess the temperature in the source aquifer

Table 2.2: *Geothermometers and the temperature range over which they are applicable. Note X is used to symbolise the concentration or saturation of the mineral when the chemical formula is too long (e.g., for Quartz), nsl denotes geothermometers with no steam loss and wsl denotes those with steam loss.*

Geothermometer	Equation	Range	Case studies
Quartz (nsl)	$T(°C) = \frac{1309}{5.19 - logX} - 273.15$	0 - 250 °C	Duchi et al. (1995)
			Bajjali et al. (1997)
			Brugger et al. (2005)
Quartz (wsl)	$T(°C) = \frac{1522}{5.75 - logX} - 273.15$	0 - 250 °C	Fournier and Rowe (1966)
			Ingebritsen et al. (1992)
			Duchi et al. (1995)
Chalcedony	$T(°C) = \frac{1302}{4.69 - logX} - 273.15$	0 - 250 °C	Duchi et al. (1995)
			Bajjali et al. (1997)
			Brugger et al. (2005)
a-Cristobalite	$T(°C) = \frac{781}{4.51 - logX} - 273.15$	0 - 200 °C	Duchi et al. (1995)
Amorphous silica	$T(°C) = \frac{731}{4.52 - logX} - 273.15$	0 - 250 °C	Duchi et al. (1995)
Na/K (Fournier)	$T(°C) = \frac{1217}{log(Na/K) + 1.483} - 273.15$	>150 °C	Duchi et al. (1995)
			Brombach et al. (2000)
Na/K (Truesdell)	$T(°C) = \frac{855.6}{log(Na/K) + 0.8573} - 273.15$	>150 °C	Duchi et al. (1995)
Na-K-Ca	$T(°C) = \frac{1647}{log(Na/K) + \beta(log(\sqrt{Ca}/Na) + 2.06) + 247} - 273.15$	<100 °C, β = 4/3	Ingebritsen et al. (1992)
		>100 °C, β = 1/3	Duchi et al. (1995)
$\delta^{18}O(SO_4 - H_2O)$	$a = \frac{1000 + \delta^{18}O(HSO_4)}{1000 + \delta^{18}O(H_2O)}$	>0 °C	Ingebritsen et al. (1992)
	$T(°C) = \pm \frac{1200\sqrt{2}\sqrt{1000ln(a) + 4.1}}{1000ln(a) + 4.1} - 273.15$		Bajjali et al. (1997)
P_{CO_2}	$T(°C) = (logP_{CO_2} + 3.78)0.0168^{-1}$	100-350 $°C$	Gemici and Tarcan (2002)

(Fournier, 1981; Giggenbach, 1988). Geothermometry has been extensively applied to studies of fault-controlled springs to estimate the temperature in the source aquifer (e.g., Ingebritsen et al., 1992; Duchi et al., 1995; Bajjali et al., 1997; Brombach et al., 2000; Goff et al., 2000; Gemici and Tarcan, 2002; Brugger et al., 2005; Apollaro et al., 2012). Each geothermometer has a specific temperature range over which it is valid. The width of these temperature ranges vary between geothermometers, which means geothermometers with a large range can be used to approximately estimate the temperature, which subsequently can be refined using geothermometers with a narrower temperature range. For example, in a study of the Paralana hot springs (South Australia), Brugger et al. (2005) used the saturation indices of quartz and chalcedony to estimate temperatures and refined these estimates using the saturation indices of other minerals with narrower temperature ranges (e.g., illite, montmorillonite, K-feldspar, muscovite). Table 2.2 shows studies of fault-controlled spring systems where geothermometers were applied and the temperature range over which they are suitable.

2.3.4 Geophysical investigation techniques to determine fault structure and properties

Geophysical techniques are a non-intrusive approach that have been used to assess subsurface hydrogeological processes (Revil et al., 2012; Inverarity et al., 2016; Banks et al., 2019). Both faults and springs have unique physical properties that are discernible using geophysical techniques. For example, the fault core may have a vastly greater density than the surrounding protolith, resulting in gravity anomalies in the vicinity of faults (Hochstein and Nixon, 1979). While springs can feature resistive zones due to fluid and gases in permeable conduits (Inverarity et al., 2016).

A common first phase in hydrogeological investigations is to identify the locations of faults in large, poorly understood regions. Seismic surveys can assist by locating faults in regions up-to several kilometres in extent (Brogi et al., 2012). Similarly, magnetic and gravitational anomalies can be used to identify the location of faults using field measurements, airborne surveys or remote sensing products (Hochstein and Nixon, 1979; Ingebritsen et al., 1992; Finn and Morgan, 2002). Another secondary source of information is the location of springs themselves, as the geographical location of springs may indicate the fault location, which can be particularly clear when springs are aligned along a fault trace (e.g., Brogi et al., 2012). Together, these techniques provide a useful approach to identify the locations of faults for further study, particularly in data-poor areas where little subsurface information is available.

Once fault locations are identified, studying the structure (i.e., the core and damage zone) and properties (e.g., permeability, saturation) of the fault is often of interest. Electrical resistivity tomography can be applied to characterise fracture networks in the damage zone of a fault (Byrdina et al., 2009; Carbonel et al., 2013). For example, Byrdina et al. (2009)

used electrical resistivity tomography transects to image faults in the area surrounding the Syabru-Bensi springs (Nepal) and concluded that resistive zones observed beneath springs were the result of fractures acting as conduits for the flow of water and gas. Applying multiple geophysical techniques in combination can provide complementary information. For example, Inverarity et al. (2016) conducted a study using self-potential, magnetotellurics and time-domain electromagnetics to image four mound springs in the Great Artesian Basin. Transects across the spring sites revealed an increase in self potential beneath the spring vents (which was hypothesised to represent upwards groundwater flow through a fault), while magnetotellurics and time-domain electromagnetics were used to image the geological structure and faults existing beneath the springs. Thus, the results from the three geophysical methods applied by Inverarity et al. (2016) were combined to create a conceptual model of flow through faults to each of the springs.

2.4 Numerical modelling

Although analytical solutions exist for evaluating groundwater flow and solute transport within faults (e.g., Robinson and Werner, 2017), hydrological modelling of field-scale fault-controlled spring systems has thus far required the implementation of numerical methods (e.g., Folch and Mas-Pla, 2008; Magri et al., 2010; Yager et al., 2013). The representation of faults within numerical models depends on the intended use of the model. Types of groundwater models that include fault-controlled spring systems can be subdivided into: (1) Regional-scale, groundwater management models (e.g., Brunetti et al., 2013; OGIA, 2019; OGIA, 2020), and (2) Local-scale, process-investigation models (e.g., López and Smith, 1995; Abbo et al., 2003; Sebben and Werner, 2016a). Both scales of fault-analysis face limitations. For example, the simulation of the fine-scale processes known to control the flow through faults is difficult at the resolution of regional-scale models, particularly if solute transport is considered (Weatherill et al., 2008; Sebben and Werner, 2016b). On the other hand, groundwater management issues that require representation of the flow through faults, such as the impacts of pumping, mining and climate variability in faulted aquifers, typically require consideration of large scales, and therefore, process-investigation models may have limited capacity to inform management decision making.

The main features of faults, described in Section 2.2.1, are represented to varying degrees in previous modelling studies, often due to limits imposed by model discretisation and associated model run times. Typically, there are three different approaches to the representation of faults in mathematical models, consistent with the categorisation suggested by Medici et al. (2021) for fracture flow in carbonate-rock aquifers, as: (1) cases where the fault core and damage zone may be integrated into a single unit or treated separately, but both are represented as equivalent porous media using macro-scale hydraulic properties (e.g., Bense and Person, 2006; Magri et al., 2010); (2) the fault core and damage zone are integrated into a single unit, and treated as a discrete conduit, whereby flow within the fault can be considered as Darcian (e.g., Poulet et al., 2021) or non-Darcian (e.g., Liu et al., 2017). The latter applies when fluxes are sufficiently high to violate the linearity assumptions of Darcian flow; (3) the fault core and damage zone are integrated into a single unit and represented as a network of discrete fractures (e.g., Huang et al., 2019). Caine et al. (1996) refers to categories (2) and (3) as 'localised conduit' and 'distributed conduit' representations, respectively.

The flow of groundwater through faults is often presumed to occur in a similar manner to flow through fractures (e.g., Caine and Forster, 1999), which is far more widely studied than flow through faults. Fracture flow may be Darcian or non-Darcian, depending on whether discharge is linearly or non-linearly related (respectively) to the head gradient (e.g., Reimann et al., 2011). Typically, the transition between Darcian and non-Darcian flow (which is typically associated with laminar and turbulent conditions) in fractures is predicted from the Reynolds number (Re), as given by Li et al. (In press) for a single fracture:

$$R_e = \frac{2bq}{2v} \tag{2.5}$$

where $2b$ is the characteristic length for rock fractures, typically assumed to be the fracture aperture [L], q is the specific discharge [L T^{-1}], and v is the kinematic viscosity [L^2 T^{-1}]. According to Quinn et al. (2020), there is disagreement about the critical Reynolds number representing the change of flow regime within fractures, although they reported that this is generally found to be <20. Li et al. (in press) suggest an R_e value of about 0.9 as the upper limit for Darcian flow in fractures. They found that open fractures of aperture greater than 2.5 10^{-4} m involved non-Darcian flow, whereas the flow within smaller fractures could be treated as Darcian.

Where faults are treated as a fracture or network of fractures, the equivalent hydraulic conductivity of the fracture (K_f [L T^{-1}]) is commonly adopted in models. K_f is related to the fracture aperture via the cubic law, as (Witherspoon et al., 1980):

$$K_f = \frac{2b^2 \rho g}{12\mu} \tag{2.6}$$

where μ is fluid density [M L^{-3}], g is acceleration of gravity [L T^{-2}], and μ is the dynamic fluid viscosity [M L^{-1}T^{-1}]. Sebben and Werner (2016a, 2016b) used this approach in their analyses of solute transport in single fractures within otherwise permeable aquifers.

2.4.1 Equivalent porous media

The most common approach for regional- and local-scale numerical investigations (i.e., scales larger than a few 10s of metres) commonly adopt the representation of faults described above as Category (1), i.e., the equivalent porous media approach for the fault core and damage zone (e.g., Bense and Person, 2006; Magri et al., 2010). In representing the fault core and damage zone as equivalent porous media, small-scale flow processes expected in the fractures of the damage zone are neglected.

The porous media properties assigned to the core and damage zones, when these zones are explicitly represented in numerical models, vary over several orders of magnitude across modelling case studies. For example, Taillefer et al. (2017) used an equivalent porous media for the damage zone, with permeability four orders of magnitude greater than the core zone. Magri et al. (2010, 2012) also adopted a large permeability ratio between the two zones in their finite-element models, although the numerical value of the ratio is not given (i.e., the isotropic hydraulic conductivity of the core zone is reported as $\approx$0 m/year, with an isotropic value of 32 m/year attributed to the damage zone). These core-damage zone contrasts in permeability exceed the average permeability ratio between the two zones obtained by Scibek (2020) and Forster and Evans (1991) (i.e., two orders of magnitude difference; Section 2.2.1).

When adopting the equivalent porous media approach and treating the core and damage zone as a single unit, faults may be assigned an anisotropic hydraulic conductivity, where the hydraulic conductivity parallel to the fault plane is greater than the one perpendicular to it (e.g., López and Smith, 1996; Bense et al., 2003; Bense et al., 2008). Other cases adopt isotropic hydraulic properties and neglect the enhanced permeability parallel to the fault or the reduced permeability perpendicular to the fault. For example, Marshall et al.

(2020) neglected the damage zone and represented the fault as a barrier to flow, with low permeability (relative to the protolith) assigned to the fault. López and Smith (1995) and Folch and Mas-Pla (2008) adopted higher permeability (relative to the protolith) for the fault to represent its tendency to transmit flow along the fault axis. Scanlon et al. (2003) used the Horizontal-Flow Barrier (HFB) package of MODFLOW (Hsieh and Freckleton, 1993) to represent faults implicitly as isotropic, low-permeability features (the HFB package cannot simulate anisotropic features) in simulations of the Barton Springs Edwards Aquifer (USA).

McCallum et al. (2018) included the modified conductance approach or "Manzocchi method" (e.g., Manzocchi et al., 1999) as a variation to the equivalent porous media approach. In the Manzocchi method, fault properties are represented by adopting "transmissivity multipliers", which are functions that modify the flow terms at the model cells where faults are located, rather than explicit representation of faults and their conductance properties. While the Manzocchi method is not commonly applied in groundwater flow studies, it is widely applied in the petroleum industry, as discussed by Turnadge et al. (2018). Application examples of the Manzocchi method can be found in Manzocchi et al. (2010), Michie et al. (2018), Wilson et al. (2020), and Islam and Manzocchi (2021), among others.

McCallum et al. (2018) undertook a comparison between the Manzocchi method and the equivalent porous media. Their numerical modelling results demonstrated that in cases where a fault acts as a barrier to flow, either method to represent the fault can be adopted. However, in cases where the fault acted as a conduit to flow, there was poor agreement between the two methods of representing faults.

2.4.2 Discrete conduits

Caine and Forster (1999) suggested that strike-slip faults (Figure 2.2c, d) may be treated as localised, discrete conduits, representing flow within the space between adjacent slipped walls of the fault. Grant (2020) advised that the fault core may be converted to a conduit for fluid movement if, prior to faulting, the protolith was over-consolidated, causing dilation and enhanced fracturing of the core. For example, Coates et al. (1994) suggested that Moosy Brook Spring (USA) is an example of a fault-controlled spring caused by a localised conduit-type fault, where spring discharge between 189 and 227 L/min was observed.

The simulation of faults as discrete conduits requires the application of 'hybrid models' (Reimann et al., 2011), wherein one-dimensional features can be embedded into n-dimensional models (e.g., Shoemaker et al., 2008; Sebben and Werner, 2016a, 2016b; Poulet et al., 2021). When flow through discrete apertures is Darcian, the cubic law applies (equation (6)), whereas non-Darcian flow requires application of nonlinear, pipe flow equations, such as the Forchheimer and Darcy-Weisbach equations (e.g., Shoemaker et al., 2008; Qian et al., 2015). The choice of approach depends on Re (equation (5)). Both laminar and turbulent flow can be simulated using common groundwater flow codes, such as the Conduit Flow Process (CFP) of MODFLOW-2005 (Shoemaker et al., 2008) or the conduit flow model capability of FEFLOW (Diersch, 2014). Both codes allow conduits to be embedded into the porous matrix.

Fang and Zhu (2018) reported that the adoption of the cubic law and the assumption of Darcian flow to simulate large fractures leads to overestimates of groundwater flow rates. Similarly, Reimann et al. (2011) found that the assumption of laminar flow within conduits overestimated groundwater discharge via springs. More generally, Scanlon et al. (2003) concluded that the validity of a groundwater model to estimate flow rates is limited if laminar flow is assumed in a faulted system. However, groundwater numerical investigations rarely adopt non-Darcian flow to represent faults (e.g., Liu et al., 2017; Xue et al., 2019). Rather, non-Darcian flow is more frequently applied for the study of karst conduits (e.g., Saller et al., 2013; Reimann et al., 2011; Kavousi et al, 2020; Zheng et al., 2021), which have considerably larger apertures than fractures.

2.4.3 Discrete fracture networks

The representation of faults using fracture networks allows for the analysis of local-scale processes that arise within the complex geological structures of faults, including localised permeability distributions (e.g., Caine and Forster, 1999). However, there are few examples of these in the published literature (e.g., Herbert, 1996; Caine and Forster, 1999; Huang et al., 2019; Volatili et al., 2019). Numerical models adopting discrete fracture networks (not necessarily related to faults) often apply stochastic techniques (e.g., de Dreuzy et al., 2012; Li et al., 2020) to explore the uncertainty that arises from the lack of sufficient field data to characterise fracture networks (Herbert, 1996; Medici et al., 2021). The stochastic representation of discrete fracture networks represents the most complex approach to the simulation of faults (Turnadge et al., 2016) and requires the largest computational burden (McCallum et al., 2018). Attempts to capture the physical realism of fracture networks using simpler, more-efficient representations have been made by Romano et al. (2017, 2020), who provides examples of the conversion from discrete fracture networks to equivalent porous media, allowing for more efficient simulation of large-scale fractured systems.

2.4.4 Numerical modelling case studies of fault-controlled springs

Despite the significant number of studies relying on numerical modelling to understand groundwater flow systems affected by faults (e.g., Bense et al., 2013), the numerical simulation of fault-controlled springs is scarce. Table 2.3 lists the study objectives, model characteristics, and conceptualisations for nine modelling case studies found in the published literature.

Table 2.3 shows that in the context of groundwater flow, the equivalent porous media approach is the most widely used to represent the influence of faults, whereas the adoption of a specified head is the most common approach to treat fault-controlled springs in models. MODFLOW and FEFLOW are the most commonly applied codes adopted in studying fault-controlled spring systems. Only one regional-scale study (that used FEFLOW), undertaken by Brunetti et al. (2013), was apparent in the literature, using the earlier definition of regional-scale (Section 2.4).

2.5 Management

Due to the high levels of ecological endemism, cultural significance and heritage values associated with many springs, their protection is a critical priority for environmental and natural resource management (Hatton and Evans, 1998; McMorran, 2008; Kresic, 2010; Brake et al., 2019). However, effective spring management, i.e., to achieve ecological and other objectives, presents multiple, substantial challenges. These include the high sensitivity of many spring environments and their ecosystems to disturbances, which requires a precautionary approach to avoid potentially irreversible damage (e.g., Kresic, 2010). The loss of many significant spring complexes worldwide over the past century (e.g., Fensham et al., 2016b; Silcock et al., 2020) highlights their vulnerability to human pressures.

Human pressures on springs can lead to serious environmental degradation and/or the extinction of rare or endangered ecosystems (Ponder, 1986; Fensham et al., 2010) due to changes in the flow rate, wetland area or water chemistry. Management regimes aimed at protecting springs were generally broadly applicable to both fault-controlled springs and other spring types, rather than being specifically focused on fault-controlled springs. These regimes often involved the use of drawdown trigger levels, which define maximum allowable drawdown thresholds that can be used to instigate changes to activities that modify

Table 2.3: *Examples of numerical modelling case studies of fault-controlled springs.*

Reference	Objective	Scale	Approach/model	Fault and spring conceptualisation
López and Smith (1995)	Fault-controlled thermal springs in hypothetical mountainous landscape	Local	Finite-element (3D)/Galerkin numerical method	Fault: Homogeneous, isotropic equivalent porous medium of uniform width Spring: Constant specified head (equal to the land surface)
López and Smith (1996)	Fault-controlled thermal springs in hypothetic mountainous landscape	Local	Finite-element (3D)/Galerkin numerical method	Fault: Heterogeneous, anisotropic equivalent porous medium of uniform width Spring: Constant specified head (equal to the land surface)
Abbo et al. (2003)	Fault-controlled onshore and offshore springs at Lake Kinneret, Israel	Local	Finite-difference (3D)/MODFLOW-M3TDMS	Fault: Homogeneous, anisotropic equivalent porous medium of uniform width Spring: Time-dependent specified head
Folch and Mas-Pla (2008)	Surface-groundwater interaction through faults in Selva basin, Catalunya, Spain	Local	Finite-difference (2D)/MODFLOW	Fault: Homogeneous, isotropic equivalent porous medium of uniform width Spring (stream): Constant specified head
Magri et al. (2010)	Fault-controlled thermal springs in Aegean region, western Turkey	Local	Finite-element (2D)/FEFLOW	Fault: Explicit representation of the core and damage zone as homogeneous, isotropic equivalent porous medium of uniform width Spring: Constant specified head (equal to the land surface)
Magri et al. (2012)	Seawater circulation in fault-controlled thermal springs in Aegean region, western Turkey	Local	Finite-element (2D)/FEFLOW	Fault: Explicit representation of the core and damage zone as homogeneous, isotropic equivalent porous medium of uniform width Spring: Constant specified head (equal to the land surface)
Brunetti et al. (2013)	Fault-controlled thermal springs in Tivoli, Italy	Regional	Finite-element (3D)/FEFLOW	Fault: Homogeneous, isotropic equivalent porous medium of uniform width Spring: Constant specified head (equal to the land surface)
Yager et al. (2013)	Fault-controlled springs in a karst aquifer in Shenandoah Valley, USA	Local	Finite-difference (3D)/MODFLOW	Fault: Homogeneous, anisotropic equivalent porous medium of uniform width Spring: Head-dependent flow boundary
Üner and Dogan (2021)	Fault-controlled thermal springs in Western Anatolia, Turkey	Local	Finite-volume (2D)/ANSYS FLUENT	Fault: Explicit representation of the core and damage zone as homogeneous, isotropic equivalent porous medium of uniform width Spring: Recharge boundary condition

water levels in an aquifer (Currell, 2016; Doody et al., 2017). Such approaches may be attractive due to their apparent simplicity and ease of application (e.g., Werner et al., 2011). However, Currell (2016) pointed out several potential pitfalls, particularly if triggers are not complemented with additional monitoring and compliance criteria (e.g., a combination of water level, flow, and ecological-based indicators). Additionally, groundwater head and flow patterns in the vicinity of faults are often complicated and may change dramatically over relatively short distances (e.g., on either side of a fault and/or between overlying aquifers in a faulted sequence; Bense and Van Balen, 2004). It may not be immediately obvious where the most appropriate locations and depths are to monitor groundwater levels that drive spring discharge, and/or what the appropriate threshold levels are to achieve certain management objectives. Identifying the relationships between changes in aquifer hydraulic head and spring discharge rates can be difficult as spring discharge rates are dependent on the fault conductance (see Section 2.2.2), which is difficult to accurately measure. Nevertheless, establishing relationships between water level patterns, spring discharge and the associated habitat characteristics and functions supporting sensitive species have been shown to be important for effectively managing these systems (Eamus et al., 2006; Fensham et al., 2010). Detailed field investigations are especially important in fault-controlled spring systems as faulting and other geological heterogeneity can make the discharge pathways, and thus appropriate monitoring indicators difficult to establish (e.g., Wu et al., 2011).

Currell (2016) and Noorduijn et al. (2018) demonstrated that a reliance on trigger-level-based management systems may fail to consider reductions in spring discharge that are not necessarily apparent from monitoring drawdown. For example, observation wells that are situated at or near the spring location may not show drawdown from human activities until significant time-lags have passed, after which the impacts arising from groundwater extraction may be permanent (Alley et al., 2002). This was illustrated by Bredehoeft and

Durbin (2009) who used a threshold for spring discharge as a trigger for stopping pumping. In their simulation, the management action was taken at a 10% reduction in spring discharge. However, even with management action, spring discharge continued to decline for ≈25 years to a maximum reduction of discharge of ≈18%, and it took a further ≈100 years for the spring discharge to recover to above the 10% flow reduction threshold.

Many studies aimed at managing groundwater-dependent ecosystems have identified the importance of baseline and ongoing assessments that integrate knowledge from remote sensing, field-based monitoring, modelling and expert knowledge (Eamus et al., 2006; Humphreys, 2009; Doody et al., 2017). In addition to data obtained using traditional scientific measurement and sampling techniques, information about long-term hydrological and ecological functioning and variability of springs can be gained from historical records, indigenous knowledge, and archaeological evidence (Florek, 1993; Fensham et al., 2016a; Brake et al., 2019; Silcock et al., 2020).

2.6 Future challenges and research opportunities

Despite extensive bodies of research on faults and springs separately, there remains significant challenges and knowledge gaps to be addressed in each phase of hydrogeological investigations of fault-controlled spring systems. The key challenges and research opportunities are discussed below.

2.6.1 Hydrogeological processes

Characterising the relationships between spring discharge rates and ecosystem functioning (including the associated vulnerability of these ecosystems to changes in spring discharge rates) is a critical area for future research. In addition to surface discharge, near-surface discharge (i.e., subterranean leakage to the near-surface) is an often-overlooked contribution of springs to ecosystems that can occur in the area surrounding a fault-controlled spring. Near-surface discharge can occur via lateral leakage from the subsurface structures (e.g., faults) beneath springs regardless of whether the spring actively discharges to the surface or not. For example, in a study of Francis Swamp (Australia), Lewis et al. (2013) observed low surface temperatures (relative to ambient conditions) in areas with and without active spring vents. This suggested subsurface seepage may be occurring in these areas. This type of near-surface discharge has been acknowledged as critical for certain groundwater-dependent ecosystems (see type 3 GDEs in Eamus et al. (2006)) and warrants further investigation as it may be as (if not more) sensitive to water level changes than surface discharge.

The hydrogeological processes relating to springs that emanate from faults remain poorly understood, limiting the ability to effectively manage these systems. In particular, future studies into the relationship between fault type (e.g., Figure 2) and spring occurrence will provide much needed understanding on the functioning of fault-controlled spring systems. Future research would benefit from combined laboratory and in situ studies of fault permeability (e.g., packer tests or pumping tests; see Bense et al. (2013) for additional approaches) to provide insights into permeability ratios between measurements taken along the fault trace where springs occur and where springs are absent. Additionally, knowledge and datasets from other disciplines (e.g., structural geology, petroleum, mining) could be translated into the field of hydrogeology to improve the understanding of fault properties and behaviour.

Measurements of spring discharge provide a rare opportunity to directly observe groundwater fluxes, something that is otherwise extremely difficult in hydrogeology. Direct spring discharge measurements provide useful information that has been used to characterise groundwater flow conditions and constrain numerical models (e.g., Manga, 1997; Saar and Manga, 2004; Martínez-Santos et al., 2014). Technology is not a limitation for monitoring spring discharge rates, as proven techniques can be applied to monitor spring discharge rates (see Section 2.3.1). In contrast to typical groundwater measurements, spring discharge rates can be measured without installing wells, substantially reducing the cost of measurements. Despite a variety of methods being available (direct measurements, Darcy's law, chemical tracers and remote sensing; see Section 2.3.1), spring discharge measurements are not a routine part of water resource monitoring regimes. The availability of daily or sub-daily spring discharge estimates could provide significant benefits to management. Ideally, spring discharge time series could be viewed in the same light as stream and well hydrographs, which are routinely monitored.

As discussed in Section 2.2.2, tectonic activity often influences fault behaviour (e.g., by opening new fractures or clearing mineral precipitates), which can have dramatic impacts upon spring discharge rates and water properties. Despite the potential for earthquakes to impact fault-controlled spring systems, these impacts are rarely considered in practice. Thus, the management of fault-controlled spring systems would benefit from increased collaboration between water managers and seismologists.

2.6.2 Field investigation techniques

Much can be learnt about fault-controlled spring systems from surface conditions. Previous studies have demonstrated the use of travertine structures (e.g., Brogi and Capezzuoli, 2009; Love et al., 2013b; Priestley et al., 2018), wetland area (e.g., Lewis et al., 2013) and fossilised pollen and diatoms (e.g., Ashley et al., 2004) to assess the spring discharge rates and historical variability. However, there is scope for this work to be expanded and for the consideration of additional surface features. For example, the hydrobiids discussed by Ponder and Colgan (2002) can be used as an indicator of spring discharge permanence, due to their limited tolerance to dry conditions. Additionally, indigenous knowledge, paintings and artefacts provide an underutilised source of information to construct a historic record of spring locations (Fensham et al., 2016b).

Characterising whether a fault acts as a conduit or barrier to flow requires detailed investigations into the geological properties of the fault. Relationships based on the relative proportions of core and damage zone (see Section 2.2.1) are a good starting point to determine whether a fault will act as a conduit or barrier to flow. However, detailed field studies will invariably be required to properly characterise the fault behaviour and properties. As springs often have high ecological and cultural values, invasive techniques (e.g., trenching or drill holes) may not be appropriate. This means future studies of fault-controlled spring systems should consider non-invasive techniques to investigate these systems. Geophysics can provide a non-invasive approach to characterise subsurface geology and to identify areas of vertical flow. For example, Inverarity et al. (2016) found self-potential can be helpful to identify the locations of vertical flow beneath springs, while magnetotellurics and time-domain electromagnetics can be used to identify faults and other high conductivity pathways. Hydraulic tomography using artificial stimuli (e.g., pumping tests) and natural stimuli (e.g., changes in river stage, lightning, earthquakes, barometric pressure changes) have been applied to characterise faults and fractures over both local and basin scales (e.g., Yeh and Lee, 2007; Yeh et al., 2008; Zha et al., 2016). The further use of geophysics and application of hydraulic tomography techniques to assess the subsurface characteristics of fault-controlled spring systems will provide a much-improved understanding of these systems.

Understanding the relationship between source aquifers and spring discharge is important to assess the vulnerability of springs to external stresses (Boy-Roura et al., 2013; Davis et al., 2017). Identifying the source aquifer and monitoring the relevant hydraulic head can be difficult if monitoring infrastructure is deemed a risk to ecologically significant ecosystems (e.g., Inverarity et al., 2016) or where large hydraulic head differences exist across a fault zone (e.g., Bense and Van Balen, 2004). Detailed understanding of fault-controlled spring systems can be obtained through the collection spring discharge hydrographs, hydrochemical time-series and the creation of a database of spring discharge and aquifer hydrographs. For example, Boy-Roura et al. (2013) collected nitrate concentration time-series from spring discharge to monitor the nitrate mass recharge rates. Similarly, spring discharge hydrograph databases have been created for karst systems (e.g., Olarinoye et al. (2020)) and could be extended to include non-karst fault-controlled spring systems.

Studies of karst systems have developed various tracer and hydrograph analysis techniques (e.g., Taylor and Greene, 2005; Goldscheider et al., 2008; Luhmann et al., 2012). Tracers have been used to identify flow directions, velocities and conduits between recharge and discharge areas, including springs (e.g., Taylor and Greene, 2005; Goldscheider et al., 2008; Luhmann et al., 2012). Examples of tracers given by Goldscheider et al. (2008) include dyes (e.g., uranine, eosin, pyranine), dissolved salts (e.g., sodium, potassium, bromide) and particles (e.g., fluorescent microspheres, bacteria, bacteriophages). Similarly, spring discharge hydrograph analysis is well developed for karst systems to provide information on aquifer properties and the response of spring discharge to external stresses (Taylor and Greene, 2005). For example, techniques are presented to estimate transmissivity from the recession of spring-discharge hydrographs (Taylor and Greene, 2005). Although not directly applied to fault-controlled springs, many of these techniques are relevant, and their translation would be a valuable future contribution.

The proportion of spring discharge contributed from potential source aquifers can be assessed through the comparison of spring water samples and wells cased in potential source aquifers. When water samples are available from potential source aquifers and springs, mixing models can be used to relate the concentrations of ions or isotopes to the proportion of water contributed to spring discharge from each aquifer. However, in data sparse areas where groundwater samples are not available, noble gases (e.g., ^{4}He, ^{40}Ar, ^{20}Ne) can provide an approach to assess the contribution from different sources to spring discharge. The concentrations of these gases are known in the atmosphere, the mantle, and in the crust (Gilfillan et al., 2011). Thus, analyses of noble gasses can be used to determine whether spring discharge shows evidence of being sourced from shallow aquifers or recent recharge (i.e., if the concentration is similar to that in the atmosphere), or if the sample is more consistent with a deeper source (i.e., if the concentration is similar to that in the mantle or the crust). Other isotopes can provide complementary information, for example, the stable isotopes of water in spring discharge can be used to infer recharge elevation, recharge seasonality and the amount of evapotranspiration. $\delta^{13}C$ in spring discharge can be used to assess the contribution of deep waters through a comparison with the concentrations in the mantle, the atmosphere, biological sources or the concentrations in potential source aquifers. Travertine structures can provide an alternate method of obtaining $\delta^{13}C$ from spring discharge. As these structures often reflect precipitation of minerals from spring discharge that has occurred over a long timescale, these deposits may provide a historic record of $\delta^{13}C$. In particular, a greater focus on the development of strategies to characterise springs primarily using analytes that can be obtained without the use of invasive monitoring infrastructure will assist in the management of fault-spring systems.

Temperature has been used to identify spring vents (e.g., Lewis et al., 2013), characterise aquifer permeability fields (e.g., Saar, 2011), estimate the depth of spring source-waters with geothermometry (e.g., Fournier, 1981; Kharaka and Mariner, 1989) and calculate spring discharge using a heat flux approach (e.g., Haselwimmer et al., 2013). Although not demonstrated in the reviewed case studies, newer geothermometry techniques are available (see Arnorrson (2000)), and the application of these techniques to fault-controlled springs would represent a valuable future contribution. Furthermore, the use of heat as a tracer to quantify spring discharge remains largely underutilised, a point that has been made about the use of heat as a tracer in hydrogeology more generally (Kurylyk and Irvine, 2019). Benefits of the use of heat as a tracer to quantify fluid flows include the availability of robust, low-cost sensors (Anderson, 2005; Irvine et al., 2017; Kurylyk et al., 2019) and the fact that temperature-based methods can be used to produce time series estimates of fluid flows (Irvine et al., 2020). Temperature-time series approaches can be used to estimate spring discharge using temperature sensor pairs (e.g., Hatch et al., 2006; Keery et al., 2007), or using other signal processing techniques that allow for multiple frequencies (aside from simple diurnal) and for two or more depths (e.g., Vandersteen et al., 2015). Several software packages are available to facilitate the application of these methods (e.g., Irvine et al., 2015; Vandersteen et al., 2015; Ford et al., 2021). Active heat tracer methods provide an alternative approach to quantify discharge whereby an artificial heat source is used to estimate groundwater flux (e.g., Lewandowski et al., 2011; Banks et al., 2018).

2.6.3 Numerical modelling

Given the widespread use of numerical models in groundwater management, significant benefits can come from improved numerical representation of fault-controlled springs. Although faults are typically composed of complex fracture networks, the extensive body of literature on modelling of fractured rock systems has not been translated into guidance on fault simulation. McCallum et al. (2018) identified that the type of numerical approach is important when faults act as conduits to flow. However, the comparison undertaken by McCallum et al. (2018) did not include the treatment of faults as fracture networks. A host of opportunities to further investigate the optimal numerical techniques to treat fault-derived springs remains. For example, the new unstructured grid version of MODFLOW (Panday et al., 2017) provides new capabilities to better represent faults in equivalent porous media models without significantly increasing the computational burden (McCallum et al., 2021). However, further investigations are required to determine appropriate modelling approaches to represent fault-controlled springs, including further investigation into the use of discrete conduits and discrete fracture networks.

Regional-scale models impose a significant computational challenge, especially if fault-related flow process are simulated. The applicability of numerical permeameters for the upscaling of fault hydraulic properties (e.g., Lupton et al., 2019) should be further investigated to improve the computational performance of faulted groundwater systems. Formal uncertainty analysis of groundwater flow systems affected by faults is also lacking in the current published literature.

2.6.4 Management of fault-controlled springs

Given their ecological and spiritual importance, the management of springs emanating from faults the management of these fault-controlled spring systems will benefit from the adoption of a structured management approach (e.g., adaptive management) with pre-defined mitigation strategies. These mitigation strategies should consider whether the impacts are reversible and the time scales of impacts (Thomann et al., 2020). When impacts are irreversible or reversible only over significant periods of time (e.g., centuries), the need for monitoring protocols for early detection of impacts becomes increasingly important. Numerical modelling can be an important tool to inform managers of the effectiveness of proposed mitigation strategies.

Management regimes should to identify: (1) the source aquifer(s) and major discharge pathway(s); (2) the spring geomorphic threshold(s) required to maintain discharge to the surface; (3) the relationship(s) between water level patterns in the source aquifer(s) and flow rates at the springs; (4) the ecological thresholds (e.g., spring discharge rates) required to sustain habitat for a particular species and/or ecological communities; and (5) the stakeholder perspectives on the significance and value of the spring(s). A comprehensive understanding of the hydrogeological functioning of springs is essential for the effective and science-based management of these systems. Hence, studies that integrate spring ecosystem responses within hydrological models, to assess ecosystem changes due to development pressures, are a critical area for future research. This is especially important for projects that may irreversibly compromise the ecological and/or cultural values of a system (Thomann et al., 2020).

Further to these recommendations, the use of comprehensive post audits of management plans could consider a range of factors including the choice and efficacy of mitigation measures, and the relationship between the use of prescribed management strategies and positive or negative management outcomes. Detailed post audits can help to retrospectively identify strategies that were effective (or ineffective) for the management of fault-controlled spring systems and encourage effective management by learning from past management experiences.

Conclusions

This review of fault-controlled springs revealed fundamental shortcomings in the present understanding of these systems. Characteristics of fault-controlled spring systems that remain poorly understood include the translation of source-aquifer hydraulic head to spring discharge rates, the fault structure and hydraulic properties (and their representation in models), and the impact of fault activity on spring discharge rates. A critical barrier to the characterisation of many fault-controlled spring systems is the need to protect spring expression features (e.g., calcareous mound structures) and accompanying wetlands, which often have high cultural and ecological values, from invasive methods of investigation (e.g., drilling). Studies of fault-controlled springs have typically focussed on one specific component of the system (e.g., the spring, the fault, or groundwater-dependent ecosystems) rather than the broader system and the interdependencies between components. Thus, a greater emphasis is needed on the analysis of interactions between faults and springs. This will allow spring measurements to be used in evaluating fault properties, amongst other benefits of considering faults and springs as connected, interdependent systems. This will also help to identify the sensitivity of fault-controlled spring systems to natural and anthropogenic forcings; a critical requirement of spring and spring-dependent ecosystem management. Finally, we recommend the establishment of several well-characterized field examples within both natural and modified hydrogeological settings to help elucidate critical functions and to advance the current understanding of fault-controlled spring systems.

CHAPTER 3

APPLICATION OF INDICATOR KRIGING TO HYDRAULIC HEAD DATA TO TEST ALTERNATIVE CONCEPTUAL MODELS FOR SPRING SOURCE AQUIFERS

Published in the Journal of Hydrology: Keegan-Treloar, R., Werner, A.D., Irvine, D.J., Banks, E.W., 2021. Application of Indicator Kriging to hydraulic head data to test alternative conceptual models for spring source aquifers. J. Hydrol. 601, 126808.

Approximate contribution of co-authors: Robin Keegan-Treloar (80%), Adrian Werner (10%), Dylan Irvine (5%) and Eddie Banks (5%).

Abstract

Hydraulic head distributions can inform spring source-water characterisation by determining whether aquifers meet the thresholds required to sustain spring flow. Assessing hydraulic head data can be challenging in areas where data are sparsely distributed and subject to variable measurement uncertainty. Geostatistical methods can be used to estimate hydraulic head values at unmeasured locations with quantitative uncertainty estimates. While these methods have been applied extensively for hydraulic head estimation in management contexts, no studies have used these approaches for spring source-water conceptual model testing. In this study, an investigation into the hydraulic head distribution was conducted through the application of Ordinary Indicator Co-Kriging. Interpolated hydraulic head estimates were used to quantitatively assess the plausibility of source-aquifer conceptual models for the Doongmabulla Springs Complex (DSC), Queensland, Australia. The results offer insights into the likelihood of alternative source aquifers having adequate head to support flow to eight springs within the DSC. Probabilities of adequate head to support the springs ranged from 0.03 to 0.12 for the Permian Formations, compared to <0.01 to 0.49 for the Triassic Formations. Analyses indicated that the Triassic Formations are more likely to have adequate hydraulic head to support spring flow. However, significant uncertainty exists in the conceptual model assessment due to hydraulic head measurement scarcity, particularly in the vicinity of the springs. These findings have important implications given that the Permian Formations will be dewatered by the operation of the nearby Carmichael coal mine. The techniques employed here can inform conceptual model uncertainties arising from the interpretation of sparsely distributed hydraulic head datasets, a major benefit

over traditional interpolation methods.

3.1 Introduction

In hydrogeological investigations, the development of conceptual models requires the synthesis of uncertain observations and expert knowledge, leading to multiple plausible conceptual models (Oreskes et al., 1994; Neuman and Wierenga, 2003). When mathematically modelled, alternative conceptual models may provide vastly different estimates of hydrogeological behaviour, despite comparable consistency with field observations (Oreskes et al. 1994; Bredehoeft 2003; Neuman and Wierenga, 2003). This leads to non-uniqueness in the mathematical representations of hydrogeological systems. The importance of considering alternative conceptual models has been recognised (Neuman and Wierenga, 2003; Bredehoeft, 2005; Enemark et al., 2019); however, such conceptual models are rarely considered in practice (Bredehoeft, 2005). Failure to consider alternative conceptual models is problematic, as it can result in underestimation of the uncertainty of predictions (e.g., hydraulic heads, groundwater fluxes, solute concentrations) (Enemark et al., 2019). The importance of considering conceptual model uncertainty for decision making is well recognised in management frameworks, such as adaptive management (e.g., Williams et al., 2009; Thomann et al., 2020).

Hydraulic head is a measure of fluid potential that is used to determine groundwater flow patterns (Freeze and Cherry, 1979) and to inform conceptual model development (Neuman and Wierenga, 2003). Hydraulic head measurements are typically sparsely distributed and collected infrequently with varying precision (Post and von Asmuth, 2013; Rau et al., 2019). Expert knowledge and mathematical models are invariably needed to interpret hydraulic head data and predict hydraulic heads at unmeasured locations. Hydraulic head data may be analysed manually by contouring (e.g., Salama et al., 1996; Siegel, 2008), or through the use of automated mathematical approaches such as Kriging (e.g., Bastin and Gevers, 1985; Nikroo et al., 2010; Varouchakis and Hristopulos, 2013; Quay et al., 2020), or inverse distance weighted interpolation (e.g., Philip and Watson, 1986; Varouchakis and Hristopulos, 2013). By manually contouring hydraulic head data, hydrogeologists can include their understanding of the system into the interpretation (Kresic, 2006). For example, information on the subsurface hydrogeological features (e.g., faults or dykes), surface features (e.g., lakes or rivers), or physical properties (e.g., changes in hydraulic conductivity), may assist in the interpretation of regional flow directions, boundary effects (e.g., no-flow boundaries), and recharge/discharge stresses (Salama et al., 1996; Siegel, 2008). In contrast, automated techniques provide the ability to assess a wide range of alternative conceptual models through interpolation algorithms, which is generally infeasible with manual contouring. However, it is often challenging to include qualitative expert knowledge and understanding into automated analyses. Failure to consider expert knowledge and understanding can result in unrealistic interpretations of the hydraulic head (Salama et al., 1996; Siegel, 2008; Peeters et al., 2010). For example, in a case study of the Cuballing catchment, Western Australia, Salama et al. (1996) described hydraulic head predictions that intersect the surface elevation for unconfined aquifers.

Automated interpolation approaches applied to groundwater datasets include various forms of Kriging, which is used routinely to interpolate datasets in developing hydrogeological conceptual models. Journel (1983) developed a modified form of Kriging, Indicator Kriging (IK), whereby data are transformed to binary indicators of 1 for values less than or equal to a threshold value or 0 otherwise. The resulting indicators are termed ‘indicator-transformed values’. The probability of a value less than or equal to the threshold value can be estimated at unmeasured locations by Kriging the indicator-transformed values. This process can be applied for a series of threshold values using Co-Kriging to estimate the conditional cumulative distribution function (CCDF) at unmeasured locations.

The IK technique makes no distribution assumptions and allows for a quantitative assessment of the uncertainty of predicted values at unmeasured locations (Journel, 1983). However, in cases of high measurement uncertainty, the use of a binary indicator transform (i.e., either 0 or 1) may be problematic as the measured values could plausibly be coded as either of the indicator values, leading to uncertainty in the indicator-transformed values. Furthermore, IK can result in predictions at unmeasured locations outside of the 0 to 1 bounds of probability (Journel, 1986). To address these limitations, Journel (1986) extended the technique to include expert knowledge in the form of constraints and prior probability distributions. The constraints ensure predictions lie within reasonable limits, while the prior probability distributions allow the inclusion of uncertain information based on observations or expert knowledge. In this way, IK provides the ability to overcome issues of unrealistic predictions and allows the user to include their qualitative expert knowledge into the modelling process.

In hydrogeology, IK has been widely applied to assess the probability of values of interest being above or below a chosen threshold based on a set of observations (e.g., Saito and Goovaerts, 2002; Liu et al., 2004; Lyon et al., 2006; Arslan, 2012; Anane et al., 2014; Chica-Olmo et al., 2014; Varouchakis et al., 2020). For example, IK has been used to compare contaminant concentrations with thresholds for remediation (e.g., Saito and Goovaerts, 2002), to assess water quality parameters against guidelines for water use (e.g., Arslan, 2012; Anane et al., 2014; Chica-Olmo et al., 2014), and to evaluate the probability of saturated soil conditions (e.g., Lyon et al., 2006). IK has also been used to evaluate the probability of hydraulic heads dropping below a threshold value selected to avoid groundwater depletion (Varouchakis et al., 2020). Despite the widespread use of IK throughout the field of hydrogeology, we are unaware of any studies that have used IK to assess the probability of alternative aquifers having adequate hydraulic head to drive spring flow.

This study applies IK to hydraulic head data to assess the likelihood of alternative conceptual models relating to the source of discharge from a spring complex. The method evaluates the probability that an aquifer has adequate hydraulic head to meet a threshold required for spring flow. This threshold, referred to as the 'spring geomorphic threshold' (SGT), is defined as the topographical elevation in the vicinity of a spring vent that controls whether the spring will discharge to the surrounding landscape (Merrick, 2015; Currell et al., 2017).

The springs considered in this study are part of the ecologically and culturally significant Doongmabulla Springs Complex (DSC), located in Queensland, Australia (Fensham et al., 2016; Currell et al., 2017; Currell et al., 2020). The flow contribution to the DSC from underlying aquifers (i.e., the Triassic-aged and Permian-aged formations of the Galilee Basin) is disputed (Currell et al., 2017; Currell et al., 2020). Since the nearby Carmichael coal mine is expected to dewater the deeper Permian Formations to support mining activities (Currell et al., 2017; Currell et al., 2020), a better understanding of the water source to the DSC is essential for the ongoing conservation efforts.

3.2 Study area

The DSC is a collection of freshwater springs located in the Galilee Basin, Queensland, Australia (Figure 3.1). The DSC provides water to an extensive wetland system, that is listed in the national directory of important wetlands in Australia (Environment Australia, 2001). These wetlands offer niche habitat for several endangered species and are culturally significant to the Wangan and Jagalingou people (Fensham et al., 2016; Currell et al., 2017).

The eight springs examined in this study (see Figure 3.1c) were selected for being representative of the varying spring morphologies throughout the DSC. These springs were classified into two categories based on the spring morphology. The first category, discharge springs, are hypothesised to occur due to artesian discharge via vertical conduits in flatter areas (Fensham et al., 2016). In contrast, the second category, outcrop springs, are hypothesised to occur due to lateral discharge in areas of sloping topography, where the Triassic Formations outcrop (Fensham et al., 2016). The discharge springs show a variety of surface expressions; such as mounded vegetated areas with pooled water (e.g., springs B, C, D and E), a modified dam surrounding a spring vent (e.g., spring F), springs with discrete vents that discharge to wetland systems (e.g., Spring A), and small vegetated areas without visible pooled surface water (e.g., spring G, photograph shown in Figure 3.2b). The outcrop spring examined in this study (spring H, photograph shown in Figure 3.2a) did not have a visible discrete vent but rather a large pooled area ($\approx$100 m2), which discharges to an extensive wetland system. The surface expression of the spring vent is important for characterising the SGTs, as they vary between springs surrounded by mounds or dams and those in flatter areas. In the case of discrete mound-form springs, the SGT is the minimum elevation of the mound over which spring water flows while, in flatter areas, with more diffuse springs, the SGT is simply the topographic elevation of the spring discharge point. The SGTs for the springs considered in this study were measured in May 2019 using a Trimble R10 Integrated GNSS System with a precision of 8 mm horizontal and 15 mm vertical (Trimble Navigation Limited, 2014).

The Triassic Formation aquifers (see Figure 3.1b) consist of the Moolayember Formation, made up of sandstones and siltstones, the Clematis Formation, composed of siltstone,

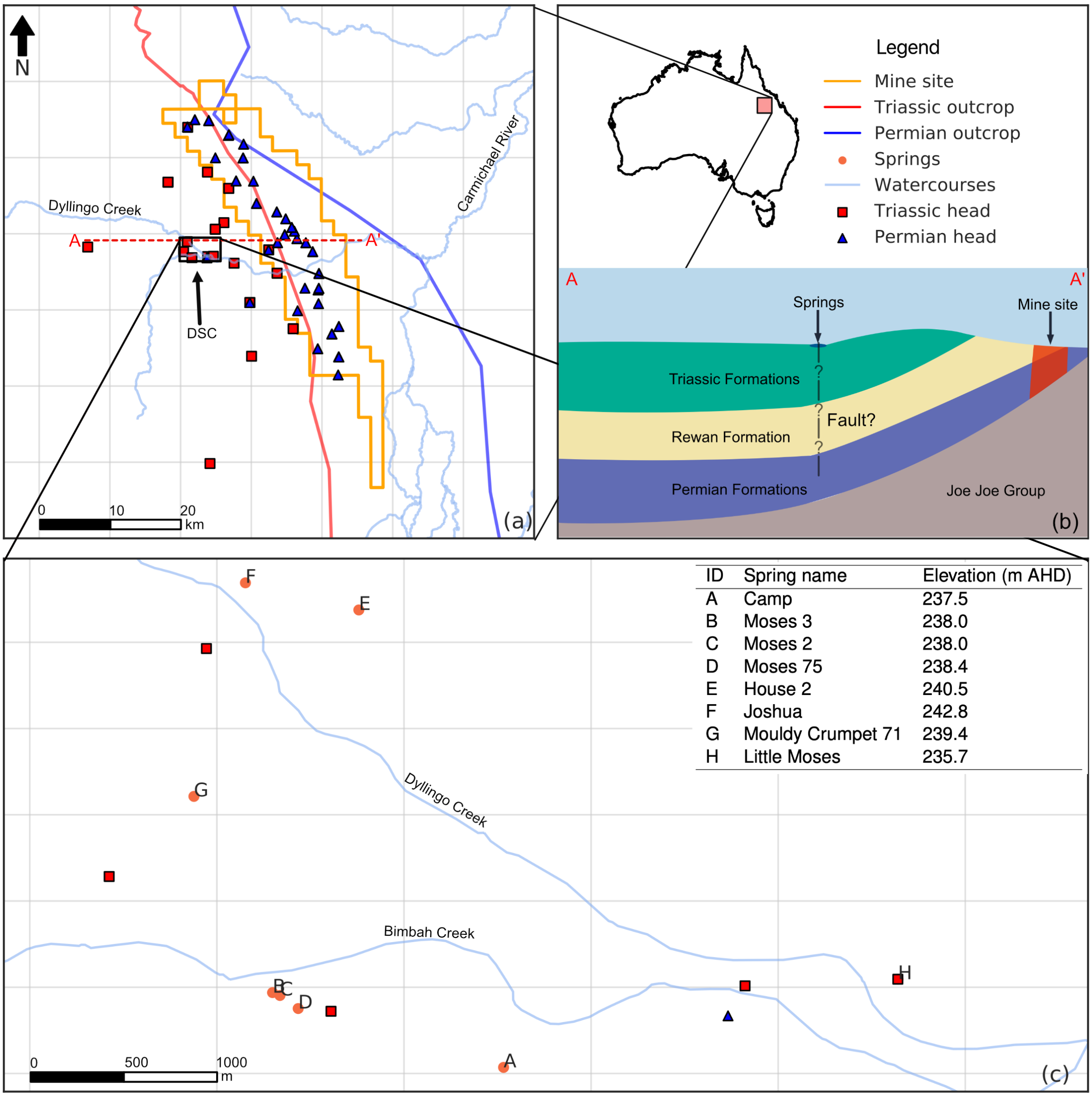

Figure 3.1: *Map of the study area, showing: (a) wells with hydraulic head measurements in the Permian and Triassic Formations and the formation extents, (b) a simplified conceptual diagram (not to scale) of the stratigraphy, and (c) the locations and SGT elevations of the eight DSC springs investigated in this study. The red line showing A-A' in (a) is the approximate transect of (b). Spring elevations in (c) are relative to the Australian Height Datum (AHD), where 0 m AHD is approximately mean sea level.*

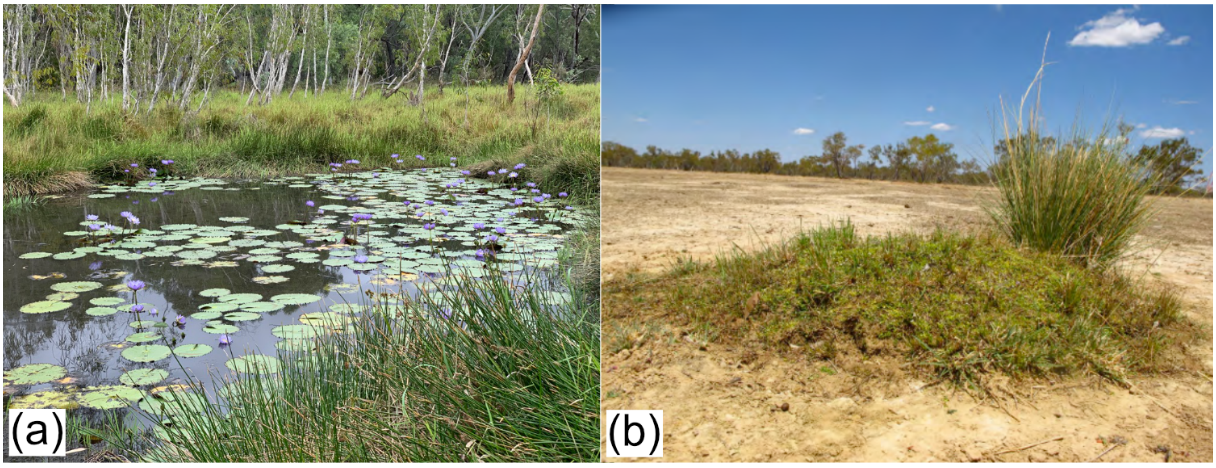

Figure 3.2: *(a) Little Moses, an outcrop spring at the DSC (Spring H; Fig. 1). (b) Mouldy Crumpet spring (Spring G; Fig. 1) at the DSC reproduced with permission from Fensham et al. (2016).*

sandstone and mudstone, and the Dunda Beds, consisting of predominantly sandstone (AECOM, 2021). The Triassic Formations are separated from the Permian Formations by the Triassic-aged Rewan Formation (Figure 3.1b), primarily composed of siltstone, fine-grained sandstone, clays and mudstone (AECOM, 2021). The Rewan Formation is considered a competent aquitard, at least in the areas where monitoring infrastructure has been installed (AECOM, 2021). The Permian Formations (Figure 3.1b) consist of the Bandanna Formation, made up of lithic sandstone, siltstone, and coal seams, which overlies the Colinlea Sandstone, composed of quartz sandstone, conglomerate with minor shale, and coal seams (AECOM, 2021).

There are several proposed and active mining developments throughout the Galilee Basin that target the coal seams in the Permian Formations in areas where these formations outcrop along the edge of the basin. These developments include the currently under construction Carmichael coal mine, located approximately 8 km to the east of the DSC (Figure 3.1a). The imminent mining operations will potentially dewater the Permian Formations that underlie the Triassic Rewan Formation aquitard (Figure 3.1b) (Currell et al., 2017). The Triassic Formations, which outcrop to the west of the mine site, are unlikely to be impacted directly by the mine construction (Currell et al., 2017). However, it is currently unclear whether dewatering and associated reductions in hydraulic head in the Permian Formations will propagate through the Rewan Formation and impact the water levels in the Triassic Formations (Currell et al., 2017; CSIRO and Geoscience Australia, 2019). Furthermore, if the springs rely (even partially) on groundwater from the Permian Formations, mine-induced reductions in pressure could lead to the cessation of spring flow (Currell et al., 2017; Currell et al., 2020). Despite these concerns, the mine was approved (Currell et al., 2020).

Currently, there exist two conceptual models explaining the source of water to the DSC (Currell et al., 2017). The first conceptualisation assumes that the Rewan Formation (see Figure 3.1b) is a competent, laterally extensive aquitard comprised of sediments that do not allow significant vertical flow (Bradley, 2015). In this conceptual model, the DSC relies entirely on groundwater from the Triassic Formations (Bradley, 2015). The mine-induced drawdown in the Permian Formations will be less likely to impact the springs in this case (Bradley, 2015). The second conceptualisation proposes that the DSC may receive water, at least in part, from the Permian Formations via leakage or preferential flow (e.g., via faulting) through the Rewan Formation (Webb, 2015). In this case, the drawdown in the Permian Formations will more likely pose a significant threat to the long-term survival of the DSC (Webb, 2015). The outcomes of these previous studies highlight that further work is required to identify the potential risk of mine impacts on the springs.

3.3 Data sources

The data used in this study were collated from the Queensland Groundwater Database, the Department of State Development (2018) and the AECOM (2021) report. A total of 34 and 78 wells had available hydraulic head measurements in the Triassic and Permian Formations, respectively. Some of these wells featured extensive time-series of up to 10 years of daily measurements (6 and 39 in the Triassic and Permian, respectively), while others (28 and 39 in the Triassic and Permian, respectively) featured few ($\leq$10) measurements. Figure 3.3a displays the time-series data for well ID 158090_A in the Triassic Formations. The range of variability is relatively low ($\approx$0.6 m), indicating reasonably consistent hydraulic head conditions over the 7-year measurement period. Six wells in the Triassic Formations featured time-series data, and the temporal variability of these wells varied from $\approx$1 m to $\approx$0.2 m with an average range of $\approx$0.4 m. The remaining 28 wells in the Triassic Formations featured few ($\leq$10) or single measurements.

Figure 3.3b shows hydraulic head time-series in well ID 158069_A in the Permian Formations. The period 2015 to mid-2017 displays a seasonal pattern with a range of 0.2 m. The hydraulic head values have a small range ($\approx$0.4 m), indicating that the groundwater conditions have remained relatively stable over the measurement period. In total, 39 wells in the Permian Formations had time-series data, and the range of measurements varied between <0.1 m and $\approx$5 m with an average of $\approx$1.9 m. The other 39 wells in the Permian Formations featured few ($\leq$10) or single measurements. A table of the hydraulic head data available from each well in the Triassic and Permian Formations is provided as Supplementary Material 1 (see Appendix B).

3.4 Methods

The methodology aims to evaluate the likelihood that hypothesised spring source aquifers have sufficient hydraulic head to support discharge to eight springs in the DSC. This process can be separated into (i) assessing the uncertainty of the available hydraulic head measurements, (ii) transforming the hydraulic head data to 'indicator-transformed values' relative to threshold values, (iii) characterising the semi-variance, and (iv) applying Ordi-

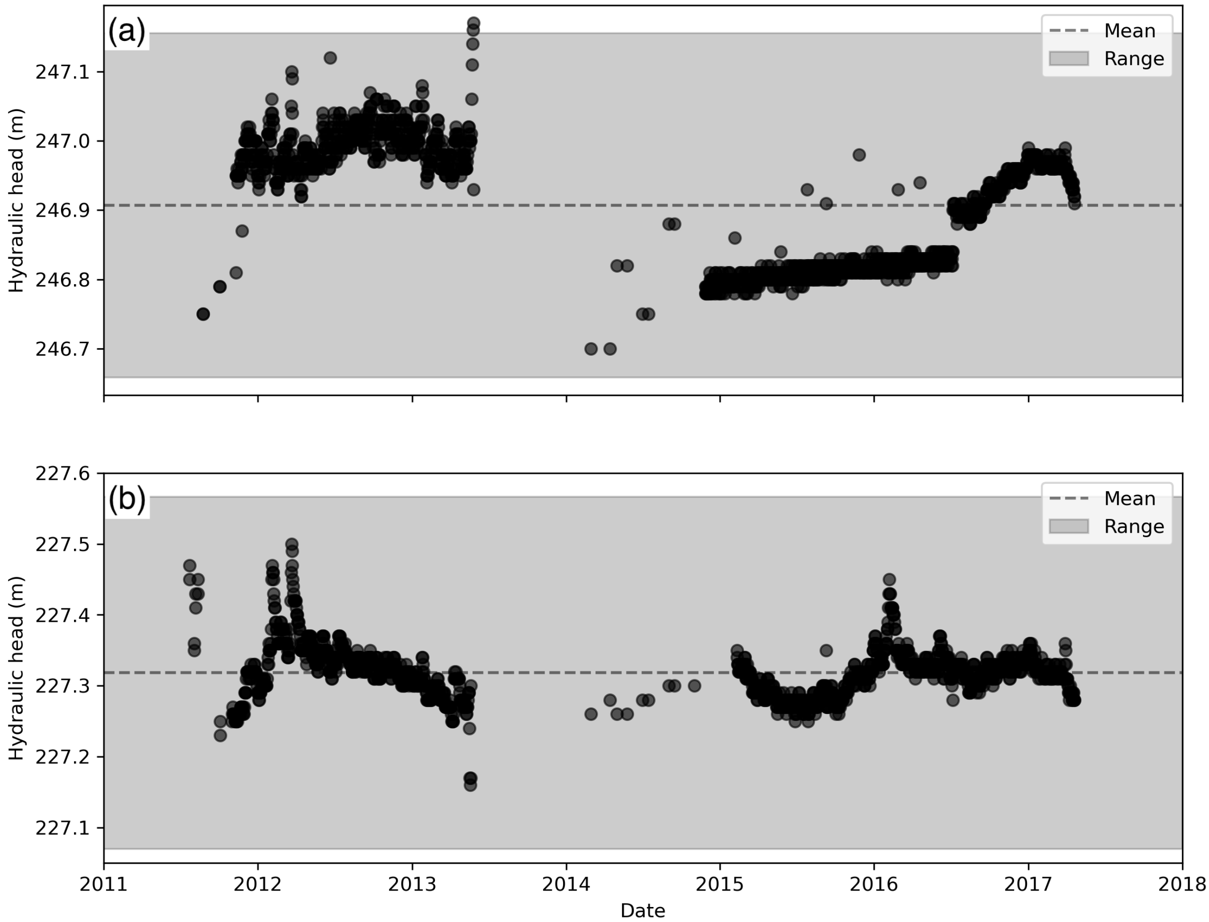

Figure 3.3: *Examples of hydraulic head time series with the mean (dashed line) and uncertainty ranges (grey shading) derived following the methods outlined in Section 3.4.1 (a) shows well ID 158090_A in the Triassic Formations, while (b) shows well ID 158069_A in the Permian Formations.*

nary Co-Kriging to make predictions at unmeasured locations.

3.4.1 Hydraulic head measurement uncertainty

Prior to the commencement of mine site dewatering in 2019, it was presumed that seasonal and random variations in head occur around a stationary mean value, and otherwise, the groundwater system was in a steady state. The steady-state assumption was reasonable, as there was limited groundwater abstraction in the area, and where multi-year records were available, the range was relatively small, on average approximately <0.4 and 1.9 m in the Triassic and Permian Formations, respectively (see Section 3.3). Where time-series data were available, the mean hydraulic head (denoted $\overline{h}(x)$) for each well was estimated as the arithmetic mean of pre-2019 records, except in the case of wells influenced by pumping or where only post-2019 records were available. In the case of pumping, the mean was estimated by discarding measurements that were believed to be influenced by pumping and estimating the mean. For wells that only featured post-2019 records, the earliest dated measurement was selected to represent the mean as this measurement was expected to be least impacted by mine site dewatering. In total, all Triassic wells and 73 Permian wells were estimated from the mean of pre-2019 records, while 3 Permian wells were interpreted to be influenced by pumping and 2 Permian wells featured only post-2019 records. Hydrographs and interpretations for each well are provided in Supplementary Material 2 (see Appendix B).

In this study, uncertainty is considered as a combination of accuracy and precision, whereby measurement precision is defined as the spread of measurements around the mean, and the measurement accuracy is the closeness of the mean to the true value (Post and von Asmuth, 2013). We consider explicitly the major factors expected to influence measurement uncertainty, including the temporal variability of hydraulic head measurements, the hydraulic head measurement technique, and the elevation survey method (Post and von Asmuth, 2013; Rau et al., 2019). Other sources of uncertainty are modelled implicitly using a nugget-effect parameter in the semi-variogram models (see Diggle et al., 1998).

The uncertainty due to the range of measurements above and below the mean was denoted as $\sigma_t(x)$, and where adequate data were available (i.e., >10 measurements), this was manually interpreted from hydrographs of the time-series data based on the range of measurements about the mean excluding clear outliers (e.g., measurements influenced by pumping). In cases with inadequate time-series (i.e., $\leq$10 measurements), values of 0.4 and 1.9 m were assigned based on the average of the ranges observed from time-series in the Triassic and Permian Formations, respectively. An additional 2 m of uncertainty was added to wells with single measurements (i.e., a total $\sigma_t(x)$ of 2.4 and 3.9 m for the Triassic and Permian, respectively) to reflect the uncertainty in groundwater levels following well construction and the lack of measurement repeatability.

Hydraulic head measurements were assigned an elevation survey uncertainty (denoted $\sigma_e(x)$), based on the elevation survey method detailed in the metadata. The reference elevation (e.g., top of casing) is the point from which water levels are measured at well locations and was presumed to be measured with three alternative levels of uncertainty: (1) high-precision survey ($\sigma_e(x)$ = 0.04 m; Garrido et al., 2011), (2) global positioning system ($\sigma_e(x)$ = 1.8 m; Wing and Frank, 2011), and (3) estimated elevation from Digital Elevation Model (DEM), for which $\sigma_e(x)$ was presumed to be 5 m, based on the average of the 'bare areas' and 'shrubland' scenarios described by Rexer and Hirt (2014). In the absence of a reported survey method, $\sigma_e(x)$ was set to 5 m, assuming the poorest precision method. These $\sigma_e(x)$ values were presumed to be normally distributed and were multiplied by 2 to construct intervals reflecting the range of plausible elevation values above and below the elevation measurement.

Measurement uncertainty arising from instrument error (denoted $\sigma_m(\boldsymbol{x})$) varies between measurement techniques, including dip meters, automated loggers, vibrating wire piezometers and drill stem tests (Rau et al., 2019). In the absence of detailed reporting on the instrument specification or data collection methods, a conservative approach was adopted by assigning measurements collected with dip meters, automated loggers or vibrating wire piezometers a value for $\sigma_m(\boldsymbol{x})$, consistent with the poorest precision method (i.e., dip meter with $\sigma_m(\boldsymbol{x})$ = 8.4 mm; Rau et al., 2019). These $\sigma_m(\boldsymbol{x})$ values were presumed to be normally distributed so were multiplied by 2 to represent the range of plausible values around the measurement.

It was presumed that each of the considered sources of uncertainty (i.e., elevation survey method, water level measurement technique and temporal variability) were independent. Therefore, the range around the mean was estimated as:

$$\sigma_h(\boldsymbol{x}) = \sigma_t(\boldsymbol{x}) + \sigma_e(\boldsymbol{x}) + \sigma_m(\boldsymbol{x}) \tag{3.1}$$

3.4.2 Indicator transformation

The hydraulic head values for each well were converted to indicator-transformed values based on the probability of the measurement being less than or equal to a specified threshold value. A set of m hydraulic head threshold values were selected (denoted $\boldsymbol{a} = [a_1, ..., a_m]$) to discretise the range of plausible values at the spring locations. In our study, we defined 16 thresholds discretised with variable spacing starting with 7 SGT elevations (two springs shared the same threshold) and 9 equal p-quantiles from 0-1 derived from the empirical cumulative distribution function (ECDF) as described by Goovaerts (2009). Once the thresholds were defined, the probability of the hydraulic head measurement being less than or equal to a threshold value (denoted a_i) was estimated from the mean $\overline{h}(\boldsymbol{x})$ and range $\sigma_h(\boldsymbol{x})$ using the uniform cumulative distribution function (Grimmett and Stirzaker, 2020):

$$I(\boldsymbol{x}, a_i) = \begin{cases} 0, & a_i < \overline{h}(\boldsymbol{x}) - \sigma_h(\boldsymbol{x})/2 \\ \frac{a_i - (\overline{h}(\boldsymbol{x}) - \sigma_h(\boldsymbol{x})/2)}{\sigma_h(\boldsymbol{x})}, & a_i \in [\overline{h}(\boldsymbol{x}) - \sigma_h(\boldsymbol{x})/2, \overline{h}(\boldsymbol{x}) + \sigma_h(\boldsymbol{x})/2] \\ 1, & a_i > \overline{h}(\boldsymbol{x}) + \sigma_h(\boldsymbol{x})/2 \end{cases} \tag{3.2}$$

Where $I(\boldsymbol{x}, a_i)$ is the probability that a measurement is less than or equal to a_i.

3.4.3 Characterising the semi-variance

For Ordinary Co-Kriging, it is necessary to characterise the semi-variance of each variable and between each of the variables, which in the current study are indicator-transformed values. The experimental semi-variogram ($\gamma(\Delta x)$) consists of semi-variance values (γ) that are a function of distance between observation points, and is obtained from (Cressie, 1993):

$$\gamma(\Delta x) = \frac{1}{2|N(\Delta x)|} \sum_{N(\Delta x)} \Big(I(\boldsymbol{x_k}, a_i) - I(\boldsymbol{x_l}, a_i) \Big)^2 \tag{3.3}$$

Here, $N(\Delta x)$ is a set of observation well pairs separated by Euclidean distance $||\boldsymbol{x_k} - \boldsymbol{x_l}|| = \Delta x$, $|N(\Delta x)|$ is the number of data pairs in $N(\Delta x)$, and $I(\boldsymbol{x_k}, a_i)$ and $I(\boldsymbol{x_l}, a_i)$ are the indicator-transformed hydraulic head values, for a threshold value a_i, at the locations $\boldsymbol{x_k}$ and $\boldsymbol{x_l}$, respectively. The semi-variogram is obtained by applying Equation 3.3 to a set of values of Δx.

The semi-variance between variables (here, indicator-transformed hydraulic head values) can be assessed not only as a function of the distance between measurement sites (i.e., Equation 3.3) but also incorporating differences between values of $I(\boldsymbol{x}, a_i)$ that arise between elements of $\boldsymbol{a}$. This leads to a modified form of Equation 3.3, whereby γ is calculated as a function of $I(\boldsymbol{x}, a_i)$ for alternate values within the vector $\boldsymbol{a}$ (i.e., a_i and a_j, where a_j is an alternate hydraulic head threshold value to a_i, both of which are elements of $\boldsymbol{a}$). This gives the experimental cross semi-variogram, $\gamma(\Delta x, a_{i,j})$, obtained as (Wackernagel, 1995):

$$\gamma(\Delta x, a_{i,j}) = \frac{1}{2|N(\Delta x)|} \sum_{N(\Delta x)} \Big(I(\boldsymbol{x_k}, a_i) - I(\boldsymbol{x_l}, a_i)\Big)\Big(I(\boldsymbol{x_k}, a_j) - I(\boldsymbol{x_l}, a_j)\Big) \tag{3.4}$$

Here, $a_{(i,j)}$ refers to alternative hydraulic head threshold values a_i and a_j. Note that Equation 3.4 reduces to Equation 3.3 if $a_i = a_j$. In practice, Equations 3.3 and 3.4 are applied to bins of Δx values, thereby obtaining γ for a set of Δx bins.

The choice of the number of bins in the experimental semi-variogram is an essential consideration as there exists a trade-off between overly smooth semi-variance values (when using too few bins) and noisy semi-variance values (when using too many bins). In the current study, 9 bins of Δx values, ranging from 0-3,787 m to 30,299-34,087 m, were adopted for the Triassic Formations, while 14 Δx bins (0-1,398 m to 18,174, 19,572 m) were used for the Permian Formations. The number of Δx bins and maximum Δx values were selected to ensure that all bins contained a reasonable count of data pairs, albeit this was a subjective choice. This resulted in at least 22 data pairs in each Δx bin within the experimental semi-variograms for the Triassic Formations. In comparison, the experimental semi-variograms for the Permian Formations contained at least 103 data pairs. This difference in the count is due to the Permian Formations having 78 samples available compared with the Triassic Formations, which had 34 samples.

For Ordinary Co-Kriging, it is necessary to know γ at distances other than the discrete distances estimated with Equations 3.3 and 3.4 and for γ to be negative definite (Cressie, 1993). This is achieved by fitting empirical mathematical models to the relationships between semi-variance and distance for experimental semi-variograms and experimental cross semi-variograms. Commonly used models include the nugget, Gaussian, exponential, spherical, and Matérn models (Goovaerts, 1997). These semi-variogram models can be added together to construct more complex model structures (Goovaerts, 1997). For example, the nugget model characterises the discontinuity of the semi-variance at the origin (i.e., at or near a separation distance of zero), which can be included in a model structure (e.g., with the Gaussian model) to characterise the measurement error and micro-scale variability (Diggle et al., 1998).

In our study, isotropic semi-variogram models were used due to insufficient data to characterise anisotropy properly. The range was selected based on the range of the experimental semi-variogram of the indicator-transformed values for the median value. The median was used because the experimental semi-variogram is best defined when approximately half the data lies on either side of the threshold value (Journel, 1983). The fit of this range was visually assessed against the experimental semi-variograms at all other thresholds. Where the range was not appropriate for an experimental semi-variogram, an additional model structure was added to include the range of that experimental semi-variogram. Next, the sills and nuggets were modified to fit the experimental semi-variograms and experimental cross semi-variograms subject to a constraint of positive semi-definiteness (i.e., all eigenvalues are non-negative). In this study, the parameters of range, sill and nugget were estimated using weighted least-squares with weights proportional to $\frac{|N(\Delta x)|}{\Delta x^2}$ following Pebesma and Graeler (2020). When the condition of positive semi-definiteness is not met, it is necessary to apply a correction. In this study, we used the gstat package (Pebesma, 2004) in the R statistical language (Ihaka and Gentleman, 1996), which corrects for non-positive definite matrices by setting any negative eigenvalues to zero (Pebesma and Graeler, 2020).

The choice of semi-variogram models was qualitative based on the visual assessment of graphs of the fit of the semi-variogram models to the experimental semi-variance. We elected not to use leave-one-out cross-validation (LOO-CV) for semi-variogram model selection, as some of the semi-variogram models required the use of multiple nested model structures, which meant the number of possible model combinations increased substantially (e.g., 6 candidate models in a 2-model nested structure have 15 possible combinations). As such, the semi-variogram models were selected qualitatively based on the shape of the experimental semi-variance. LOO-CV was used as an exploratory technique to assess how well the chosen model represented the available data and identify the locations where the model performed poorly. The LOO-CV results were evaluated using summary statistics (i.e., mean error (ME), mean absolute error (MAE) and mean standardised squared residual (MSSR); see Goovaerts (2009) for details) and a spatial analysis of the residuals.

3.4.4 Predictions using Ordinary Co-Kriging

In applying Ordinary Co-Kriging to estimate the probability of hydraulic head values less than or equal to a set of threshold values, it is necessary to develop semi-variogram models of the indicator-transformed values for each threshold (see Section 3.4.3) and cross semi-variogram models between each the indicator-transformed values for each threshold (see Section 3.4.3). The indicator-transformed values for all thresholds at a well location x can be represented as:

$$\overline{\boldsymbol{I}}(\boldsymbol{x}, \boldsymbol{a}) = [I(\boldsymbol{x}, a_1) \; ... \; I(\boldsymbol{x}, a_m)] \tag{3.5}$$

Given that a_1 is the first value in a set of m thresholds, and a_m is the last threshold in $\boldsymbol{a}$. The probabilities of hydraulic head values at unmeasured locations ($\boldsymbol{x}_*$) being less than or equal to the threshold values (denoted $\overline{\boldsymbol{I}}^*(\boldsymbol{x}_*, \boldsymbol{a})$) can be estimated using a linear combination of $\overline{\boldsymbol{I}}(\boldsymbol{x}, \boldsymbol{a})$ for each of the n observation well locations (Myers, 1982):

$$\overline{\boldsymbol{I}}^*(\boldsymbol{x}_*, \boldsymbol{a}) = \sum_{j=1}^{n} \overline{I}^*(x_j, \boldsymbol{a})\boldsymbol{\lambda}_j \tag{3.6}$$

Here, $\boldsymbol{\lambda}_j$ is a matrix of weights, which are found by solving the equation (Myers, 1982):

$$\sum_{j=1}^{n} \overline{\gamma}(\boldsymbol{x}_i - \boldsymbol{x}_j)\boldsymbol{\lambda}_j + \overline{\boldsymbol{\mu}} = \overline{\gamma}(\boldsymbol{x}_i - \boldsymbol{x}_*) \quad i = 1 \dots m \tag{3.7}$$

subject to the constraint:

$$\sum_{j=1}^{n} \boldsymbol{\lambda}_j = \boldsymbol{I} \tag{3.8}$$

Where $\overline{\boldsymbol{\mu}}$ is a of Lagrange parameters found by the solution of Equation 3.7, $\overline{\gamma}(\boldsymbol{x}_i - \boldsymbol{x}_j)$ is a matrix with the semi-variance between sites $\boldsymbol{x}_i$ and $\boldsymbol{x}_j$ given by the semi-variogram model for the indicator-transformed values for each threshold (as the diagonal elements) and the cross semi-variograms between indicator-transformed values for separate thresholds (as the off-diagonal elements), $\overline{\gamma}(\boldsymbol{x}_i - \boldsymbol{x}_*)$ is a matrix with the semi-variance between the sites $\boldsymbol{x}_i$ and $\boldsymbol{x}_*$ and $\boldsymbol{I}$ is the identity matrix.

Once the probabilities of hydraulic head values less than or equal to each threshold were calculated, order-relation corrections were applied to ensure a valid CCDF. In this study, we corrected the CCDF using the average of the upwards and downwards corrections as described by Deutsch and Journel (1998). After order-relation corrections were applied, linear interpolation (see Deutsch and Journel, 1998) was used to interpolate between the threshold values examined in this study. Interpolation was used to allow for the prediction of hydraulic head values at selected probabilities (e.g., the median or quartiles) and of the probability of hydraulic heads less than or equal to specified threshold values (e.g., SGTs). Additionally, the mean was estimated from the CCDF using the procedure outlined by Goovaerts (2009).

3.5 Results and Discussion

The following sections outline and discuss: (i) the semi-variogram models and cross-validation results, (ii) the regional hydraulic head distributions in the Triassic and Permian Formations, (iii) the likely hydraulic head values and associated uncertainties at the spring locations, (iv) the CCDF for hydraulic heads in the Triassic and Permian Formations and the probabilities of hydraulic heads in each formation exceeding SGTs, (v) the likelihood of the alternate conceptual models for the source of water to the springs, and (vi) the uncertainties and future directions for this study.

3.5.1 Semi-variogram models and cross-validation

Sixteen threshold values were used, leading to 120 direct and cross experimental semi-variograms. Figure 3.4 shows the semi-variogram models for 5 selected p-quantiles for the indicator transformed values in Triassic and Permian Formations. The 5 p-quantiles were chosen as representative values to show the fit of the semi-variogram models to the variety of semi-variance values derived from the experimental semi-variograms of the indicator transformed values for different thresholds. As shown in Figure 3.4, the semi-variogram models in the Triassic Formations have a short range fit of 10,280 m for p = 0.125 and p =

0.25, which increases to 21,012 m for p = 0.5, meaning hydraulic head values became dissimilar over a shorter distance for p = 0.125 and p = 0.25 when compared with p = 0.5. This could be related to physical differences resulting in varying ranges for different p-quantiles or few measurements at extreme thresholds to populate semi-variograms (Journel, 1983). This meant it was necessary to use a nested model with a short range for the lower p-quantiles and a larger range for the higher p-quantiles. We selected the Gaussian model for the model structures as the shape of the semi-variance in the short-range (<10,000 m) had a shape similar to that of the Gaussian model. We used a three-model nested structure consisting of the nugget, the Gaussian with a range of 5140 m, and the Gaussian with a range of 10506 m. The sills and nugget values were set using a linear model of coregionalization as described in Section 3.4.3. For example, the model structure for p=0.5 consisted of a nugget of 0.02 m^2, a Gaussian with a range of 10506 m and a sill of 0.60 m^2 and a Gaussian with a range of 5140 m and a sill of 0.07 m^2. As there were 120 semi-variograms, the sill and nugget for each semi-variogram are provided in Supplementary Material 3 (see Appendix B). The semi-variance for p = 0.75 and p = 0.875 was low ($\approx$0 m^2) due to most measurements having a high probability ($\approx$1) of being less than these thresholds, leading to a consistent spatial distribution that yielded low semi-variance values. As the SGTs are located between p = 0.125 and p = 0.5, where the semi-variance is better defined, the low semi-variance values for the higher p-quantiles should not influence the SGT probability estimates.

The experimental semi-variance and semi-variogram models for 5 p-quantiles in the Permian Formations are shown in Figure 3.4. The semi-variogram models exhibit a long range of 21,000 m, which is consistent between the semi-variance for the varying p-quantiles. A two-model nested structure was used comprising of the nugget and the spherical model with a range of 21,000 m. The sills and nuggets were fitted for each model using a lin-

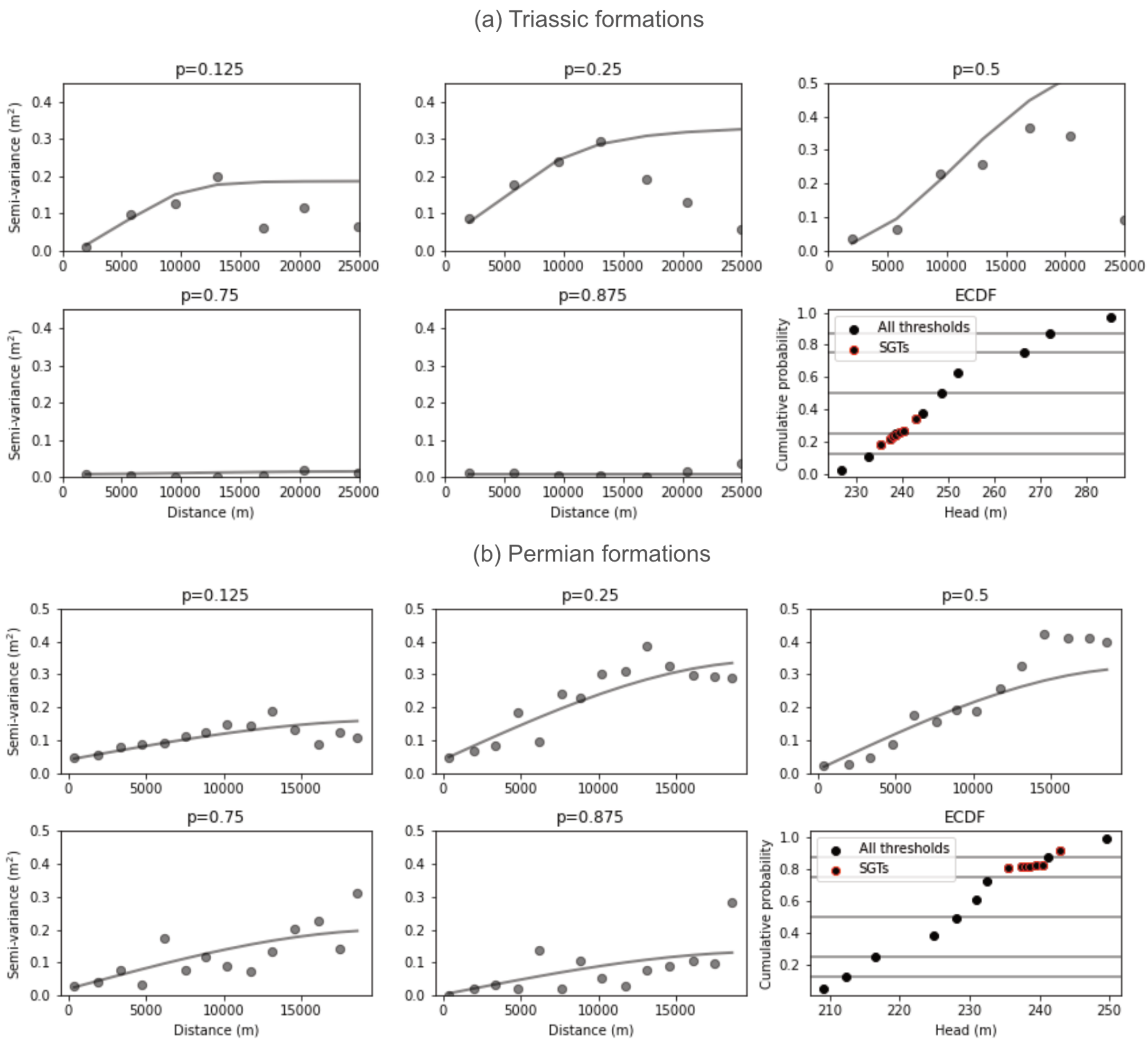

Figure 3.4: *The semi-variogram models for hydraulic head measurements in (a) the Triassic and (b) the Permian Formations shown with the empirical cumulative distribution function (ECDF) signifying each threshold with the SGTs circled in red.*

ear model of coregionalization (see Section 3.4.3). For p = 0.5, the two-model structure consisted of a nugget of 0.01 m^2 and a spherical model with a range of 21,000 m and a sill of 0.31 m^2. The nugget and sill for each of the semi-variogram models are provided in Supplementary Material 4 (see Appendix B). The semi-variance for all of the shown p-quantiles were well defined, likely due to adequate samples to properly characterise the semi-variance, including at extreme p-quantiles (e.g., p = 0.125 or p = 0.875).

For the Triassic Formations, the model had a ME of 0.83 m, a MAE of 5.06 m and a MSSR of 0.66. The ME indicated a low model bias as the ME was close to 0, suggesting the model was not overly biased towards over or under-predicting values. The MAE of 5.06 m suggested the model did not perform well at all data points. Cross-validation predictions near the edge of the study area had higher residuals than predictions near the springs. This is expected given that the fundamental assumption of the model is that points closer together are more similar (i.e., have a lower semi-variance). Importantly, the residuals in the vicinity of the springs were lower (i.e., between 0 and -3.9 m), indicating good model performance in the area of interest (Figure 3.5b). Additionally, the MSSR of 0.66 indicated that the prediction variance was larger than the squared residuals, suggesting the model over-estimated the prediction uncertainty, at least for the observation locations.

LOO-CV was conducted with the data for the Permian Formations. The results yielded a ME of -0.11 m, a MAE of 1.64 m, and a MSSR of 0.41. This indicated that the model for the Permian Formations had a low bias (i.e., the ME was close to 0) and had good predictive abilities, at least for the observation locations, as signified by the low MAE. The MSSR suggested that prediction variance was greater than the squared residuals, indicating that the model overestimated prediction uncertainty, at least for the observation locations. Spatially, the LOO-CV residuals in the Permian Formations suggested low errors (<5 m) throughout

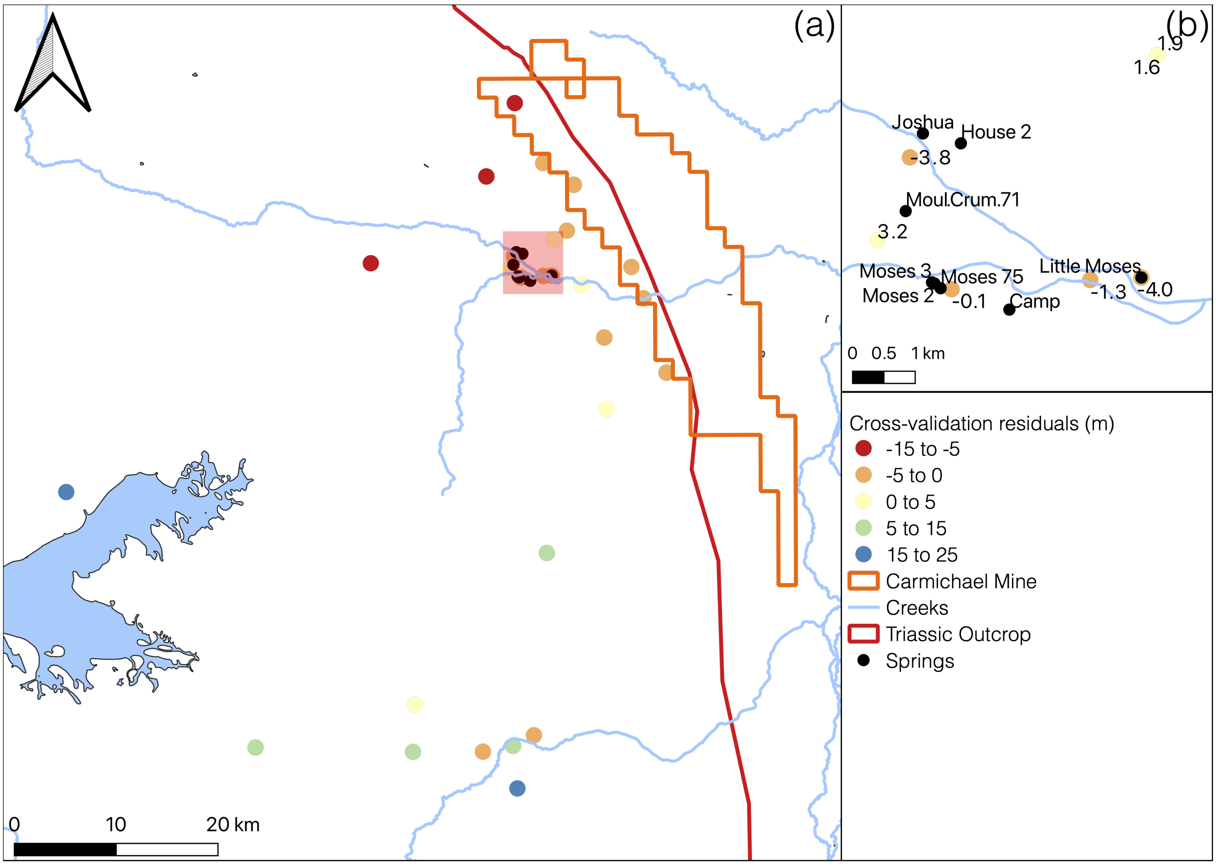

Figure 3.5: *Spatial distribution of residuals from leave-one-out cross-validation in the Triassic Formations with (a) showing a regional scale and (b) an inset map of the shaded red area in (a).*

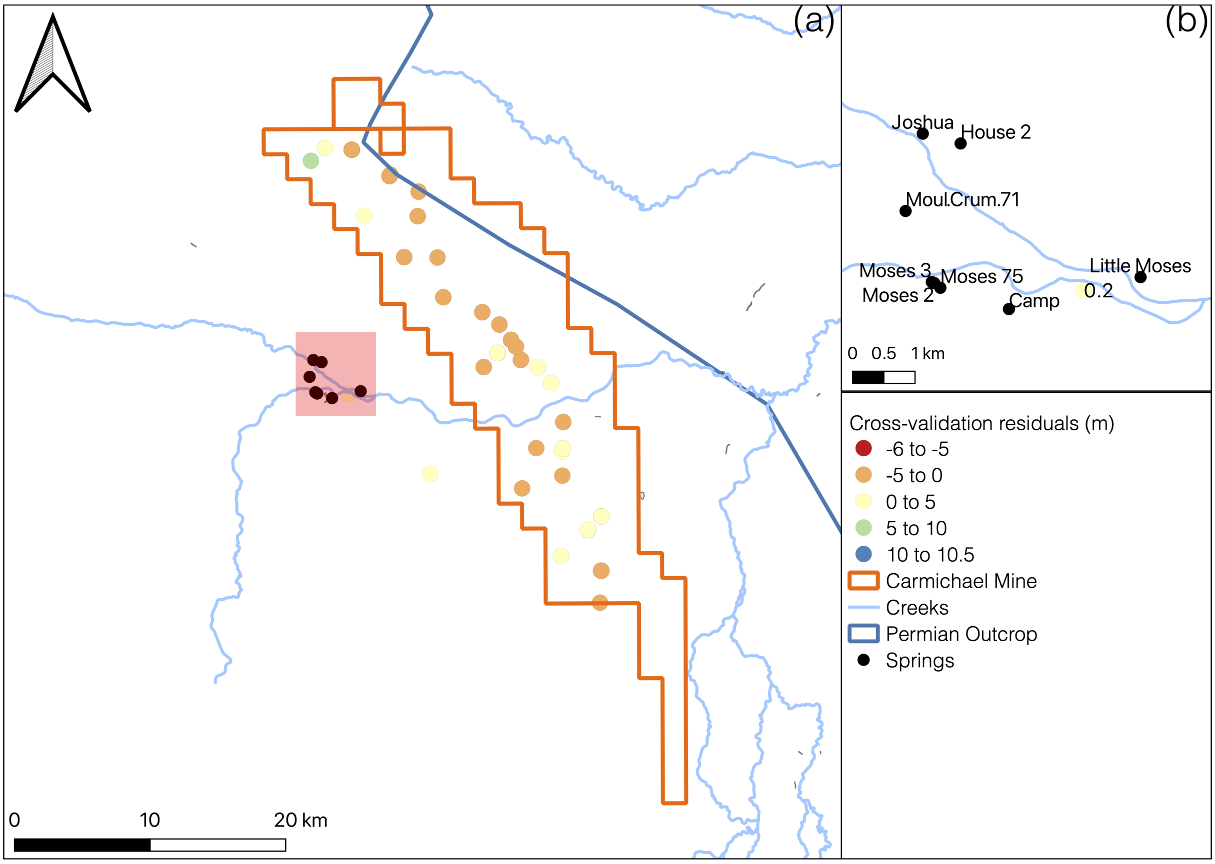

Figure 3.6: *Spatial distribution of residuals from leave-one-out cross-validation in the Permian Formations with (a) showing a regional scale and (b) an inset map of the shaded red area in (a).*

the study area (Figure 3.6a). Most importantly, only one well was available near the spring locations, and the residual at this location was 0.3 m (Figure 3.6b). This suggested that the model performed well in this area, despite few available measurements.

3.5.2 Regional hydraulic head distributions

The regional hydraulic head distributions can provide an indication of recharge areas, discharge areas and flow directions. Figure 3.7 displays the mean hydraulic head distributions in the Triassic Formations (Figure 3.7a) and the Permian formations (Figure 3.7b). The mean hydraulic head distribution in the Triassic Formations suggests higher hydraulic heads (>250 m) to the north, south and west of the springs, with a lower head near the springs (230-240 m) and a continued decrease to the east. The lower hydraulic heads near the springs may indicate discharge occurring to the springs and/or the Carmichael River. This

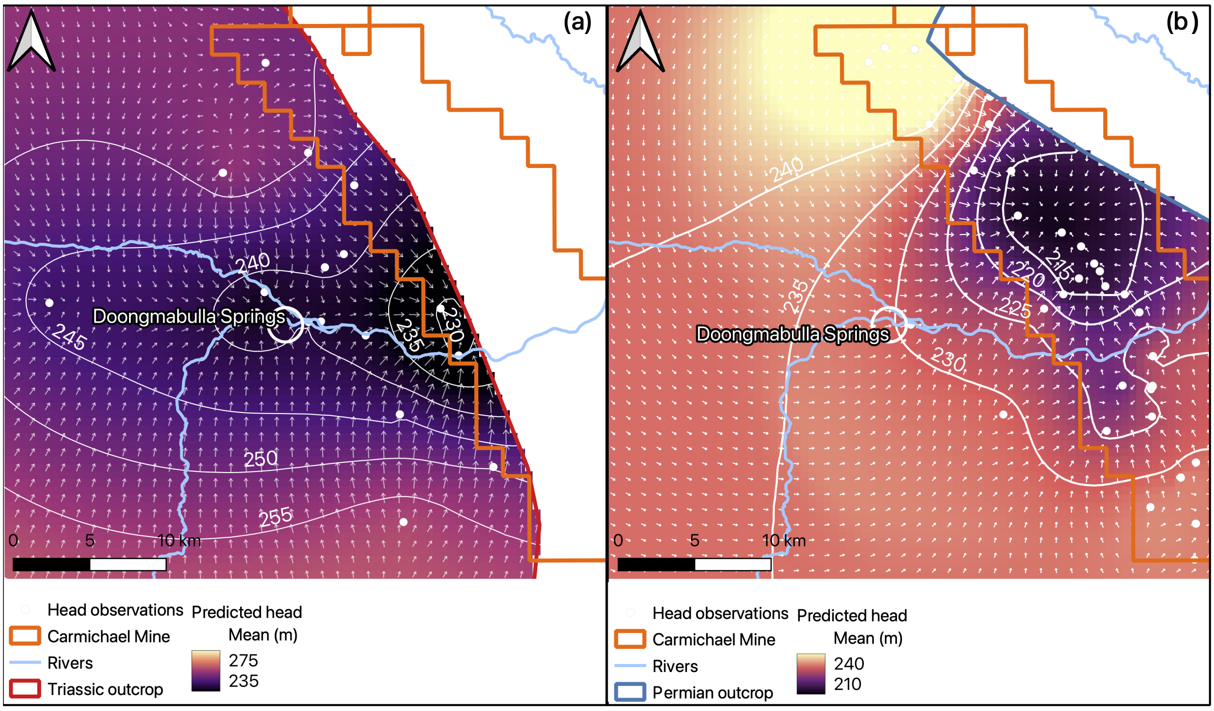

Figure 3.7: *Mean hydraulic head distributions in (a) the Triassic and (b) the Permian Formations.*

is consistent with the findings of Adani Mining (2013), who found that water in the Clematis Formation (a Triassic unit) flowed towards the DSC and Carmichael River. Furthermore, in both interpretations of the regional flow directions, the flow appears to continue to the east of the springs. As the formations outcrop to the east, it is plausible there may be flow from the Triassic Formations to other formations beyond the Galilee Basin.

The mean predictions in the Permian Formations suggest higher hydraulic heads (230-240 m) to the north, south and west of the study area, which lowers to $\approx$ 215 m in the mine area. Again, this is consistent with the flow directions interpreted by Adani Mining (2013) in the Colinlea Formation (a Permian unit). This pattern could indicate the presence of a discharge source in the mine site area. However, as no surface water bodies are observed, this may suggest discharge to another aquifer unit or groundwater extraction.

Table 3.1: The mean, median, quartiles, and interquartile range for the hydraulic head in the Triassic Formations at each spring location.

Spring ID (SGT m)	Mean (m)	Median (m)	Q1 (m)	Q3 (m)	Q3 – Q1 (m)
A (237.5)	236.4	236.8	234.5	238.5	3.9
B (238.0)	236.7	236.9	235.2	238.3	3.1
C (238.0)	236.6	236.9	235.2	238.3	3.2
D (238.4)	236.6	236.9	235.1	238.3	3.2
E (240.5)	237.3	237.3	235.4	239.0	3.6
F (242.8)	236.8	237.0	235.3	238.5	3.3
G (239.4)	236.8	237.0	235.5	238.4	2.9
H (235.7)	235.8	235.5	232.7	239.4	6.8

3.5.3 Hydraulic head estimates at spring locations

The CCDF for each spring was used to calculate statistics representing the likely hydraulic head values and associated uncertainties at the spring locations. These statistics consisted of the mean, median, first quartile (Q1), third quartile (Q3), and interquartile range (Q3 – Q1). Table 3.1 displays these statistics for the hydraulic head estimates in the Triassic Formations at each spring location. The mean hydraulic head estimates in the Triassic Formations range from 235.8 m at spring H to 237.3 m at spring E. The median is larger than the mean for all spring locations, except springs E and H, indicating that the CCDF is not symmetric and has a negative skew. The negative skew indicates a wider range of plausible values less than the mean compared to the range of values greater than the mean. The uncertainty in the mean estimate can be represented using the quartile values Q1 and Q3, which reflect the bounds about the mean within which there is a 0.5 probability of the true value residing. The lower quartile, Q1, ranges from 232.7 m at spring H to 235.5 m at spring G. While the upper quartile, Q3, ranges from 238.3 m at springs B, C and D to 239.4 m at spring H. The interquartile range, Q3 – Q1, for estimates at the spring locations in the Triassic Formations ranges from 2.9 m to 6.8 m.

Table 3.2: *The mean, median, quartiles, and interquartile range for the hydraulic head in the Permian Formations at each spring location.*

Spring ID (SGT m)	Mean (m)	Median (m)	Q1 (m)	Q3 (m)	Q3 - Q1 (m)
A (237.5)	230.2	230.2	227.5	232.2	4.7
B (238.0)	230.9	230.6	228.0	232.5	4.5
C (238.0)	230.8	230.6	228.0	232.5	4.5
D (238.4)	230.8	230.6	227.9	232.5	4.5
E (240.5)	230.4	230.6	227.0	233.3	6.3
F (242.8)	231.1	230.9	227.4	233.9	6.6
G (239.4)	231.1	230.8	227.9	233.2	5.4
H (235.7)	228.5	229.1	226.3	231.6	5.3

Table 3.2 displays the mean, median, quartiles and interquartile range in the Permian Formations at the spring locations. The mean hydraulic head estimates in the Permian Formations range from 228.5 m at spring H to 231.1 m at springs F and G. The mean values are greater than the median for all springs, except for springs A, E and H. This suggests that the CCDF has a positive skew, indicating a larger range of plausible values greater than the median. The first quartile, Q1, ranges from 226.3 m at spring H to 228 m for springs B and C. While the third quartile, Q3, ranges from 231.6 m at spring H to 233.9 m at spring F. The interquartile ranges of Permian Formations range from 4.5 m for springs B, C and D to 6.6 m at spring F.

The mean values in the Permian Formations are less than the SGTs for all springs, while the mean values for these springs in the Triassic Formations are less than the SGTs for all springs except spring H. The SGTs are within the interquartile range for the hydraulic head in the Triassic Formations for springs A, B, C and H. In contrast, the SGTs at all spring locations are higher than Q3 for the hydraulic heads in the Permian Formations.

Tables 3.1 and 3.2 show that the estimated mean hydraulic head values are greater in the Triassic Formations than the Permian Formations for all springs. This difference between hydraulic head values in the Permian and Triassic Formations indicates the potential vertical direction of groundwater flow if hydraulic connectivity exists across the Rewan Formation aquitard. This hydraulic head difference has implications for interpreting the source aquifer for the DSC springs, and various scenarios can be developed whereby hydraulic head differences across the Rewan Formation influence conceptual model development. For example, it may be possible that connectivity exists across the Rewan Formation near the springs and the Permian Formations provide a source of water to the Triassic Formations, which in turn are a source of water to the DSC. In this case, that scenario appears unlikely as the hydraulic heads in the Triassic Formations appear higher than those in the Permian Formations, suggesting the potential for downwards flow.

3.5.4 Spring geomorphic threshold probabilities

The estimated probabilities (i.e., $\overline{I}^*(x_*, a)$) that hydraulic heads at spring locations are less than or equal to thresholds (i.e., a) are shown in Figure 3.8, in the form of CCDFs. Probabilities range from 0 to 1. That is, probabilities for spring B of non-exceedance of 233 and 239 m are 0 and 1 (respectively) in the Triassic Formations, while corresponding non-exceedance probabilities for the Permian Formations are 0 and 1 for elevations of 220 and 245 m, respectively. Figure 3.8 shows that the CCDF for Permian Formations changes more gradually than the CCDF for the Triassic Formations due to the larger range of hydraulic head values for the Permian Formations. This is a consequence of the greater uncertainty in Permian hydraulic head values (relative to Triassic hydraulic heads) at spring locations, as outlined in Section 3.5.3.

The estimates shown in Figure 3.8 appear similar for some springs (e.g., Springs B, C and D) due to the close proximity of these locations (see Figure 3.1c). For tabulated values of estimated probabilities, the reader is directed to Table A.1 (for the Triassic Formations)

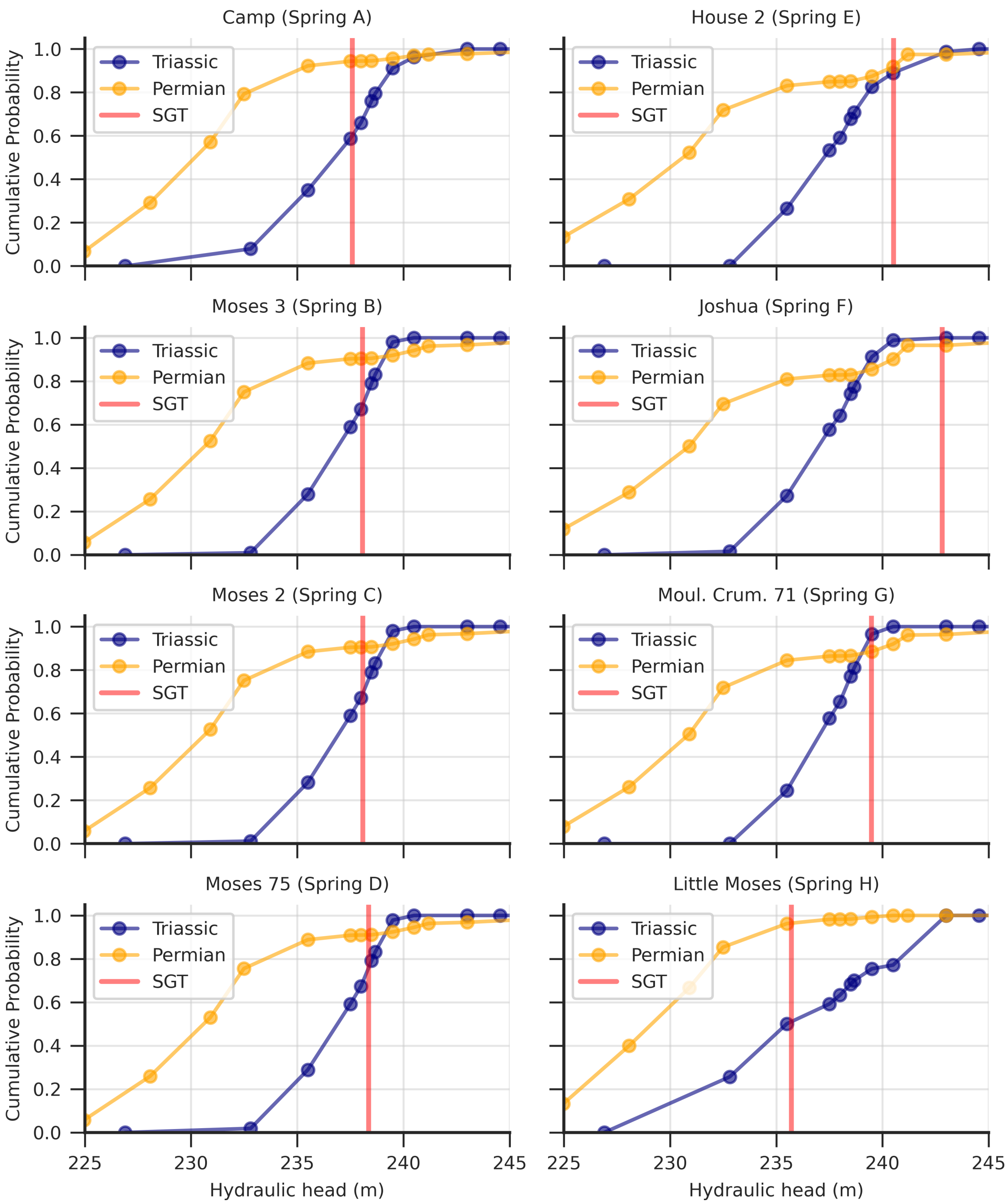

Figure 3.8: *Conditional cumulative distribution functions describing the probability of hydraulic head values less than hydraulic head thresholds for eight spring locations in the DSC. The red line indicates the spring geomorphic threshold (SGT) for each spring. See Figure 3.1c for spring locations.*

and Table A.2 (for the Permian Formations) in Appendix A. Tables A.1 and A.2 show that the majority of probabilities abide by order relations, with order-relation corrections applying predominantly to probabilities near the limits of 0 and 1. The order-relation deviations at extreme values are not unexpected, given the lack of data available to populate semi-variograms beyond the hydraulic head elevation limits, as discussed by Deutsch and Journel (1998).

CCDFs for the Triassic and Permian Formations can be used to assess the probability of each formation having adequate hydraulic head to exceed individual SGTs, referred to hereafter as 'SGT probabilities'. SGT probabilities are identified in Figure 3.8 by the intersection of red lines (SGTs) and CCDF curves. The probabilities of the Triassic and Permian Formations having hydraulic heads exceeding the SGTs are given in Table 3.3. These were obtained by subtracting values of $\overline{I}^*(x_*, a)$ from one. The probability that head in the Triassic Formations exceeds SGTs at the spring locations range from <0.01 to 0.49, while the probability that Permian Formation heads exceed SGTs ranges from 0.03 to 0.12. The results indicate that Triassic Formations have a moderate probability ($\geq$0.24) of adequate hydraulic head to support the southern springs (A, B, C and D) and a south-eastern spring (H), but lower probabilities ($\leq$0.11) of adequate hydraulic head to support the northern springs (E, F, G). Results also indicate a lower probability ($\leq$0.12) that the Permian Formations have adequate head to exceed the SGTs of all springs. Notably, the Triassic Formations have a higher probability of hydraulic heads exceeding spring SGTs than the Permian Formations for all springs except springs F and G.

3.5.5 The likelihood of alternate conceptual models

The likelihood of the alternate conceptual models for the source of water to the DSC can be considered based on the regional hydraulic head distributions (Section 3.5.2), likely

Table 3.3: *The probabilities of adequate hydraulic head to exceed SGTs for the springs in the Triassic and Permian Formations.*

	Probabilities	
Spring ID (SGT m)	Triassic	Permian
A (237.5)	0.40	0.06
B (238.0)	0.31	0.10
C (238.0)	0.31	0.09
D (238.4)	0.24	0.09
E (240.5)	0.11	0.08
F (242.8)	<0.01	0.03
G (239.4)	0.04	0.12
H (235.7)	0.49	0.04

hydraulic head values at spring locations (Section 3.5.3), and SGT probabilities (Section 3.5.4). The regional hydraulic head distributions in the Triassic Formations suggested higher head in the north, south and west of the study area reducing towards lower head near the springs and along the Carmichael river to the west (Figure 3.7a). This may suggest the occurrence of discharge (e.g., spring flow or baseflow to the river) from the Triassic Formations in this area. While, the hydraulic head distribution in the Permian Formations suggests higher heads to the north, south and west, lowering to a minimum in the mine site area (Figure 3.7b). As no surface water bodies are observed in this area, this pattern may indicate discharge occurring to another formation. These hydraulic head distributions suggest that the Triassic Formations display a pattern more consistent with discharge to the DSC than that observed in the Permian Formations.

The likely hydraulic head values at the spring locations indicate the potential vertical flow directions if connectivity existed across the Rewan Formation in these locations. The results suggest that the hydraulic head at the spring locations are likely higher in the Triassic Formations than in the Permian Formations (Table 3.1 and Table 3.2). This indicates that if connectivity existed in these locations, flow directions would likely be downwards from the Triassic to the Permian Formations, which implies it is unlikely that the Permian Formations could be contributing water to the Triassic Formations in this area.

The Triassic Formations have a higher probability than the Permian Formations of adequate hydraulic head to support spring flow to springs A, B, C, D, E and H. SGT probabilities for springs F and G were low for both formations suggesting inconclusive findings for these springs. Overall, the hydraulic head evidence interpreted from regional head distributions, potential vertical flow directions and SGT probabilities suggests that the Triassic Formations are more likely than the Permian Formations to provide a source of water to springs A, B, C, D, E and H, while results for spring F and G were inconclusive. Despite these findings, it remains plausible that the Permian Formations may indirectly support the springs by providing a source of water to the Triassic Formations via connectivity at a location away from the spring sites. Thus, although the Triassic Formations may present as the principal source of water at the spring locations (i.e., due to hydraulic heads exceeding the SGT and flow directions converging towards the DSC), the Permian Formations may nevertheless contribute indirectly to spring flow via leakage to, and pressurisation of, the Triassic Formations at another location. In this scenario, the Permian Formations may indirectly support spring flow even though Permian heads do not exceed Triassic heads at the spring locations.

Nevertheless, if connectivity exists across the Rewan Formation at a location, then drawdown in the Permian Formations due to mine site dewatering may impact the DSC. That is, if drawdown in the Permian Formations propagates through connections between the two formations, this will induce a net downward flux (relative to the natural, pre-mining conditions) regardless of the natural head gradient (and flow direction) across the Rewan Formation. The resulting drawdown could result in the reduction or cessation of flow from the DSC, even if the Permian Formations do not discharge either into the Triassic Formations or directly to the springs. Thus, for mining activities to potentially affect spring discharge, there need only to be connectivity between the Permian and Triassic Formations, close enough to the DSC that mining-induced drawdown in either formation can reach the springs.

3.5.6 Uncertainties and future directions

Conceptual models are often accepted or rejected based on their consistency with the observed data (Enemark et al., 2019). However, the consistency of a model with observed data does not ensure that the model is a valid representation of the system (Oreskes et al., 1994), and this consistency may change as new data becomes available (Enemark et al., 2019). In our case, both conceptual models are reasonably consistent with observations (see Section 3.5.1), but give a low probability of adequate head to support spring flow, particularly for springs F and G. This may be explained as either a type I error, where a valid conceptual model has not been considered, or a type II error, where an invalid conceptual model has been adopted (Neuman, 2003).

A plausible error type II error is that the conceptual models did not consider the vertical stratification of hydraulic head measurements within each formation. In this study, most of the available measurements, particularly in the Triassic Formations, were taken at shallow depths, making it difficult to characterise the vertical stratification of hydraulic heads within the formations. A recently drilled well (August 2020) in the Triassic Formation suggests an increase in the head with depth, and as the analysis in the Triassic Formations is based primarily on shallow measurements, it is plausible that it may underestimate the potential of the Triassic Formations to support spring flow. Similarly, vertical stratification of hydraulic heads within the Permian Formations may exist, which could influence modelling outcomes. However, there is a lack of measurements outside of the mine site to identify any vertical head stratification in the Permian Formations. Future studies should consider the vertical stratification within these formations and how this influences modelling outcomes, which would require the installation of piezometers to monitor the head at various depths in both the Permian and Triassic Formations.

Alternately, there could be a valid conceptual model being ignored (e.g., a conceptual model where the shallow Tertiary or deeper Joe Joe Formation that underlies the Permian Formation provide water to the spring), or there may be a lack of data to properly interrogate these conceptual models. Although there were more data points in the Permian Formations than the Triassic Formations (i.e., 78 and 34, respectively), these data were clustered in a region near the margin of the study area, with only a few measurements in the region near the springs (Figure 3.1). The Kriging weights given by the solution of Equation 3.7 take into account the redundancy of measurements, whereby measurements located close to one another may convey little additional information (Diggle et al., 1998). As such, many of the data points within localised data clusters were largely redundant and provided minimal additional information about the regional hydraulic head distribution. In contrast, the Triassic Formations had measurements over a wider spatial distribution and, therefore, less data redundancy than those of the Permian Formations (Figure 3.1). Furthermore, the Permian had only a single well (ID:190229_A) near the spring locations, which meant the findings in the Permian Formations at the spring locations were highly dependent on the quality of this measurement. This was a single measurement collected on the same day as drilling, without a reported survey method, and thus was assigned a mean of 229.86 m (i.e., the measured value) and a range of 222.9 to 236.8 m, based on the considered uncertainties. As demonstrated by the cross-validation map of residuals (Figure 3.6), the inclusion of this well had little impact on the mean predictions as the predicted value at this well (when censoring the observation) was 229.57 m, which is within 0.3 m of the observed head value.

However, the inclusion of this observation reduced the uncertainty of predictions substantially in the vicinity of the springs. This influenced the SGT probabilities for the Permian Formations by reducing the plausibility of adequate head to meet the SGTs.

The modelling of the impacts of mine induced drawdown on the DSC outlined in the environmental impact statement assumes that the source aquifer is the Triassic Formations and that adaptive management will be applied to mitigate impacts upon the springs (Adani Mining, 2013). However, studies by other investigators (e.g., Webb, 2015; Currell et al., 2017; CSIRO and Geoscience Australia, 2019; Werner et al., 2019; Currell et al., 2020) have suggested that there is substantial uncertainty in the source aquifer of the DSC and that the Permian conceptualisation remains plausible. The results of this study indicate that the Triassic conceptualisation is more likely than the Permian conceptualisation, although both conceptualisations remain plausible. Significant uncertainty exists in our assessment due to hydraulic head measurement scarcity in the vicinity of the springs and the analysis only considering a single data type (Neuman and Wierenga, 2003). Furthermore, the locations and degree of inter-aquifer connectivity across the Rewan Formation aquitard is a major source of uncertainty (CSIRO and Geoscience Australia, 2019), which will control how the drawdown in the Permian Formations will impact the DSC. Despite the remaining conceptual model uncertainties and the unsuitability of adaptive management to scenarios with time-delayed or irreversible impacts (Currell et al., 2017; Thomann et al., 2020), the mine has been approved. Future studies should aim to reduce the conceptual model uncertainty to identify potential impacts and mitigation strategies. This could be achieved through the installation of additional monitoring wells at various depths in the major formations as well as by analysing other data types, including hydrochemistry and geophysical surveys, and investigating the degree of inter-aquifer connectivity across the Rewan Formation aquitard at and away from the DSC.

Conclusions

Knowledge of hydraulic head distributions throughout aquifers can assist in hydrogeological conceptual model development and assessment. Ordinary Indicator Co-Kriging is a geostatistical interpolation technique that estimates hydraulic head values and their uncertainties at unmeasured locations. These hydraulic head estimates can be used to quantitatively assess the probability of hydraulic heads exceeding specified thresholds at unmeasured locations. Additionally, when expert knowledge is available for physical thresholds in the hydrogeological system (e.g., hydraulic head thresholds required for spring flow), the likelihood of conceptual models meeting these physical thresholds can be quantitatively assessed. This approach is widely applicable throughout hydrogeology in the assessment of conceptual models.

The application of the Ordinary Indicator Co-Kriging in conceptual model assessment was demonstrated using the hydraulic head data from the alternate hypothesised source aquifers of the DSC. The analysis indicated likelihoods ranging from <0.01 to 0.49 that the Triassic Formations have adequate hydraulic head to support flow to the DSC springs assessed here, while there was a lower likelihood (i.e., 0.03 to 0.12) that the springs could derive water from the deeper Permian Formations. These results suggest that the Triassic Formations have a higher likelihood of adequate hydraulic head than the Permian Formations. However, significant uncertainty exists in the conceptual model assessment due to hydraulic head measurement scarcity in the vicinity of the springs (particularly in the Permian Formations) and the analysis only considering a single data type. Furthermore, the locations and degree of inter-aquifer connectivity across the Rewan Formation aquitard is a major source of uncertainty, which will influence the likelihood of alternate conceptual models and control how the drawdown in the Permian Formations will impact the DSC. As such, we suggest that further studies are conducted to complement this research through the collection of additional hydraulic head measurements, analysis of other data types, including hydrochemistry and geophysical surveys, and further investigation into the degree of inter-aquifer connectivity across the Rewan Formation aquitard at and away from the DSC.

CHAPTER 4

IDENTIFYING GROUNDWATER RECHARGE AND DISCHARGE ZONES USING GEOSTATISTICAL SIMULATION OF HYDRAULIC HEAD AND ITS DERIVATIVES

Keegan-Treloar, R., Irvine, D.J., Werner, A.D. and Banks, E.W., 2022. Identifying groundwater recharge and discharge zones using geostatistical simulation of hydraulic head and its derivatives. Journal of Hydrology, p.128993.

Approximate contribution of co-authors: Robin Keegan-Treloar (85%), Dylan Irvine (5%), Adrian Werner (5%) and Eddie Banks (5%).

Abstract

Identifying groundwater flow directions and the locations of recharge and discharge areas is critical for effective groundwater management. Groundwater flow directions, the concavity and the locations of extrema (i.e., minima and maxima) can be assessed using the first and second derivatives of the hydraulic head surface. We developed a geostatistical method to jointly simulate hydraulic head and its first and second derivatives using sequential Gaussian simulation. The derivative values were used to identify regional groundwater flow directions, and the second derivative test was used to probabilistically map the concavity and the locations of extrema in the hydraulic head surface. By comparing the mapped concavity and extrema to known features, it was possible to attribute areas of recharge and discharge to physical features of the system, such as rivers, lakes and geological outcrops. This was applied to Triassic aquifers in the Galilee Basin (Queensland, Australia) to delineate the likely recharge and discharge areas. This provided an objective assessment of likely recharge and discharge zones and their uncertainty, which is an important addition to a region where the hydrogeology has been the subject of much conjecture.

4.1 Introduction

Hydraulic head gradients are important in hydrogeological studies, as they are proportional to the rate of groundwater flow and control the flow directions, which provides critical information for understanding groundwater systems (Pardo-Igúzquiza and Chica-Olmo, 2004). However, hydraulic head measurements are typically sparsely distributed point measurements (Rau et al., 2019), which can make interpretation of hydraulic gradients challenging.

To address these challenges, Philip and Kitanidis (1989) provided a modified form of Ordinary Kriging that allowed for the direct estimation of hydraulic head gradients from sparse hydraulic head observations. They applied their approach to estimate the regional groundwater flow directions in the Wolfcamp aquifer in northern Texas, USA. Pardo-Igúzquiza and Chica-Olmo (2004) further developed this approach, using Universal Kriging to account for a systematic trend in the mean. The benefits of geostatistical approaches over other techniques for mapping hydraulic head gradients (e.g., numerical modelling) include that they are generalisable, do not require specification of boundary conditions or geological properties, and can provide quantitative estimates of uncertainty. However, the results are dependent on the semi-variogram model and fitting a representative model can be challenging when working with small datasets (Goovaerts, 1997). Additionally, the grid resolution and number of realisations influence model run times, as can be the case with numerical modelling.

Developing conceptual models of groundwater systems, including by mapping groundwater flow directions and locations of recharge and discharge areas, is critical for effective groundwater management (Enemark et al., 2019; Thomann et al., 2020). The concavity (i.e., concave up or concave down) and the locations of extrema (i.e., minima, maxima or inflection points) in the hydraulic head surface (see Figure 4.1) can be identified using information from the first and second derivatives of the inferred hydraulic head surface. Although previous work has used Kriging to estimate the first derivatives of hydraulic head surface (e.g., Philip and Kitanidis, 1989; Pardo-Igúzquiza and Chica-Olmo, 2004), no studies have used geostatistics to calculate higher-order derivatives and use these to map concavity and extrema in the hydraulic head surface. Herein, we extend the work of Philip and Kitanidis (1989) and Pardo-Igúzquiza and Chica-Olmo (2004), to simulate realizations of the first and second derivatives of the hydraulic head surface using sequential Gaussian simulation. We

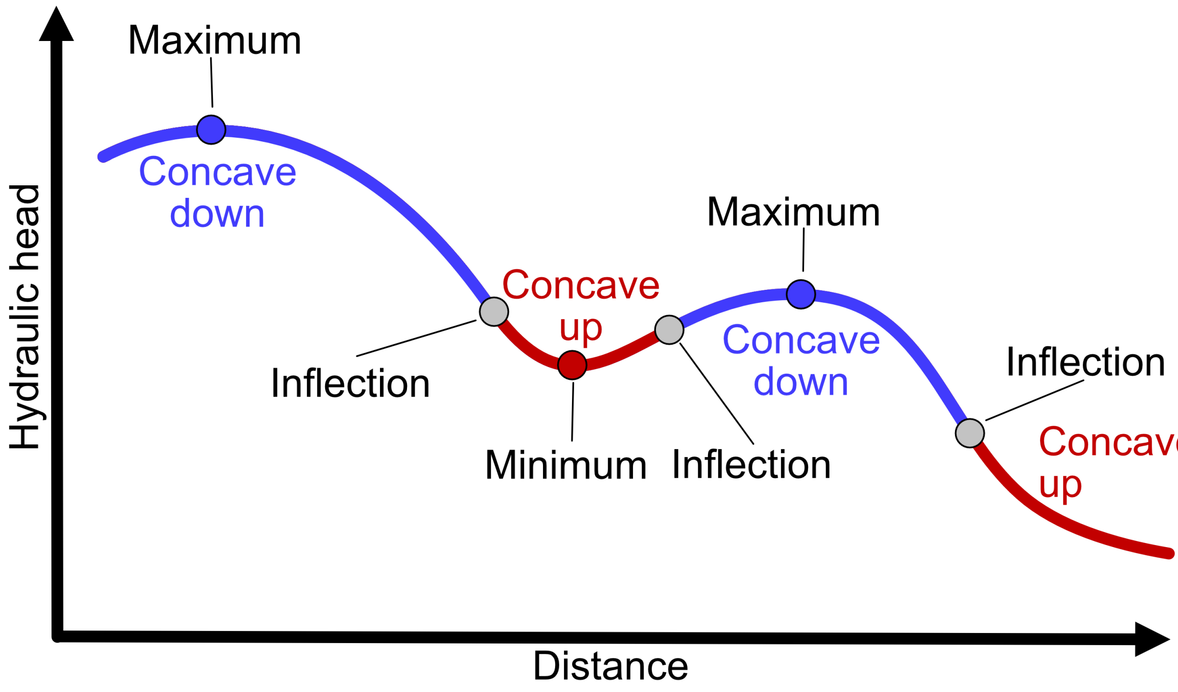

Figure 4.1: *Illustration of a 2D hydraulic head surface showing concave up areas (red) and concave down areas (blue) labelled with dots marking minimum, maximum and inflection points.*

show how realizations of the derivatives of hydraulic heads can be used to probabilistically map the locations of extrema and concavity of the hydraulic head surface, which can subsequently be compared with known surface features (e.g., rivers, lakes, geological outcrops) to identify plausible recharge and discharge areas. We apply the technique to sparsely distributed hydraulic head data from the Triassic aquifers of the Galilee Basin in Queensland, Australia. This provides an objective assessment of the likely recharge and discharge areas for the Triassic aquifers of the Galilee Basin, which is vital to inform the ongoing debate regarding the hydrogeology of the region (Currell et al., 2020). The approaches presented here represent a significant advancement in the use of hydraulic head data to map recharge and discharge areas.

4.2 Methods

4.2.1 Hydraulic head and derivative simulation

Consider the random function $\boldsymbol{Z}(\boldsymbol{u})$ observed at a set of coordinates $\boldsymbol{u}$ (e.g., $\boldsymbol{u_1} = [x_1, y_1]$) of shape $n \times 2$. A single realization of plausible values ($\boldsymbol{Z}^*(\boldsymbol{u}^*)_k$) at a set of m unobserved locations ($\boldsymbol{u}^*$) can be found using sequential Gaussian simulation (Goovaerts, 1997). Sequential Gaussian simulation is an iterative process where first a coordinate ($\boldsymbol{u}_i^*$) is randomly selected from the set $\boldsymbol{u}^*$. Next, simple Kriging is used to estimate the mean (Cressie, 1990; Goovaerts, 1997):

$$\boldsymbol{Z}(\boldsymbol{u_i}^*) = \boldsymbol{\lambda}^T \boldsymbol{Z}(\boldsymbol{u}) + (\mathbf{1}_n - \boldsymbol{\lambda}^T \mathbf{1}_n)\mu \tag{4.1}$$

Where $\boldsymbol{\lambda} = \boldsymbol{C}(\boldsymbol{u}, \boldsymbol{u}_i^*)[\boldsymbol{C}(\boldsymbol{u}, \boldsymbol{u}) + \boldsymbol{I} + \sigma^2]$, $\boldsymbol{C}(\boldsymbol{u}, \boldsymbol{u}_i^*)$ is the covariance between $\boldsymbol{u}$ and $\boldsymbol{u}_i^*$, $\boldsymbol{C}(\boldsymbol{u}, \boldsymbol{u})$ is the covariance between $\boldsymbol{u}$, $\mathbf{1_n}$ is a vector of ones of length n, $\boldsymbol{\sigma^2}$ is a vector of the variance associated with each observation, and μ is a constant known mean. The $\boldsymbol{\sigma^2}$ term regularizes the model to prioritize fitting higher quality measurements (i.e., low variance measurements) over those of lesser quality (i.e., high variance measurements). The variance of the hydraulic head timeseries available for each well can be assigned based on the measurement metadata (e.g., elevation survey method, water level measurement method; see Rau et al. (2019) and Post and von Asmuth (2013)) and the temporal variability in the hydrograph (see Keegan-Treloar et al. (2021)). Alternately, $\boldsymbol{\sigma^2}$ can be set to a constant value if all measurements have comparable error, or to 0 if the value is known exactly (e.g., from a computer simulation). μ can be chosen based on known values (e.g., if the function is known to converge towards a constant value), the arithmetic mean of the observation values, or the best linear unbiased estimate (Cressie, 1990; Goovaerts, 1997). The best linear unbiased estimate is defined as (Cressie, 1990):

$$\mu = (\mathbf{1}_n(\boldsymbol{C}(\boldsymbol{u},\boldsymbol{u}) + \boldsymbol{I}\boldsymbol{\sigma}^2)^{-1})^T \frac{\boldsymbol{Z}(\boldsymbol{u})}{(\mathbf{1}_n(\boldsymbol{C}(\boldsymbol{u},\boldsymbol{u}) + \boldsymbol{I}\boldsymbol{\sigma}^2)^{-1})^T\mathbf{1}_n} \tag{4.2}$$

The variance associated with estimates from Equation 4.1 is calculated as (Cressie, 1990; Goovaerts, 1997):

$$\sigma^2(\boldsymbol{u}_i^*) = C(\boldsymbol{u}_i^*, \boldsymbol{u}_i^*) - \boldsymbol{\lambda}\boldsymbol{C}(\boldsymbol{u}, \boldsymbol{u}_i^*) \tag{4.3}$$

Once $Z(\boldsymbol{u}_i^*)$ and $\sigma^2(\boldsymbol{u}_i^*)$ have been estimated, a value $Z^*(\boldsymbol{u}_i^*)$ is randomly drawn from a normal distribution:

$$Z^*(\boldsymbol{u}_i^*) = N(Z(\boldsymbol{u}_i^*), \sigma^2(\boldsymbol{u}_i^*)) \tag{4.4}$$

$Z^*(\boldsymbol{u}_i^*)$ is then treated as an observed value by appending $Z^*(\boldsymbol{u}_i^*)$ to $Z(\boldsymbol{u})$, $\boldsymbol{u}_i^*$ to $\boldsymbol{u}$, and 0 to $\boldsymbol{\sigma}^2$. Equations 4.1, 4.3 and 4.4 are repeated until $Z^*(\boldsymbol{u}_i^*)$ has been simulated for the m locations in $\boldsymbol{u}^*$. Note Equation 4.2 is only applied on the first iteration to estimate a stationary value of μ from $\boldsymbol{Z}(\boldsymbol{u})$.

The term Kriging is a synonym for what is known as Gaussian processes in the machine learning community (Rasmussen and Williams, 2006). The derivative of a Gaussian process is itself a Gaussian process, and consequently, Gaussian processes can be used to estimate the derivatives of a function (Solak et al., 2003; Rasmussen and Williams, 2006; Duvenaud, 2014). Estimates of partial derivatives can be obtained by differentiating the covariance and mean functions, and Kriging as usual (Philip and Kitanidis, 1989; Pardo-

Igúzquiza and Chica-Olmo, 2004; Duvenaud, 2014). As μ is assumed to be constant in Equation 4.1, and the derivative of a constant value is 0, Equation 4.1 simplifies to:

$$\overline{Z}(u_i{}^*) = \overline{\lambda}^T Z(u) \tag{4.5}$$

Where a realization of the partial derivatives is given by:

$$\overline{Z}(u^*) = \Big[\frac{\partial Z(u^*)}{\partial x^*} \frac{\partial Z(u^*)}{\partial y^*} \frac{\partial^2 Z(u^*)}{\partial x^{*2}} \frac{\partial^2 Z(u^*)}{\partial y^{*2}} \frac{\partial^2 Z(u^*)}{\partial x^* \partial y^*}\Big] \tag{4.6}$$

and:

$$\overline{\lambda} = [C(u,u) + I\sigma^2]^{-1} \Big[\frac{\partial C(u,u^*)}{\partial x^*} \frac{\partial C(u,u^*)}{\partial y^*} \frac{\partial^2 C(u,u^*)}{\partial x^{*2}} \frac{\partial^2 C(u,u^*)}{\partial y^{*2}} \frac{\partial^2 C(u,u^*)}{\partial x^* \partial y^*}\Big] \tag{4.7}$$

Where $\frac{\partial C(u,u^*)}{\partial x^*}$ is the derivative of the covariance function with respect to x^*, $\frac{\partial C(u,u^*)}{\partial y^*}$ is the derivative of the covariance function with respect to y^*, $\frac{\partial^2 C(u,u^*)}{\partial x^{*2}}$ is the second derivative of the covariance function with respect to the x^*, $\frac{\partial^2 C(u,u^*)}{\partial y^{*2}}$ is the second derivative of the covariance function with respect to y^*, and $\frac{\partial^2 C(u,u^*)}{\partial x^* \partial y^*}$ is the partial derivative of the covariance function with respect x^* and y^*. Note that as the partial derivatives are conditioned solely on $Z(u)$, the Kriging can be applied independently for each partial derivative (e.g., using $\overline{\lambda} = [C(u,u) + I\sigma^2]^{-1}\frac{\partial C(u,u^*)}{\partial x}$ to estimate $\frac{\partial Z(u^*)}{\partial x^*}$ with Equation 4.5), which may be necessary to preserve computer memory when working with large matrices. In this paper we provide the derivatives for the Gaussian covariance function (Supporting Text S1 in Appendix C).

4.2.2 Locating minima and maxima

Once a realization of $\overline{Z}(u^*)$ is generated, extrema (i.e., minima and maxima in the hydraulic head surface) can be identified using the second derivative test (Stewart, 2010). The locations of critical points are identified by finding where $\frac{\partial Z(u^*)}{\partial x^*}$ and $\frac{\partial Z(u^*)}{\partial y^*}$ are equal to 0. As $\frac{\partial Z(u^*)}{\partial x^*}$ and $\frac{\partial Z(u^*)}{\partial y^*}$ are simulated at nodes and the zero values may be located between nodes, contouring (using linear interpolation) can be used to approximate the coordinates where $\frac{\partial Z(u^*)}{\partial x^*}$ and $\frac{\partial Z(u^*)}{\partial y^*}$ are equal to zero. This allows for the coordinates of the critical points to be approximated by finding the intersections of the zero contours for $\frac{\partial Z(u^*)}{\partial x^*}$ and $\frac{\partial Z(u^*)}{\partial y^*}$. Once these points are identified, the Hessian determinant ($\boldsymbol{H}$) can be used to determine the concavity of the critical points and to classify these as minima (concave up), maxima (concave down) or inflection points (a change of the concavity from concave up to concave down or vice-versa). $\boldsymbol{H}$ is calculated as:

$$\boldsymbol{H} = \frac{\partial^2 Z(u^*)}{\partial x^{*2}} \frac{\partial^2 Z(u^*)}{\partial y^{*2}} - \frac{\partial^2 Z(u^*)}{\partial x^* \partial y^*}^2 \tag{4.8}$$

If $\boldsymbol{H} > 0$, then the location can be classified as a minimum if $\frac{\partial^2 Z(u^*)}{\partial x^{*2}} > 0$, or as a maximum if $\frac{\partial^2 Z(u^*)}{\partial x^{*2}} < 0$. If $\boldsymbol{H} < 0$, the location is an inflection point. Values of $\boldsymbol{H} = 0$ indicate that there is insufficient information to classify the location as a minimum, maximum or inflection point.

4.2.3 Identifying boundary effects

The hydraulic head gradient perpendicular to the aquifer boundary can be indicative of flow into or out of the aquifer. The hydraulic head gradient perpendicular to an aquifer boundary can be assessed at nodes (in u^*) closest to the boundary using $\frac{\partial Z(u^*)}{\partial x^*}$, $\frac{\partial Z(u^*)}{\partial y^*}$ and the angle (θ) projected perpendicular to the boundary. The resultant (r) of the vectors $\frac{\partial Z(u^*)}{\partial x^*}$,

$\frac{\partial Z(u^*)}{\partial y^*}$ can be found using:

$$r = \frac{\partial Z(u^*)}{\partial x^*} \cos\theta + \frac{\partial Z(u^*)}{\partial y^*} \sin\theta \tag{4.9}$$

Where $r > 0$ represents flow towards the boundary and out of the aquifer, $r < 0$ represents inflow into the aquifer from the boundary, and $r = 0$ represents no flow across the boundary. Where the hydraulic head gradient across the boundary is steep, this may be indicative of either high groundwater inflow/outflow or low hydraulic conductivity of the aquifer material (according to Darcy's Law).

Values of θ can be identified geometrically from a polygon of the aquifer boundary. First, all nodes within a specified buffer distance are selected, leading to k nodes denoted here as u_b^*. Next, each node of u_b^* (recalling $i = 1, \ldots, k$) is projected orthogonally onto the nearest segment of the boundary polygon. The orthogonal projections onto each boundary segment are $x_p = x_1 + (x_2 - x_1)t$ and $y_p = y_1 + (y_2 - y_1)t$, where t is given by:

$$t = \frac{(x_i^* - x_1)(x_2 - x_1) + (y_i^* - y_1)(y_2 - y_1)}{(x_2 - x_1)^2 + (y_2 - y_1)^2} \tag{4.10}$$

Where the coordinates (x_1, y_1, x_2 and y_2) are the vertices of each face of the boundary polygon.

The nearest boundary segment/s to each node can be identified using the condition $h = \min(h)$, where $h = \sqrt{(x_i^* - x_p)^2 + (y_i^* - y_p)^2}$ and the resulting projections, x_p and y_p, are calculated with the equations $x_p = x_i^* + \sum(x_p - x_i^*)$ and $y_p = y_i^* + \sum(y_p - y_i^*)$. The angle of u_{bi}^* projected on the boundary is obtained as $\theta_i = \mathrm{atan2}(y_p - y_i^*, x_p - x_i^*)$, where atan2 is a modified version of arctan, which handles special cases to ensure the resulting vector is oriented correctly with respect to the unit circle. This process is repeated for all nodes in $\boldsymbol{u}_b^*$, yielding $\boldsymbol{\theta} = [\theta_1, \ldots, \theta_k]$.

4.3 Case study of the Galilee Basin, Australia

4.3.1 Study site and data description

We applied the method described above, in the Galilee Basin (Queensland, Australia), which is part of the Great Artesian Basin. The Galilee Basin outcrops to the east and is overlain by the Eromanga Basin to the west (Moya et al., 2016). The stratigraphy of the Galilee Basin is composed of Triassic-aged formations that overlie deeper Permian-aged formations. The aquifers of the Triassic and Permian-aged formations are composed mostly of sandstones separated by aquitards of siltstones and mudstones (Moya et al., 2016). The Permian-aged formations contain coal seams and are the target of proposed open-cut and underground mining, including the Carmichael Coal Mine (Figure 4.2). Currell et al. (2020) and Keegan-Treloar et al. (2021) provide further details of the mine and surrounding hydrogeology. The shallower Triassic-aged formations have been hypothesized to provide a source of water to the culturally and ecologically significant Doongmabulla Springs Complex (Currell et al., 2020), amongst alternative possible source aquifers. Given the potential impacts of mining developments in the area, characterizing the regional hydrogeology including the groundwater flow directions and the locations of likely recharge and discharge areas is of critical importance.

The Triassic formations have a good spatial distribution of hydraulic head data to the east where landholders target the upper formations for water supply, primarily for stock and domestic use (Figure 4.2). However, fewer measurements are available to the west where the Galilee Basin is overlain by the Eromanga Basin and the Triassic formations are at substan-

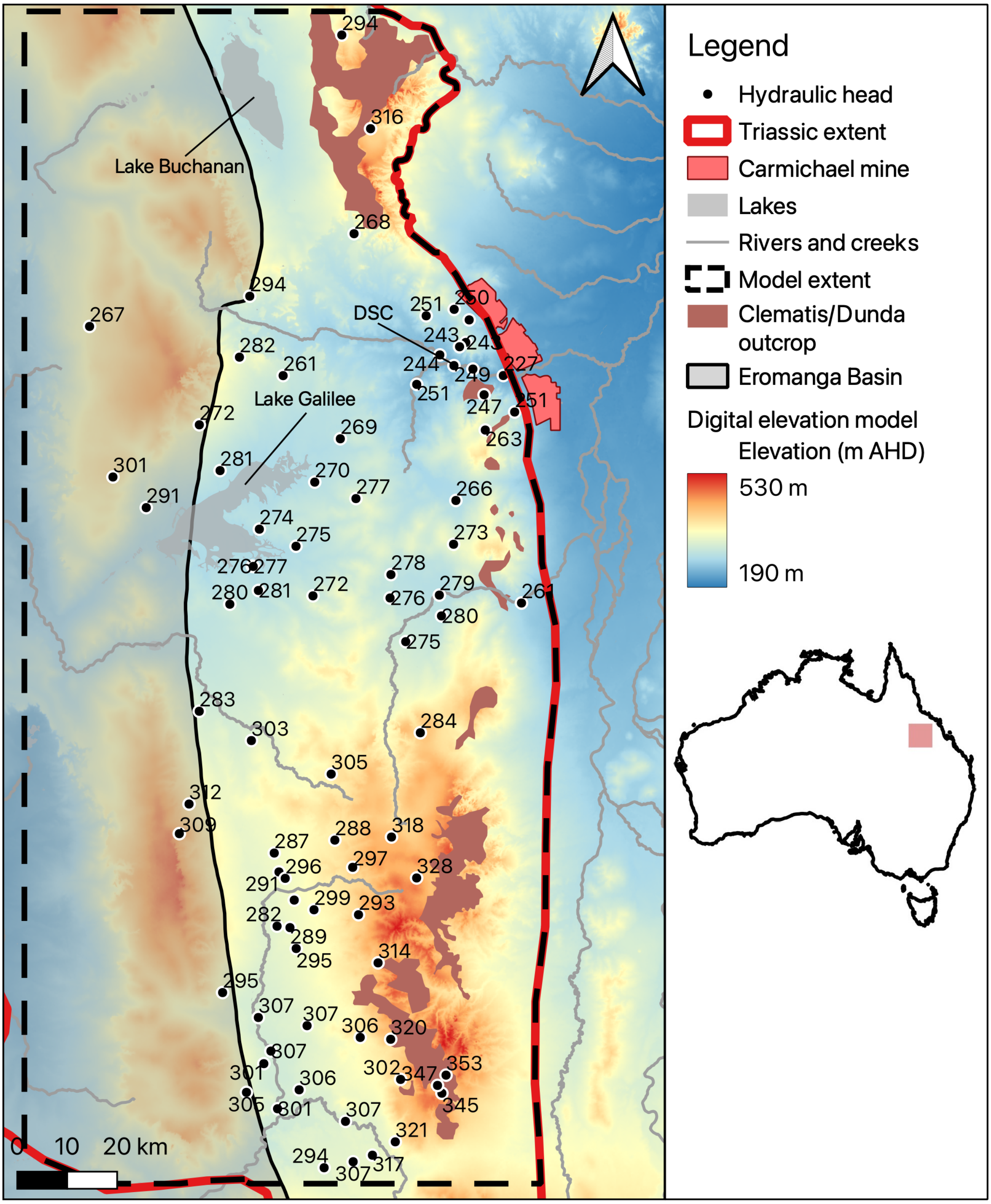

Figure 4.2: *Study area map that includes the Triassic extent (red line), Clematis/Dunda outcrop areas (brown), rivers, creeks and lakes (grey), the DSC (Doongmabulla Springs Complex), the Carmichael Mine (red areas), hydraulic head measurements in m AHD marked with the black circles, Eromanga Basin extent (grey shading with black outline) and the surface elevation in m AHD (blue to red colormap) from three second version of the Shuttle Radar Topographic Mission digital elevation model. The extent of the geostatistical model applied in this study is shown with the black dashed lines.*

tial depth. In this study hydraulic head data were collated from the Queensland Groundwater Database (http://qldspatial.information.qld.gov.au/catalogue/), the Queensland Department of State Development (2018), and AECOM (2021). Hydrographs were plotted and a single value was selected as the representative steady-state water level for each well, following the approach used by Keegan-Treloar et al. (2021) (see Figures S1-S9 in Appendix C). The steady-state assumption was assumed to be reasonable as there was limited groundwater extraction (mainly just stock and domestic use) and mine site dewatering had not yet impacted the Triassic formations. In total, there were 81 hydraulic head observations in the Triassic formations, ranging from 227.23 m to 352.66 m above the Australian Height Datum (see Table S1).

4.3.2 Hydraulic head and derivative simulation

The hydraulic head and derivative simulations of the Galilee Basin were run using Python, using libraries that come with a standard Anaconda installation. In the simulations, a regular grid ($\boldsymbol{u}^*$) was defined, with 1000 m intervals in the x and y directions. The 1000 m interval was selected to ensure reasonable model run times given the large extent of the study area (see Figure 4.2). The global mean was calculated using the best linear unbiased estimate and 100 realisations of hydraulic head and partial derivatives were generated. The minima, maxima and the concavity of the hydraulic head surface were mapped using the hydraulic head and partial derivatives realisations, and a polygon of the aquifer boundary (as per the methods).

4.4 Results and discussion

4.4.1 Preliminary geostatistical data analysis

The D'Agostino and Pearson (1973) test was applied to the null hypothesis of the hydraulic head data being normally distributed and the null hypothesis could not be rejected using significance level of 0.05 (p = 0.89, k = 0.23). The experimental semi-variance of the hydraulic head data was estimated using the gstat library (Pebesma, 2004) in R. A Gaussian semi-variogram model was fitted to the experimental semi-variance by minimizing the sum of the squared differences. Following Philip and Kitanidis (1989) and Pardo-Igúzquiza and Chica-Olmo (2004), the semi-variogram model was separated into a continuous model (the Gaussian semi-variogram model) and a discontinuous model (the nugget effect semi-variogram model). This was necessary, as the spatial variability must be continuous, including at the origin, for the derivatives to be calculated (Philip and Kitanidis, 1989). The continuous semi-variogram model was converted to a covariance model using the relationship that the semi-variogram is equal to the sill minus the covariance. The sill of the discontinuous model was used to parameterize σ^2, which regularizes the Kriging model to avoid overfitting uncertain observations (see Equation 4.1) and essentially filters out the measurement error (see Philip and Kitanidis, 1989). The resulting semi-variogram models (shown in Figure 4.3) were composed of a nugget model with a sill of 32 m^2 and Gaussian model with a range of 27,072 m and a sill of 506 m^2.

4.4.2 Hydraulic head predictions

Following the preliminary geostatistical analysis, 100 realizations of hydraulic head and partial derivatives of hydraulic head were generated using sequential Gaussian simulation. The variability between realizations can be attributed to the values at model nodes being

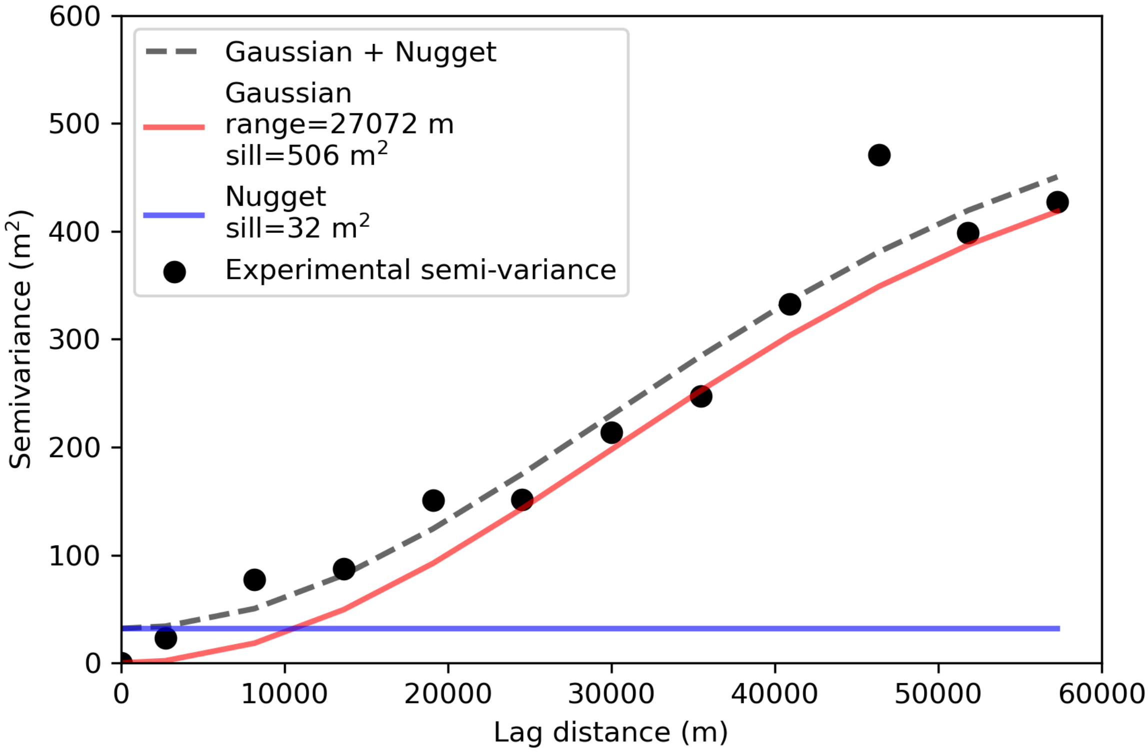

Figure 4.3: *The semi-variogram models in the Triassic formations showing the discontinuous nugget effect semi-variogram model (blue), the continuous Gaussian semi-variogram model (red) and the addition of the discontinuous and continuous semi-variogram models (black dashed line).*

simulated sequentially by drawing from a normal distribution parametrised by the estimated mean and variance for a randomly selected node. This was followed by treating the simulated value as an observation that was included in the simulation of subsequent nodes (as described in Section 4.2.1). Figure 4.4a and Figure 4.4b show contours of hydraulic head for realizations 1 and 2, respectively. As shown, the realizations have the largest differences in the areas where there are few hydraulic observations and small differences near hydraulic head observations. This is expected, as the model is conditioned on the hydraulic head observations, such that predictions made close to observed data will closely match the observed values. Alternately, the prediction uncertainty will increase further away from observations leading to a larger range of plausible values. Figure 4.4c shows the average hydraulic head of all realizations contoured over a heat map of the standard deviation of all realizations. As shown, the standard deviation is low (e.g., 0–5 m) close to observations and higher (up to 25 m) further away from the observations (i.e., in the north-west and south-west of the study area). We elected to hash out areas where the standard deviation was greater or equal to 15 m as predictions and inferences of extrema or concavity in these areas were highly uncertain. The contour where the standard deviation in the hydraulic head equals 10 m is also shown with a dotted line.

The average hydraulic head is higher to the north-east and south-east and lower in the central eastern area near the aquifer boundary (Figure 4.4c). As water flows from high to low hydraulic head, it appears that recharge areas are in the north-eastern and south-eastern areas, while discharge occurs mainly in the central-eastern area, coinciding with the Doongmabulla Springs Complex and the Carmichael River (and the proposed site of the Carmichael Coal Mine; Figure 4.2). There is also indication of boundary inflows in the south-west and outflows to the north-west, although these areas are highly uncertain ($\sigma \geq 10$ m). Note that the individual realizations (i.e., Figures 4.4a and 4.4b) show substantial variability

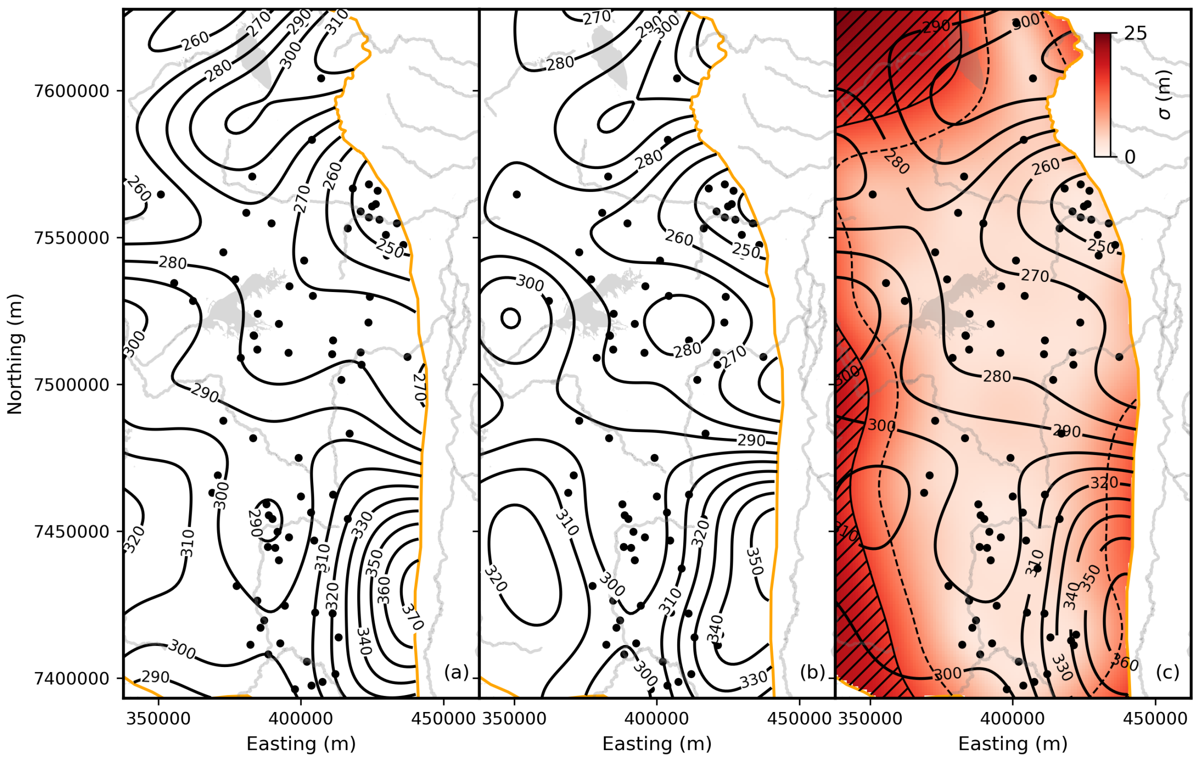

Figure 4.4: *(a) and (b) Hydraulic head contours (black lines) of realizations 1 and 2 (respectively), along with the location of hydraulic head observations (black dots). (c) Contours of the mean hydraulic head from all realizations (black lines), the standard deviation of all realizations (red heat map), and hydraulic head observation locations (black dots). The hashed area shows where σ > 15 m, while the dotted line shows σ = 10 m. Rivers, creeks and lakes are shaded grey in the background.*

in flow direction (inferred as flow perpendicular to the hydraulic head contours) near and through the boundary relative to that shown in the averaged results (Figure 4.4c). Similarly, the locations of likely recharge and discharge areas are variable between realizations (e.g., the recharge area in Figure 4.4a is further east in Figure 4.4b). As there is significant variability between realizations and it is unfeasible to examine all realizations in detail, an alternative approach is required to interpret the regional flow directions and likely recharge and discharge zones.

4.4.3 Minima and maxima in the hydraulic head surface

Extrema (minima, maxima and inflection points) in the hydraulic head surface were identified (see Section 4.2.2) and assigned to nodes within a 5000 m radius. This approach allows a comparison between realizations by counting the frequency of each grid node being proximal to an extremum. The buffer size of 5000 m was chosen after testing a wide range of values such that it created visible zones where extrema in hydraulics heads were obtained. Additionally, the component of flow orthogonal to the boundary was used to classify boundary nodes as minima (flow out of the boundary), maxima (flow in through the boundary) or neither (flow is parallel to the boundary) as described in Section 4.2.3. These were discrete classifications (i.e., minima, maxima or neither) and did not consider the magnitude of the gradient both in and out of the boundary or the steepness of the surface around the minima or maxima.

Figures 4.5b and 4.5c show realizations of hydraulic head with the locations of minima (red areas) and maxima (blue areas). The arrows are shown every 10 nodes along the boundary to indicate if flow is in (maxima) or out (minima). Some extrema occur frequently between realizations (e.g., r2 and d4 in Figure 4.5b and Figure 4.5c), while other extrema occur less frequently (e.g., r3, r4, r5 and d3 in Figure 4.5c are not present in Figure 4.5b). The

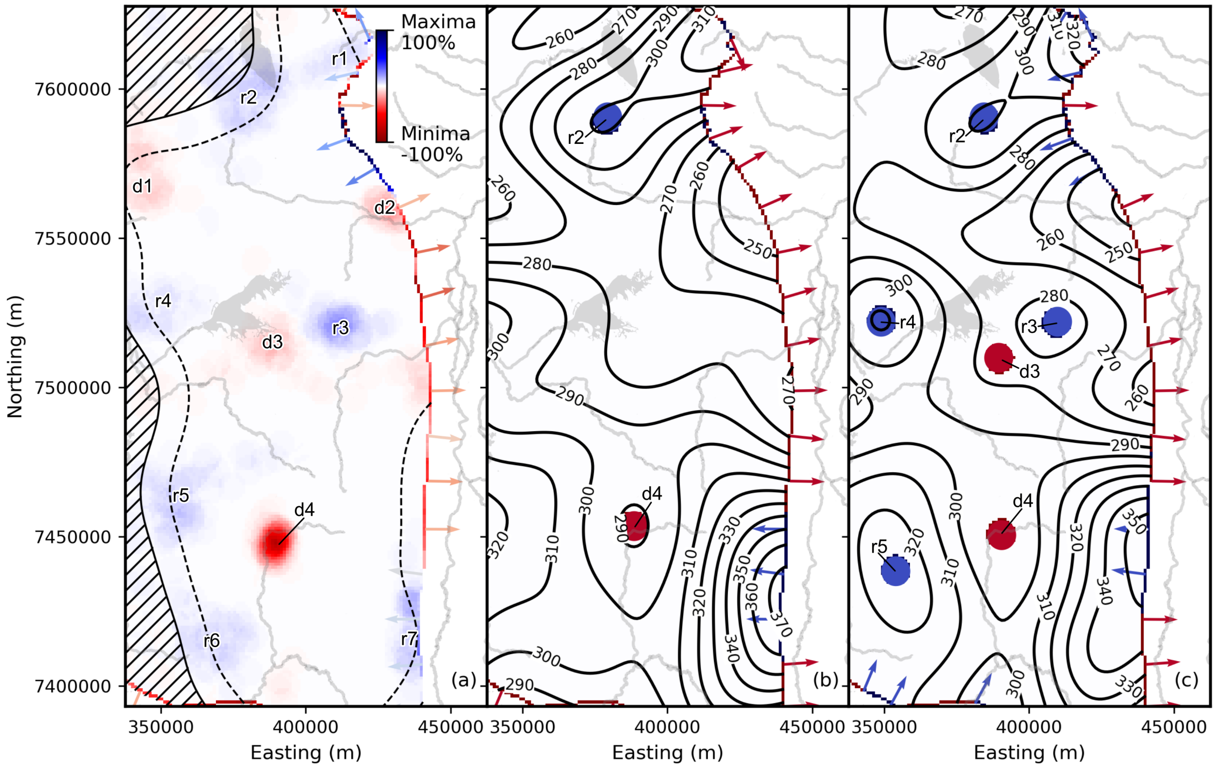

Figure 4.5: *(a) Relative percentage of realizations being minima (red) or maxima (blue). (b) and (c) show realizations of hydraulic head (black contours) with minima marked in red and maxima marked in blue. For visualization, arrows (not to scale) have been added at the edge of the basin every 10 nodes of the grid to show whether the flow orthogonal to the boundary is out (minimum) or in (maximum), with the color gradation in (a) representing the relative percentage of realizations where the edge node is a minimum or maximum. Minima and maxima have been labelled consecutively with the pretext "d" for discharge and "r" for recharge.*

flow directions orthogonal to the boundary suggest flow is out through most of the eastern boundary (red pixels and arrows; Figure 4.5a-c). However, areas to the south in Figure 4.5b and Figure 4.5c, and two areas to the north in Figure 4.5c suggest inwards flow (blue pixels and arrows). All 100 realizations annotated with minima and maxima are provided online (https://doi.org/10.6084/m9.figshare.20225571.v1).

The summary of results represented in Figure 4.5a shows the relative percentage of realizations (i.e., (total minimum – total maximum) / total realizations · 100%) where each node is a minimum (red) or maximum (blue) from the 100 realizations. The relative percentage for each node is a continuous index (shown with the color gradation between blue and red) ranging from -100% (all realizations are minimum) to 100% (all realizations are maximum) with an intermediate value of 0%. As shown in Figure 4.5a, seven maxima (r1 to r7) and four minima (d1 to d4) were identified from the analysis of the ensemble. The lighter shades of red or blue suggest zones are less common between analyses (e.g., r3 and d3) than those zones with darker shades of red or blue (e.g., d4).

Of these areas, r1 and r7 are likely recharge areas where the Triassic formation outcrops along the eastern margin of the basin and where groundwater recharge has been hypothesized to occur (Evans et al., 2018). There is also evidence of flow into the basin along the eastern edge to the north and south, near r1 and r7 as shown by the blue arrows. The maxima r2, r4, r5 and r6 lie beneath the Eromanga Basin (Figure 4.2) and could represent areas of inter-aquifer connectivity where the Triassic formations obtain water from the Permian formations. This is in agreement with Moya et al. (2015) who found hydrochemical evidence of mixing between the Triassic and Permian aged units to the west where the Rewan formation is thin. The minima d4 may be a discharge area that forms a groundwater divide between flow from the hypothesized recharge areas to the south-west (r5 and r6) and the south-east (r7). This hypothesized discharge area (d4) is also located over a river, indicating the river may be gaining in this region. The geological and topographical causes of the r3 recharge area are less apparent. It is plausible that there may be unmapped outcrops of the Triassic units in the region of r3, as it is at a topographic high point (see Figure 4.2).

The minimum d3 is located between r3 and r4, suggesting that it could be a sink for water from these hypothesized recharge areas. As d3 is located near Lake Galilee (i.e., see Figure 4.2), it is plausible that this could represent surface discharge occurring from the Triassic units given the hypersaline lake. Similarly, the minimum d4 is located between recharge areas to the south-west (r5 and r6) and a recharge area to the south-east (r7) overlies a river. This suggests that the river may receive groundwater from the Triassic units in this area. The discharge area d2 is located over the Carmichael River and in a region that coincides with the Doongmabulla Springs Complex. This observation indicates that the Triassic units may be contributing groundwater to the river and/or springs in this area. There is also minima along most of the eastern margin of the basin (red arrows), which suggests that discharge may be occurring along the edges of the basin possibly to geological formations beyond the Galilee Basin or to surface features. The cause of the minimum d1 is less apparent as the Triassic formations are at significant depth beneath the Eromanga Basin in this area.

4.4.4 Concavity of the hydraulic head surface

From a flow perspective, concave up areas can be interpreted as flow converging towards a low point, while concave down areas can be interpreted as flow dispersing away from a high point. In some cases, the concavity may be more informative than minima or maxima for identifying potential recharge or discharge areas or groundwater extraction. For example, if recharge is occurring over a large area, the concavity may be more informative of the recharge areas than the peak (maxima). Figure 4.6b and Figure 4.6c show two realizations of hydraulic head with the concave up and concave down areas marked in red and blue, respectively. As shown, the concave down areas are generally associated with high hydraulic head values, while the concave up areas are generally located near low hydraulic head values, as expected (see Figure 4.1). All 100 realizations annotated with concavity are provided online (https://doi.org/10.6084/m9.figshare.20225796.v1).

Figure 4.6a displays the relative percentage of realizations where each node was concave up or concave down (i.e., (total concave up – total concave down) / total realizations · 100%). As shown, there are five concave up areas (d1-d5) and seven concave down areas

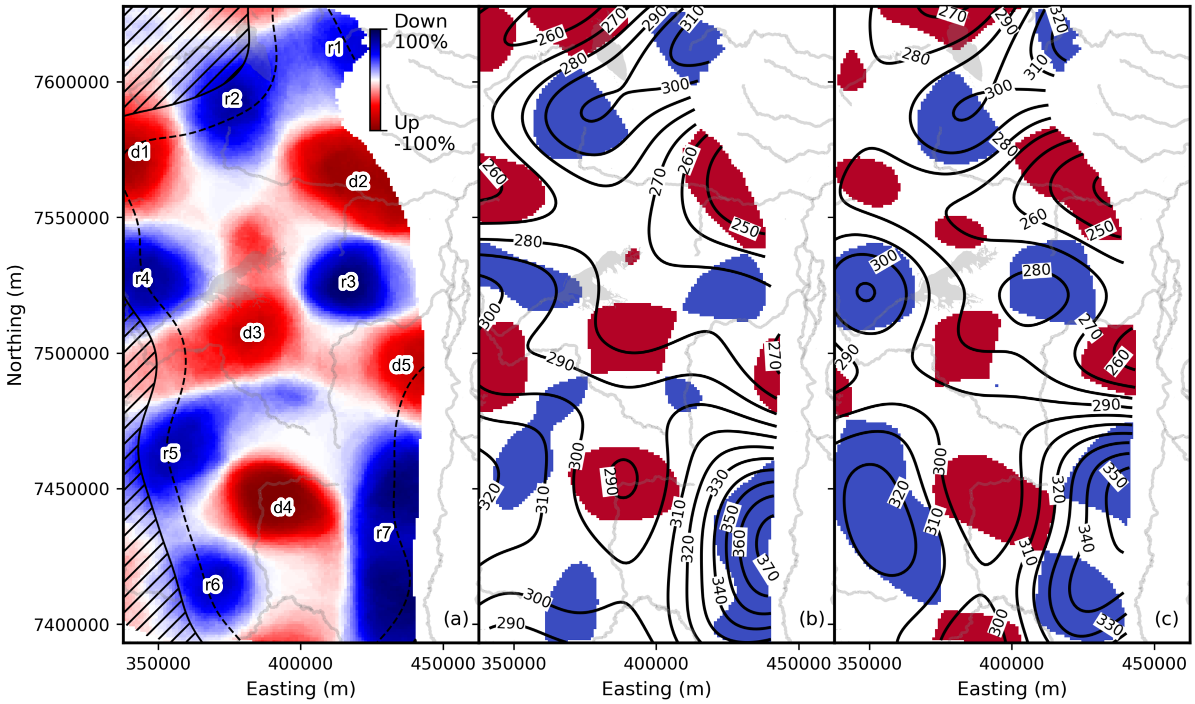

Figure 4.6: *(a) Relative percentage of realizations where each node is concave up or concave down. The hashed area shows where σ is 15 m or greater and the dotted line represents the σ = 10 m contour. (b) and (c) show the concavity of the hydraulic head surface for two realizations with blue areas concave up and red areas concave down. Concave up and concave down areas are labelled with the pretext "d" for discharge and "r" for recharge.*

(r1-r7). The concave down areas r1, r3 and r7 are located near the edge of the basin where the Triassic formations outcrop. It is plausible that these areas may be associated with inflow at the edge of outcrop areas that were identified by Evans et al. (2018). The concave down areas r4, r5 and r6 may reflect flow from the Permian formations due to a thinning of the Rewan formation aquitard in the area (Moya et al., 2015).

The concave up area d4 likely represents discharge to a river, which may act as a groundwater divide between the hypothesized recharge areas r5, r6, and r7. The concave up areas d2 and d5 along the eastern margin of the basin likely represent discharge out of the basin. In the case of d2, the concave up area could be representative of discharge to the Carmichael River and/or the Doongmabulla Springs Complex. The concave up area d3 is located near Lake Galilee and a river (Edie Creek), suggesting that the Triassic units may be contributing water to these surface features. The cause of the concave up area d1 is less obvious, as the Triassic formations are located at substantial depth beneath the Eromanga Basin in this area.

4.4.5 Combined analysis of minima, maxima and concavity

Expert knowledge of a study area can help to determine whether a hypothesized recharge or discharge area is likely to be discrete or diffuse. In areas where there are discrete surface features (e.g., rivers, creeks, wells, or springs), the use of extrema may be most informative of recharge or discharge areas, because these more likely coincide with easily recognizable recharge/discharge features within the landscape. Alternately, in areas where there are diffuse surface features (e.g., stands of vegetation, wetlands, exposed outcrop areas, etc.), then the use of concavity may be more informative to identify zones of recharge or discharge. This is notwithstanding that both localized and diffuse recharge/discharge are likely to create both extrema and concavity in the hydraulic head surface. Nevertheless, we suggest that concavity and extrema are interpreted in conjunction with knowledge of surface features to decide which is most appropriate to identify the causes and spatial extent of recharge and discharge.

The combined use of extrema and concavity were used to develop a recharge/discharge area map (Figure 4.7). Recharge near the edge of the basin is expected to be diffuse infiltration from rainfall events where the Triassic formations are thin, weathered and exposed (Evans et al., 2018). In these regions the concavity was selected as being representative of recharge areas r1 and r7. Similarly, area r2 is located near lake Buchanan, suggesting that the lake may act as a diffuse source of recharge to the underlying aquifers. The remaining hypothesized recharge areas are located at substantial depth beneath the Eromanga Basin far from known outcrop areas or lakes. The maxima were selected to represent these areas as these may represent isolated areas of connectivity between the Triassic and Permian for-

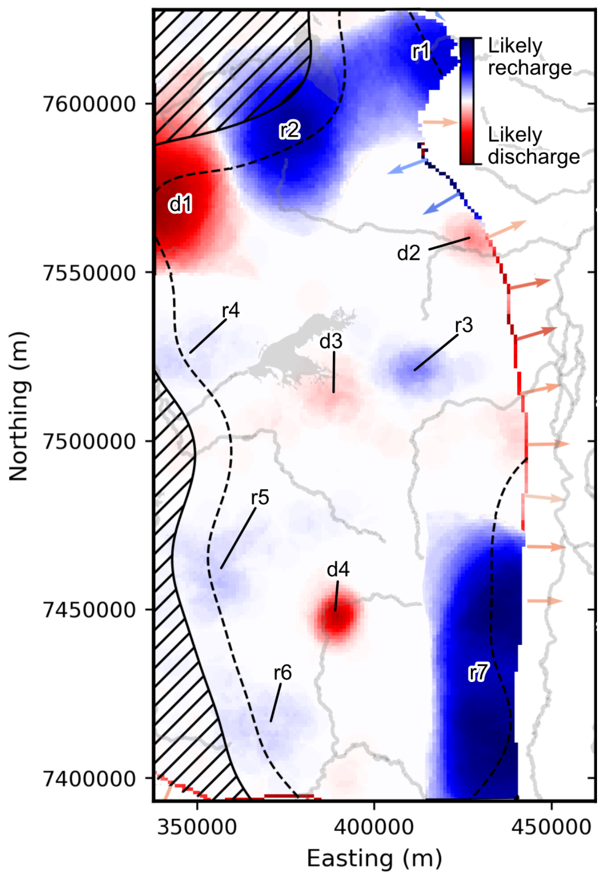

Figure 4.7: *Selected recharge (blue) and discharge areas (red) from the combined interpretation of the concavity and extrema in conjunction with the locations of rivers and lakes.*

mations (Moya et al., 2015). As d2, d3 and d4 are proximal to surface features (i.e., rivers, springs and lakes), the extrema approach was selected as representative of the discharge areas. The cause of d1 was less apparent as the Triassic formations were located at significant depth beneath the Eromanga Basin in this area. Therefore, it was assumed that d1 may be best represented using the concavity as it could represent discharge to other aquifers such as the Hutton Sandstone (Moya et al., 2015). Needless to say, these interpretations are preliminary and require further work to validate the nature of groundwater inflow/outflow within the regions of interest described above.

From a regional flow perspective, recharge appears to occur in the outcrop areas to the north-east and south-east (r1 and r7) and in the vicinity of Lake Buchanan (r2). There are also other plausible recharge areas (r3, r4, r5 and r6), although further investigation is required to determine the characteristics of these areas (e.g., inter-aquifer leakage, unmapped outcrops, etc.). There are plausible discharge areas near the Alice River to the south (d4), Lake Galilee (d3), and the Doongmabulla Springs Complex and the Carmichael River (d2). The area near the Carmichael Mine (see Figure 4.2) appears to be a regional discharge point (see Figure 4.7), and dewatering as part of the mining operation needs to account for influxes from both the Triassic and Permian units. There are important implications for the potential for mine-induced impacts to the Doongmabulla Springs Complex from this interpretation. If the Triassic system is the source of water to the springs and is connected to the mine area (as suggested here), then there is an elevated risk of drawdown propagating to the springs. This hypothesis warrants further analysis.

4.4.6 Uncertainties and future directions

A common criticism of Kriging techniques is that the resulting estimates are often unnaturally smooth and not globally accurate, honoring neither the semi-variogram nor the measurement histogram (Caers, 2000; Yamamoto, 2005). So, while Kriging estimation may be locally accurate (i.e., provide the best estimates at individual prediction locations), the smoothness will result in an overestimation of lower values and an underestimation of higher values. Conditional simulations, such as sequential Gaussian simulation, honor both the semi-variogram model and the measurement histogram, guaranteeing global accuracy, albeit with a trade-off of decreased local accuracy (Caers, 2000). Thus, sequential Gaussian methods can better capture the spatial transitions between extreme values, although simulated values at individual prediction locations may be less optimum than those produced by Kriging (Goovaerts, 1997). In this study, sequential Gaussian simulation was used in preference to Kriging, as global accuracy (i.e., an accurate transition between extreme values) was more important than local accuracy (i.e., the best estimates at each prediction location). The trade-off between poorer local accuracy and better global accuracy means that simulated hydraulic head and hydraulic gradients may have been less optimal than those produced using Kriging at individual prediction sites. Future studies should consider whether local or global accuracy is most important to the phenomenon of interest and choose a simulation or Kriging method accordingly.

Choosing between concavity and extrema for the identification of recharge/discharge areas is challenging when the data are sparse. Data sparsity issues were demonstrated in this study by different realizations inferring recharge and discharge at the same location. Secondary sources of information, such as the locations of surface features (e.g., rivers, lakes, springs, swamps), can provide a sanity check and critical information on whether a recharge/discharge feature is likely diffuse or discrete. Thus secondary information can assist in selecting the appropriate method (extrema vs. concavity). However, this is a binary solution (i.e., either choosing the concavity or extrema for recharge/discharge locations), and rather there may be a spectrum between the two. Instead, the recharge source may encompass an area around the maximum that does not cover the entirety of the concave down area. Thus, in future studies, there may be a need to delineate an area encompassing the extrema to represent the likely recharge/discharge areas. This could be aided by considering additional datasets such as hydrochemistry or age tracers.

The analyses conducted here categorized features in the hydraulic head surface as recharge, discharge or neither, without consideration of the magnitude of the recharge/discharge rates. The impacts of this approach are that a small feature (e.g., mild concavity) received the same weighting as a larger feature (e.g., steep concavity) in the analysis. This simple categorization of features was selected to make it straightforward to compare a single variable (i.e., recharge, discharge or neither) rather than two variables (i.e., recharge, discharge or neither and the varying magnitude of each). It may be possible to infer the magnitude of recharge/discharge features, at least within individual realizations. For example, by assessing the magnitude of the second derivatives for concavity/extrema and/or the first derivatives along the boundaries. However, the interplay between hydraulic conductivity and recharge, in creating head gradients, would need to be considered. Therefore, future studies could extend the method proposed here to include the magnitude of recharge/discharge features for individual realizations.

The coefficient of variation (i.e., standard deviation/mean) of all realizations was lowest for the hydraulic head values, increased with the first derivative and was highest for the second derivative (see Figure S10 in Appendix C). This was expected given that a small change in the hydraulic head values may result in large changes in the first derivatives and possibly even the reversal of flow directions, leading to large coefficients of variability between realizations. Similarly, as the second derivative captures the change in the first derivative, the second derivative will have a higher coefficient of variability between realizations than the first derivative. This leads to a pattern where the coefficient of variation is lowest for the function values and increases with the order of the derivative. This emphasizes the potential benefits of including derivative information within the modelling process. Hydraulic gradient observations can be included as a secondary variable in co-Kriging, and as the simulated first derivatives are more uncertain than the hydraulic head values themselves, the information value of gradient observations are higher than that of regular hydraulic head observations. Expert knowledge of the locations of recharge or discharge features could be encoded by adding nodes at the feature locations, setting the first derivatives at these locations to zero (as the first derivative equals 0 for minima and maxima), and co-Kriging these data with available hydraulic head observations. For example, if a river is known to be losing or gaining along a reach, nodes could be added with a first derivative value of zero and this could be co-Kriged with hydraulic head observations to reduce the uncertainty.

Supporting Text S2 in Appendix C provides details on how the Kriging equations can be modified to include first derivative observations.

Conclusions

We developed a geostatistical method to model the concavity and locations of extrema in the hydraulic head surface. The new method extends previous work by using sequential Gaussian simulation to jointly simulate hydraulic head and the partial derivatives of the hydraulic head surface to identify the concavity and locations of extrema in the hydraulic head surface. The resultant maps of extrema and concavity can be interpreted with maps of known surface features to attribute the variation in the hydraulic head surface to recharge or discharge from known features such as geological outcrops, rivers, and lakes.

This was applied to the Galilee Basin to map the regional flow directions and the concavity and extrema of the hydraulic head surface. Likely recharge and discharge areas were identified by comparing maps of concavity and extrema with known features to attribute variations in the hydraulic head surface to recharge or discharge processes. These findings have important implications for the Galilee Basin, as they provide evidence suggesting recharge is likely to occur predominantly in the north-east and south-east where the Triassic formations outcrop, while discharge is apparent near several rivers, lakes and the Doongmabulla Springs Complex. Notably, this indicates that the Triassic formations may provide a source of water to the Carmichael River and the Doongmabulla Springs Complex, which has important implications given the potential for dewatering at the nearby Carmichael Coal Mine to impact hydraulic head in the Triassic formations, and potentially, discharge from the Doongmabulla Springs Complex.

The sequential Gaussian approach presented here is easy to apply, computationally efficient and requires only commonly available hydraulic head data. We facilitate the application of the technique through a worked example available online (DOI:10.5281/zenodo.6655359). The approach can be extended to include derivative observations, which due to the higher uncertainty in derivative values relative to hydraulic head values, are of higher information value than hydraulic head observations. The inclusion of first derivative observations is particularly attractive as expert knowledge of recharge/discharge features (e.g., rivers, springs) can be encoded by setting the first derivative values to zero at the feature locations, and co-Kriging to constrain the analysis. Simulating the concavity and locations of extrema in the hydraulic head surface represents a substantial advancement in the geostatistical analysis of hydraulic head data sets by informing the locations of recharge and discharge areas and offering objective interpretation of recharge and discharge processes.

CHAPTER 5

CONCEPTUALISATION OF A REGIONAL FLOW SYSTEM (GALILEE BASIN, AUSTRALIA) USING MAJOR ION CHEMISTRY AND ENVIRONMENTAL ISOTOPES

Robin Keegan-Treloar, Eddie W. Banks, Ian Cartwright, Dylan J. Irvine, and Adrian D. Werner

Approximate contribution of co-authors: Robin Keegan-Treloar (80%), Eddie Banks (10%), *Ian Cartwright (5%), Dylan Irvine (2.5%) and Adrian Werner (2.5%).*

Abstract

Developing conceptual models is a critical step in hydrogeological studies and requires multiple lines of evidence, particularly in data-sparse systems. This study examined the hydrochemistry of the Triassic-aged aquifers in the Galilee Basin (Australia) to identify recharge areas, discharge areas and the hydrochemical processes occurring along flow paths. A key focus was the relevance to the iconic Doongmabulla Springs Complex (DSC). We found good agreement between recharge and discharge areas identified in an earlier study (using a technique that utilised derivatives of hydraulic head) and those suggested from the interpretation of hydrochemical data. The main hydrochemical processes controlling TDS variations were silicate weathering in the deeper Clematis Formation and Dunda Beds, and evapotranspiration in the overlying Moolayember Formation. These findings suggest that the Clematis Formation and Dunda Beds are hydrochemically distinct from the Moolayember Formation, which has important implications for future monitoring and modelling activities. Additionally, analysis of Na/Cl ratios and total dissolved solids in a transect near the DSC suggest that the springs may receive water from a mixture of a relatively shallow, local flow path and a deeper regional flow path, with the two sources having contrasting salinities. This observation is highly relevant to previous concerns about threats to the DSC, because changes to groundwater flow paths due to mine-induced drawdown may impact the relative contributions to spring discharge from different sources, potentially modifying the hydrochemistry of spring discharge. The results highlight the need to assess the sensitivity of spring-dependent ecosystems to the hydrochemistry of spring discharge. Further analysis of the potential for water chemistry changes with anticipated modifications to the regional hydrogeology is also needed.

5.1 Introduction

Recently, several coal mining and coal seam gas projects have commenced in the Galilee Basin (Queensland, Australia) or are undergoing regulatory approval processes (Evans et al., 2018). These developments include the controversial Carmichael Coal Mine, an open-cut and underground coal mine covering an area of ≈28,000 hectares (Currell et al., 2020), which has raised concerns about potential adverse impacts to the regional groundwater flow regime, rivers and streams, and the ecologically and culturally significant Doongmabulla Springs Complex (Currell et al., 2017; Currell et al., 2020; Keegan-Treloar et al., 2021). The Galilee Basin is remote and until recently it remained largely untouched by anthropogenic activities. As such, existing knowledge of the hydrochemistry of the basin is based on limited data, mostly in mine lease areas along the eastern boundary. Given the limited understanding of the regional hydrogeology and the potential impact from coal mining and coal seam gas developments on the water resources, there is a clear need to improve the knowledge of the regional hydrogeology of the basin, including conceptual models of the primary hydrogeochemical processes.

The understanding of the hydrochemistry of the Galilee Basin is based mainly on the studies of Moya et al. (2015) and Moya et al. (2016). Moya et al. (2015) examined the hydrochemistry of the Galilee and Eromanga Basins using multivariate statistical techniques. They observed that water in the main Triassic-aged aquifer, the Clematis Formation, evolved from Na-Cl type in recharge areas to Na-HCO_3 type with increasing distance from the eastern margin of the Galilee Basin. This was hypothesised to be representative of carbonate dissolution occurring along the flow path. Moya et al. (2016) built upon this by using environmental tracers and isotopes to assess inter-aquifer connectivity and groundwater age along flow paths in the Galilee and Eromanga Basins. In the western area of the Galilee

Basin, analysis of methane gas suggested that there is hydraulic interconnectivity (likely due to faulting) between the deeper Permian-aged Betts Creek Beds and the shallower Jurassic-aged Hutton sandstone units. Moya et al. (2016) concluded that faults may play an important role in inter-aquifer connectivity in the central Galilee Basin.

Keegan-Treloar et al. (2021) and Chapter 4 developed a conceptual model of the regional groundwater flow and recharge/discharge areas for the Triassic aquifers of the Galilee Basin using hydraulic head data and geostatistical methods. Data sparsity in the western areas of the Galilee Basin limited the interpretability of flow conditions over much of the basin. As the conceptual model presented in Chapter 4 was based solely on head data, there is a need to extend and compare the interpretations by incorporating other data types, such as hydrochemical information. This study aims to improve and refine the hydrogeological conceptual model of the Triassic aquifers by examining hydrochemical evidence of recharge areas, the hydrochemical evolution of waters along flow paths and the consistency of aquifer chemistry with discharge from springs. Furthermore, system understanding (e.g., recharge areas, discharge areas) obtained from hydrochemistry will be compared with the previous hydraulic head-based study (Chapter 4) to assess the validity of the hydraulic head-based recharge/discharge area analysis. The updated conceptual model aims to improve the understanding of the Triassic-aged groundwater flow system by reducing the uncertainty in locations of regional recharge and discharge, which is critical for the protection of groundwater-dependent ecosystems, including the DSC, given that the Triassic aquifers likely provide an important source of water to these environments (Keegan-Treloar et al., 2021). This is particularly relevant in the context of extensive mining and coal seam gas activities that are planned or underway in the basin, requiring a better characterisation of the recharge/discharge areas and hydrochemical evolution along flow paths to inform management decision-making.

5.2 Study site

The Galilee Basin (Figure 5.1a) underlies the Eromanga Basin, and to the west it is bounded by the Drummond and Bowen Basins that extend southward beneath the Surat Basin (Figure 5.1b). The upper stratigraphic units of the Galilee and Eromanga Basins are considered part of the Great Artesian Basin (GAB) (Habermehl and Lau, 1997; Kellett, et al., 2003; Moya et al., 2016). Groundwater recharge to the Galilee Basin is believed to occur to the east where the basin outcrops, which is supported by groundwater age estimates based on ^{36}Cl data that showed an increase in age along the inferred groundwater flow path from east to west (Moya et al., 2016).

The study area is semi-arid with a mean annual rainfall of ≈543 mm/yr (Bureau of Meteorology station number 35264). The topography is mostly subdued with a topographical high along the eastern margin of the Eromanga Basin, which forms a boundary for the catchments draining to the large salt lakes, Lake Galilee and Lake Buchanan (Evans et al., 2018). Creeks and rivers are mostly ephemeral, except for reaches of the Carmichael River that are believed to receive baseflow from the Triassic aquifers and the nearby Doongmabulla Springs Complex (DSC) (Currell et al., 2017; Evans et al., 2018). The DSC consists of permanent freshwater springs, supporting approximately 160 wetlands (Currell et al., 2017). These wetlands are critical habitat for endangered species, including the Black Throated Finch and Waxy Cabbage palm, and collectively the springs are considered of high cultural significance to the Wangan and Jagalingou People (Wangan and Jagalingou Family Council, 2015; Currell et al., 2017).

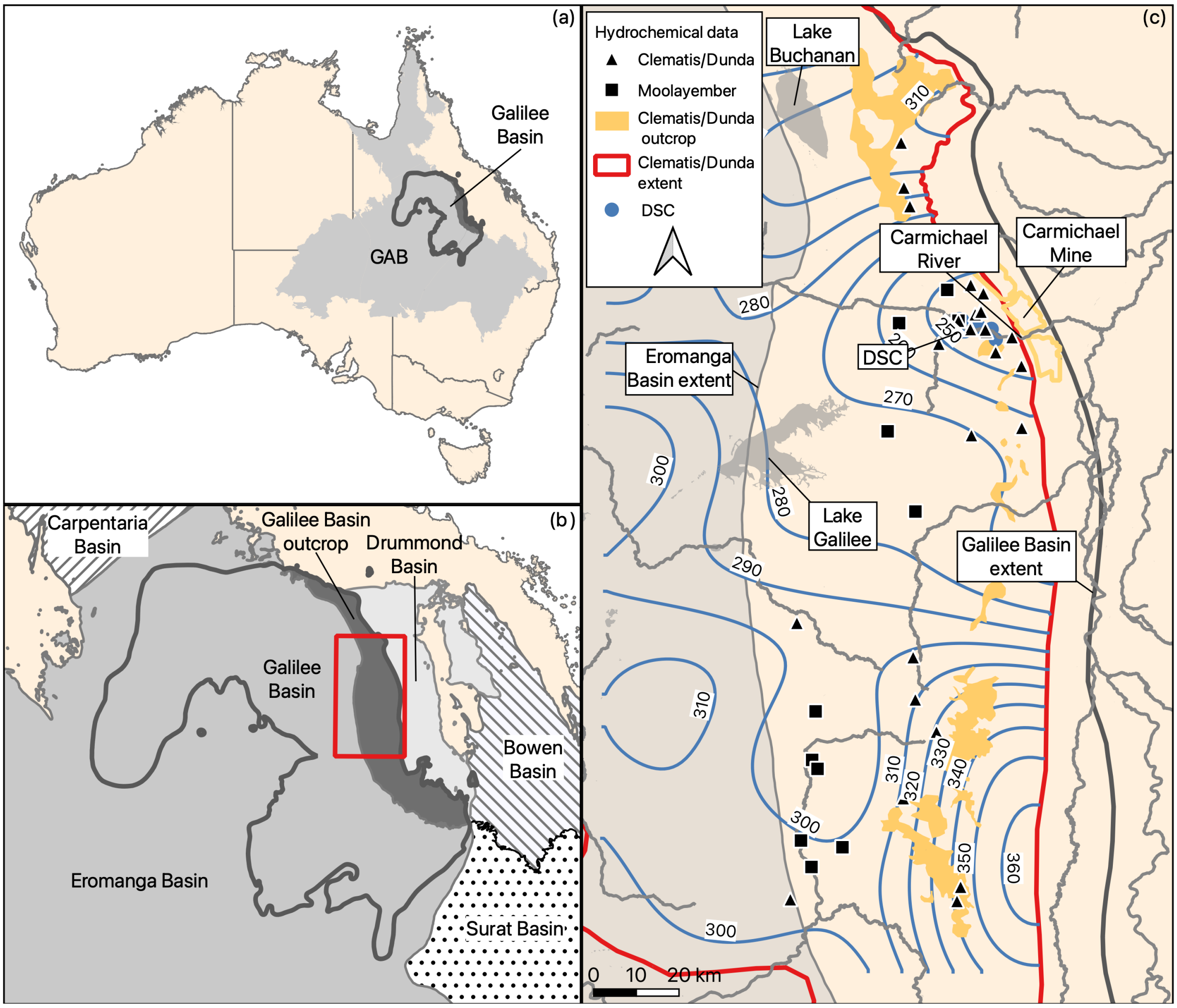

Figure 5.1: *(a) Location of the Galilee Basin and the Great Artesian Basin (GAB), Australia; (b) The Galilee Basin and surrounding geological basins within the study area (red rectangle); (c) The study area marked with wells from the Clematis/Dunda Formations (black triangles) and Moolayember Formation (black rectangles), hydraulic head contours (blue lines), and the location of the DSC (blue circles). The major surface features and the extent of the Galilee and Eromanga Basins are labelled. For descriptions of Formations, see Figure 5.2.*

5.2.1 Hydrogeology

The stratigraphy of the study area includes the Triassic-aged Moolayember Formation, Clematis Formation, Dunda Beds and Rewan Formations, which overly the Permian-aged Betts Creek Beds and Joe Joe Group (Figure 5.2). The Moolayember Formation is composed of siltstone and mudstone and is considered a low permeability unit. The Clematis Formation and Dunda Beds are considered the main Triassic aquifers and are comprised of sandstones, siltstones and mudstones. There is likely a high degree of connectivity between the Clematis Formation and Dunda Beds. These aquifer units are underlain by the Rewan Formation, consisting of mudstone, siltstone and sandstone (Jiang, 2014). The Rewan Formation is considered a low permeability unit with an average thickness of 160 m (Evans et al., 2017). Beneath the Rewan Formation are the Permian-aged Bandanna and Colinlea Formations, which are grouped as the Betts Creek Beds and are considered as aquifers. The lithology of the Betts Creek Beds includes sandstone, siltstone and coal (Allen and Fielding, 2007). Notably, the coal seams of the Betts Creek Beds are the target of several active and proposed mining and coal seam gas operations (Currell et al., 2017; Currell et al., 2020). Beneath the Betts Creek Beds is the Joe Joe Group, which is composed of mudstones, siltstones and some coal.

Previous studies have suggested that groundwater flow in the Clematis Formation is from recharge areas in the north-east and south-east of the Galilee Basin, where the Clematis Formation outcrops, towards either the DSC/Carmichael River or to the west towards the Galilee Basin boundary where the basin's sediments are in contact with faults and/or the overlying Surat Basin or underlying Eromanga Basin (Evans et al., 2018; AECOM, 2021; Keegan-Treloar et al., 2021; see Figure 5.1). There is evidence of localised recharge along much of the eastern margin of the Galilee Basin, although the primary areas of recharge

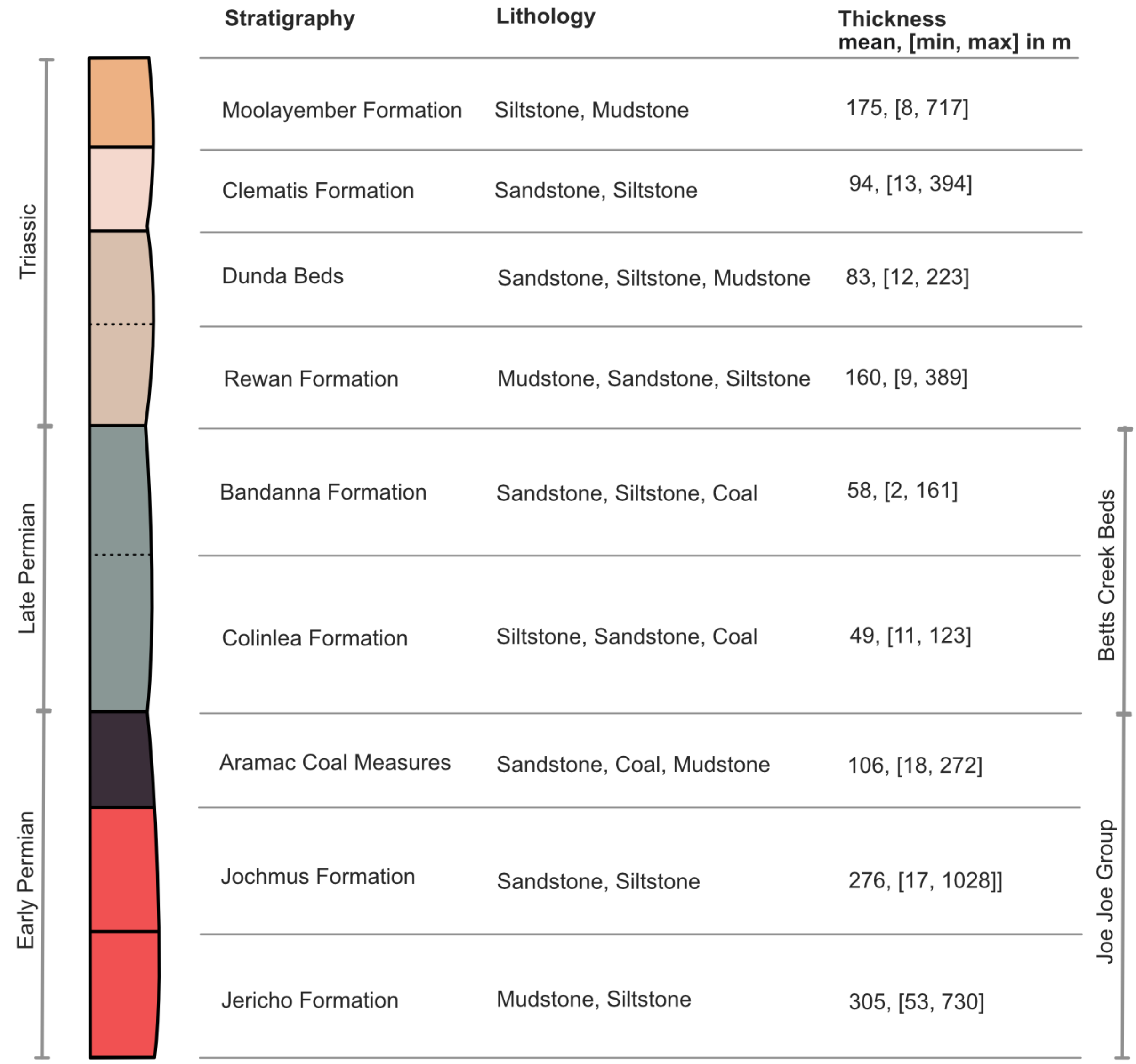

Figure 5.2: *The stratigraphy, lithology and thickness (mean, minimum and maximum) of the Triassic and Permian-aged Formations of the Galilee Basin. Adapted from Allen and Fielding (2007) and Evans et al. (2017).*

appear to be in the north-east and south-east (Evans et al., 2018; Keegan-Treloar et al., 2021). In the DSC/Carmichael River area within the central-eastern part of the Galilee Basin, the derived potentiometric surface based on available hydraulic head data sets from the Triassic Formation aquifers is about 10 m higher than that in the underlying Permian-aged Formation aquifers, with hydraulic heads in the order of 240 and 230 m AHD (metres above Australian Height Datum), respectively (Keegan-Treloar et al., 2021). As such, the Triassic Formation aquifers have a higher likelihood than the Permian-aged Formations of having adequate hydraulic head to meet a threshold required to support spring flow at the DSC, although the Permian-aged Formations cannot be ruled out of having hydraulic connection with the springs (Keegan-Treloar et al., 2021).

5.3 Methods

5.3.1 Data sources

The current study collated hydrochemical and isotope data for the Galilee Basin from the published literature (Moya et al., 2016), industry reports (AECOM, 2021), government reports (Department of State Development, 2018), environmental data reporting by Bravus Mining (formerly ADANI Mining Group) (https://www.bravusmining.com.au/sustainability/environment/environmental-reporting-and-approvals/) and the Queensland Groundwater Database (https://www.data.qld.gov.au/dataset/groundwater-database-queensland). Where data were duplicated between reports/papers and the Queensland Groundwater Database, the Queensland Groundwater Database was selected as the preferred data source as this was in a consistent format and has been subjected to established quality control measures.

Hydrochemistry and isotope data sets were available from groundwater monitoring wells completed in the Clematis Formation, Dunda Beds and Moolayember Formation along the margin of the Galilee Basin and within the basin. However, the available data become increasingly sparse with distance towards the west, as the depth of the Galilee Basin increases beneath the Eromanga Basin. In this study the Clematis Formation and Dunda Beds were considered as a single unit as there is likely a high degree of connectivity between these units. In total, 329 hydrochemistry samples were available from 34 wells in the Clematis Formation/Dunda Beds and 23 samples were available in the Moolayember Formation from 12 wells. The locations of these wells are shown in Figure 5.1c. A single value was chosen for each sampling site by selecting the most recent sample with a charge balance error of less than 5%. Where no samples with a charge balance error less than 5% were available, the sample with the lowest charge balance was selected. The relevant dataset is provided in Supporting Material 1 in Appendix D. The choice to represent each well with a single measurement was considered reasonable, as where time-series data were available, the total dissolved solids remained approximately constant over time.

In addition to the data collated from other sources, one recent sample collected in 2019 from Camp Spring, a spring in the DSC, was included in the dataset (unpublished data). Camp Spring has a discrete discharge vent (in contrast to most other springs that are submerged beneath pooled water), and therefore can be considered as representative of the groundwater contributing to the DSC, at least for that particular vent, with minimal impacts from precipitation or evapotranspiration.

5.3.2 Data quality and geochemical analyses

HCO_3 and CO_3 concentrations were calculated from alkalinity (as $CaCO_3$) and pH using PHREEQC (Parkhurst and Appelo, 2013). The electrical balance was calculated for all samples. Without comprising the data integrity of the sparse data set, several samples that had an electrical charge balance error greater than 5% were retained but were subjected to additional scrutiny. Where the error was due to missing analytes (e.g., alkalinity), the sample was censored in analyses dependent on the missing analyte (e.g., total dissolved solids, HCO3), but included where the analysis was not influenced by the missing analyte (e.g., Na/Cl ratios).

Mineral saturation indices were calculated with PHREEQC (Parkhurst and Appelo, 2013) using the available hydrochemistry data. Ionic concentrations, ionic ratios, and saturation indices were analysed using a combination of Piper plots (e.g., Piper, 1944), bivariate scatter plots and spatial mapping.

5.3.3 Isotopic data and analyses

Stable isotopes of water (δ^2H and δ^{18}O), strontium isotope ratios (^{87}Sr/^{86}Sr) and δ^{13}C were collated from Moya et al. (2016) and a dataset provided by the Queensland Herbarium (2020). There was a total of 15 samples from the Clematis Formation/Dunda Beds, 8 samples from the Moolayember Formation and 1 sample from Camp Spring. Unfortunately, ^{87}Sr/^{86}Sr data were not available for Camp Spring. The isotopic data sets were analysed spatially and with bivariate plots to identify groundwater recharge areas and to determine plausible weathering processes along groundwater flow paths. Tables with the isotope data are provided in Supporting Material 2 in Appendix D.

5.4 Results and discussion

5.4.1 Major ion chemistry

The hydrochemistry of groundwater is effectively a spatially averaged property that represents the integration of physical and hydrogeochemical processes along a flow path. In this study we show the hydrochemical data sets together with a constructed map of likely diffuse groundwater recharge and discharge areas based on the concavity and extrema of the potentiometric surface in the study area (Chapter 4). The hydraulic head data represent current hydraulic conditions (i.e., at the time of measurement), and can be used to inform the locations of possible recharge/discharge areas, compared to hydrochemistry, which represents an integration of various physical and geochemical processes over time.

The base map in Figure 5.3 shows a map of possible recharge (blue) and discharge areas (red), based on a previous study of the hydraulic head data (Chapter 4) that examined the concavity (i.e., concave up or concave down) of different equiprobable realisations of the potentiometric surface for the Triassic-aged aquifers. The total dissolved solids (TDS) from the Clematis Formation, Dunda Beds and Moolayember Formation aquifers are shown as markers with colour gradation from white to red, representing increasing TDS values. Spatially, there is low TDS in the southern outcrop areas, which increases to the west. In the northern outcrop area, there is a low TDS value (223 mg/L) that increases towards the DSC. In the region of the DSC and Carmichael River (outlined in black Figure 5.3a), the TDS values range from 121 to 866 mg/L (Figure 5.3b). An examination of the screen depths of these bores indicates that the deeper wells have a higher TDS (474 to 866 mg/L) compared to the shallow wells (121 to 186 mg/L) and the intermediate depth wells have a TDS between the deeper and shallower wells. Camp Spring had a TDS of 417 mg/L, which is similar to the TDS observed in three wells (413, 411 and 486 mg/L) near the DSC (Figure 5.3c). This suggests the spring waters are consistent with either a mixture of groundwater from different depths or from the mid-depth of the Clematis Formation/Dunda Beds.

The water type of the Clematis Formation/Dunda Beds aquifer varies between Na-Cl type and Na-HCO_3 type (Figure 5.4). Whereas the water type for samples from the Moolayember Formation are entirely Na-Cl type and the sample from Camp Spring appears to be a mixture of Na-Cl and Na-HCO_3 type water.

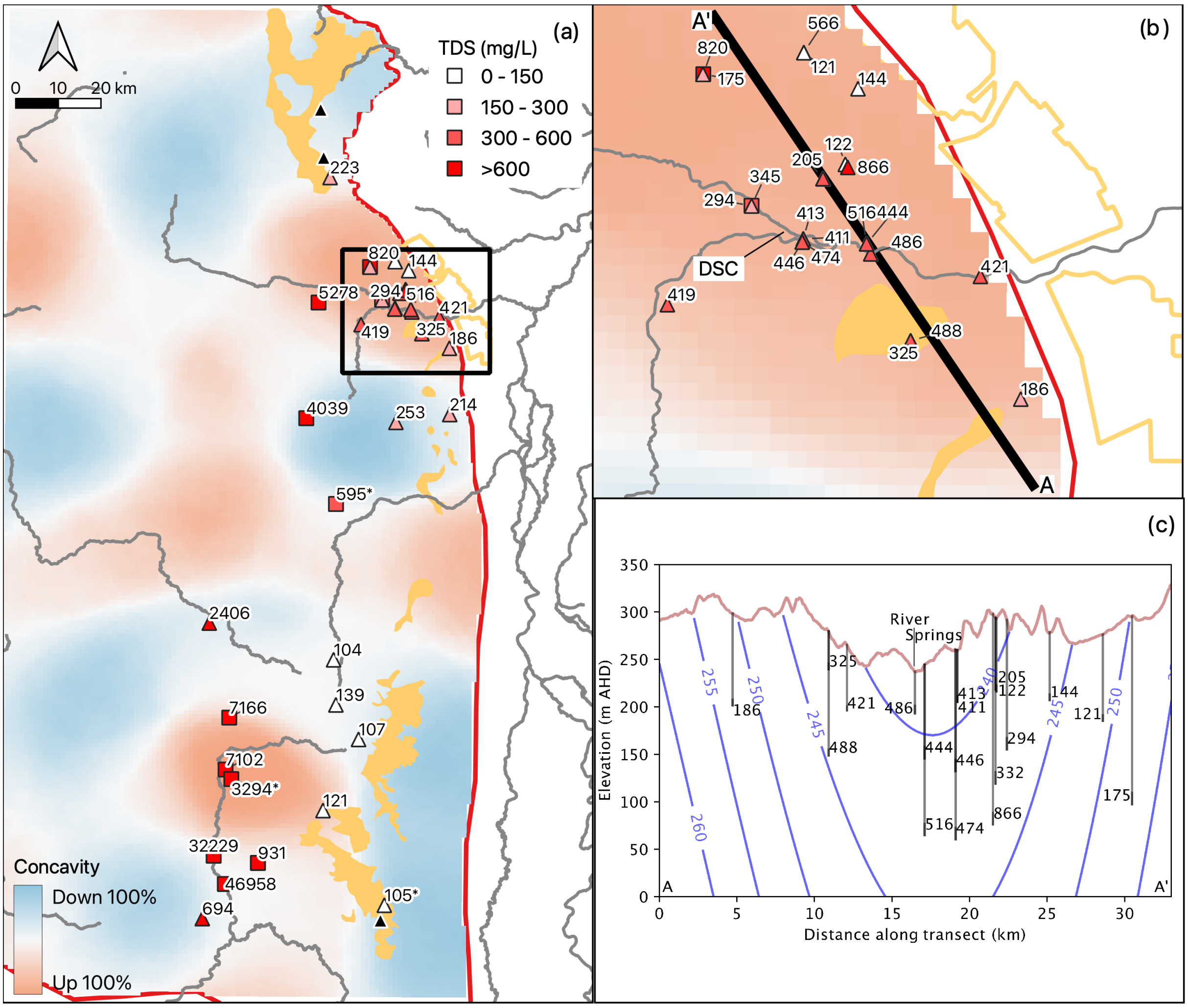

Figure 5.3: *(a) Spatial distribution of total dissolved solids (TDS) in the Clematis Formation and Dunda Beds (triangles) and Moolayember Formation (squares). Note the same colour gradation is used for both groups of TDS observations. The colour bar in the lower left of (a) shows the proportion of realisations where the potentiometric surface was concave up or concave down, which is an indicator of likely recharge (blue) or discharge areas (red) from Chapter 4. (b) Inset map of the DSC region outlined in black in (a). (c) Cross section of the transect A to A' shown in (b) displaying TDS trends with depth and the hydraulic head contours (blue lines) that show groundwater discharge towards the DSC and the Carmichael River. Black triangles denote wells where accurate TDS measurements were not available.*

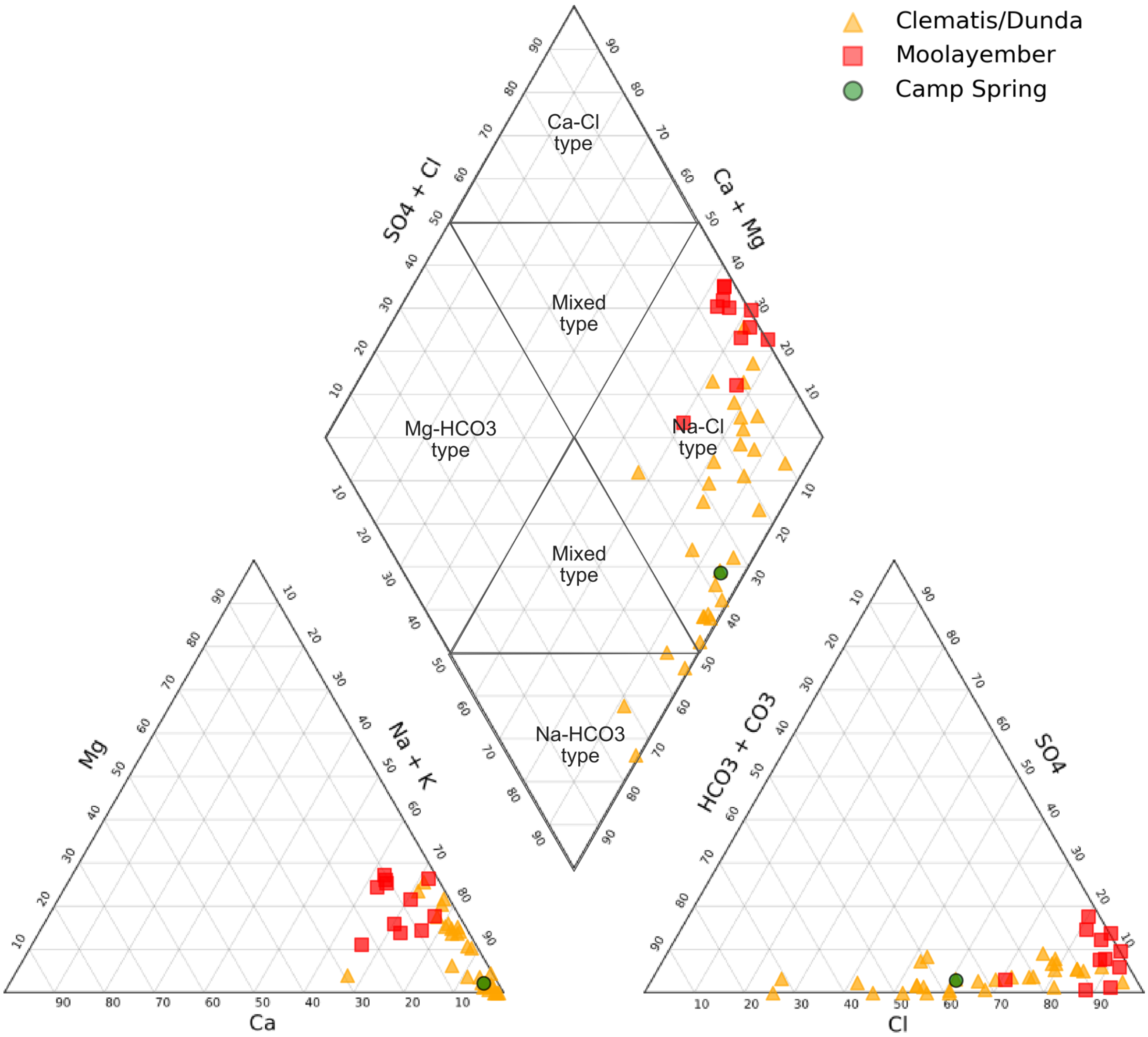

Figure 5.4: *Piper plot of the hydrochemistry in the Clematis Formation/Dunda Beds (orange triangles), the overlying Moolayember Formation (red rectangles) and Camp Spring (green circle).*

Plots of Na/Cl ratios vs TDS for the Moolayember Formation and the Clematis Formation and Dunda Beds are shown in Figure 5.5a. The TDS in the Clematis Formation and Dunda Beds ranges from ≈100 mg/L to ≈900 mg/L and the Na/Cl ratios increase with higher TDS, albeit without a clear linear trend. The Moolayember Formation has higher TDS and Na/Cl ratios that are approximately constant, with a median value of 0.82. This trend of constant Na/Cl ratios with increasing TDS could be explained by evapotranspiration or halite dissolution. However, halite dissolution is considered unlikely as significant amounts halite have not been reported in other investigations of the regional hydrogeology that include the Moolayember Formation (e.g., Moya et al., 2016; Evans et al., 2018). The Na/Cl ratios for the Clematis Formation and Dunda Beds mostly exceed one with low TDS values, suggesting silicate weathering. Silicate weathering in the Clematis Formation and Dunda Beds is further supported by the ratio of HCO_3/(HCO_3 + CO_3 +Cl + SO_4) that increases with higher Na/Cl ratios (Figure 5.5b). Camp Spring has a Na/Cl ratio of 1.3 and HCO_3/(HCO_3 + CO_3 +Cl + SO_4) ratio of 0.35, suggesting weathering of silicate minerals in the groundwater that is discharging at the DSC (Figure 5.5a and 5.5b).

Na/Cl ratios in the Moolayember Formation are between 0.5 and 1.0 for the majority of wells throughout the study area, suggesting evapotranspiration is the key process influencing TDS in the Moolayember Formation (Figure 5.6a). Na/Cl ratios and TDS in the Clematis Formation/Dunda Beds are low in the northern outcrop area (0.85 and 223 mg/L, respectively), and generally increase to the south-east in the area near the DSC and the Carmichael River, suggesting silicate weathering may be occurring along this flow path. In the south-eastern area where the Clematis Formation/Dunda Beds outcrop, Na/Cl ratios range from 1.0 to 1.5 with TDS between 104 and 139 mg/L, suggesting some silicate weathering has occurred. Further south of the DSC and Carmichael River there are low Na/Cl ratios (0.89 and 1.02) and low TDS values (253 and 214 mg/L) in the Clematis For-

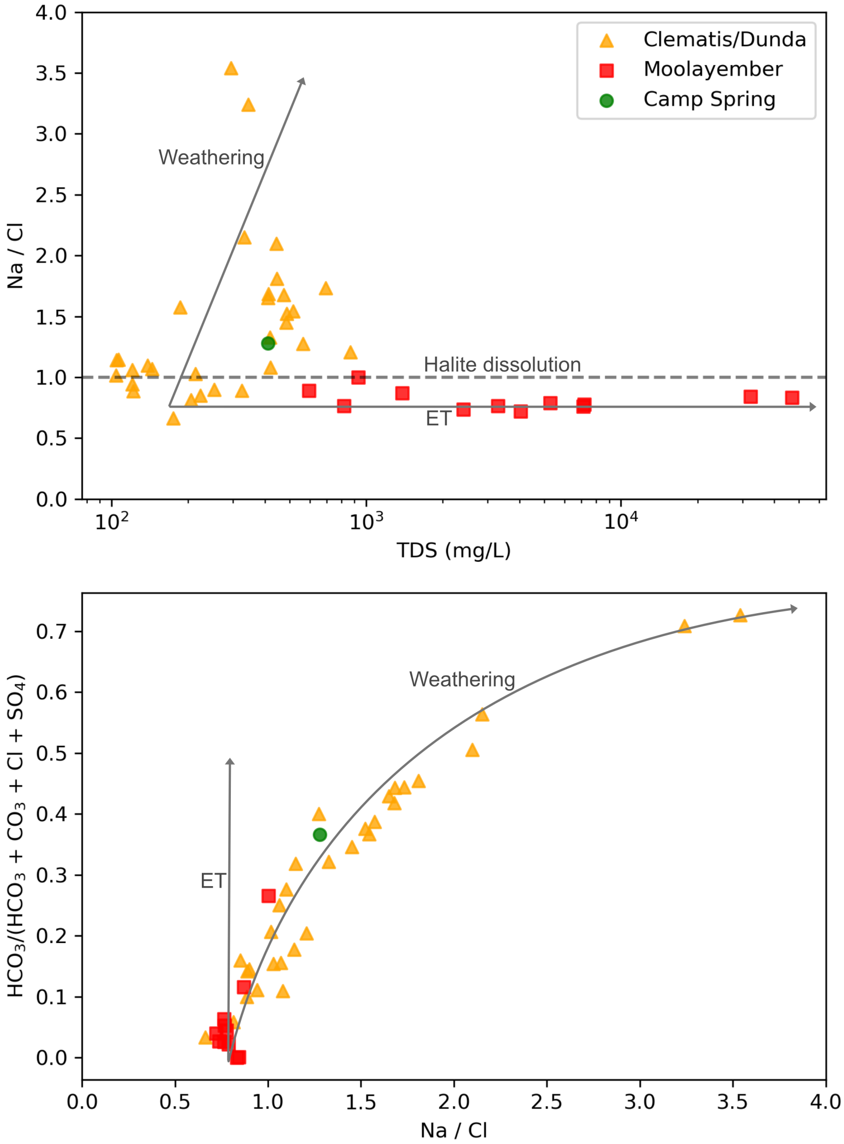

Figure 5.5: *Major ion ratios for samples from the Clematis Formation and Dunda Beds (orange triangles), Moolayember Formation (red squares) and Camp Spring (green circle) showing (a) Na/Cl ratios versus TDS and (b) $HCO_3/(HCO_3 + CO_3 + Cl + SO_4)$ ratios versus Na/Cl ratios. Note the log scale on the x-axis of (a).*

mation/Dunda Beds, which is likely indicative of recharge.

Na/Cl values in the Clematis Formation/Dunda Beds vary substantially in the locality of the DSC/Carmichael River (Figure 5.6b). The Na/Cl ratios are shown with depth along transect A- A' shows the Na/Cl ratios in the Clematis Formation/Dunda Beds with depth (Figure 5.6c). There is a high Na/Cl ratio (1.6) with low TDS (186 mg/L) at the southern end, while at the northern end, towards the Carmichael River, there is a low ratio of 0.9 at a shallow well near the surface (250 m AHD). At intermediate depths (200 m AHD) the ratios are 1.1 and for the deeper wells (75- 150 m AHD), the ratios are generally greater than 1.5. To the north of the DSC and Carmichael River, there is a similar trend of lower Na/Cl ratios in the shallower wells and higher ratios with increasing depth, although this relationship is less clear than to the south (Figure 5.6a). Notably, the Na/Cl ratios of the water flowing from the north towards the DSC and Carmichael River ranges from 0.8 to 1.7 with a mean of 1.2, which closely matches the ratio observed in Camp Spring (1.3).

The saturation indices (SI) of various minerals are shown relative to TDS in Figure 5.7. All of the water samples are undersaturated (log saturation index < 0) with respect to anhydrite, halite and gypsum (Figures 5.7a, c, f). Samples that are saturated (log saturation index > 0) with aragonite (Figure 5.7b), calcite (Figure 5.7d), and dolomite (Figure 5.7e) are generally located in the northern and southern outcrop areas of the Clematis Formation/Dunda Beds. These SI values may suggest dissolution of aragonite, calcite, and dolomite in the unsaturated zone or evapotranspiration during recharge. Conversely, the SI for anhydrite, halite and gypsum are lowest for the samples in these outcrop areas, and shows an increase along the inferred groundwater flow paths, although never reaching saturation. These findings suggest precipitation of minerals is unlikely to be a major process contributing to the hydrochemistry of the Triassic aquifers. The SI for Camp Spring are below saturation and

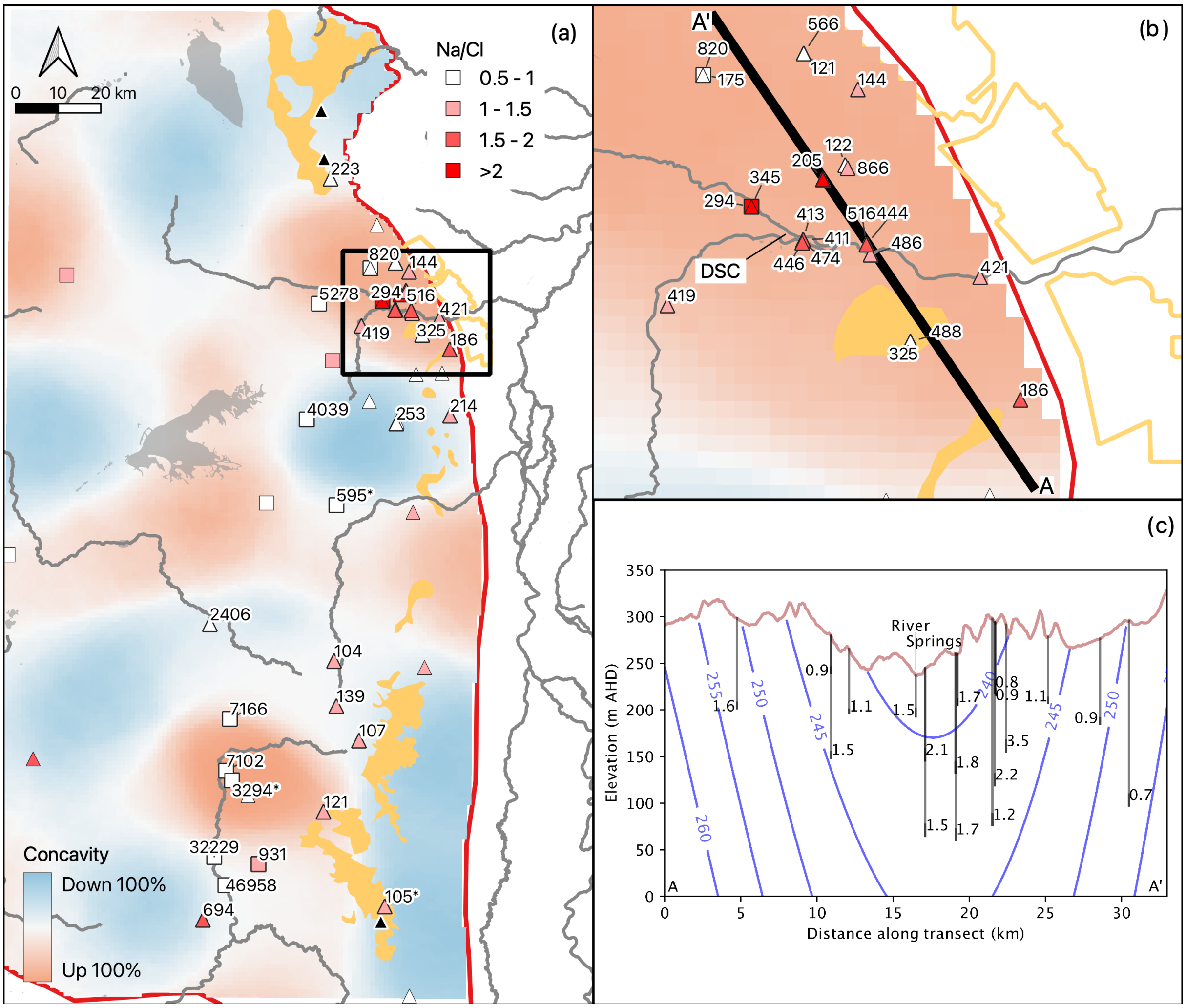

Figure 5.6: *(a) Na/Cl ratios in the Clematis Formation/Dunda Beds (triangles) and the Moolayember Formation (squares). Colour of the markers denotes the Na/Cl ratio, while labelled values denoting the TDS (mg/L). Wells with Na/Cl but no TDS measurements are unlabelled. (b) Inset map showing the black rectangle in (a). (c) The transect A to A' shown in (b) displaying the Na/Cl ratio with elevation. Black triangles denote wells where no Na or Cl measurements were available.*

within the clusters of the Triassic aquifers for all minerals.

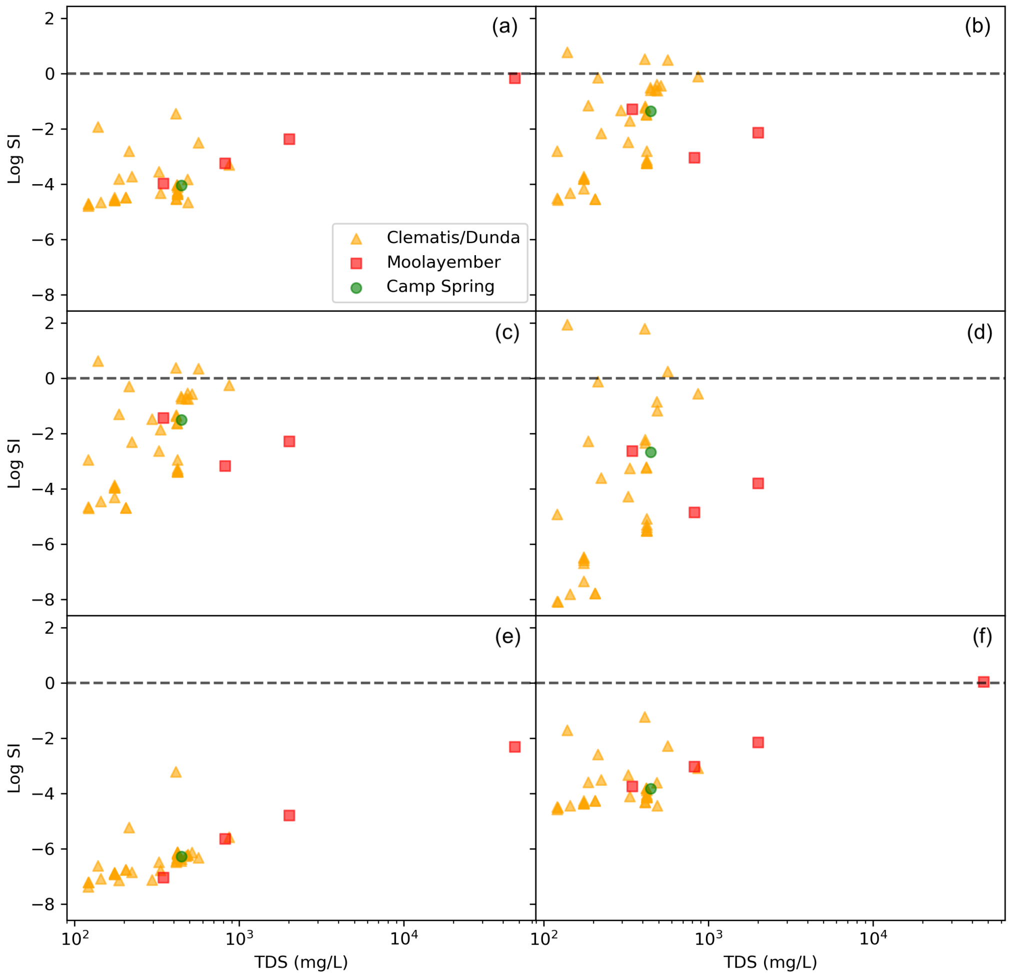

Figure 5.7: *Mineral saturation indices in the Clematis Formation/Dunda Beds (orange triangles) and the Moolayember Formation (red squares) with the log saturation index (Log SI) on the y-axis and the TDS on the x-axis (log-scale). (a) Anhydrite, (b) Calcite, (c) Aragonite, (d) Dolomite, (e) Halite, and (f) Gypsum.*

5.4.2 Stable isotopes of water

The stable isotopes of water can be used to discriminate between physical processes that fractionate the isotopes (e.g., evaporation) and those that do not (e.g., transpiration). As there are no rainfall stations in the Galilee Basin the local meteoric water line (LMWL) for Charleville, Queensland the nearest site as recorded in the Global Network for Isotopes in Precipitation (GNIP) database (IAEA/WMO, 2021) was adopted. Although Charleville is ≈400 km south of the Carmichael Coal Mine, it has a similar climate and it is located a similar distance from the coastline making it a logical choice to compare stable isotope data from the Galilee Basin (Moya et al., 2016; Hollins et al., 2018). The LMWL for Charleville is δ^2H = 8.1 δ^{18}O + 12.6 ‰, which has a similar slope to the global meteoric water line (GMWL) δ^2H = 8.0 δ^{18}O + 10 ‰ (Craig, 1961).

The stable isotopes of water for the Clematis Formation/Dunda Beds and the Moolayember Formation range from δ^2H =-47.8‰ to δ^2H =-23.1‰ and δ^{18}O = -7.1‰ to -4.3‰ (Figure 5.8a). All the samples (apart from well HD02) have lower δ^2H and δ^{18}O than the weighted mean rainfall, suggesting the aquifers are likely recharged by winter rainfall. The samples from the Clematis Formation/Dunda Beds follow the trend δ^2H = 10.7 δ^{18}O + 8.1 ‰, which plots beneath the LMWL and above the GMWL. The well HD02 is an outlier from this trend likely due to its proximity to the Carmichael River, with the enriched δ^2H and δ^{18}O values indicative of infiltration of summer surface water from the river. In contrast, samples from the Moolayember Formation plot along a line with a lower slope, given by the equation δ^2H = 4.8 δ^{18}O + 11.2 ‰. This trend is commonly observed where evaporation is the dominant physical process (Cook and Herczeg, 2000). The sample from Camp Spring lies beneath the LMWL, with lower δ^2H and δ^{18}O than the weighted mean rainfall, likely suggesting winter recharge.

The relationship between δ^2H and Cl was used to identify evaporation and transpiration trends in the data set. In the Clematis Formation/Dunda Beds, the groundwater samples become more isotopically enriched in δ^2H with increasing Cl until chloride concentrations approach 90 mg/L (Figure 5.8b). Samples with Cl > 90 mg/L show a transpiration trend with relatively constant δ^2H with increasing Cl concentrations. These trends could represent an increase in Cl, initially due to evaporation during rainfall infiltration near the ground surface and subsequent transpiration processes prior to groundwater recharge. A similar, although noisier trend is observed in the Moolayember Formation. The Camp Spring samples do not lie on either the evaporation or transpiration trend.

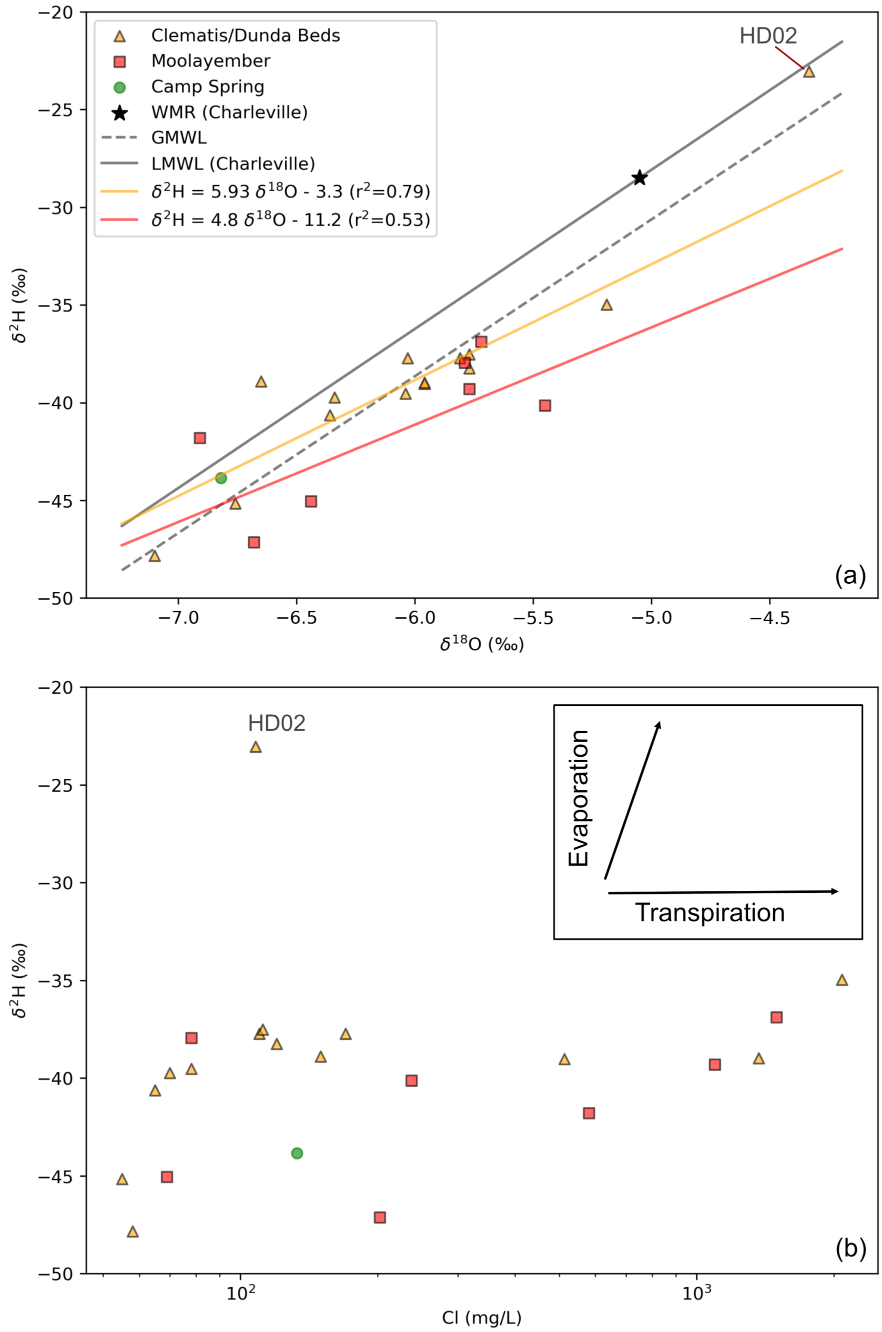

Figure 5.8: *Stable isotopes of water. (a) δ^2H versus δ^{18}O data for the Triassic units shown with the linear line of best fit, GMWL, LMWL and weighted mean rainfall for Charleville (WMR). (b) δ^2H versus Cl (log-scale) with annotated likely physical processes. Note HD02 was removed from the trendline fitting in (a) as it is considered an outlier.*

5.4.3 Strontium and Carbon Isotopes

$^{87}Sr/^{86}Sr$ ratios for the Triassic aquifers in the study area of the Galilee Basin are displayed spatially in Figure 5.9a. Values were classified into three groupings: (1) $^{87}Sr/^{86}Sr$ ratios less than or equal to the ratio in recent rainfall at the site ($^{87}Sr/^{86}Sr$ = 0.7125); (2) $^{87}Sr/^{86}Sr$ ratios between that of recent rainfall and the lower end of expected values for silicate weathering ($^{87}Sr/^{86}Sr$ = 0.7150; De Caritat et al., 2005); and (3) $^{87}Sr/^{86}Sr$ ratios greater than 0.7150, a threshold indicative of silicate weathering (De Caritat et al., 2005). We infer that the low ratios represent recharge, the intermediate ratios some weathering of silicate minerals and the higher ratios silicate weathered waters. There are wells with $^{87}Sr/^{86}Sr$ ratios that are similar to rainfall in the likely recharge areas to the south-west and to the south-east of the DSC. In Figure 5.9a, $^{87}Sr/^{86}Sr$ ratios generally increase with distance along the inferred groundwater flowpaths, indicating silicate weathering. Although, there are some outliers from this trend in the Moolayember Formation (e.g., a low $^{87}Sr/^{86}Sr$ ratio of 0.706 for two samples in the north-west of the study area).

The two main sources of Sr to the Triassic aquifers are recharge and from silicate weathering. Rainfall collected near the DSC in April 2021 had an $^{87}Sr/^{86}Sr$ ratio of 0.7125, which is greater than modern seawater (0.7090; Aberg et al., 1989). This is expected because $^{87}Sr/^{86}Sr$ typically increases with distance inland due to mixing with atmospheric aerosols (Raiber et al., 2009). $^{87}Sr/^{86}Sr$ in rainfall is influenced by changes in climatic conditions and the predominant wind directions, which causes temporal variability in the $^{87}Sr/^{86}Sr$ ratios over geological time (Cook and Herczeg, 2000). There is a trend of constant $^{87}Sr/^{86}Sr$ ratios with increasing Sr concentrations in many of the groundwater samples from the Clematis Formation/Dunda Beds and the Moolayember Formation, which suggests evapotranspiration may be occurring during groundwater recharge (Figure 5.9b). Whereas other samples from the Clematis Formation/Dunda Beds display a trend of higher $^{87}Sr/^{86}Sr$ ratios with increasing Sr concentrations, which suggests silicate weathering.

High $^{87}Sr/^{86}Sr$ values, and low Sr/Na ratios suggest the addition of Sr and Na as a by-product from the weathering of silicate minerals with high ^{87}Rb content (Brennan et al., 2014). Higher Sr/Na ratios and lower $^{87}Sr/^{86}Sr$ ratios (typically <0.710) can be an indicator of carbonate weathering (De Caritat et al., 2005). However, the Sr/Na ratios are lower than those expected due to carbonate weathering. Additionally, carbonate weathering would be expected to lead to decreased $^{87}Sr/^{86}Sr$ ratios with increased $\delta^{13}C$ and this trend is not apparent in the available data (see Figure 5.9c). This further supports the notion that carbonate weathering is not a dominant process along the groundwater flow path. Although, there is a single sample in the Moolayember Formation with $\delta^{13}C \approx$ -9 ‰ and $^{87}Sr/^{86}Sr$ = 0.706, where the more isotopically enriched $\delta^{13}C$ value suggests carbonate weathering is plausible (Moya et al., 2016).

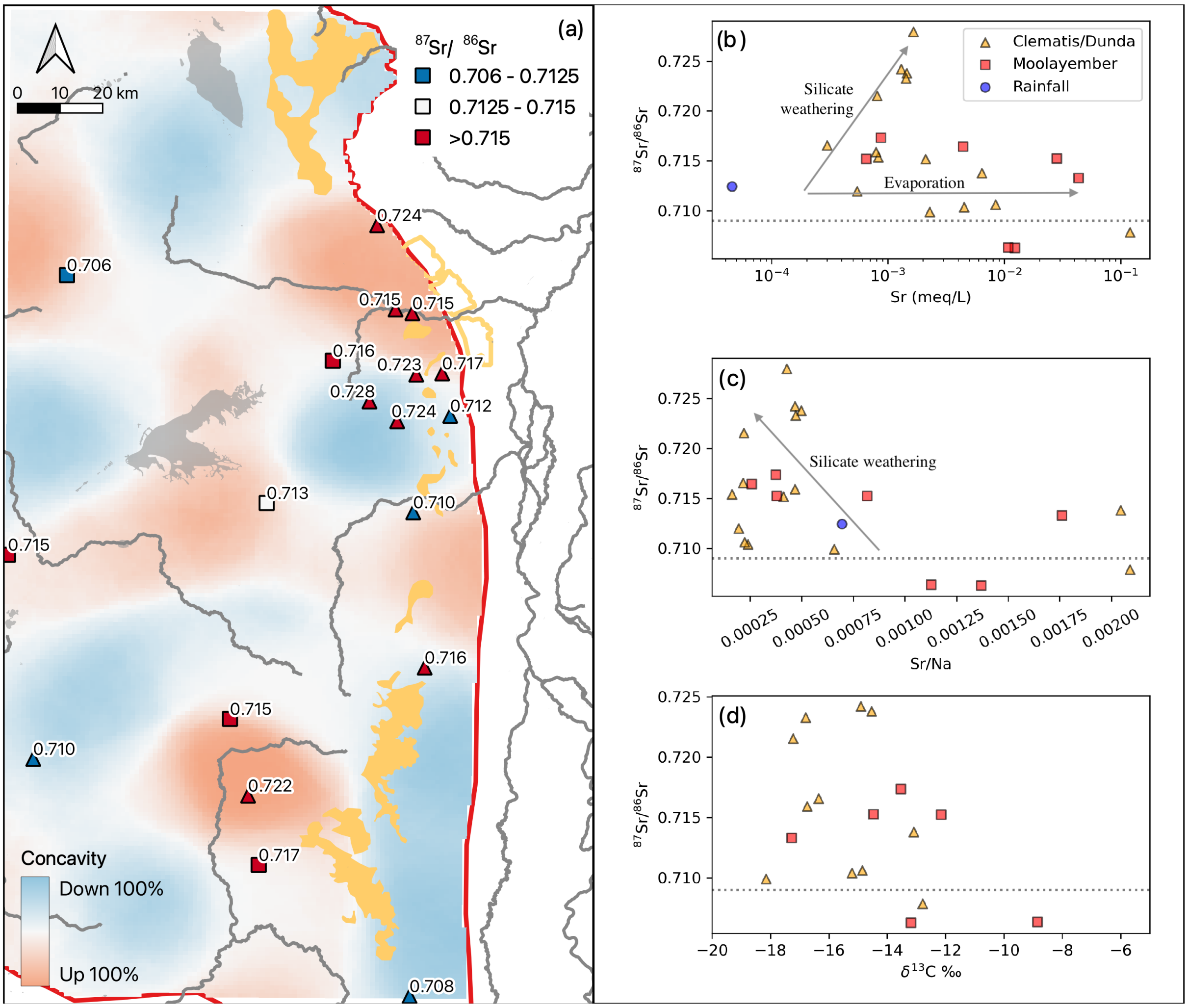

Figure 5.9: *$^{87}Sr/^{86}Sr$ ratio data in the study area. (a) Spatial maps of $^{87}Sr/^{86}Sr$ ratios in the Clematis Formation/Dunda Beds (triangles) and the Moolayember Formations (squares), and scatterplots showing (b) $^{87}Sr/^{86}Sr$ vs Sr, (c) $^{87}Sr/^{86}Sr$ vs Sr/Na and (d) $^{87}Sr/^{86}Sr$ vs $\delta^{13}C$. Dotted lines in (b, c, d) denote modern seawater $^{87}Sr/^{86}Sr$ ratios.*

5.5 Hydrogeochemical conceptual model

The hypothesised locations of diffuse groundwater recharge and discharge areas in the study area as identified in Chapter 4 are supported by the hydrochemical signatures of the groundwater samples from the Clematis Formation/Dunda Beds and Moolayember Formation aquifers. In the recharge areas r1, r3 and r7 (Figure 5.10), the groundwater samples from the Clematis Formation/Dunda Beds have a low TDS (<250 mg/L), low Na/Cl ratios (<1.5) and Na/Cl water type. Additionally, in recharge areas r3, r5 and r7 where $^{87}Sr/^{86}Sr$ samples were available, low $^{87}Sr/^{86}Sr$ ratios (0.708-0.712) suggest a signature similar to rainfall. Throughout the study area the stable isotopes of water in the Clematis Formation/Dunda Beds are mostly consistent with winter recharge (as the stable isotopes plot to the left of the weighted mean rainfall; see Figure 5.8a) and the stable isotope vs Cl trends suggest evaporation is initially the dominant process during recharge (Figure 5.8b). Subsequently, as water infiltrates beneath the evaporation extinction depth, the dominant process becomes transpiration, as signified by a subsequent transpiration trend. Overall, these findings support the hypothesised recharge areas r1, r3, r5 and r7, however, there is insufficient data to assess the recharge areas r2, r4 or r6 in the western region of the study area.

The location of the diffuse groundwater discharge area, d2, likely represents water discharging to the DSC and the Carmichael River from a northern flow path from r1 and a combination of a regional flow path from r7 and more localised recharge from r3 from the south. This is supported by the vertical stratification of TDS and Na/Cl ratios in the south (see Figure 5.3c and 5.6c) and hydrochemical signature from Camp Spring, which is a mixture of weathered and less weathered waters (see Figure 5.4 and 5.5). There are few groundwater wells within the vicinity of the likely discharge areas d3 and d4., However, based on surface features, d3 may discharge to Lake Galilee, which is saline and d4 may

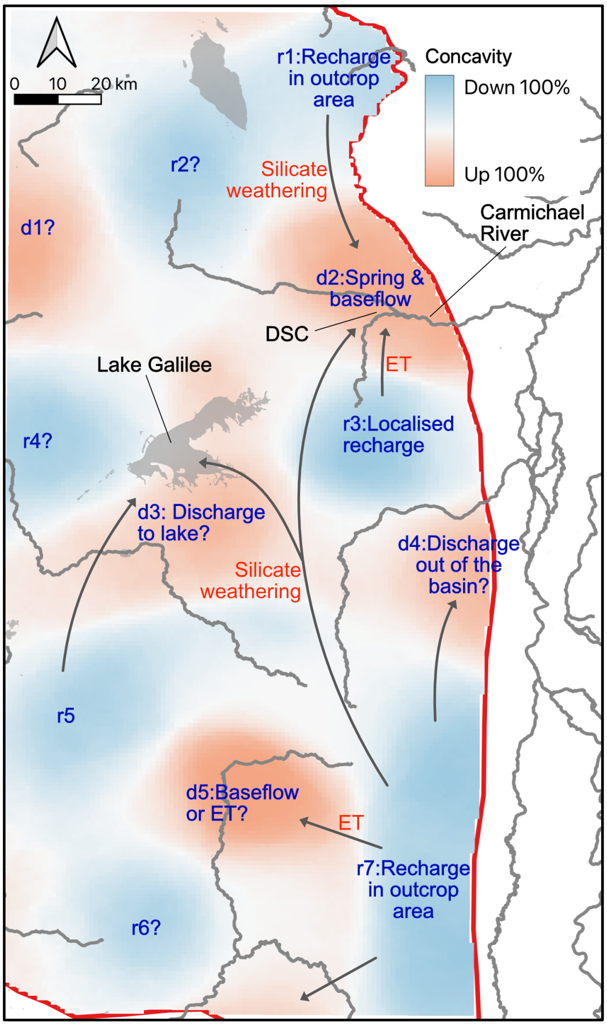

Figure 5.10: *Regional scale hydrogeochemical conceptual model of the study area in the Galilee Basin. Relative percentage of realisations where the hydraulic head surface is concave up (red) or concave down (blue) labelled in blue with potential recharge zones r1-r7 and potential discharge zones d1-d5 (as per Chapter 4), and in red for hydrogeochemical processes affecting the chemistry of groundwater along inferred groundwater flow paths and with increased residence times.*

be associated with other Formations and structural features along the eastern boundary of the Galilee Basin. Groundwater samples located close to the likely discharge area d5 have a high TDS and a low Na/Cl ratio, suggesting evaporation is occurring along the inferred flow path from the recharge area, r7. There is insufficient hydrochemical data available to assess the likely discharge area, d1, at the western margin of the study area.

We found multiple lines of evidence to suggest that the dominant weathering process along groundwater flow paths within the Triassic-age aquifers is silicate weathering. Firstly, the waters evolve from Na-Cl type to Na-HCO_3 type, with increasing TDS, Na/Cl ratios increasing with higher TDS, and HCO_3 also increasing with higher Na/Cl ratios. Evidence of the weathering of silicate minerals is further supported by $^{87}Sr/^{86}Sr$ ratios that increase with distance from the recharge areas r5, r7 and r3, where the samples have higher $^{87}Sr/^{86}Sr$ ratios and lower Sr/Na ratios, suggesting the release of radiogenic Sr from ^{87}Rb rich silicate minerals. There findings differ from those of Moya et al. (2016) who suggested carbonate weathering was the dominant process. This is likely due to our study examining a wider range of analytes on a smaller spatial scale, enabling us to differentiate between carbonate and silicate weathering.

In contrast, evapotranspiration appears to be the main process responsible for the TDS variation in the Moolayember Formation, as signified by the Na/Cl ratios that remain relatively constant with increasing TDS (see Figure 5.5a), paired with an evaporation trend for the stable isotopes of water (see Figure 5.8b). These observations suggest that the Moolayember Formation may be exposed to significant evapotranspiration either during recharge, or due to tree water use in areas where the water table is shallow. The high evapotranspiration rates likely obfuscate weathering trends in the Moolayember Formation.

5.6 Implications

We found that where hydrochemistry and isotope data were available, there was an agreement between the conceptual model of recharge and discharge areas from hydraulic head modelling (Keegan-Treloar et al., under review) and those identified from the hydrochemistry and isotope data sets. This agreement reduces the uncertainty of the hydrogeological conceptual model for the Triassic aquifers in study area of the Galilee Basin. Unfortunately, the recharge/discharge areas located to the west remain uncertain due to sparsely available data. As recharge and discharge areas inferred by the hydrochemistry data are time-integrated, the agreement with the hydraulics suggests the regional groundwater flow system has remained largely similar to the historic conditions. This observation is perhaps not surprising given that prior to mine dewatering activities, there has been limited groundwater abstraction in the Galilee Basin.

Hydrochemical evidence (including relationships between TDS and Na/Cl ratios with depth) suggests that there may be a layered flow system where the discharge area, d2, receives a mixture of older groundwater from a longer, deeper flow path (likely from r7) that shows silicate weathering and more recent recharge from a shorter shallower flow path (likely r3). Major ion chemistry suggests that the water discharging from Camp Spring is consistent with a mixture of the low TDS waters from the shallow southern flow path (r3) and the higher TDS waters from the south-eastern deeper flow path (r7) and the northern flow path from recharge area, r1. This observation suggests that the shallow, southern flow from r3 may be integral to maintaining the low salinity of the spring discharge at the DSC. If the mining operations that are located to the east of DSC impact this shallower flow path (e.g., through drawdown propagation), the salinity of spring discharge may increase together with a decline in aquifer pressure, potentially impacting the sensitive ecosystems receiving water from the DSC. Given the current mine-dewatering in the Galilee Basin, future studies that investigate how changes in the contribution to spring discharge from local and deeper regional scale flow paths impact the quality of spring discharge will be of major benefit.

The TDS variations in the groundwater from the Moolayember Formation appear to be controlled predominantly by evapotranspiration, while silicate weathering was the dominant control of the TDS of waters in the Clematis Formation and the Dunda Beds. Notably, the TDS in the Moolayember Formation was up to an order of magnitude larger than that of the Clematis Formation and the Dunda Beds. As the hydrochemistry of the Moolayember Formation is distinctly different from that of the Clematis Formation and Dunda Beds, there is likely limited connectivity between the Moolayember Formation and the Clematis Formation/Dunda Beds. This observation suggests that the Moolayember Formation should be treated as a separate unit from the Clematis Formation/Dunda Beds, which has important implications for future modelling of interconnectivity between the major aquifer systems. Whereas the Clematis Formation and Dunda Beds are hydrochemically indistinguishable, suggesting similar mineralogy and/or hydraulic connectivity between these units.

5.7 Uncertainties and future directions

The scarcity of hydrochemical and isotopic data in the Galilee Basin remains an issue for revising the hydrogeological conceptual model of the multi-layered aquifer system, particularly in the western portion of the study area. The data scarcity in study area prevented the assessment of hypothesised recharge areas r2, r4 and r6 and the hypothesised discharge areas d1, d3, d4 and d5 from Chapter 4. Further groundwater sampling near the mine site will inform any potential impacts from mine dewatering, whereas sampling to the west will better inform the regional hydrogeology. Ideally, future groundwater sampling could include major/minor ions, stable isotope and age tracer data. Sampling will likely occur as more mining and coal seam gas activities begin in the Galilee Basin. However, we emphasise the urgent need for further sampling campaigns throughout the Galilee Basin to properly characterise the baseline hydrochemistry.

In this study, few age tracer data were available, which prevented the determination of age variations along flow paths in the study area. Some limited age data was available from Moya et al. (2016), who collected four ^{36}Cl/Cl samples from the Triassic units of the Galilee Basin and found that ^{36}Cl/Cl ratios were higher in the eastern region (^{36}Cl/Cl $\approx$ 90) and lower in the western region (^{36}Cl/Cl $\approx$ 27), indicating a significant increase in groundwater age from the eastern outcrop areas to the western areas where the Galilee Basin is overlain by the Eromanga Basin. The suggested increase in age supports the general trends observed in this study, although the sparsity of the ^{36}Cl observations restricted a more detailed assessment of age trends on a more local scale. An improved understanding of the distribution of groundwater age would be valuable to assess recharge and discharge areas, and to identify water sources of the DSC and Carmichael River. For example, given that ^{14}C can be utilised to determine ages ranging between 2000 and 30,000 years (e.g., Clark and Fritz, 2013), ^{14}C from wells screened at various depths near the DSC and Carmichael River, along groundwater flow paths and from springs could be particularly useful. Assessing the age along flow paths would also be useful to approximate groundwater velocities, which could inform future numerical modelling of the region.

The inter-aquifer connectivity between the Triassic and Permian-aged units is expected to be significant due to faulting across the Rewan Formation (e.g., Moya et al., 2015; Evans et al., 2018). This study focussed solely on the hydrochemistry of the Triassic aquifers and the Permian-aged units were not examined due to poor data availability. Thus, it was not possible to investigate important questions concerning inter-aquifer connectivity between

Triassic and Permian Formations in this study. Future studies could utilise major and minor ion chemistry and vertical hydraulic head gradients to characterise inter-aquifer mixing. However, data sparsity remains a challenge in the Galilee Basin, and additional bores, particularly in the Permian-aged units, would need to be installed. In the meantime, novel techniques, including inverse hydrochemical modelling from spring discharge or geophysical studies, may be useful to improve the understanding of the relationships between the Triassic and Permian-aged aquifers (Keegan-Treloar et al., 2022).

Conclusions

The hydrochemistry and isotope data utilised in this study supported findings with respect to the locations of groundwater recharge and discharge areas that were previously identified using hydraulic head data. The main recharge areas are in the southern and northern outcrop areas, with localised recharge to the south of the DSC and Carmichael River and south of Lake Galilee. Evapotranspiration was apparent in the hydrochemical signature in the recharge areas, and weathering of silicate minerals was apparent along groundwater flow paths towards the discharge areas. These observations reduce the uncertainty in the regional conceptual model of recharge and discharge areas. Although, uncertainty still remains due to data sparsity, particularly in the western region of the study area of the Galilee Basin. These uncertainties could be reduced through additional field sampling in the western regions of the Galilee Basin.

The hydrochemistry of the Moolayember Formation was distinctly different from that of the Clematis Formation and Dunda Beds, particularly with respect to Na/Cl ratios and salinity. These differences in the hydrochemical signature have implications for how the Triassic aquifers in the region are characterised and considered in the hydrogeological conceptual model. The findings suggest that the Moolayember Formation should be considered a separate aquifer unit, while the Clematis Formation and Dunda Beds may be combined as they were hydrochemically indistinguishable. This finding differs from previous conceptualisations that have treated the Triassic units as a single aquifer. We suggest that the Moolayember Formation be treated as a separate aquifer from the Clematis Formation and Dunda Beds in future field campaigns and numerical modelling.

Vertical stratification of the hydrochemical signatures in the Triassic aquifers within the study area of the DSC and Carmichael River suggest a combination of local and regional scale flow paths with differing salinities. The impacts of adjacent mining activities and mine-induced drawdown in these aquifers may influence the hydraulic gradients and the contributions of the local and regional scale flow paths as well as the salinity of waters discharging to receiving environments. This finding has important implications for the spring-dependent DSC and Carmichael River ecosystems, where changes in salinity may impact the ecological functioning of these spring-dependent ecosystems.

CHAPTER 6

CONCLUSIONS

6.1 Summary of findings

The loss of many ecologically and culturally significant springs emphasises the importance of understanding these systems and their role in a broader, regional hydrogeological context. Regional hydrogeological systems and the role of springs in these systems are often poorly understood due to sparsely distributed data and limited understanding of important processes. Conducting fieldwork to characterise remote sites can be challenging, and it is often necessary to utilise pre-existing datasets. This thesis produced four studies to assess the role of fault-driven springs, and how to best utilise available (but sparse) datasets to inform hydrogeological systems that contain important springs. Specifically, these studies focused on: (Chapter 2) a review of the current state of knowledge of fault-controlled spring systems; (Chapters 3 and 4) developing a framework using geostatistics and hydraulic head observations to inform conceptual models of regional hydrogeological systems; and (Chapter 5) the use of hydrochemical data to further inform the regional scale conceptual models. Chapters 3, 4 and 5 were applied to the case study of the Doongmabulla Spring Complex (DSC), an ecologically and culturally significant spring complex in the Galilee Basin, Queensland, Australia.

The key findings from each of the four specific studies are as follows:

1. The review of fault-controlled spring systems synthesised the disparate knowledge of faults and springs (each of which have been reviewed separately) in a unified way for the first time. The review identified that key spring characteristics (e.g., discharge rates, hydrochemistry, etc.) are not routinely monitored, despite these observations providing vital information on subsurface properties and processes. The review demonstrated that monitoring of spring characteristics can be undertaken using existing techniques (e.g., water sampling or direct spring discharge measurements) at a fraction of the cost of typical groundwater monitoring infrastructure (e.g., wells). Findings also highlight the innovative techniques that have been developed to utilise these data in numerical modelling, groundwater age calculations, and in the estimation of regional hydraulic properties. Substantial knowledge gaps were identified in the current understanding of fault-controlled spring systems, including methods to identify spring-source aquifers, the relationships between aquifer hydraulic head and spring flow rates, and in the application of methods for characterising fault geological and hydrogeological properties. Furthermore, the relationships between spring discharge properties (e.g., flow rates, temperature, chemistry) and ecological functioning require further investigation to better understand how changes in spring discharge properties may impact receiving ecosystems. Thus, integrating ecosystem

responses with hydrogeological modelling is a critical area for future research. The review highlighted the need for management of fault-controlled springs to adopt a structured management approach that considers both the surface and subterranean regimes as a single interconnected system.

2. The likelihood of alternate source aquifers having adequate hydraulic head to support spring flow from the DSC was assessed for the Triassic- and Permian-aged aquifers of the Galilee Basin. For the first time in a hydrogeological application, Ordinary Indicator Co-Kriging was utilised with sparsely distributed hydraulic head measurements to construct cumulative distribution functions (CCDFs) to investigate spring source aquifers. The likelihoods from the CCDFs ranged from <0.01 to 0.49 for the Triassic-aged Formations, and from 0.03 to 0.12 for the deeper Permian-aged Formations. These results suggest that the Triassic-aged Formations have a higher likelihood of sufficient hydraulic head to support the springs than the Permian-aged Formations and the hydraulic head is likely only slightly greater than the spring geomorphic thresholds. This observation suggests that even a small change in the aquifer hydraulic head in the shallower Triassic-aged Formations may lead to the cessation of spring flow, which has important implications given the potential impacts of mine site dewatering from the nearby Carmichael Coal Mine. The advantage of Ordinary Indicator Co-Kriging over other techniques for regions such as the Galilee, where sparse head data of vary quality are available is that it provides a quantitative estimate of uncertainty.

3. A novel geostatistical technique was developed to probabilistically map extrema (i.e., minima and maxima) and concavity (i.e., concave up or concave down) in the potentiometric surface inferred from a sparse dataset of hydraulic heads. Likely recharge and discharge areas in Triassic-aged aquifers of the Galilee Basin were identified by

comparing maps of concavity and extrema in the hydraulic head surface with known surface features such as geological outcrops, rivers, and lakes. Results suggested that recharge is likely to occur predominantly in the north-east and south-east of the study area, where the Triassic-aged Formations outcrop. Whereas, discharge is apparent near several rivers, lakes and the DSC. The research demonstrates the importance of the Triassic Formations as a source of water to surface features, including the DSC, which emphasises potential widespread impacts from dewatering at the Carmichael Coal Mine. Benefits of the technique over existing methods (e.g., numerical modelling) include that it provides a probabilistic map of recharge and discharge areas, which is essential to represent the uncertainty of modelling in data sparse regions. This approach is broadly applicable to studies aiming to identifying recharge and discharge areas on a regional scale and further use is facilitated through a worked example provided online (DOI:10.5281/zenodo.6655359).

4. The available hydrochemical and isotope data for the Galilee Basin was collated and examined to identify hydrochemical signatures of recharge, chemical weathering along flow paths and the properties of discharge waters. Recharge and discharge areas identified using hydrochemistry and isotope data were consistent with those identified from interpretation of hydraulic head data in Chapter 4, providing an additional line of evidence to the head-based findings. Findings from the hydrochemical and isotope data suggest that the main recharge areas in the study region are in the southern and northern outcrop areas, with localised recharge to the south of the DSC and Carmichael River, and the south of Lake Galilee. Analyses of major ions chemistry and salinity suggests that evapotranspiration was the dominant process controlling TDS variations in the Moolayember Formation, while silicate weathering was the dominant process controlling TDS variations in the Clematis Formation and

Dunda Beds. Conceptually, these findings suggest that the Moolayember Formation should be considered a separate unit as it appears hydrochemically distinctly different from the Clematis Formation and Dunda Beds. This finding differs from previous conceptualisations that have treated the Triassic-aged units as a single aquifer. Vertical stratification of hydrochemistry in a transect across the DSC and Carmichael River area suggests a combination of local and regional scale flow paths of differing salinity. Mine-induced drawdown may influence the contributions of the local and regional scale flow paths, changing the discharge chemistry. This finding has important implications for spring-dependent ecosystems that are often highly sensitive to salinity variations.

6.2 Implications of findings for the Doongmabulla Springs Complex

The findings from the research conducted in this thesis inform the conceptualisation of the DSC and the surrounding region. Overall, the Triassic Formations appear more likely than the Permian Formations to have sufficient hydraulic head to support spring flow. Regionally, hydraulic and hydrochemical evidence suggest that recharge to the Triassic Formations occurs in the outcrop areas to the north-east and south-east with flow occurring from these areas towards the DSC. Hydrochemically, discharge water from the DSC is consistent with that of the Triassic Formations supporting the hypothesis that the Triassic Formations are a source of water to the DSC. In addition to being a potential source of discharge to the DSC, the Triassic Formations also have minima and concave up areas in the hydraulic head surface near several rivers and lakes, suggesting that the Triassic Formations may be an important source of water to surface water features. However, substantial uncertainties remain, and further studies are required.

6.3 Future work

6.3.1 Fault-controlled springs

This thesis represents a significant contribution to the knowledge of fault-controlled spring systems. However, knowledge gaps remain, and further studies of these systems are required. Key future research directions for fault-controlled springs are outlined below.

1. Spring discharge measurements provide a unique opportunity to directly observe groundwater fluxes, which is typically very difficult in hydrogeology. A stronger emphasis should be placed on the regular monitoring of spring discharge, as this provides a valuable source of secondary information on aquifer behaviour and low-cost monitoring methods are readily available. Several studies have demonstrated that spring discharge can be useful to constrain geological properties in numerical modelling. However, this is not common practice, and there is limited guidance on the assimilation of these measurements. Further investigations are needed to develop guidance on the assimilation of spring discharge measurements in numerical modelling.

2. Currently, the relationships between changes in spring discharge rates and ecosystem responses remain poorly understood. There is an urgent need for multidisciplinary research to develop guidance for integrating ecosystem responses to spring discharge changes into hydrogeological modelling. Through characterising these relationships, management could identify the ecosystem consequences from changes in spring discharge and identify allowable changes to spring discharge rates that preserve ecosystem values.

3. The faults controlling spring discharge often intersect multiple aquifer units, leading to complex mixing where spring discharge represents a mixture of waters from different

aquifer units. Changes to the aquifer hydraulic head can modify mixing processes, altering the hydrochemistry of spring discharge. As ecosystems are often highly sensitive to changes in hydrochemistry, characterising mixing processes and the consequences of alterations in aquifer hydraulic head on spring discharge hydrochemistry is an important area for future research. Numerical modelling to demonstrate the mixing processes where faults intersect multiple aquifer units would assist in interpreting mixing processes and quantifying how changes to aquifer hydraulic head may impact spring discharge chemistry.

6.3.2 Improving the conceptual model of the Doongmabulla Spring Complex and the Galilee Basin

This thesis improves the understanding of the conceptual model of the DSC and Galilee Basin. However, uncertainties remain, and further research is required, particularly given the potential impacts of dewatering associated with the Carmichael Mine on the DSC. Future research directions for the DSC and Galilee Basin region are outlined below.

1. Currently, the DSC spring discharge rates are not being monitored. This is problematic as without understanding the spring discharge baseline conditions, including seasonal variability, identifying whether changes in spring discharge are due to mine site dewatering or natural variation is a major challenge. Measuring spring discharge rates from at least some springs is critical to determine the baseline conditions and monitor changes in spring discharge rates due to mine site dewatering. Additionally, spring discharge rates would provide a useful constraint for future numerical modelling. The need to install monitoring equipment to obtain baseline observations (or near baseline) is urgent, given that mine site dewatering activities have already commenced.

2. The lack of available data in the Permian-aged Formations restricted the ability to characterise inter-aquifer connectivity between the Triassic and Permian-aged units. An airborne electromagnetic survey was flown for Geoscience Australia in 2017, and a detailed analysis of the survey would be beneficial in identifying faults and areas of likely inter-aquifer connectivity. The collection of additional water samples from the Permian-aged units for major/minor ions, stable isotopes and age tracers would be beneficial in identifying inter-aquifer connectivity and mixing. Ideally, water samples could be collected to the west of the Carmichael Mine, where few measurements are currently available. However, data sparsity remains challenging, and additional bores, particularly in the Permian-aged units, would need to be installed. In the meantime, novel techniques, utilising hydraulic head, inverse modelling from spring discharge or geophysics, may be useful to improve the understanding of the relationships between the Triassic and Permian-aged aquifers.

3. In this study, few age-tracer data were available, which prevented an analysis of variations in groundwater age along flow paths. Understanding how the groundwater age evolves spatially would provide valuable information to assess recharge and discharge areas and the contribution of flow from different flow paths. Future sampling campaigns could collect a suite of age tracers including ^{14}C from wells screened at various depths near the DSC and Carmichael River, along groundwater flow paths and from springs. The groundwater ages along flow paths, in springs and the variability of age with depth near the DSC and Carmichael River, could inform the characterisation of the proportion of local and regional scale flow paths contributing to the spring flow. Assessing the variations in age along flow paths would also be useful to approximate groundwater velocities, which would inform future numerical modelling of the region.

REFERENCES

AECOM, 2021. Groundwater Management and Monitoring Program - Carmichael Coal Project.

Abbo, H., Shavit, U., Markel, D., Rimmer, A., 2003. A numerical study on the influence of fractured regions on lake/ groundwater interaction; the Lake Kinneret (Sea of Galilee) case. J. Hydrol. 283, 225–243. https://doi.org/10.1016/S0022-1694(03)00273-7

Aberg, G., Jacks, G., Joseph Hamilton, P., 1989. Weathering rates and 87Sr/86Sr ratios: An isotopic approach. J. Hydrol. 109, 65–78. https://doi.org/10.1016/0022-1694(89)90007-3

Adani Mining, 2013. Environmental Impact Statement (EIS) - Carmichael Coal Mine and Rail Project. Retrieved from: https://www.statedevelopment.qld.gov.au/coordinator-general/assessments-and-approvals/coordinated-projects/completed-projects/carmichael-coal-mine-and-rail-project/eis-documents

D’Agostino, R., Pearson, E.S., 1973. Tests for Departure from Normality. Biometrika 60,

613. https://doi.org/10.2307/2335012

Alçiçek, H., Bülbül, A., Alçiçek, M.C., 2016. Hydrogeochemistry of the thermal waters from the Yenice Geothermal Field (Denizli Basin, Southwestern Anatolia, Turkey). J. Volcanol. Geotherm. Res. 309, 118–138. https://doi.org/10.1016/j.jvolgeores.2015.10.025

Allen, J.P., Fielding, C.R., 2007. Sedimentology and stratigraphic architecture of the Late Permian Betts Creek Beds, Queensland, Australia. Sediment. Geol. 202, 5–34. https://doi.org/10.1016/j.sedgeo.2006.12.010

Alley, W.M., Healy, R.W., LaBaugh, J.W., Reilly, T.E., 2002. Flow and storage in groundwater systems. Science (80-.). 296, 1985–1990. https://doi.org/10.1126/science.1067123

Amoruso, A., Crescentini, L., Petitta, M., Rusi, S., Tallini, M., 2011. Impact of the 6 April 2009 L'Aquila earthquake on groundwater flow in the Gran Sasso carbonate aquifer, Central Italy. Hydrol. Process. 25, 1754–1764. https://doi.org/10.1002/hyp.7933

Anane, M., Selmi, Y., Limam, A., Jedidi, N., Jellali, S., 2014. Does irrigation with reclaimed water significantly pollute shallow aquifer with nitrate and salinity? An assay in a perurban area in North Tunisia. Environ. Monit. Assess. 186, 4367–4390. https://doi.org/10.1007/s10661-014-3705-x

Anderson, M.P., 2005. Heat as a ground water tracer. Ground Water 43, 951–968. https://doi.org/10.1111/j.1745-6584.2005.00052.x

Apollaro, C., Dotsika, E., Marini, L., Barca, D., Bloise, A., De Rosa, N., Doveri, M., Lelli, M., Muto, F., 2012. Chemical and isotopic characterization of the thermomineral water of

Terme Sibarite springs (Northern Calabria, Italy). Geochem. J. 46, 117–129. https://doi.org/10.2343/geochemj.1.0166

Appello, C., Postma, D., 2010. Geochemistry, Groundwater and Pollution, 2nd ed. A.A. Balkema Publishers, Leiden, Netherlands.

Arnorrson, S., 2000. Isotopic and chemical techniques in geothermal exploration, development and use. Sampling methods, data handling and interpretation. Vienna.

Arslan, H., 2012. Spatial and temporal mapping of groundwater salinity using ordinary kriging and indicator kriging: The case of Bafra Plain, Turkey. Agric. Water Manag. 113, 57–63. https://doi.org/10.1016/j.agwat.2012.06.015

Ashley, G.M., Mworia, J.M., Muasya, A.M., Owen, R.B., Driese, S.G., Hover, V.C., Renaut, R.W., Goman, M.F., Mathai, S., Blatt, S.H., 2004. Sedimentation and recent history of a freshwater wetland in a semi-arid environment: Loboi Swamp, Kenya, East Africa. Sedimentology 51, 1301–1321. https://doi.org/10.1111/j.1365-3091.2004.00671.x

Bajjali, W., Clark, I.D., Fritz, P., 1997. The artesian thermal groundwaters of northern Jordan: Insights into their recharge history and age. J. Hydrol. 192, 355–382. https://doi.org/10.1016/S0022-1694(96)03082-X

Banks, E.W., Hatch, M., Smith, S., Underschultz, J., Lamontagne, S., Suckow, A., Mallants, D., 2019. Multi-tracer and hydrogeophysical investigation of the hydraulic connectivity between coal seam gas formations, shallow groundwater and stream network in a faulted sedimentary basin. J. Hydrol. 578, 124132. https://doi.org/10.1016/j.jhydrol.2019.124132

Banks, E.W., Shanafield, M.A., Noorduijn, S., McCallum, J., Lewandowski, J., Batelaan, O., 2018. Active heat pulse sensing of 3-D-flow fields in streambeds. Hydrol. Earth Syst. Sci. 22, 1917–1929. https://doi.org/10.5194/hess-22-1917-2018

Bastin, G., Gevers, M., 1985. Identification and optimal estimation of random fields from scattered point-wise data. Automatica 21, 139–155. https://doi.org/10.1016/0005-1098(85)90109-8

Battani, A., Deville, E., Faure, J.L., Jeandel, E., Noirez, S., Tocqué, E., Benoît, Y., Schmitz, J., Parlouar, D., Sarda, P., Gal, F., le Pierres, K., Brach, M., Braibant, G., Beny, C., Pokryszka, Z., Charmoille, A., Bentivegna, G., Pironon, J., de Donato, P., Garnier, C., Cailteau, C., Barrès, O., Radilla, G., Bauer, A., 2010. Geochemical study of natural CO2 emissions in the French Massif Central: How to predict origin, processes and evolution of CO2 leakage. Oil Gas Sci. Technol. 65, 615–633. https://doi.org/10.2516/ogst/2009052

Bense, V.F., Person, M.A., 2006. Faults as conduit-barrier systems to fluid flow in siliciclastic sedimentary aquifers. Water Resour. Res. 42. https://doi.org/10.1029/2005WR004480

Bense, V.F., Gleeson, T., Loveless, S.E., Bour, O., Scibek, J., 2013. Fault zone hydrogeology. Earth Sci. Rev. 127, 171–192. https://doi.org/10.1016/j.earscirev.2013.09.008

Bense, V.F., Person, M.A., Chaudhary, K., You, Y., Cremer, N., Simon, S., 2008. Thermal anomalies indicate preferential flow along faults in unconsolidated sedimentary aquifers. Geophys. Res. Lett. 35. https://doi.org/10.1029/2008GL036017

Bense, V.F., Van Balen, R., 2004. The effect of fault relay and clay smearing on groundwater flow patterns in the Lower Rhine Embayment. Basin Res. 16, 397–411.

https://doi.org/10.1111/j.1365-2117.2004.00238.x

Bense, V.F., Van Balen, R.T., De Vries, J.J., 2003. The impact of faults on the hydrogeological conditions in the Roer Valley Rift System: An overview. Geol. en Mijnbouw/Netherlands J. Geosci. 82, 41–54. https://doi.org/10.1017/S0016774600022782

Bethke, C.M., Johnson, T.M., 2008. Groundwater age and groundwater age dating. Annu. Rev. Earth Planet. Sci. 36, 121–152. https://doi.org/10.1146/annurev.earth.36.031207.124210

Bignall, G., Browne, P., 1994. Surface hydrothermal alteration and evolution of the Te Kopia Thermal Area, New Zealand. Geothermics 23, 645–658. https://doi.org/10.1016/0375-6505(94)90023-X

Blackwell, D.D., 1978. Heat flow and energy loss in the Western United States. Mem. Geol. Soc. Am. 152, 175–208. https://doi.org/10.1130/MEM152-p175

Bogan, M.T., Noriega-Felix, N., Vidal-Aguilar, S.L., Findley, L.T., Lytle, D.A., Gutiérrez-Ruacho, O.G., Alvarado-Castro, J.A., Varela-Romero, A., 2014. Biogeography and conservation of aquatic fauna in spring-fed tropical canyons of the southern Sonoran Desert, Mexico. Biodivers. Conserv. 23, 2705–2748. https://doi.org/10.1007/s10531-014-0745-z

Bonada, N., Rieradevall, M., Prat, N., 2007. Macroinvertebrate community structure and biological traits related to flow permanence in a Mediterranean river network. Hydrobiologia 589, 91–106. https://doi.org/10.1007/s10750-007-0723-5

Boy-Roura, M., Menció, A., Mas-Pla, J., 2013. Temporal analysis of spring water data to assess nitrate inputs to groundwater in an agricultural area (Osona, NE Spain). Sci. Total Environ. 452–453, 433–445. https://doi.org/10.1016/j.scitotenv.2013.02.065

Bräuer, K., Kämpf, H., Koch, U., Strauch, G., 2011. Monthly monitoring of gas and isotope compositions in the free gas phase at degassing locations close to the Nový Kostel focal zone in the western Eger Rift, Czech Republic. Chem. Geol. 290, 163–176. https://doi.org/10.1016/j.chemgeo.2011.09.012

Bradley, J.W., 2015. Adani Mining Pty Ltd vs. Land Services of Coast and Country Inc & Ors, 206 Further statement of evidence – geology and hydrogeology (groundwater conceptualisation). Retrieved from: http://envlaw.com.au/wp-content/uploads/carmichael8.pdf

Brake, L., Harris, C., Jensen, A., Keppel, M., Lewis, M., Lewis, S., 2019. Great Artesian Basin Springs: a Plan for the Future. Evidence-based methodologies for managing risks to spring values.

Bredehoeft, J.D., 2003. From Models to Performance Assessment: The Conceptualization Problem. Ground Water 41, 571–577. https://doi.org/10.1111/j.1745-6584.2003.tb02395.x

Bredehoeft, J., 2005. The conceptualisation model problem - Surprise. Hydrogeol. J. 13, 37–46. https://doi.org/10.1007/s10040-004-0430-5

Bredehoeft, J., Durbin, T., 2009. Ground water development - The time to full capture problem. Ground Water 47, 506–514. https://doi.org/10.1111/j.1745-6584.2008.00538.x

Brehme, M., Blöcher, G., Cacace, M., Kamah, Y., Sauter, M., Zimmermann, G., 2016.

Permeability distribution in the Lahendong geothermal field: A blind fault captured by thermal–hydraulic simulation. Environ. Earth Sci. 75. https://doi.org/10.1007/s12665-016-5878-9

Brennan, S.R., Fernandez, D.P., Mackey, G., Cerling, T.E., Bataille, C.P., Bowen, G.J., Wooller, M.J., 2014. Strontium isotope variation and carbonate versus silicate weathering in rivers from across Alaska: Implications for provenance studies. Chem. Geol. 389, 167–181. https://doi.org/10.1016/j.chemgeo.2014.08.018

Brogi, A., Capezzuoli, E., 2009. Travertine deposition and faulting: The fault-related travertine fissure-ridge at Terme S. Giovanni, Rapolano Terme (Italy). Int. J. Earth Sci. 98, 931–947. https://doi.org/10.1007/s00531-007-0290-z

Brogi, A., Capezzuoli, E., Buracchi, E., Branca, M., 2012. Tectonic control on travertine and calcareous tufa deposition in a low-temperature geothermal system (Sarteano, Central Italy). J. Geol. Soc. London. 169, 461–476. https://doi.org/10.1144/0016-76492011-137

Brombach, T., Marini, L., Hunziker, J.C., 2000. Geochemistry of the thermal springs and fumaroles of Basse-Terre Island, Guadeloupe, Lesser Antilles. Bull. Volcanol. 61, 477–490. https://doi.org/10.1007/PL00008913

Brugger, J., Long, N., McPhail, D.C., Plimer, I., 2005. An active amagmatic hydrothermal system: The Paralana hot springs, Northern Flinders Ranges, South Australia. Chem. Geol. 222, 35–64. https://doi.org/10.1016/j.chemgeo.2005.06.007

Brunetti, E., Jones, J.P., Petitta, M., Rudolph, D.L., 2013. Assessing the impact of large-scale dewatering on fault-controlled aquifer systems: A case study in the Acque Albule basin (Tivoli, central Italy). Hydrogeol. J. 21, 401–423.

https://doi.org/10.1007/s10040-012-0918-3

Brusca, L., Aiuppa, A., D'Alessandro, W., Parello, F., Allard, P., Michel, A., 2001. Geochemical mapping of magmatic gas-water-rock interactions in the aquifer of Mount Etna volcano. J. Volcanol. Geotherm. Res. 108, 199–218. https://doi.org/10.1016/S0377-0273(00)00286-9

Bryan, K., 1919. Classification of springs. J. Geol. 27, 522–561.

Byrdina, S., Revil, A., Pant, S.R., Koirala, B.P., Shrestha, P.L., Tiwari, D.R., Gautam, U.P., Shrestha, K., Sapkota, S.N., Contraires, S., Perrier, F., 2009. Dipolar self-potential anomaly associated with carbon dioxide and radon flux at Syabru-Bensi hot springs in central Nepal. J. Geophys. Res. Solid Earth 114, 1–14. https://doi.org/10.1029/2008JB006154

CSIRO, Geoscience Australia, 2019. Carmichael Coal Mine Advice on Groundwater Management and Monitoring and Groundwater Dependent Ecosystem Management plans to the Department of the Environment and Energy.

Caers, J., 2000. Adding local accuracy to direct sequential simulation. Math. Geol. 32, 815–850. https://doi.org/10.1023/A:1007596423578

Caine, J.S., Forster, C.B., 1999. Fault zone architecture and fluid flow: Insights from field data and numerical modeling, in: American Geophysical Union. pp. 101–127. https://doi.org/10.1029/GM113p0101

Caine, Jonathan, S., Evans, James, P., Forster, Craig, B., 1996. Fault zone architecture and permeability structure. Geology 24, 1025–1028. https://doi.org/10.1130/0091-7613(1996)024<1025:FZAAPS>2.3.CO;2

Carbonel, D., Gutiérrez, F., Linares, R., Roqué, C., Zarroca, M., McCalpin, J., Guerrero, J., Rodríguez, V., 2013. Differentiating between gravitational and tectonic faults by means of geomorphological mapping, trenching and geophysical surveys. The case of the Zenzano Fault (Iberian Chain, N Spain). Geomorphology 189, 93–108. https://doi.org/10.1016/j.geomorph.2013.01.020

Cartwright, I., Weaver, T., Tweed, S., Ahearne, D., Cooper, M., Czapnik, K., Tranter, J., 2002. Stable isotope geochemistry of cold CO2-bearing mineral spring waters, Daylesford, Victoria, Australia: Sources of gas and water and links with waning volcanism. Chem. Geol. 185, 71–91. https://doi.org/10.1016/S0009-2541(01)00397-7

Carvalho Dill, A.M.M., Stigter, T.Y., Brito, R., Chícharo, M.A., Chícharo, L., 2014. The combined use of radio frequency-electromagnetic surveys and chemical and biological analyses to study the role of groundwater discharge into the Guadiana estuary. Ecohydrology 7, 291–300. https://doi.org/10.1002/eco.1345

Celico, F., Petrella, E., Celico, P., 2006. Hydrogeological behaviour of some fault zones in a carbonate aquifer of Southern Italy: An experimentally based model. Terra Nov. 18, 308–313. https://doi.org/10.1111/j.1365-3121.2006.00694.x

Chen, J., Zhao, X., Sheng, X., Dong, H., Rao, W., Su, Z., 2006. Formation mechanisms of megadunes and lakes in the Badain Jaran Desert, Inner Mongolia. Chinese Sci. Bull. 51, 3026–3034. https://doi.org/10.1007/s11434-006-2196-8

Chica-Olmo, M., Luque-Espinar, J.A., Rodriguez-Galiano, V., Pardo-Igúzquiza, E., Chica-Rivas, L., 2014. Categorical indicator kriging for assessing the risk of groundwater nitrate pollution: The case of Vega de Granada aquifer (SE Spain). Sci.

Total Environ. 470–471, 229–239. https://doi.org/10.1016/j.scitotenv.2013.09.077

Chivas, A.R., De Deckker, P., Nind, M., Thiriet, D., Watson, G., 1986. The pleistocene palaeoenvironmental record of Lake Buchanan: An atypical Australian playa. Palaeogeogr. Palaeoclimatol. Palaeoecol. 54. https://doi.org/10.1016/0031-0182(86)90121-5

Choubey, V.M., Bartarya, S.K., Ramola, R.C., 2000. Radon in Himalayan springs: A geohydrological control. Environ. Geol. 39, 523–530. https://doi.org/10.1007/s002540050463

Clark, I.D., Fritz, P., 2013. Environmental Isotopes in Hydrogeology. CRC Press. https://doi.org/10.1201/9781482242911

Coates, D.R., Timofeeff, N.P., Caine, J.S., Davis, W.D., 1994. Hydrogeology of the Northern Shawangunk Mountains, Ulster County, New York. Consulting Report Prepared for Mohonk Preserve. Inc. pp. 81.

Cook, P., Herczeg, A.L., 2000. Environmental Tracers in Subsurface Hydrology. Springer US.

Cook, P.G., Banks, E.W., Marshall, S.K., Harrington, G.A., Batlle-Aguilar, J., Dogramaci, S., Turnadge, C., 2022. Inferring fault hydrology using groundwater age tracers. J. Hydrol. 610, 127905. https://doi.org/10.1016/j.jhydrol.2022.127905

Cox, S.C., Menzies, C.D., Sutherland, R., Denys, P.H., Chamberlain, C., Teagle, D.A.H., 2015. Changes in hot spring temperature and hydrogeology of the Alpine Fault hanging wall, New Zealand, induced by distal South Island earthquakes. Geofluids 15, 216–239. https://doi.org/10.1111/gfl.12093

Cox, S.C., Rutter, H.K., Sims, A., Manga, M., Weir, J.J., Ezzy, T., White, P.A., Horton, T.W., Scott, D., 2012. Hydrological effects of the M w 7.1 Darfield (Canterbury) earthquake, 4 September 2010, New Zealand. New Zeal. J. Geol. Geophys. 55, 231–247. https://doi.org/10.1080/00288306.2012.680474

Craig, H., 1961. Isotopic Variations in Meteoric Waters. Science (80-.). 133, 1702–1703. https://doi.org/10.1126/science.133.3465.1702

Cressie, N., 1990. The origins of kriging. Math. Geol. 22, 239–252. https://doi.org/10.1007/BF00889887

Cressie, N.A.C., 1993. Statistics for Spatial Data, Technometrics, Wiley Series in Probability and Statistics. John Wiley & Sons, Inc., Hoboken, NJ, USA. https://doi.org/10.1002/9781119115151

Criss, R.E., 2010. A Darcian model for the flow of Big Spring and the hydraulic head in the Ozark aquifer, Missouri, USA. Acta Carsologica 39, 379–387. https://doi.org/10.3986/ac.v39i2.106

Crossey, L.J., Fischer, T.P., Patchett, P.J., Karlstrom, K.E., Hilton, D.R., Newell, D.L., Huntoon, P., Reynolds, A.C., de Leeuw, G.A.M., 2006. Dissected hydrologic system at the Grand Canyon: Interaction between deeply derived fluids and plateau aquifer waters in modern springs and travertine. Geology 34, 25–28. https://doi.org/10.1130/G22057.1

Crossey, L.J., Karlstrom, K.E., Springer, A.E., Newell, D., Hilton, D.R., Fischer, T., 2009. Degassing of mantle-derived CO2 and He from springs in the southern Colorado Plateau region - Neotectonic connections and implications for groundwater systems. Bull. Geol. Soc. Am. 121, 1034–1053. https://doi.org/10.1130/B26394.1

Curewitz, D., Karson, J.A., 1997. Structural settings of hydrothermal outflow: Fracture permeability maintained by fault propagation and interaction. J. Volcanol. Geotherm. Res. 79, 149–168. https://doi.org/10.1016/S0377-0273(97)00027-9

Currell, M.J., 2016. Drawdown "Triggers": A Misguided Strategy for Protecting Groundwater-Fed Streams and Springs. Groundwater 54, 619–622. https://doi.org/10.1111/gwat.12425

Currell, M.J., Irvine, D.J., Werner, A.D., McGrath, C., 2020. Science sidelined in approval of Australia's largest coal mine. Nat. Sustain. https://doi.org/10.1038/s41893-020-0527-4.

Currell, M.J., Werner, A.D., McGrath, C., Webb, J.A., Berkman, M., 2017. Problems with the application of hydrogeological science to regulation of Australian mining projects: Carmichael Mine and Doongmabulla Springs. J. Hydrol. 548, 674–682. https://doi.org/10.1016/j.jhydrol.2017.03.031

Davis, J.A., Kerezsy, A., Nicol, S., 2017. Springs: Conserving perennial water is critical in arid landscapes. Biol. Conserv. 211, 30–35. https://doi.org/10.1016/j.biocon.2016.12.036

De Caritat, P., Kirste, D., Carr, G., McCulloch, M., 2005. Groundwater in the Broken Hill region, Australia: Recognising interaction with bedrock and mineralisation using S, Sr and Pb isotopes. Appl. Geochemistry 20, 767–787. https://doi.org/10.1016/j.apgeochem.2004.11.003

De Filippis, L., Billi, A., 2012. Morphotectonics of fissure ridge travertines from geothermal areas of Mammoth Hot Springs (Wyoming) and Bridgeport (California). Tectonophysics 548–549, 34–48. https://doi.org/10.1016/j.tecto.2012.04.017

De Filippis, L., Faccenna, C., Billi, A., Anzalone, E., Brilli, M., Özkul, M., Soligo, M., Tuccimei, P., Villa, I.M., 2012. Growth of fissure ridge travertines from geothermal springs of Denizli Basin, western Turkey. Bull. Geol. Soc. Am. 124, 1629–1645. https://doi.org/10.1130/B30606.1

Deane, D., Harding, C., Aldridge, K., Goodman, A., Gehrig, S., Nicol, J., Brookes, J., 2017. Predicted risks of groundwater decline in seasonal wetland plant communities depend on basin morphology. Wetl. Ecol. Manag. 1–14. https://doi.org/10.1007/s11273-017-9578-3

Della Porta, G., 2015. Carbonate build-ups in lacustrine, hydrothermal and fluvial settings: Comparing depositional geometry, fabric types and geochemical signature. Geol. Soc. Spec. Publ. 418, 17–68. https://doi.org/10.1144/sp418.4

Demlie, M., Wohnlich, S., Ayenew, T., 2008. Major ion hydrochemistry and environmental isotope signatures as a tool in assessing groundwater occurrence and its dynamics in a fractured volcanic aquifer system located within a heavily urbanized catchment, central Ethiopia. J. Hydrol. 353, 175–188. https://doi.org/10.1016/j.jhydrol.2008.02.009

Department of State Development infrastructure and Planning, 2014. Carmichael Coal Mine and Rail project: Coordinator-General's evaluation report on the environmental impact statement. 63 George Street, Brisbane Qld 4000, Australia.

Deutsch, C. V., Journel, A.G., 1998. GSLIB: geostatistical software library and user's guide. Second edition.

Diersch, H.-J. G., 2014. FEFLOW: Finite Element Modeling of Flow, Mass and Heat Transport in Porous and Fractured Media. FEFLOW: Finite element modeling of flow, mass and heat transport in porous and fractured media. pp. 996. https://doi:10.1007/978-3-642-38739-5

Diggle, P.J., Tawn, J.A., Moyeed, R.A., 1998. Model-based geostatistics, Journal of the Royal Statistical Society. Series C: Applied Statistics. https://doi.org/10.1111/1467-9876.00113

Doody, T.M., Hancock, P.J., Pritchard, J.L., 2017. Information Guidelines Explanatory Note: Assessing groundwater-dependent ecosystems. Report prepared for the Independent Expert Scientific Committee on Coal Seam Gas and Large Coal Mining Development through the Department of the Environment and Energy, C.

de Dreuzy, J.R., Méheust, Y., Pichot, G., 2012. Influence of fracture scale heterogeneity on the flow properties of three-dimensional discrete fracture networks (DFN). J. Geophys. Res. B Solid Earth 117, 1–21. https://doi.org/10.1029/2012JB009461

Duchi, V., Minissale, A., Vaselli, O., Ancillotti, M., 1995. Hydrogeochemistry of the Campania region in southern Italy. J. Volcanol. Geotherm. Res. 67, 313–328. https://doi.org/10.1016/0377-0273(94)00109-T

Durner, W., 1994. Hydraulic conductivity estimation for soils with heterogeneous pore structure. Water Resour. Res. 30, 211–223. https://doi.org/10.1029/93WR02676

Duvenaud, D.K., 2014. Automatic Model Construction with Gaussian Processes.

Eamus, D., Froend, R., Loomes, R., Hose, G., Murray, B., 2006. A functional methodology for determining the groundwater regime needed to maintain the health of groundwater-dependent vegetation. Aust. J. Bot. 54, 97. https://doi.org/10.1071/BT05031

Ellis, A.J., Wilson, S.H., 1955. Heat from the Wairakei-Taupo thermal region calculated from the chloride output. New Zeal. J. Sci. 36.

Enemark, T, Peeters, L.J., Mallants, D., Batelaan, O., 2019. Hydrogeological conceptual model building and testing: A review. J. Hydrol. 569, 310–329. https://doi.org/10.1016/j.jhydrol.2018.12.007.

Environment Australia, 2001. A Directory of Important Wetlands in Australia, Third Edition. Canberra.

Erman, A., Erman, D.C., 1995. Spring Permanence , Trichoptera Species Richness , and the Role of Drought. J. Kansas Entomol. Soc. 68, 50–64.

Evans, T., Kellett, J., Harris-Pascal, C., Radke, B., Cassel, R., Karim, F., Hostetler, S., Galinec, V., Dehelean, A., Caruanan, L., Kilgour, P., 2017. Observations analysis, statistical analysis and interpolation for the Galilee subregion.

Evans, T., Pavey, C., Cassel, R., Ransley, T., Sparrow, A., Kellett, J., Galinec, V., Dehelean, A., Bell, J., Caruana, L., Kilgour, P., 2018. Conceptual modelling for the Galilee subregion. Product 2.3 for the Galilee subregion from the Lake Eyre Basin Bioregional Assessment.

Fairley, J.P., Hinds, J.J., 2004. Rapid transport pathways for geothermal fluids in an active Great Basin fault zone. Geology 32, 825–828. https://doi.org/10.1130/G20617.1

Falcone, R.A., Carucci, V., Falgiani, A., Manetta, M., Parisse, B., Petitta, M., Rusi, S., Spizzico, M., Tallini, M., 2012. Changes on groundwater flow and hydrochemistry of the Gran Sasso carbonate aquifer after 2009 L'Aquila earthquake. Ital. J. Geosci. 131, 459–474. https://doi.org/10.3301/IJG.2011.34

Fang, H., Zhu, J., 2018. Simulation of groundwater exchange between an unconfined aquifer and a discrete fracture network with laminar and turbulent flows. J. Hydrol. 562, 468–476. https://doi.org/10.1016/j.jhydrol.2018.05.022

Fatchen, T., 2001. Vegetated wetland area as an index of mound spring flows, in: 4th Mound Spring Researchers Forum, National Parks and Wildlife, Adelaide, South Australia. pp. 5–8.

Faulds, J.E., Varga, R.J., 1998. The role of accommodation zones and transfer zones in the regional segmentation of extended terranes. Spec. Pap. Geol. Soc. Am. 323, 1–45. https://doi.org/10.1130/0-8137-2323-X.1

Faulds, J., Coolbaugh, M., Bouchot, V., Moeck, I., Oğuz, K., Cedex, O., 2008. Characterizing Structural Controls of Geothermal Reservoirs in the Great Basin, USA, and Western Turkey: Developing Successful Exploration Strategies in Extended Terranes. World C, 25–29.

Faulds, J.E., Olson, E.L., Harlan, S.S., McIntosh, W.C., 2002. Miocene extension and fault-related folding in the Highland Range, southern Nevada: A three-dimensional perspective. J. Struct. Geol. 24, 861–886. https://doi.org/10.1016/S0191-8141(01)00116-X

Felton, G.K., Currens, J.C., 1994. Peak flow rate and recession-curve characteristics of a karst spring in the Inner Bluegrass, central Kentucky. J. Hydrol. 162, 99–118. https://doi.org/10.1016/0022-1694(94)90006-X

Fensham, R.J., Fairfax, R.J., 2003. Spring wetlands of the Great Artesian Basin, Queensland, Australia. -Wetlands Ecol. Manag. 11, 343–362.

Fensham, R., Ponder, W., Fairfax, R.J., 2010. The community of native species dependent on natural discharge of groundwater from the Great Artesian Basin.

Fensham, R., Silcock, J., Laffineur, B., MacDermott, H., 2016. Lake Eyre Basin Springs Assessment Project: Hydrogeology, cultural history and biological values of springs in the Barcaldine, Springvale and Flinders River supergroups, Galilee Basin springs and Tertiary springs of western Queensland. Brisbane. Retrieved from: https://www.publications.qld.gov.au/dataset/lake-eyre/resource/c5d1813b-73a4-4e05-aa86-39a8ed3045fb

Fensham, R.J., Silcock, J.L., Powell, O., Habermehl, M.A., 2016b. In Search of Lost Springs: A Protocol for Locating Active and Inactive Springs. Groundwater 54, 374–383. https://doi.org/10.1111/gwat.12375

Finn, C.A., Morgan, L.A., 2002. High-resolution aeromagnetic mapping of volcanic terrain, Yellowstone National Park. J. Volcanol. Geotherm. Res. 115, 207–231. https://doi.org/10.1016/S0377-0273(01)00317-1

Florek, S., 1993. Archaeology of the Mound Spring Campsites Near Lake Eyre in South Australia.

Folch, A., Mas-Pla, J., 2008. Hydrogeological interactions between fault zones and alluvial aquifers in regional flow systems. Hydrol. Process. 22, 3476–3487. https://doi.org/10.1002/hyp.6956

Ford, R.G., Lien, B.K., Acree, S.D., Ross, R.R., 2021. Spreadsheet Tools for Quantifying Seepage Flux Across the GW-SW Interface. Water Resour. Res. 57. https://doi.org/10.1029/2019WR026232

Forster, C.B., Evans, J.P., 1991. Hydrogeology of thrust faults and crystalline thrust sheets: Results of combined field and modeling studies. Geophys. Res. Lett. 18, 979–982. https://doi.org/10.1029/91GL00950

Fournier, R.O., 1981. Application of Water Geochemistry to Geothermal Exploration and Reservoir Engineering. Geotherm. Syst. Princ. Case Hist. 109–143.

Fournier, R.O., 1989. Geochemistry and Yellowstone National. Annu. Rev. Earth Planet. Sci. 17, 13–53.

Fournier, R.O., O., Rowe, J.J., 1966. Estimation of underground temperatures from the silica content of water from hot springs and wet-steam wells. Am. J. Sci. 264, 685–697. https://doi.org/10.2475/ajs.264.9.685

Fournier, R.O., White, D.E., Truesdell, A.H., 1976. Convective heat flow in Yellowstone National Park, in: Proceedings of the 2nd UN Symposium on the Development and Use of Geothermal Resources, San Francisco. pp. 731–739.

Freeze, A.R., Cherry, J.A., 1979. Groundwater. Prentice-Hall INC, Eaglewood Cliffs, New Jersey.

Friedman, I., Norton, D.R., 2007. Is Yellowstone Losing Its Steam. Integr. Geosci. Stud. Gt. Yellowstone Area Volcanic, Hydrothermal Tecton. Process. Yellowstone Ecosyst. 1717, 271–298.

Frondini, F., Caliro, S., Cardellini, C., Chiodini, G., Morgantini, N., 2009. Carbon dioxide degassing and thermal energy release in the Monte Amiata volcanic-geothermal area (Italy). Appl. Geochemistry 24, 860–875. https://doi.org/10.1016/j.apgeochem.2009.01.010

Frontier Economics, 2016. Economic output of groundwater dependent sectors in the Great Artesian Basin.

Garrido, M.S., Giménez, E., de Lacy, M.C., Gil, A.J., 2011. Surveying at the limits of local RTK networks: Test results from the perspective of high accuracy users. Int. J. Appl. Earth Obs. Geoinf. 13, 256–264. https://doi.org/10.1016/j.jag.2010.12.001

Gemici, Ü., Tarcan, G., 2002. Hydrogeochemistry of the Simav geothermal field, western Anatolia, Turkey. J. Volcanol. Geotherm. Res. 116, 215–233. https://doi.org/10.1016/S0377-0273(02)00217-2

Gentry, W.M., Burbey, T.J., 2004. Characterization of ground water flow from spring discharge in a crystalline rock environment. J. Am. Water Resour. Assoc. 40, 1205–1217. https://doi.org/10.1111/j.1752-1688.2004.tb01580.x

Giggenbach, W.F., 1988. Geothermal solute equilibria. Derivation of Na-K-Mg-Ca geoindicators. Geochim. Cosmochim. Acta 52, 2749–2765. https://doi.org/10.1016/0016-7037(88)90143-3

Gilfillan, S.M.V., Wilkinson, M., Haszeldine, R.S., Shipton, Z.K., Nelson, S.T., Poreda, R.J., 2011. He and Ne as tracers of natural CO2 migration up a fault from a deep reservoir. Int. J. Greenh. Gas Control 5, 1507–1516. https://doi.org/10.1016/j.ijggc.2011.08.008

Gillies, S. & others, 2007. Shapely: manipulation and analysis of geometric objects, Available at: "https://github.com/Toblerity/Shapely"

Goff, F., Shevenell, L., 1987. Travertine deposits of Soda Dam, New Mexico, and their implications for the age and evolution of the Valles caldera hydrothermal system (

USA). Geol. Soc. Am. Bull. 99, 292–302. https://doi.org/10.1130/0016-7606(1987)99<292:TDOSDN>2.0.CO;2

Goff, F., McMurtry, G.M., Counce, D., Simac, J.A., Roldán-Manzo, A.R., Hilton, D.R., 2000. Contrasting hydrothermal activity at Sierra Negra and Alcedo volcanoes, Galapagos Archipelago, Ecuador. Bull. Volcanol. 62, 34–52. https://doi.org/10.1007/s004450050289

Goldscheider, N., Meiman, J., Pronk, M., Smart, C., 2008. Tracer tests in karst hydrogeology and speleology. Int. J. Speleol. 37, 27–40. https://doi.org/10.5038/1827-806X.37.1.3

Goovaerts, P., 1997. Geostatistics for Natural Resources Characterization. Oxford University Press.

Goovaerts, P., 2009. AUTO-IK: A 2D indicator kriging program for the automated non-parametric modeling of local uncertainty in earth sciences. Comput. Geosci. 35, 1255–1270. https://doi.org/10.1016/j.cageo.2008.08.014

Grant, N.T., 2020. Stochastic modelling of fault gouge zones: implications for fault seal analysis. Geological Society, London, Special Publications, 496(1), pp.163-197

Grimmett, G., Stirzaker, D., 2020. Probability and random processes. Oxford university press.

Grobe, M., Machel, H.G., 2002. Saline groundwater in the Münsterland Cretaceous Basin, Germany: Clues to its origin and evolution. Mar. Pet. Geol. 19, 307–322. https://doi.org/10.1016/S0264-8172(02)00019-3

Gudmundsson, A., 2000. Active fault zones and groundwater flow. Geophys. Res. Lett.

27, 2993–2996. https://doi.org/10.1029/1999GL011266

Habermehl, M.A., Lau, J.E., 1997. Hydrogeology of the Great Artesian Basin, Australia (map at scale 1: 2,500,000). Aust. Geol. Surv. Organ. Canberra.

Halihan, T., Love, A., Keppel, M., Dailey, M.K.M., Berens, V., Wohling, D., 2020. Evidence for groundwater mixing at Freeling Spring Group, South Australia. Hydrogeol. J. 28, 313–323. https://doi.org/10.1007/s10040-019-02069-x

Hancock, P.L., Chalmers, R.M.L., Altunel, E., Çakir, Z., 1999. Travitonics: Using travertines in active fault studies. J. Struct. Geol. 21, 903–916. https://doi.org/10.1016/S0191-8141(99)00061-9

Haselwimmer, C., Prakash, A., Holdmann, G., 2013. Quantifying the heat flux and outflow rate of hot springs using airborne thermal imagery: Case study from Pilgrim Hot Springs, Alaska. Remote Sens. Environ. 136, 37–46. https://doi.org/10.1016/j.rse.2013.04.008

Haszeldine, R.S., Quinn, O., England, G., Wilkinson, M., Shipton, Z.K., Evans, J.P., Heath, J., Crossey, L., Ballentine, C.J., Graham, C.M., 2005. Natural geochemical analogues for carbon dioxide storage in deep geological porous reservoirs, a United Kingdom perspective. Oil Gas Sci. Technol. 60, 33–49. https://doi.org/10.2516/ogst:2005004

Hatch, C.E., Fisher, A.T., Revenaugh, J.S., Constantz, J., Ruehl, C., 2006. Quantifying surface water-groundwater interactions using time series analysis of streambed thermal records: Method development. Water Resour. Res. 42, 1–14. https://doi.org/10.1029/2005WR004787

Hatton, T., Evans, R., 1998. Dependence of Ecosystems on Groundwater and its Significance to Australia. L. Water Resour. 12/98, 77.

Heasler, H.P., Jaworowski, C., Foley, D., 2009. Geothermal systems and monitoring hydrothermal features. Geol. Monit. 105–140.

Heeswijck, A., 2006. THE STRUCTURE, SEDIMENTOLOGY, SEQUENCE STRATIGRAPHY AND TECTONICS OF THE NORTHERN DRUMMOND AND GALILEE BASINS, CENTRAL QUEENSLAND, AUSTRALIA. James Cook University of North Queensland.

Heinicke, J., Koch, U., 2000. Slug flow - A possible explanation for hydrogeochemical earthquake precursors at Bad Brambach, Germany. Pure Appl. Geophys. 157, 1621–1641. https://doi.org/10.1007/pl00001053

Held, S., Schill, E., Schneider, J., Nitschke, F., Morata, D., Neumann, T., Kohl, T., 2018. Geochemical characterization of the geothermal system at Villarrica volcano, Southern Chile; Part 1: Impacts of lithology on the geothermal reservoir. Geothermics 74, 226–239. https://doi.org/10.1016/j.geothermics.2018.03.004

Henchiri, M., Ben Ahmed, W., Brogi, A., Alçiçek, M.C., Benassi, R., 2017. Evolution of pleistocene travertine depositional system from terraced slope to fissure-ridge in a mixed travertine-alluvial succession (Jebel El Mida, Gafsa, Southern Tunisia). Geodin. Acta 29, 20–41. https://doi.org/10.1080/09853111.2016.1265398

Herbert, A.W., 1996. Modelling approaches for discrete fracture network flow analysis. pp. 213–229. https://doi.org/10.1016/S0165-1250(96)80027-7

Hochstein, M.P., Nixon, I.M., 1979. Geophysical study of the Hauraki depression, North

Island, New Zealand. New Zeal. J. Geol. Geophys. 22, 1–19. https://doi.org/10.1080/00288306.1979.10422550

Hoke, L., Poreda, R., Reay, A., Weaver, S.D., 2000. The subcontinental mantle beneath southern New Zealand, characterised by helium isotopes in intraplate basalts and gas-rich springs. Geochim. Cosmochim. Acta 64, 2489–2507. https://doi.org/10.1016/S0016-7037(00)00346-X

Hollins, S.E., Hughes, C.E., Crawford, J., Cendón, D.I., Meredith, K.M., 2018. Rainfall isotope variations over the Australian continent – Implications for hydrology and isoscape applications. Sci. Total Environ. 645, 630–645. https://doi.org/10.1016/j.scitotenv.2018.07.082

Hsieh, P.A., Freckleton, J.R., 1993. Documentation of a computer program to simulate horizontal-flow barriers using the U.S. Geological Survey's modular three-dimensional finite-difference ground-water flow model. Open-File Report 92-477. California, USA.

Huang, H., Chen, Z., Wang, T., Xiang, C., Zhang, L., Zhou, G., Sun, B., Wang, Y., 2019. Nitrate distribution and dynamics as indicators to characterize karst groundwater flow in a mined mineral deposit in southwestern China. Hydrogeol. J. 27, 2077–2089. https://doi.org/10.1007/s10040-019-01987-0

Humphreys, W.F., 2009. Hydrogeology and groundwater ecology: Does each inform the other? Hydrogeol. J. 17, 5–21. https://doi.org/10.1007/s10040-008-0349-3

Hynes, H., 1970. The Ecology of Running Waters. University of Toronto Press.

IAEA/WMO, 2021. Global Network of Isotopes in Precipitation. The GNIP Database.

Accessible at: http://www.iaea.org/water.

Ihaka, R., Gentleman, R., 1996. R: A Language for Data Analysis and Graphics. J. Comput. Graph. Stat. 5, 299–314.

Ingebritsen, S.E., Galloway, D.L., Colvard, E.M., Sorey, M.L., Mariner, R.H., 2001. Time-variation of hydrothermal discharge at selected sites in the Western United States: Implications for monitoring. J. Volcanol. Geotherm. Res. 111, 1–23. https://doi.org/10.1016/S0377-0273(01)00207-4

Ingebritsen, S.E., Sherrod, D.R., Mariner, R.H., 1992. Rates and patterns of groundwater flow in the Cascade Range Volcanic Arc, and the effect on subsurface temperatures. J. Geophys. Res. 97, 4599. https://doi.org/10.1029/91JB03064

Inverarity, K., Heinson, G., Hatch, M., 2016. Groundwater flow underneath mound spring tufas from geophysical surveys in the southwestern Great Artesian Basin, Australia. Aust. J. Earth Sci. 63, 857–872. https://doi.org/10.1080/08120099.2016.1261942

Irvine, D.J., Briggs, M.A., Lautz, L.K., Gordon, R.P., McKenzie, J.M., Cartwright, I., 2017. Using Diurnal Temperature Signals to Infer Vertical Groundwater-Surface Water Exchange. Groundwater, 55(1): 10-26. DOI:10.1111/gwat.12459

Irvine, D.J., Kurylyk, B.L., Briggs, M.A., 2020. Quantitative guidance for efficient vertical flow measurements at the sediment–water interface using temperature–depth profiles. Hydrol. Process. 34, 649–661. https://doi.org/10.1002/hyp.13614

Irvine, D.J., Lautz, L.K., Briggs, M.A., Gordon, R.P., McKenzie, J.M., 2015. Experimental evaluation of the applicability of phase, amplitude, and combined methods to determine water flux and thermal diffusivity from temperature time series using

VFLUX 2. J. Hydrol. 531, 728–737. https://doi.org/10.1016/j.jhydrol.2015.10.054

Islam, M. S., Manzocchi, T., 2021. A novel flow-based geometrical upscaling method for representing fault zones with two-phase fault rock properties into a dynamic reservoir model. Scientific Reports, 11(1). https://doi:10.1038/s41598-021-99024-2

Jewell, P.W., Rahn, T.A., Bowman, J.R., 1994. Hydrology and Chemistry of Thermal Waters Near Wells, Nevada. Ground Water 32, 657–665. https://doi.org/10.1111/j.1745-6584.1994.tb00902.x

Jiang, Z., 2014. Analysis and modelling of the hydraulic conductivity in aquitards: application to the Galilee Basin and the Great Artesian Basin, Australia.

Journel, A.G., 1983. Nonparametric estimation of spatial distributions. J. Int. Assoc. Math. Geol. 15, 445–468. https://doi.org/10.1007/BF01031292

Journel, A.G., 1986. Constrained interpolation and qualitative information-The soft kriging approach. Math. Geol. 18, 269–286. https://doi.org/10.1007/BF00898032

van der Kamp, G., 1995. The Hydrogeology of Springs in Relation to the Biodiversity of Spring Fauna : A Review. J. Kansas Entomol. Soc. 68, 4–17.

Karaisaoğlu, S., Orhan, H., 2018. Sedimentology and geochemistry of the Kavakköy Travertine (Konya, central Turkey). Carbonates and Evaporites 33, 783–800. https://doi.org/10.1007/s13146-018-0436-z

Kavousi, A., Reimann, T., Liedl, R., Raeisi, E., 2020. Karst aquifer characterization by inverse application of MODFLOW-2005 CFPv2 discrete-continuum flow and transport model. J. Hydrol. 587, 124922. https://doi.org/10.1016/j.jhydrol.2020.124922

Kazemi, G.A., Lehr, J.H., Perrochet, P., 2006. Groundwater age. John Wiley & Sons.

Keegan-Treloar, R., Werner, A.D., Irvine, D.J., Banks, E.W., 2021. Application of Indicator Kriging to hydraulic head data to test alternative conceptual models for spring source aquifers. J. Hydrol. 601, 126808. https://doi.org/10.1016/j.jhydrol.2021.126808

Keery, J., Binley, A., Crook, N., Smith, J.W.N., 2007. Temporal and spatial variability of groundwater-surface water fluxes: Development and application of an analytical method using temperature time series. J. Hydrol. 336, 1–16. https://doi.org/10.1016/j.jhydrol.2006.12.003

Keppel, M.N., Clarke, J.D.A., Halihan, T., Love, A.J., Werner, A.D., 2011. Mound springs in the arid Lake Eyre South region of South Australia: A new depositional tufa model and its controls. Sediment. Geol. 240, 55–70. https://doi.org/10.1016/j.sedgeo.2011.08.001

Kharaka, Y.K., Mariner, R.H., 1989. Chemical Geothermometers and Their Application to Formation Waters from Sedimentary Basins, in: Thermal History of Sedimentary Basins. Springer New York, New York, NY, pp. 99–117. https://doi.org/10.1007/978-1-4612-3492-0_6

King, C.Y., Basler, D., Presser, T.S., Evans, W.C., White, L.D., Minissale, A., 1994. In search of earthquake-related hydrologic and chemical changes along Hayward Fault. Appl. Geochemistry 9, 83–91. https://doi.org/10.1016/0883-2927(94)90055-8

Tóth, Á., Kovács, S., Kovács, J., Mádl-Szőnyi, J., 2022. Springs regarded as hydraulic features and interpreted in the context of basin-scale groundwater flow. J. Hydrol. 610. https://doi.org/10.1016/j.jhydrol.2022.127907

Kresic, N., 2006. Hydrogeology and groundwater modeling. CRC press.

Kresic, N., 2010. Types and classifications of springs, in: Groundwater Hydrology of Springs. Elsevier Inc., pp. 31–85. https://doi.org/10.1016/B978-1-85617-502-9.00002-5

Kuo, T., Fan, K., Kuochen, H., Han, Y., Chu, H., Lee, Y., 2006. Anomalous decrease in groundwater radon before the Taiwan M6.8 Chengkung earthquake. J. Environ. Radioact. 88, 101–106. https://doi.org/10.1016/j.jenvrad.2006.01.005

Kurylyk, B.L., Irvine, D.J., 2019. Heat: An Overlooked Tool in the Practicing Hydrogeologist's Toolbox. Groundwater, 57(4): 517-524. DOI:10.1111/gwat.12910

Kurylyk, B.L., Irvine, D.J., Bense, V.F., 2019. Theory, tools, and multidisciplinary applications for tracing groundwater fluxes from temperature profiles. Wiley Interdisciplinary Reviews-Water, 6(1). DOI:10.1002/wat2.1329

La Rosa, A., Pagli, C., Keir, D., Sani, F., Corti, G., Wang, H., Possee, D., 2019. Observing Oblique Slip During Rift Linkage in Northern Afar. Geophys. Res. Lett. 46, 10782–10790. https://doi.org/10.1029/2019GL084801

Lewandowski, J., Angermann, L., Nützmann, G., Fleckenstein, J.H., 2011. A heat pulse technique for the determination of small-scale flow directions and flow velocities in the streambed of sand-bed streams. Hydrol. Process. 25, 3244–3255. https://doi.org/10.1002/hyp.8062

Lewis, S., Evans, T., Pavey, C., Holland, K., Henderson, B., Kilgour, P., Dehelean, A., Karim, F., Viney, N., Post, D., Schmidt, R., Sudholz, C., Brandon, C., Zhang, Y., Lymburner, L., Dunn, B., Mount, R., Gonzalez, D., Peeters, L., O' Grady, A., Dunne, R., Ickowicz, A., Hosack, G., Hayes, K., Dambacher, J., Barry, S., 2018. Impact and risk analysis for the Hunter subregion.

Lewis, M., White, D., Gotch, T., 2013. Allocating Water and Maintaining Springs in the Great Artesian Basin: Spatial Survey and Remote Sensing of Artesian Springs of the Western Great Artesian Basin. Canberra.

Li, X., Li, D., Xu, Y., Feng, X., 2020. A DFN based 3D numerical approach for modeling coupled groundwater flow and solute transport in fractured rock mass. Int. J. Heat Mass Transf. 149. https://doi.org/10.1016/j.ijheatmasstransfer.2019.119179

Liu, C.W., Jang, C.S., Liao, C.M., 2004. Evaluation of arsenic contamination potential using indicator kriging in the Yun-Lin aquifer (Taiwan). Sci. Total Environ. 321, 173–188. https://doi.org/10.1016/j.scitotenv.2003.09.002

Liu, N., Pan, L., Cheng, J., 2017. Numerical Modeling of CO2 and Brine Leakage through Open Fracture in a Fault Zone: Open Channel Flow or Darcy Flow. Geofluids 2017. https://doi.org/10.1155/2017/9035032

Love, A., Shand, P., Crossey, L., Harrington, G., Rousseau-Gueutin, P., 2013a. Allocating Water and Maintaining Springs in the Great Artesian Basin: Groundwater Discharge of the Western Great Artesian Basin. Canberra.

Love, A.J., Shand, P., Karlstrom, K., Crossey, L., Rousseau-Gueutin, P., Priestley, S., Wholing, D., Fulton, S., Keppel, M., 2013b. Geochemistry and Travertine Dating Provide New Insights into the Hydrogeology of the Great Artesian Basin, South Australia. Procedia Earth Planet. Sci. 7, 521–524. https://doi.org/10.1016/j.proeps.2013.03.065

Luhmann, A.J., Covington, M.D., Alexander, S.C., Chai, S.Y., Schwartz, B.F., Groten, J.T., Alexander, E.C., 2012. Comparing conservative and nonconservative tracers in karst and using them to estimate flow path geometry. J. Hydrol. 448–449, 201–211.

https://doi.org/10.1016/j.jhydrol.2012.04.044

Lupton, N., Janardhanan, S., Connell, L.D. and Pickett, T., 2019. Improving groundwater models to better represent coal seam gas extraction impacts in the Namoi region. CSIRO Report Number EP193251. CSIRO, Canberra

Lyon, S.W., Lembo, A.J., Walter, M.T., Steenhuis, T.S., 2006. Defining probability of saturation with indicator kriging on hard and soft data. Adv. Water Resour. 29, 181–193. https://doi.org/10.1016/j.advwatres.2005.02.012

Magri, F., Akar, T., Gemici, U., Pekdeger, A., 2010. Deep geothermal groundwater flow in the Seferihisar-Balçova area, Turkey: Results from transient numerical simulations of coupled fluid flow and heat transport processes. Geofluids 10, 388–405. https://doi.org/10.1111/j.1468-8123.2009.00267.x

Magri, F., Akar, T., Gemici, U., Pekdeger, A., 2012. Numerical investigations of fault-induced seawater circulation in the Seferihisar-Balçova Geothermal system, western Turkey. Hydrogeol. J. 20, 103–118. https://doi.org/10.1007/s10040-011-0797-z

Manga, M., 1997. A model for discharge in spring-dominated streams and implications for the transmissivity and recharge of quaternary volcanics in the Oregon Cascades. Water Resour. Res. 33, 1813–1822. https://doi.org/10.1029/97WR01339

Manga, M., 1999. On the timescales characterizing groundwater discharge at springs. J. Hydrol. 219, 56–69. https://doi.org/10.1016/S0022-1694(99)00044-X

Manzocchi, T., Childs, C., Walsh, J.J., 2010. Faults and fault properties in hydrocarbon flow models. Geofluids, 10(1-2), 94-113. https://doi:10.1111/j.1468-8123.2010.00283.x

Manzocchi, T., Walsh, J.J., Nell, P., Yielding, G., 1999. Fault transmissibility multipliers for flow simulation models. Pet. Geosci. 5, 53–63. https://doi.org/10.1144/petgeo.5.1.53

Mariner, R.H., Presser, T.S., Evans, W.C., Pringle, M.K.W., 1990. Discharge rates of fluid and heat by thermal springs of the Cascade Range, Washington, Oregon, and northern California. J. Geophys. Res. 95, 19517–19531. https://doi.org/10.1029/JB095iB12p19517

Marshall, S.K., Cook, P.G., Konikow, L.F., Simmons, C.T., Dogramaci, S., 2020. Conjoint use of hydraulic head and groundwater age data to detect hydrogeologic barriers. Hydrogeol. J. 28, 1003–1019. https://doi.org/10.1007/s10040-019-02095-9

Martínez-Santos, P., Díaz-Alcaide, S., Castaño-Castaño, S., Hernández-Espriú, A., 2014. Modelling discharge through artesian springs based on a high-resolution piezometric network. Hydrol. Process. 28, 2251–2261. https://doi.org/10.1002/hyp.9760

Marty, B., 1995. Nitrogen content of the mantle inferred from N2–Ar correlation in oceanic basalts. Nature 377, 326–329. https://doi.org/10.1038/377326a0

Marty, B., Dauphas, N., 2003. The nitrogen record for crust-mantle interaction and mantle convection from Archean to Present. Earth Planet. Sci. Lett. 206, 397–410. https://doi.org/10.1016/S0012-821X(02)01108-1

Mas-Pla, J., Trilla, J., Valls, M.L., 1992. Radiocarbon dating of travertines precipitated from freshwater. Radiocarbon 34, 677–685. https://doi.org/10.1017/S0033822200063967

Mathon, B.R., Schoonen, M.A., Riccardi, A.L., Borda, M.J., 2015. Measuring flow rates and characterizing flow regimes in hot springs. Appl. Geochemistry 62, 234–246. https://doi.org/10.1016/j.apgeochem.2015.04.007

McCallum, J.L., Noorduijn, S.L., Simmons, C.T., 2021. Including vertical fault structures in layered groundwater flow models. Groundwater, 59(6), 799-807. https://doi:10.1111/gwat.13120

McCallum, J., Simmons, C., Mallants, D., Batelaan, O., 2018. Simulating the groundwater flow dynamics of fault zones: A comparison of methods for representing fault properties and a regional implementation

McMorran, C., 2008. Understanding the "heritage" in heritage tourism: Ideological tool or economic tool for a Japanese hot springs resort? Tour. Geogr. 10, 334–354. https://doi.org/10.1080/14616680802236329

Medici, G., Smeraglia, L., Torabi, A., Botter, C., 2021. Review of Modeling Approaches to Groundwater Flow in Deformed Carbonate Aquifers. Groundwater 59, 334–351. https://doi.org/10.1111/gwat.13069

Meinzer, O.E., 1923. Outline of ground-water hydrology, with definitions.

Merrick, N., 2015. Land Services of Coast and Country Inc. v Adani Mining Pty Ltd. Expert Report to the Land Court by Dr Noel Patrick Merrick. Retrieved from: http://envlaw.com.au/wp-content/uploads/carmichael10.pdf

Meyer, A., Meyer, E.I., 2000. Discharge regime and the effect of drying on macroinvertebrate communities in a temporary karst stream in East Westphalia (Germany). Aquat. Sci. 62, 216–231. https://doi.org/10.1007/PL00001333

Michie, E.A.H., Yielding, G., Fisher, Q.J., 2018. Predicting Transmissibilities of Carbonate-hosted Fault Zones. https://doi:10.1144/SP459.9

Mitchell, T.M., Faulkner, D.R., 2009. The nature and origin of off-fault damage surrounding strike-slip fault zones with a wide range of displacements: A field study from the Atacama fault system, northern Chile. J. Struct. Geol. 31, 802–816. https://doi.org/10.1016/j.jsg.2009.05.002

Moya, C.E., Raiber, M., Taulis, M., Cox, M.E., 2015. Hydrochemical evolution and groundwater flow processes in the galilee and eromanga basins, great artesian Basin, Australia: A multivariate statistical approach. Sci. Total Environ. 508, 411–426. https://doi.org/10.1016/j.scitotenv.2014.11.099

Moya, C.E., Raiber, M., Taulis, M., Cox, M.E., 2016. Using environmental isotopes and dissolved methane concentrations to constrain hydrochemical processes and inter-aquifer mixing in the Galilee and Eromanga Basins, Great Artesian Basin, Australia. J. Hydrol. 539, 304–318. https://doi.org/10.1016/j.jhydrol.2016.05.016

Myers, D.E., 1982. Matrix formulation of Co-Kriging. J. Int. Assoc. Math. Geol. 14, 249–257. https://doi.org/10.1007/BF01032887

Neuman, S.P., 2003. Maximum likelihood Bayesian averaging of uncertain model predictions. Stoch. Environ. Res. Risk Assess. 17, 291–305. https://doi.org/10.1007/s00477-003-0151-7

Neuman, S.P., Wierenga, P.J., 2003. A Comprehensive Strategy of Hydrogeologic Modeling and Uncertainty Analysis for Nuclear Facilities and Sites.

Nikroo, L., Kompani-Zare, M., Sepaskhah, A.R., Fallah Shamsi, S.R., 2010. Groundwater depth and elevation interpolation by kriging methods in Mohr Basin of Fars province in Iran. Environ. Monit. Assess. 166, 387–407. https://doi.org/10.1007/s10661-009-1010-x

Noorduijn, S.L., Cook, P.G., Simmons, C.T., Richardson, S.B., 2018. Protecting groundwater levels and ecosystems with simple management approaches. Hydrogeol. J. 27, 225–237. https://doi.org/10.1007/s10040-018-1849-4

Norton, D.R., Friedman, I., 1985. Chloride flux out of Yellowstone National Park. J. Volcanol. Geotherm. Res. 26, 231–250. https://doi.org/10.1016/0377-0273(85)90058-7

OGIA, 2019. Groundwater Modelling Report – Surat Cumulative Management Area. Brisbane.

OGIA, 2020. Hydrogeological characterisation of faults in the Surat Basin Assessing fault-induced connectivity between the Walloon Coal Measures and adjacent aquifers.

Olarinoye, T., Gleeson, T., Marx, V., Seeger, S., Adinehvand, R., Allocca, V., Andreo, B., Apaéstegui, J., Apolit, C., Arfib, B., Auler, A., Barberá, J.A., Batiot-Guilhe, C., Bechtel, T., Binet, S., Bittner, D., Blatnik, M., Bolger, T., Brunet, P., Charlier, J.B., Chen, Z., Chiogna, G., Coxon, G., De Vita, P., Doummar, J., Epting, J., Fournier, M., Goldscheider, N., Gunn, J., Guo, F., Guyot, J.L., Howden, N., Huggenberger, P., Hunt, B., Jeannin, P.Y., Jiang, G., Jones, G., Jourde, H., Karmann, I., Koit, O., Kordilla, J., Labat, D., Ladouche, B., Liso, I.S., Liu, Z., Massei, N., Mazzilli, N., Mudarra, M., Parise, M., Pu, J., Ravbar, N., Sanchez, L.H., Santo, A., Sauter, M., Sivelle, V., Skoglund, R.Ø., Stevanovic, Z., Wood, C., Worthington, S., Hartmann, A., 2020. Global karst springs hydrograph dataset for research and management of the world's fastest-flowing groundwater. Sci. Data 7, 1–9. https://doi.org/10.1038/s41597-019-0346-5

Ordens, C.M., McIntyre, N., Underschultz, J.R., Ransley, T., Moore, C., Mallants, D., 2020. Preface: Advances in hydrogeologic understanding of Australia's Great Artesian Basin. Hydrogeol. J. 28, 1–11. https://doi.org/10.1007/s10040-019-02107-8

Oreskes, N., Shrader-Frechette, K., Belitz, K., 1994. Verification, Validation, and Confirmation of Numerical Models in the Earth Sciences. Science (80-.). 263, 641–646. https://doi.org/10.1126/science.263.5147.641

Panday, S., Langevin, C.D., Niswonger, R.G., Ibaraki, M., Hughes, J.D., 2017, MODFLOW-USG version 1.4.00: An unstructured grid version of MODFLOW for simulating groundwater flow and tightly coupled processes using a control volume finite-difference formulation: U.S. Geological Survey Software Release, 27 October 2017, https://dx.doi.org/10.5066/F7R20ZFJ

Pardo-Igúzquiza, E., Chica-Olmo, M., 2004. Estimation of gradients from sparse data by universal kriging. Water Resour. Res. 40, 1–17. https://doi.org/10.1029/2004WR003081

Parkhurst, D.L., Appelo, C. a. J., 2013. Description of Input and Examples for PHREEQC Version 3 — A Computer Program for Speciation, Batch-Reaction, One-Dimensional Transport, and Inverse Geochemical Calculations. U.S. Geol. Surv. Tech. Methods, B. 6, chapter A43.

Pebesma, E.J., 2004. Multivariable geostatistics in S: The gstat package. Comput. Geosci. 30, 683–691. https://doi.org/10.1016/j.cageo.2004.03.012

Pebesma, E.J., Graeler, B., 2020. Gstat User Manual.

Peeters, L., Fasbender, D., Batelaan, O., Dassargues, A., 2010. Bayesian data fusion for water table interpolation: Incorporating a hydrogeological conceptual model in kriging. Water Resour. Res. 46, 1–11. https://doi.org/10.1029/2009WR008353

Peeters, L., Ransley, T., Turnadge, C., Kellett, J., Harris-Pascal, C., Kilgour, P., Evans, T., 2018. Groundwater numerical modelling for the Galilee subregion. Product 2.6.2 for the Galilee subregion from the Lake Eyre Basin Bioregional Assessment.

Philip, R.D., Kitanidis, P.K., 1989. Geostatistical Estimation of Hydraulic Head Gradients. Ground Water 27, 855–865. https://doi.org/10.1111/j.1745-6584.1989.tb01049.x

Philip, G.M., Watson, D.F., 1986. Automatic interpolation methods for mapping piezometric surfaces. Automatica 22, 753–756. https://doi.org/10.1016/0005-1098(86)90016-6

Piper, A.M., 1944. A graphic procedure in the geochemical interpretation of water-analyses. Trans. Am. Geophys. Union 25, 914. https://doi.org/10.1029/TR025i006p00914

Ponder, W., 1986. Mound Springs of the Great Artesian Basin, in: Limnology in Australia.

Ponder, W., Colgan, D., 2002. What makes a narrow-range taxon? Insights from Australian freshwater snails. Invertebr. Syst. 16, 571–582.

Porter, J., Kingsford, R., Hunter, S., 2006. Aerial surveys of wetland birds in Eastern Australia - October 2003-2005.

Post, V.E.A., von Asmuth, J.R., 2013. Review: Hydraulic head measurements—new technologies, classic pitfalls. Hydrogeol. J. 21, 737–750. https://doi.org/10.1007/s10040-013-0969-0

Poulet, T., Lesueur, M., Kelka, U., 2021. Dynamic modelling of overprinted low-permeability fault cores and surrounding damage zones as lower dimensional interfaces for multiphysics simulations. Comput. Geosci. 150. https://doi.org/10.1016/j.cageo.2021.104719

Priestley, S.C., Karlstrom, K.E., Love, A.J., Crossey, L.J., Polyak, V.J., Asmerom, Y., Meredith, K.T., Crow, R., Keppel, M.N., Habermehl, M.A., 2018. Uranium series dating of Great Artesian Basin travertine deposits: Implications for palaeohydrogeology and palaeoclimate. Palaeogeogr. Palaeoclimatol. Palaeoecol. 490, 163–177. https://doi.org/10.1016/j.palaeo.2017.10.024

Qian, J.Z., Wang, M., Zhang, Y., Yan, X.S., Zhao, W.D., 2015. Experimental study of the transition from non-Darcian to Darcy behavior for flow through a single fracture. J. Hydrodyn. 27, 679–688. https://doi.org/10.1016/S1001-6058(15)60530-3

Quay, A., Hering, A.S., Mauter, M.S., 2020. Quantifying uncertainty in groundwater depth from sparse well data in the California Central Valley. Environ. Res. Lett. https://doi.org/10.1088/1748-9326/ab88fb

Quinn, P.M., Cherry, J.A., Parker, B.L., 2020. Relationship between the critical Reynolds number and aperture for flow through single fractures: Evidence from published laboratory studies. J. Hydrol. 581, 124384. https://doi.org/10.1016/j.jhydrol.2019.124384

Raiber, M., Webb, J.A., Bennetts, D.A., 2009. Strontium isotopes as tracers to delineate aquifer interactions and the influence of rainfall in the basalt plains of southeastern Australia. J. Hydrol. 367, 188–199. https://doi.org/10.1016/j.jhydrol.2008.12.020

Rasmussen, C., Williams, K., 2006. Gaussian Processes for Machine Learning. MIT Press.

Rau, G.C., Post, V.E.A., Shanafield, M., Krekeler, T., Banks, E.W., Blum, P., 2019. Error in hydraulic head and gradient time-series measurements: A quantitative appraisal. Hydrol. Earth Syst. Sci. 23, 3603–3629. https://doi.org/10.5194/hess-23-3603-2019

Reimann, T., Rehrl, C., Shoemaker, W.B., Geyer, T., Birk, S., 2011. The significance of turbulent flow representation in single-continuum models. Water Resour. Res. 47, 1–15. https://doi.org/10.1029/2010WR010133

Revil, A., Karaoulis, M., Johnson, T., Kemna, A., 2012. Review: Some low-frequency electrical methods for subsurface characterization and monitoring in hydrogeology. Hydrogeol. J. 20, 617–658. https://doi.org/10.1007/s10040-011-0819-x

Rexer, M., Hirt, C., 2014. Comparison of free high resolution digital elevation data sets (ASTER GDEM2, SRTM v2.1/v4.1) and validation against accurate heights from the Australian National Gravity Database. Aust. J. Earth Sci. 61, 213–226. https://doi.org/10.1080/08120099.2014.884983

Robinson, N.I., Werner, A.D., 2017. On concentrated solute sources in faulted aquifers. Adv. Water Resour. 104, 255–270. https://doi.org/10.1016/j.advwatres.2017.04.008

Rolfe, J.C., Blamey, R.K., Bennett, J.W., 1997. Remnant Vegetation and Broadscale Tree Clearing in the Desert Uplands Region of Queensland - Choice Modelling Research Reports No. 3.

Romano, V., Bigi, S., Carnevale, F., De'Haven Hyman, J., Karra, S., Valocchi, A.J., Tartarello, M.C., Battaglia, M., 2020. Hydraulic characterization of a fault zone from fracture distribution. J. Struct. Geol. 135, 104036. https://doi.org/10.1016/j.jsg.2020.104036

Romano, V., De'Haven Hyman, J., Karra, S., Valocchi, A.J., Battaglia, M., Bigi, S., 2017. Numerical modeling of fluid flow in a fault zone: A case of study from Majella Mountain (Italy). Energy Procedia 125, 556–560. https://doi.org/10.1016/j.egypro.2017.08.191

Rossini, R.A., Fensham, R.J., Stewart-Koster, B., Gotch, T., Kennard, M.J., 2018. Biogeographical patterns of endemic diversity and its conservation in Australia's artesian desert springs. Divers. Distrib. 24, 1199–1216. https://doi.org/10.1111/ddi.12757

Rowland, J.C., Manga, M., Rose, T.P., 2008. The influence of poorly interconnected fault zone flow paths on spring geochemistry. Geofluids 8, 93–101. https://doi.org/10.1111/j.1468-8123.2008.00208.x

Saar, M.O., 2011. Review: Geothermal heat as a tracer of large-scale groundwater flow and as a means to determine permeability fields. Hydrogeol. J. 19, 31–52. https://doi.org/10.1007/s10040-010-0657-2

Saar, M.O., Manga, M., 2004. Depth dependence of permeability in the Oregon Cascades inferred from hydrogeologic, thermal, seismic, and magmatic modeling constraints. J. Geophys. Res. Solid Earth 109, 1–19. https://doi.org/10.1029/2003JB002855

Saito, H., Goovaerts, P., 2002. Accounting for measurement error in uncertainty modeling and decision-making using indicator kriging and p-field simulation: application to a dioxin contaminated site. Environmetrics 13, 555–567. https://doi.org/10.1002/env.545

Sakai, H., Matsubaya, O., 1974. Isotopic geochemistry of the thermal waters of Japan and its bearing on the Kuroko ore solutions. Econ. Geol. 69, 974–991.

https://doi.org/10.2113/gsecongeo.69.6.974

Salama, R.B., Ye, L., Broun, J., 1996. Comparative study of methods of preparing hydraulic-head surfaces and the introduction of automated hydrogeological-GIS techniques. J. Hydrol. 185, 115–136. https://doi.org/10.1016/0022-1694(95)03004-2

Saller, S.P., Ronayne, M.J., Long, A.J., 2013. Comparison of a karst groundwater model with and without discrete conduit flow. Hydrogeol. J. 21, 1555–1566. https://doi.org/10.1007/s10040-013-1036-6

Sato, T., Sakai, R., Furuya, K., Kodama, T., 2000. Coseismic spring flow changes associated with the 1995 Kobe Earthquake. Geophys. Res. Lett. 27, 1219–1222. https://doi.org/10.1029/1999GL011187

Scanlon, B.R., Mace, R.E., Barrett, M.E., Smith, B., 2003. Can we simulate regional groundwater flow in a karst system using equivalent porous media models? Case study, Barton Springs Edwards aquifer, USA. J. Hydrol. 276, 137–158. https://doi.org/10.1016/S0022-1694(03)00064-7

Scibek, J., 2020. Multidisciplinary database of permeability of fault zones and surrounding protolith rocks at world-wide sites. Sci. Data 7, 1–14. https://doi.org/10.1038/s41597-020-0435-5

Scibek, J., Gleeson, T., McKenzie, J.M., 2016. The biases and trends in fault zone hydrogeology conceptual models: global compilation and categorical data analysis. Geofluids 16, 782–798. https://doi.org/10.1111/gfl.12188

Sebben, M.L., Werner, A.D., 2016b. On the effects of preferential or barrier flow features on solute plumes in permeable porous media. Adv. Water Resour. 98, 32–46.

https://doi.org/10.1016/j.advwatres.2016.10.011

Segadelli, S., Filippini, M., Monti, A., Celico, F., Gargini, A., 2021. Estimation of recharge in mountain hard-rock aquifers based on discrete spring discharge monitoring during base-flow recession. Hydrogeol. J. 29, 949–961.

Shoemaker, W.B., Kuniansky, E.L., Birk, S., Bauer, S., Swain, E.D., 2008. Documentation of a Conduit Flow Process (CFP) for MODFLOW-2005 A product of the Ground-Water Resources Program. U.S. Geol. Surv. Techniques, 50.

Siegel, D., 2008. Reductionist hydrogeology: ten fundamental principles. Hydrol. Process. 22, 4967–4970. https://doi.org/10.1002/hyp.7139

Silcock, J.L., Tischler, M.K., Fensham, R.J., 2020. Oases at the gates of hell: Hydrogeology, cultural history and ecology of the mulligan river springs, far western queensland. Proc. R. Soc. Queensl. 126, 91–108.

López, D.L., Smith, L., 1995. Fluid Flow in Fault Zones: Analysis of the Interplay of Convective Circulation and Topographically Driven Groundwater Flow. Water Resour. Res. 31, 1489–1503. https://doi.org/10.1029/95WR00422

López, D.L., Smith, L., 1996. Fluid flow in fault zones: Influence of hydraulic anisotropy and heterogeneity on the fluid flow and heat transfer regime. Water Resour. Res. 32, 3227–3235. https://doi.org/10.1029/96WR02101

Smith, H., Wood, P.J., Gunn, J., 2003. The influence of habitat structure and flow permanence on invertebrate communities in karst spring systems. Hydrobiologia 510, 53–66. https://doi.org/10.1023/B:HYDR.0000008501.55798.20

Solak, E., Murray-Smith, R., Leithead, W.E., Leith, D.J., Rasmussen, C.E., 2003.

Derivative observations in Gaussian Process Models of Dynamic Systems. Adv. Neural Inf. Process. Syst.

Springer, A.E., Stevens, L.E., 2009. Spheres of discharge of springs. Hydrogeol. J. 17, 83–93. https://doi.org/10.1007/s10040-008-0341-y

Stewart, J., 2010. Multivariable Calculus, 7th ed.

Swanson, S.K., Bahr, J.M., 2004. Analytical and numerical models to explain steady rates of spring flow. Ground Water 42, 747–759. https://doi.org/10.1111/j.1745-6584.2004.tb02728.x

Taillefer, A., Soliva, R., Guillou-Frottier, L., Goff, E. Le, Martin, G., Seranne, M., 2017. Fault-related controls on upward hydrothermal flow: An integrated geological study of the têt fault system, Eastern Pyrénées (France). Geofluids 2017. https://doi.org/10.1155/2017/8190109

Taylor, C.J., Greene, E., 2005. Hydrogeologic Characterization and Methods Used in the Investigation of Karst Hydrology. F. Tech. Estim. Water Fluxes Between Surf. Water Gr. Water 75–114.

The Department of State Development, 2018. China Stone Coal project Coordinator-General's evaluation report on the environmental impact statement.

Thomann, J.A., Werner, A.D., Irvine, D.J., Currell, M.J., 2020. Adaptive management in groundwater planning and development: A review of theory and applications. J. Hydrol. 586, 124871. https://doi.org/10.1016/j.jhydrol.2020.124871

Torabi, A., Johannessen, M.U., Ellingsen, T.S.S., 2019. Fault core thickness: Insights from siliciclastic and carbonate rocks. Geofluids 2019.

https://doi.org/10.1155/2019/2918673

Trimble Navigation Limited, 2014. Trimble R10 Datasheet.

Turnadge, C., Mallants, D., Peeters, L., 2016. Aquitard and Fault Simulation Approaches for Use in Regional-Scale Assessments of Coal Seam Gas Extraction Impacts, in: SPE Asia Pacific Oil & Gas Conference and Exhibition. SPE, Perth. https://doi.org/10.2118/182463-MS

Turnadge, C., Mallants, D., Peeters, L., 2018. Overview of aquitard and geological fault simulation approaches in regional scale assessments of coal seam gas extraction impacts, prepared by the Commonwealth Scientific and Industrial Research Organisation (CSIRO), Canberra.

Uner, S., Dogan, D. D., 2021. An integrated geophysical, hydrological, thermal approach to finite volume modelling of fault-controlled geothermal fluid circulation in Gediz Graben. Geothermics, 90. https://doi:10.1016/j.geothermics.2020.102004

Vandersteen, G., Schneidewind, U., Anibas, C., Schmidt, C., Seuntjens, P., Batelaan, O., 2015. Determining groundwater-surface water exchange from temperature-time series: Combining a local polynomial method with a maximum likelihood estimator. Water Resour. Res. 51, 922–939. https://doi.org/10.1002/2014WR015994

Varouchakis, .A., Hristopulos, D.T., 2013. Comparison of stochastic and deterministic methods for mapping groundwater level spatial variability in sparsely monitored basins. Environ. Monit. Assess. 185, 1–19. https://doi.org/10.1007/s10661-012-2527-y

Varouchakis, E.A., Theodoridou, P.G., Karatzas, G.P., 2020. Decision-Making Tool for

Groundwater Level Spatial Distribution and Risk Assessment Using Geostatistics in R. J. Hazardous, Toxic, Radioact. Waste 24. https://doi.org/10.1061/(ASCE)HZ.2153-5515.0000464

Volatili, T., Zambrano, M., Cilona, A., Huisman, B.A.H., Rustichelli, A., Giorgioni, M., Vittori, S., Tondi, E., 2019. From fracture analysis to flow simulations in fractured carbonates: The case study of the Roman Valley Quarry (Majella Mountain, Italy). Marine and Petroleum Geology, 100, 95-110. https://doi:10.1016/j.marpetgeo.2018.10.040

Wackernagel, H., 1995. Geostatistics, in: Multivariate Geostatistics. Springer Berlin Heidelberg, Berlin, Heidelberg, pp. 74–81. https://doi.org/10.1007/978-3-662-03098-1_11

Wangan and Jagalingou Family Council, 2015. Submission to the United Nations Special Rapporteur of the rights of indigenous peoples.

Weatherill, D., Graf, T., Simmons, C.T., Cook, P.G., Therrien, R., Reynolds, D.A., 2008. Discretizing the fracture-matrix interface to simulate solute transport. Ground Water 46, 606–615. https://doi.org/10.1111/j.1745-6584.2007.00430.x

Webb, J.A., 2015. Adani Mining Pty Ltd vs. Land Services of Coast and Country Inc & Ors, Expert report on groundwater impacts. Retrieved from: http://envlaw.com.au/wp-content/uploads/carmichael9.pdf

Werner, A.D., Alcoe, D.W., Ordens, C.M., Hutson, J.L., Ward, J.D., Simmons, C.T., 2011. Current Practice and Future Challenges in Coastal Aquifer Management: Flux-Based and Trigger-Level Approaches with Application to an Australian Case Study. Water Resour. Manag. 25, 1831–1853. https://doi.org/10.1007/s11269-011-9777-2

Werner, A.D., Love, A.J., Irvine, D.J., Banks, E.W., Cartwright, I., Webb, J.A., Currell, M.J., 2019. Position Paper by Concerned Scientists - Deficiencies in the scientific assessment of the Carmichael Mine impacts to the Doongmabulla Springs. Retrieved from: https://dspace.flinders.edu.au/xmlui/handle/2328/39203?show=full

White, D.C., Lewis, M.M., 2011. A new approach to monitoring spatial distribution and dynamics of wetlands and associated flows of Australian Great Artesian Basin springs using QuickBird satellite imagery. J. Hydrol. 408, 140–152. https://doi.org/10.1016/j.jhydrol.2011.07.032

White, D.C., Lewis, M.M., Green, G., Gotch, T.B., 2016. A generalizable NDVI-based wetland delineation indicator for remote monitoring of groundwater flows in the Australian Great Artesian Basin. Ecol. Indic. 60, 1309–1320. https://doi.org/10.1016/j.ecolind.2015.01.032

Williams, A.F., Holmes, J.W., 1978. A novel method of estimating the discharge of water from mound springs of the Great Artesian Basin, central Australia. J. Hydrol. 38, 263–272. https://doi.org/10.1016/0022

Williams, B.K., Szaro, R.C., Shapiro, C.D., 2009. Adaptive management: The U.S. Department of the Interior technical guide. Washington, D.C.

Wilson, P., Smith, S., Povey, D., Harris, S., 2020. Ranking and selecting fault models using flow-indicator fault properties and simple streamline simulations. Petroleum Geoscience, 27(2). https://doi:10.1144/petgeo2020-017

Wing, M.G., Frank, J., 2011. Vertical measurement accuracy and reliability of mapping-grade GPS receivers. Comput. Electron. Agric. 78, 188–194. https://doi.org/10.1016/j.compag.2011.07.006

Witherspoon, P.A., Wang, J.S.Y., Iwai, K., Gale, J.E., 1980. Validity of Cubic Law for fluid flow in a deformable rock fracture. Water Resour. Res. 16, 1016–1024. https://doi.org/10.1029/WR016i006p01016

Woith, H., Barbosa, S., Gajewski, C., Steinitz, G., Piatibratova, O., Malik, U., Zschau, J., 2011. Periodic and transient radon variations at the Tiberias hot spring, Israel during 2000-2005. Geochem. J. 45, 473–482. https://doi.org/10.2343/geochemj.1.0147

Wolaver, B.D., Diehl, T.M., 2011. Control of regional structural styles and faulting on Northeast Mexico spring distribution. Environ. Earth Sci. 62, 1535–1549. https://doi.org/10.1007/s12665-010-0639-7

Wolaver, B.D., Priestley, S.C., Crossey, L.J., Karlstrom, K.E., Love, A.J., 2020. Elucidating sources to aridland Dalhousie Springs in the Great Artesian Basin (Australia) to inform conservation. Hydrogeol. J. 28, 279–296. https://doi.org/10.1007/s10040-019-02072-2

Wood, P.J., Gunn, J., Smith, H., Abas-Kutty, A., 2005. Flow permanence and macroinvertebrate community diversity within groundwater dominated headwater streams and springs. Hydrobiologia 545, 55–64. https://doi.org/10.1007/s10750-005-2213-y

Wu, Q., Xing, L.T., Ye, C.H., Liu, Y.Z., 2011. The influences of coal mining on the large karst springs in North China. Environ. Earth Sci. 64, 1513–1523. https://doi.org/10.1007/s12665-009-0376-y

Xue, Y., Liu, Y., Dang, F., Liu, J., Ma, Z., Zhu, L., Yang, H., 2019. Assessment of the nonlinear flow characteristic of water inrush based on the Brinkman and Forchheimer seepage model. Water 11, 855. https://doi.org/10.3390/w11040855

Yager, R.M., Plummer, L.N., Kauffman, L.J., Doctor, D.H., Nelms, D.L., Schlosser, P., 2013. Comparison of age distributions estimated from environmental tracers by using binary-dilution and numerical models of fractured and folded karst: Shenandoah Valley of Virginia and West Virginia, USA. Hydrogeol. J. 21, 1193–1217. https://doi.org/10.1007/s10040-013-0997-9

Yamamoto, J.K., 2005. Correcting the Smoothing Effect of Ordinary Kriging Estimates. Math. Geol. 37, 69–94. https://doi.org/10.1007/s11004-005-8748-7

Yeh, T.C.J., Lee, C.H., 2007. Time to change the way we collect and analyze data for aquifer characterization. Ground Water 45, 116–118. https://doi.org/10.1111/j.1745-6584.2006.00292.x

Yeh, T.C.J., Lee, C.H., Hsu, K.C., Illman, W.A., Barrash, W., Cai, X., Daniels, J., Sudicky, E., Wan, L., Li, G., Winter, C.L., 2008. A view toward the future of subsurface characterization: CAT scanning groundwater basins. Water Resour. Res. 44, 1–9. https://doi.org/10.1029/2007WR006375

Zha, Y., Yeh, T.C.J., Illman, W.A., Tanaka, T., Bruines, P., Onoe, H., Saegusa, H., Mao, D., Takeuchi, S., Wen, J.C., 2016. An Application of Hydraulic Tomography to a Large-Scale Fractured Granite Site, Mizunami, Japan. Groundwater 54, 793–804. https://doi.org/10.1111/gwat.12421

Zhang, Z., Chen, Xi, Chen, Xunhong, Shi, P., 2013. Quantifying time lag of epikarst-spring hydrograph response to rainfall using correlation and spectral analyses. Hydrogeol. J. 21, 1619–1631. https://doi.org/10.1007/s10040-013-1041-9

Zheng, X., Yang, Z., Wang, S., Chen, Y.F., Hu, R., Zhao, X.J., Wu, X.L., Yang, X.L., 2021. Evaluation of hydrogeological impact of tunnel engineering in a karst aquifer by

coupled discrete-continuum numerical simulations. J. Hydrol. 597, 125765.
https://doi.org/10.1016/j.jhydrol.2020.125765

APPENDICES

Appendix A. Hydraulic head probabilities

Table A1
Probabilities of hydraulic head less than or equal to selected thresholds in the Triassic Formations at the locations of springs A to H. Values that have had order-relation corrections applied are followed by the original value in brackets.

Thresholds (m)	Spring ID (SGT in m)							
	A (237.5)	B (238.0)	C (238.0)	D (238.4)	E (240.5)	F (242.8)	G (239.4)	H (235.7)
226.9	0.0(−0.01)	0.0(−0.02)	0.0(−0.02)	0.0(−0.02)	0.0(−0.02)	0.0(−0.01)	0.0(−0.02)	0.0(0.02)
232.8	0.08	0.01	0.01	0.02	0.0(−0.01)	0.02	0.0(−0.02)	0.26
235.5	0.35	0.28	0.28	0.29	0.27	0.27	0.24	0.5
237.5	0.59	0.59	0.59	0.59	0.53	0.58	0.58	0.59
238	0.66	0.67	0.67	0.67	0.59	0.64	0.65	0.63
238.5	0.76	0.79	0.79	0.79	0.68	0.74	0.77	0.68
238.7	0.79	0.83	0.83	0.83	0.71	0.78	0.81	0.7
239.5	0.91	0.98	0.98	0.98	0.83	0.91	0.97	0.75
240.5	0.96	1.0(1.05)	1.0(1.05)	1.0(1.05)	0.89	0.99	1.0(1.05)	0.77
243	1	1	1	1	0.99	1.0(1.02)	1	1.0(1.01)
244.6	1.0(1.02)	1.0(0.99)	1.0(0.99)	1	1.0(1.04)	1.0(1.04)	1.0(0.99)	1.0(1.11)
248.7	1.0(1.01)	1.0(1.03)	1.0(1.02)	1.0(1.02)	1.0(0.94)	1.0(0.9)	1	1
252.1	1.0(0.99)	1.0(0.99)	1.0(0.99)	1.0(0.99)	1.0(0.96)	1.0(0.93)	1.0(0.98)	1.0(0.99)
266.4	1.0(0.96)	1.0(0.96)	1.0(0.96)	1.0(0.96)	1.0(0.96)	1.0(0.96)	1.0(0.96)	1.0(0.97)
272.2	1.0(0.93)	1.0(0.92)	1.0(0.93)	1.0(0.93)	1.0(0.95)	1.0(0.95)	1.0(0.93)	1.0(0.95)
285.4	1	1.0(1.01)	1.0(1.01)	1	1	1	1.0(1.01)	1

Table A2
Probabilities of hydraulic head less than or equal to selected thresholds in the Permian Formations at the locations of springs A to H. Values that have had order-relation corrections applied are followed by the original value in brackets.

Thresholds (m)	Spring ID (SGT in m)							
	A (237.5)	B (238.0)	C (238.0)	D (238.4)	E (240.5)	F (242.8)	G (239.4)	H (235.7)
209.2	0.0(0.01)	0.0(0.01)	0.0(0.01)	0	0.0(0.02)	0.0(0.01)	0.0(0.01)	0.0(0.02)
212.3	0.0(0.01)	0.0(0.01)	0.0(0.01)	0.0(0.01)	0.02(0.04)	0.0(0.03)	0.0(0.02)	0.03(0.04)
216.5	0.0(−0.02)	0.0(−0.03)	0.0(−0.03)	0.0(−0.03)	0.02(0.01)	0	0.0(−0.02)	0.03(0.01)
225	0.07	0.06	0.06	0.06	0.13	0.12	0.08	0.13
228.1	0.29	0.26	0.26	0.26	0.31	0.29	0.26	0.4
230.9	0.57	0.53	0.53	0.53	0.52	0.5	0.51	0.67
232.5	0.79	0.75	0.75	0.76	0.72	0.7	0.72	0.85
235.5	0.92	0.88	0.88	0.89	0.83	0.81	0.84	0.96
237.5	0.94	0.9	0.9	0.91	0.85	0.83	0.86	0.98
238	0.94	0.9	0.91	0.91	0.85	0.83	0.87	0.98
238.5	0.95	0.91	0.91	0.91	0.85	0.83	0.87	0.98
239.5	0.96	0.92	0.92	0.92	0.87	0.85	0.89	0.99
240.5	0.97	0.94	0.94	0.95	0.92	0.9	0.92	1
241.2	0.98	0.96	0.96	0.96	0.97(0.98)	0.97	0.96	1.0(1.01)
243	0.98	0.97	0.97	0.97	0.97	0.97(0.96)	0.96	1
249.6	1.0(0.99)	1.0(0.98)	1.0(0.98)	1.0(0.98)	1.0(0.96)	1.0(0.95)	1.0(0.96)	1

Appendix B. Supplementary Materials

Supplementary Materials can be found online with the published version of this work at https://doi.org/10.1016/j.jhydrol.2021.126808.

Appendix C. Supporting Materials

Supporting Materials are provided online at https://doi.org/10.6084/m9.figshare.20746075.v1

Appendix D. Supporting Materials

Supporting Materials are provided online at https://doi.org/10.6084/m9.figshare.21716636.v1

Appendix E. Publications

Earth-Science Reviews 230 (2022) 104058

Contents lists available at ScienceDirect

Earth-Science Reviews

journal homepage: www.elsevier.com/locate/earscirev

Fault-controlled springs: A review

Robin Keegan-Treloar [a,b], Dylan J. Irvine [c,b,a,*], S. Cristina Solórzano-Rivas [a,b], Adrian D. Werner [a,b], Eddie W. Banks [a,b], Matthew J. Currell [d,b]

[a] *College of Science and Engineering, Flinders University, Adelaide, Australia*
[b] *National Centre for Groundwater Research and Training, Adelaide, Australia*
[c] *Research Institute for the Environment and Livelihoods, Charles Darwin University, Darwin, Australia*
[d] *School of Engineering, RMIT University, Melbourne, Australia*

ARTICLE INFO

Keywords:
Groundwater-dependent ecosystems
Discrete fracture network
Preferential flow
Geological structure
Spring discharge
Groundwater management
Numerical modelling

ABSTRACT

Springs sustain groundwater-dependent ecosystems and provide freshwater for human use. Springs often occur because faults modify groundwater flow pathways leading to discharge from aquifers with sufficiently high pressure. This study reviews the key characteristics and physical processes, field investigation techniques, modelling approaches and management strategies for fault-controlled spring systems. Field investigation techniques suitable for quantifying spring discharge and fault characteristics are often restricted by high values of spring ecosystems, requiring mainly non-invasive techniques. Numerical models of fault-controlled spring systems can be divided into local-scale, process-based models that allow the damage zone and fault core to be distinguished, and regional-scale models that usually adopt highly simplified representations of both the fault and the spring. Water resources management relating to fault-controlled spring systems often involves ad hoc applications of trigger levels, even though more sophisticated management strategies are available. Major gaps in the understanding of fault-controlled spring systems create substantial risks of degradation from human activities, arising from limited data and process understanding, and simplified representations in models. Thus, further studies are needed to improve the understanding of hydrogeological processes, including through detailed field studies, physics-based modelling, and by quantifying the effects of groundwater withdrawals on spring discharge.

1. Introduction

Springs often sustain highly productive and diverse aquatic and terrestrial ecosystems (Bogan et al., 2014; Davis et al., 2017). Where springs are spatially isolated, 'ecological islands' can form (Bogan et al., 2014), providing habitats for endemic species to develop and evolve to the unique spring conditions (Davis et al., 2017). In the case of arid and semi-arid regions, springs may provide the only permanent source of water for significant distances, allowing for the survival of rare plants and a broad range of animal species (Springer and Stevens, 2009). Many ecologically and culturally significant spring complexes have been altered over the last century, attributable mainly to human-induced changes to groundwater regimes (Davis et al., 2017).

Springs occur under a variety of hydrogeological conditions, commonly due to geological features that create transmissive pathways or barriers to flow (Bryan, 1919; Curewitz and Karson, 1997; Rowland et al., 2008). These geological features include faults, which are planar fractures or discontinuities in rock where displacement has occurred (Caine et al., 1996; Bense et al., 2013). Faults may impede and/or act as preferential pathways to groundwater flow (Forster and Evans, 1991; Caine et al., 1996; Bense et al., 2013). Bryan (1919) and Meinzer (1923) define five spring types based on their subsurface geology (contact springs, fissure/fault springs, depression springs, tubular or fracture springs and volcanic springs), of which, contact springs and fissure/fault springs often occur due to faults (see Fig. 1). Springer and Stevens (2009) developed a revised inventory of 12 spring conceptual models, of which five include geological faults. Curewitz and Karson (1997) reviewed the structural settings of hot springs and found that 78% of the 822 hot springs inventoried were associated with faults. Although the review was specific to hot springs, there is evidence from case studies that other spring types (e.g., cooler 16–25 °C springs, acid sulphate springs, bubbling CO_2 springs) are commonly associated with faults (e.g., Bignall and Browne, 1994; Battani et al., 2010; Apollaro et al., 2012).

The properties of faults and the associated hydrogeological processes

* Corresponding author at: Research Institute for the Environment and Livelihoods, Charles Darwin University, Darwin, Australia.
E-mail address: dylan.irvine@cdu.edu.au (D.J. Irvine).

https://doi.org/10.1016/j.earscirev.2022.104058
Received 16 December 2021; Received in revised form 11 April 2022; Accepted 15 May 2022
Available online 21 May 2022

have been extensively reviewed (e.g., Forster and Evans, 1991; Caine et al., 1996; Bense et al., 2013; Scibek et al., 2016), as has the hydrology of springs (e.g., Meinzer, 1923; Hynes, 1970; van der Kamp, 1995; Springer and Stevens, 2009; Kresic, 2010). While faults and springs have been reviewed independently, their hydrogeological interrelation has received little attention, and the current understanding of fault-controlled spring systems is based primarily on a review of the structural settings of hot springs by Curewitz and Karson (1997) and case studies (e.g., Jewell et al., 1994; Crossey et al., 2006; Rowland et al., 2008).

This review draws on existing literature on faults and springs to establish the current state of knowledge on fault-controlled spring systems. Although the review is based primarily on case studies of fault-controlled spring systems, some of the approaches discussed can be generalised to studies of faults or springs (e.g., the methods described to quantify spring discharge in Section 3.1 are similar for fault-controlled springs and other spring types). The following aspects of fault-controlled spring systems are reviewed: (1) hydrogeological processes; (2) field investigation techniques; (3) numerical modelling; and (4) management. Finally, we outline major knowledge gaps and future research directions required to improve the protection and reliable characterisation of fault-controlled spring systems, particularly those threatened by groundwater-affecting activities.

2. Hydrogeological processes

Here, the hydrogeological processes associated with the occurrence of springs that source water from groundwater flow through faults are subdivided into: (1) fault characteristics, (2) spring and aquifer hydraulics, and (3) surface conditions and spring environments.

2.1. Fault characteristics

Faults are classified based on their angle relative to the horizontal (i.e., dip) and the relative displacement of rock on either side of the fault plane (i.e., slip) (Bense et al., 2013). There are three main classes of faults (Fig. 2). Normal faults (Fig. 2a) occur due to extensional stresses, generally leading to dips of 45–70° relative to the horizontal, although in some cases (e.g., when associated with metamorphic core complexes), normal faults can have dips at lower angles (e.g., Faulds and Varga, 1998; Faulds et al., 2008). Reverse (or thrust) faults (Fig. 2b) occur due

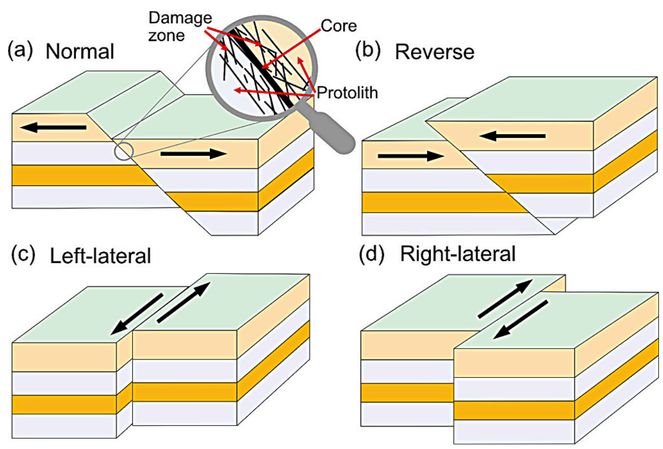

Fig. 2. Conceptual diagrams of fault classes showing: (a) normal, (b) reverse, (c) left-lateral strike-slip and (d) right-lateral strike-slip faults (stress directions indicated by black arrows). The inset shows the fault core, damage zone and protolith.

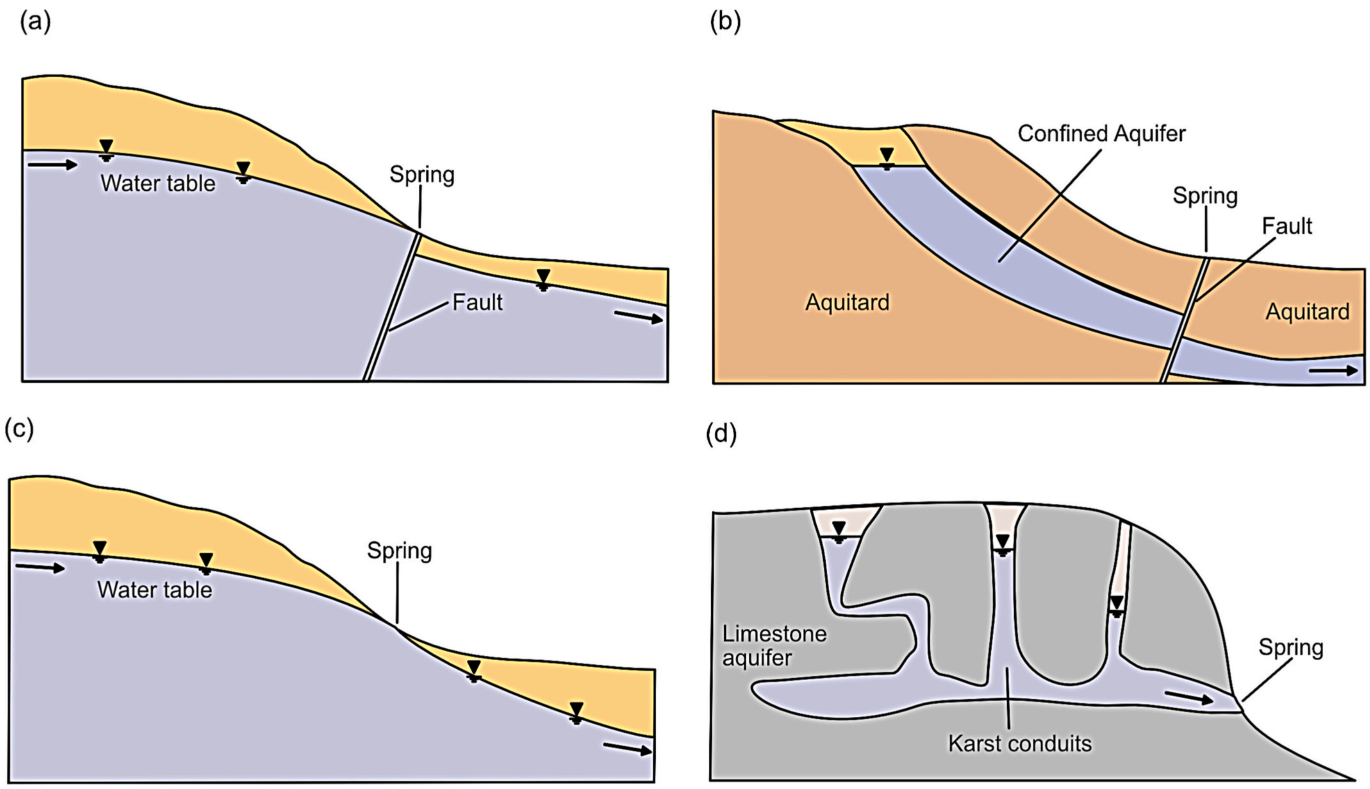

Fig. 1. Spring conceptual models for four of the spring types described by Meinzer (1923) showing: (a) a contact spring where the water table outcrops along a fault, (b) a fissure/fault spring where a fault provides a conduit for flow from a confined aquifer, (c) a depression spring where the water table intersects the surface and (d) a tubular or fracture spring where water flows through karst conduits and discharges through an orifice at lower elevation. Volcanic springs are not shown as these are typically associated with the formation of steam and have varying geological/hydraulic characteristics.

to compressional stresses, causing dips generally <<45° (Bense et al., 2013). Both normal (Fig. 2a) and reverse faults (Fig. 2b) have near-vertical slips (displacement of rock on one side of the fault relative to the other). Strike-slip faults (Fig. 2c and d) have vertical (or near-vertical) dips, with horizontal slips (Bense et al., 2013). They are classified as either left-lateral or right-lateral, based on whether the displacement is to the left (Fig. 2c) or the right (Fig. 2d) when viewed from either side. Additionally, faults can be a combination of the aforementioned four classes. For example, normal oblique-slip faults, which have been associated with hot springs (e.g., La Rosa et al., 2019), have components of both normal and strike-slip faults. The type of fault and its stress regime influence the fault permeability (e.g., extensional stresses can increase permeability). However, the fault permeability is also strongly influenced by the rock type and the fault architecture (Caine et al., 1996). This prevents the use of generic permeability models based only on the fault classification (Bense and Van Balen, 2004).

Conceptually, the fault architecture is represented using a three-component model comprising the fault core, the damage zone and the protolith (Caine et al., 1996; Mitchell and Faulkner, 2009) (Fig. 2a). The fault core is where most of the displacement has occurred, comprising deformed materials such as gouge, cataclasite, breccia and/or smear (Caine et al., 1996; Torabi et al., 2019). The damage zone surrounds the fault core and features secondary structures such as micro- or macro-fractures arising from slip and/or deformation events (Caine et al., 1996). The protolith is the surrounding material that has not been substantially modified by faulting (Bense et al., 2013).

Whether the fault acts as a barrier and/or a conduit to flow depends on its composition and the stage of fault evolution (Caine et al., 1996). For example, the core may act as a conduit immediately following deformation and later as a barrier due to the precipitation of minerals (Caine et al., 1996). Fluid flow in the damage zone is typically higher than in the fault core or protolith, occurring predominantly through fractures (e.g., Bense and Person, 2006; Folch and Mas-Pla, 2008). For example, the dataset of fault permeabilities compiled by Scibek (2020) indicate that the permeability of the damage zone is on average two orders of magnitude greater than the fault core.

The hydrogeologic behaviour of faults has been characterised in terms of the fault architecture by Caine et al. (1996), who suggested three quantitative indices:

$$F_a = W_{dz}/(W_{dz} + W_{core}) \tag{1}$$

$$F_m = mean(F_a) \tag{2}$$

$$F_s = max(F_a) - min(F_a) \tag{3}$$

Where F_a represents the relative proportion of the damage zone present in the fault, with values that vary from zero to one, W_{dz} is the damage zone width (m), and W_{core} is the core width (m). F_m is the mean of spatial variations in F_a for a given fault, and F_s is the range in F_a values for a given fault. As the damage zone is typically considered of higher permeability relative to the fault core, F_a values close to one indicate that the fault is likely to behave as a conduit to flow, whereas F_a values close to zero indicate that the fault is likely to act as a barrier (Caine et al., 1996). F_a can be calculated parallel and/or perpendicular to the fault, wherever measurements are available, to assess the relative proportions of the spatial extent of the damage zone. As W_{dz} and W_{core} can vary spatially, F_m and F_s can be useful for classifying the larger-scale behaviour of the fault (Caine et al., 1996).

Understanding the relationship between fault and spring locations is a key area of research for fault-controlled springs. Curewitz and Karson (1997) conducted an extensive review of the geological settings of hot springs. They found that hot springs generally occurred in five structural settings along fault zones, including: (1) the fault tip where the breakdown area formed from intense fracturing gives rise to springs, (2) fault interaction areas where the breakdown areas from several fault tips interact or merge into a single breakdown area, (3) locked-in fault intersection areas where faults have opposing directions of slip leading to a breakdown area in the intersection between the faults, (4) slipping fault intersection areas where faults are slipping in the same direction, and there is limited breakdown area and (5) fault traces (i.e., surface disturbance where a fault intersects the ground surface) where localised fracturing may occur due to pressures during slip. Offsets between major faults, known as accommodation zones, are a form of interaction area that has been associated with high levels of geothermal activity and the occurrence of hot springs (e.g., Curewitz and Karson, 1997; Faulds et al., 2002). These studies suggest that fault-controlled springs, particularly fault-controlled hot springs, mostly occur where multiple fault traces interact (Curewitz and Karson, 1997; Faulds et al., 2002; Faulds et al., 2008).

2.2. Spring and aquifer hydraulics

An essential condition for the occurrence of springs is that the hydraulic head within the source aquifer (i.e., the aquifer providing water to the springs) must be sufficient for water to discharge to the surface. In confined aquifers, no major flow is expected through the confining unit unless preferential pathways (e.g., faults or fractures) are present (Brehme et al., 2016). The flow rate of a spring is directly related to the hydraulic head gradient between the aquifer and the surface (Woith et al., 2011; Brehme et al., 2016). As a lower bound, the hydraulic head in the source aquifer/s must be greater than the topographic elevation at the point of spring discharge, referred to as the spring geomorphic threshold (Currell et al., 2017; Keegan-Treloar et al., 2021). The spring geomorphic threshold is the topographical elevation of the lip, mound or surface of the spring vent that the hydraulic head must exceed for the spring to discharge. If the hydraulic head in the source aquifer drops beneath the spring geomorphic threshold, the spring will cease to flow (e.g., Currell et al., 2017).

Although the conceptual model of the spring geomorphic threshold and spring discharge is simple, spring discharge rates may be temporally variable, arising from complex external stresses. For example, Criss (2010) found that spring discharge rates may be influenced by events occurring over multiple timescales. They concluded that the flow from Big Spring (Missouri, USA) represented the superposition of long-timescale regional hydraulic head gradients and short-timescale pulse-type events due to aquifer head changes following local precipitation.

Conceptually, spring discharge rates are controlled by the source-aquifer hydraulic head and the fault conductance. Assuming Darcian flow in the fault, the conductance can be defined as:

$$C_f = \frac{KA}{\Delta z} = \frac{Q}{\Delta h} \tag{4}$$

Where, C_f is the fault conductance [$L^2\,T^{-1}$], K is hydraulic conductivity of the fault zone [$L\,T^{-1}$], A is the fault zone cross-sectional area to flow (i.e., fault width × fault length) [L^2], Δz is the difference in elevation between the spring geomorphic threshold and the source aquifer [L], Q is the spring discharge [$L^3\,T^{-1}$], and Δh is the difference in elevation between the source aquifer head and the water level at the spring outlet [L]. However, as is the case in hydrogeology more generally, there are challenges in accurately quantifying K and Δh (e.g., Durner, 1994; Post and von Asmuth, 2013; Rau et al., 2019), which translate to uncertainties in estimates of C_f.

In practice the fault conductance is a difficult parameter to measure, which can present problems in the translation of aquifer hydraulic head to spring discharge rates. For example, Love et al. (2013a) compared spring discharge rates to head differences between the source aquifer and the surface for mound springs of the Great Artesian Basin (Australia). They found no predictable relationships between the hydraulic head differences and the rate of spring discharge suggesting the fault conductance was highly variable between springs. As the fault conductance was unknown, they were unable to predict how spring discharge might vary in response to future changes in aquifer hydraulic head.

The fault conductance can undergo changes if the fault is seismically active (e.g., Gudmundsson, 2000), which can lead to temporal variations in discharge. Changes in fault conductance, aquifer permeability and other aquifer properties (e.g., storativity) have been observed following earthquake events, resulting in variations in the discharge and/or water quality of the spring (e.g., Curewitz and Karson, 1997; Cox et al., 2012). For example, Cox et al. (2012) observed the emergence of new springs and a large change in groundwater levels following the magnitude 7.1 Darfield earthquake in Canterbury, New Zealand. These changes were hypothesised to be due to increased aquifer permeability, new fracture pathways, and changes in the aquifer properties (e.g., storativity and/or transmissivity). Changes in spring water temperature and hydrochemistry were also observed following the Darfield earthquake, suggesting modified contributions from shallow meteoric and deeper groundwater to spring discharge (Cox et al., 2015). As such, the impact of seismic activity on fault behaviour and spring discharge may be an important consideration in characterising and managing fault-controlled springs in tectonically active regions.

2.3. Surface conditions and spring environments

Travertine structures are a common surface expression of springs (e.g., De Filippis et al., 2012; Henchiri et al., 2017; Karaisaoğlu and Orhan, 2018), typically occurring where spring discharge is high in CO_2, leading to carbonate mineral precipitation due to differences between the partial pressures of CO_2 in the ascending water and the atmosphere (Keppel et al., 2011). Travertine deposits may occur along fault traces, indicating fault locations (Hancock et al., 1999; Brogi and Capezzuoli, 2009). Travertine structures can lead to the modification of spring discharge rates by sealing flow pathways or forming impoundments around the spring vents. For example, Soda Dam is a large dam-like structure encompassing several springs in New Mexico (USA) that significantly alters discharge to the surrounding environment (Goff and Shevenell, 1987). In areas of travertine deposition, it is often necessary that faults are active to prevent the fault from sealing, which can lead to the cessation of spring discharge (Brogi and Capezzuoli, 2009). As such, the travertine deposits surrounding springs have been extensively used to provide a historic record of the fault and spring discharge activity (e.g., Hancock et al., 1999; Brogi and Capezzuoli, 2009; Priestley et al., 2018). For example, Brogi et al. (2012) used travertine deposits around thermal springs in the Sarteano area (Italy) to reconstruct the historical locations of the main discharge areas, the record of faulting events and the physicochemical properties of the discharge waters.

Spring discharge to surface water bodies can support extensive ecosystems and niche habitats for endemic species (e.g., Wolaver and Diehl, 2011; Carvalho Dill et al., 2014). Spring-dependent ecosystems include terrestrial ecosystems surrounding the water source and aquatic ecosystems within the water source itself (Springer and Stevens, 2009). The variability, permanence and physiochemical characteristics (e.g., salinity, pH, temperature, nitrate) of spring discharge are key controls on the composition of dependent ecosystems (van der Kamp, 1995). However, detecting these relationships may be difficult, as Boy-Roura et al. (2013) found that some physiochemical characteristics of spring discharge (i.e., nitrate concentrations) remained constant annually while other characteristics (i.e., spring flow rates and electrical conductivity) were variable.

Spring discharge that provides stream baseflow can support aquatic and terrestrial species during dry periods (Rossini et al., 2018; Bonada et al., 2007). These may include secondary ecosystems that rely on spring-fed streams and lakes (e.g., Bonada et al., 2007). For example, the Doongmabulla Springs Complex (Australia) provides baseflow to the nearby Carmichael River and supports a wide diversity of endemic species, which vary between individual spring vents (Fensham et al., 2016a; Currell et al., 2017). This variability indicates permanence of discharge and relative isolation of individual springs.

Differences have been observed in taxon number and composition between springs with permanent discharge or pooled water, and those with intermittent flow (Meyer and Meyer, 2000; Wood et al., 2005). Species often have lifecycles that have adapted to the specific spring discharge conditions. For example, springs with permanent discharge or pooled water have been shown to host unique species that require constant water availability. One such example are hydrobiids (a small snail species) found around springs in the Great Artesian Basin (Australia) that cannot undergo desiccation for more than a few minutes and require neutral to basic water in their habitat (Ponder and Colgan, 2002). Conversely, intermittent springs have been shown to host species capable of tolerating dry periods (Meyer and Meyer, 2000; Wood et al., 2005). For example, in a study of springs in the English Peak District (United Kingdom), Wood et al. (2005) found species adapted to dry periods through diapause, aestivation or extended flight periods. Meyer and Meyer (2000) propose that the unique adaptions of species present in springs may be used as a proxy to determine the flow conditions. This was demonstrated by Erman and Erman (1995), who found that caddisflies, calcium concentrations, moss, rooted plants, and temperature could be used as a proxy for spring discharge permanence.

In addition to the species in springs, the historical composition of wetland flora and fauna surrounding springs can provide information on how spring discharge conditions (e.g., flow rates and water chemistry) have changed over time (Smith et al., 2003). If spring conditions change, the composition of wetland flora and fauna may change to adapt to the new flow conditions (Ashley et al., 2004; Deane et al., 2017). For example, Ashley et al. (2004) used pollen and diatom records in soil cores to assess changes in the regional hydrology resultant from past climate change events.

3. Field investigation techniques

Field investigation techniques are vital for gathering hydrogeological information to characterise and assist in the management of fault-controlled springs. Field investigation techniques include approaches to: (1) quantify spring discharge rates (e.g., weir-based methods), (2) identify source aquifers and their contribution to spring discharge (e.g., using isotopes and hydrochemistry from water samples), and (3) use geophysical techniques to investigate fault structure and properties (Fig. 3). Additionally, field campaigns routinely characterise spring ecosystem health and examine cultural and archaeological values of spring systems, although the related field techniques are not covered in the subsections that follow.

3.1. Methods for quantifying spring discharge

Quantifying spring discharge, particularly its temporal variations, provides valuable information on both ecological requirements and changes to driving factors that control spring flow. For example, spring discharge rates have been used to estimate groundwater recharge (e.g., Segadelli et al., 2021), the baseflow contribution of springs to streams (e.g., Fournier et al., 1976; Fournier, 1989; Friedman and Norton, 2007), geothermal heat flux (e.g., Fournier et al., 1976; Mariner et al., 1990), and lag times between recharge and changes in spring discharge (e.g., Manga, 1999; Celico et al., 2006). Additionally, knowledge of spring discharge rates provide insight into aquifer characteristics (e.g., permeabilities, vertical fluxes), which are useful for constraining hydrogeological models (e.g., Manga, 1997; Saar and Manga, 2004; Martínez-Santos et al., 2014). For example, Sato et al. (2000) found that spring discharge in Awaja Island (Japan) increased following an earthquake event (likely due to increased permeability), and gradually reduced following an approximately exponential trend. They used spring discharge observations to estimate the hydraulic diffusivity of the aquifer material between the spring and its recharge area using equations derived from Darcy's law.

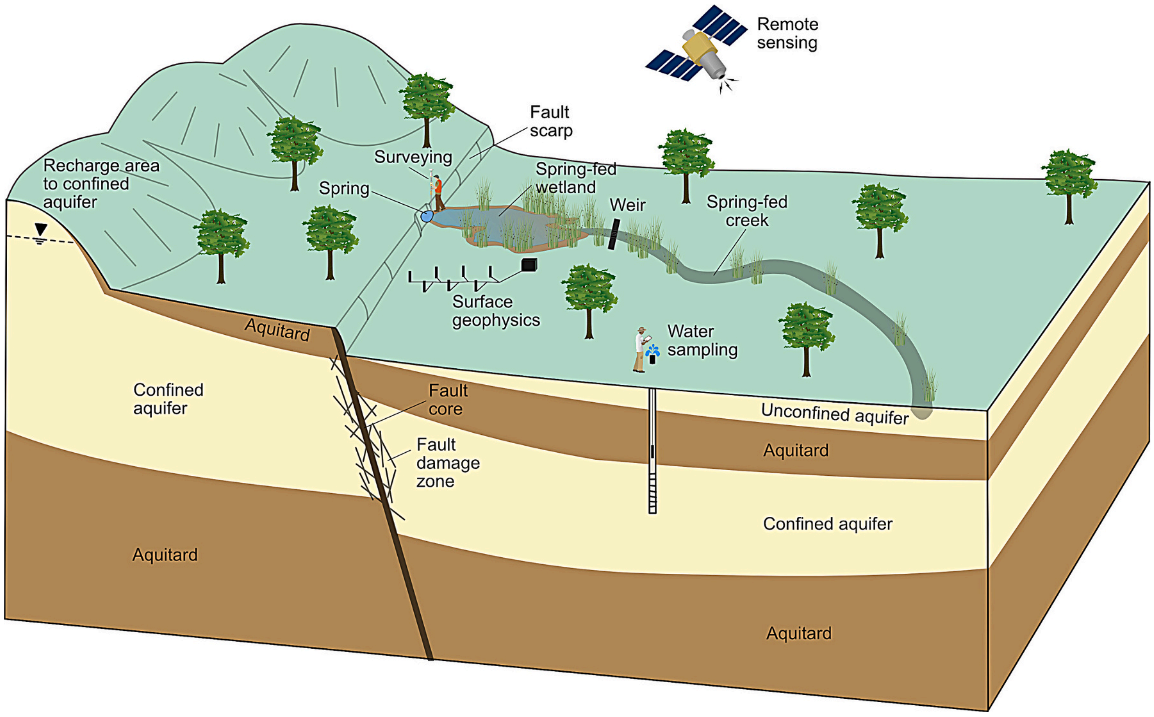

Fig. 3. Field investigation techniques for fault-controlled spring systems. Shown techniques include surface geophysics, water sampling for chemical and isotopic analysis, surveying of spring elevations, remote sensing, and a weir to measure spring discharge rates. The potentiometric surface from the recharge area to the left-hand side of the diagram is sufficient to provide flow to the spring.

Spring discharge rates have been quantified using a variety of techniques including direct flow measurements, Darcy's law-based approaches, physiochemical tracer methods and remote sensing techniques (see Table 1). The optimal method depends on the spring discharge rates being quantified, the physiochemical properties of water, the surrounding ecosystems, and the geomorphology of the spring vent. Details on the application of these techniques is provided below.

3.1.1. Direct measurements

The simplest form of direct flow measurements are timed volumetric measurements where the spring discharge is calculated from the time taken to fill a container of known volume (e.g., Gentry and Burbey, 2004; White et al., 2016; Segadelli et al., 2021). Despite the apparent simplicity of this technique, its application requires a localised discharge point, and can be problematic for springs with diffuse discharge. White et al. (2016) proposed that issues with diffuse discharge could be addressed by using flumes and sandbags to direct discharge to a measurement site. Although suitable for point in time measurements, caution is advised for the collection of long-term datasets as the modifications to the spring environment may degrade dependent ecosystems.

Weir-type approaches lead to volumetric spring discharge estimates by using either a pressure transducer or a ruler to measure the height of water that passes through a weir with a known cross-sectional area (e.g., Felton and Currens, 1994; Zhang et al., 2013; Mathon et al., 2015). The application of weir-type approaches requires discrete or directed spring discharge, as might occur within a channel or waterway (e.g., Heasler et al., 2009), or through geomorphic features or within the spring tail in the case of mound springs. Weir-type approaches have been applied to spring discharge rates of up to 1200L/s (e.g., Celico et al., 2006; Falcone et al., 2012).

Where spring discharges to a stream or creek, differential gauging can be applied to estimate spring discharge as the difference in streamflow upstream and downstream of the spring. This technique was used by Manga (1999) to obtain spring discharge rates in the range of 3200to 4800 L/s. Although, this requires that discharge can be accurately measured using a weir, which is not always possible (e.g., during high or low flows, or in areas of hyporheic exchange).

3.1.2. Darcy's law-based approaches

Approaches to calculate spring discharge based on Darcy's law use measured hydraulic gradients, flow cross-sectional areas, and hydraulic conductivity. Martínez-Santos et al. (2014) installed piezometers in springs to measure vertical head gradients, which were subsequently used, along with permeabilities obtained from slug tests, to estimate spring discharge based on Darcy's law. This was applied to the Fuentes Grandes springs (Spain), leading to an estimate of spring discharge of ~0.5 L/s. Despite the relatively simple nature of Darcy's law-based methods, these approaches are rarely applied in the literature, likely due to the high uncertainty in measurements of hydraulic conductivity.

3.1.3. Chemical tracers

The most widely applied chemical tracer technique for the quantification of spring discharge to a stream is the chloride inventory technique (e.g., Ellis and Wilson, 1955; Fournier, 1989; Friedman and Norton, 2007). Discharge rates are quantified by sampling chloride concentrations in spring discharge and in a stream in the reaches above and below where the spring contributes to streamflow (Ellis and Wilson, 1955; Fournier et al., 1976). If differences in chloride concentrations are not detectable, a salt-dilution test can be used (e.g., White et al., 2016), where a known concentration of salt is released, and the concentration is monitored downstream. The chloride inventory method is not well suited to continuous automated monitoring as typically chloride concentrations cannot be easily measured in the field, although electrical conductivity has been used as a proportional surrogate for chloride (Norton and Friedman, 1985) allowing for the analysis of temporal changes. The chloride inventory method has been demonstrated for spring discharge rates between 0.39 and 3644 L/s (Ingebritsen et al., 2001).

Table 1
Examples of spring discharge with the method and range of discharge values reported. NA (not available) denotes cases where discharge rates were not reported or were provided as a summation from multiple springs.

Method	Examples	Spring discharge (L/s)
Chloride inventory method	Ellis and Wilson (1955)	NA
	Fournier et al. (1976)	NA
	Norton and Friedman (1985)	NA
	Fournier (1989)	NA
	Mariner et al. (1990)	0.4 to 120
	Ingebritsen et al. (2001)	0.39 to 3644
	Friedman and Norton (2007)	~395 to ~3250
Wetland area as a proxy	Fatchen (2001)	0.01 to 10
	Fensham and Fairfax (2003)	NA
	White and Lewis (2011)	~5 to ~170
	White et al. (2016)	~0.001 to ~1427
Weir-type methods	Felton and Currens (1994)	14 to 71
	Swanson and Bahr (2004)	3 to 30
	Celico et al. (2006)	0 (no flow) to 440
	Heasler et al. (2009)	NA
	Amoruso et al. (2011)	65 to 166
	White and Lewis (2011)	NA
	Falcone et al. (2012)	400 to 1200
	Haselwimmer et al. (2013)	1.1 to 17
	Zhang et al. (2013)	0.1 to 6
	Mathon et al. (2015)	1 to 10
	White et al. (2016)	~0.005 to ~300
Aerial thermal imagery	Haselwimmer et al. (2013)	1.1 to 17
Manual container measurements	King et al. (1994)	~0.15 to ~0.6
	Gentry and Burbey (2004)	0.1 to 0.25
	White et al. (2016)	<0.15
	Segadelli et al. (2021)	NA
Salt dilution tests	White et al. (2016)	0.09 to 0.6
Darcy's law	Martínez-Santos et al. (2014)	~0.5
Differential stream gauging	Manga (1999)	3200 to 4800
Venturimeter	Amoruso et al. (2011)	65 to 166

3.1.4. Remote sensing

Remote sensing provides an attractive approach to quantify spring discharge, particularly for isolated data-sparse areas, as it relies on aerial- or satellite-derived products. Two main strategies have been applied, namely estimated wetland area (e.g., Williams and Holmes, 1978; White and Lewis, 2011; White et al., 2016), and aerial thermal imagery (e.g., Haselwimmer et al., 2013).

Wetland area approaches use a log-linear model to relate the spring wetland area to the spring discharge rate. Typically, a site-specific relationship is developed by measuring spring discharge rates (e.g., with a direct measurement technique) and using a log-linear regression model to develop a relationship between the wetland area and the observed spring discharge rates (e.g., Fatchen, 2001; White and Lewis, 2011). This relationship can then be used to monitor how the spring discharge rates change over time based on remotely sensed variations in the wetland area (e.g., Fatchen, 2001; White and Lewis, 2011). Generic relationships based on previous studies may be useful to provide approximate estimates of spring discharge rates. However, site-specific ecohydrological conditions will lead to different relationships between sites. Furthermore, Fatchen (2001) warned that extrapolating these relationships beyond the range of observed measurements (i.e., to extreme high or low discharge rates) can be problematic as the relationship may be valid for only a specific range of discharge rates. Wetland area-based approaches have been used to quantify spring discharge rates ranging from ~0.01 L/s (Fatchen, 2001) to ~200 L/s (Williams and Holmes, 1978).

Aerial thermal imagery can provide an alternative to wetland area-based remote sensing approaches, particularly for thermal springs. Haselwimmer et al. (2013) used remotely sensed thermal imagery (1 m pixels) to estimate spring discharge from the Pilgrim Hot Springs (Alaska). Their discharge estimates were obtained by first calculating a total heat flux from the springs and converting heat flux to a volumetric flux based on an assumed geothermal temperature for spring discharge and the thermal properties of water. This approach yielded estimates of spring discharge ranging between 1.1 L/s and 17 L/s, which was in reasonable agreement with field measurements of spring discharge. However, Haselwimmer et al. (2013) noted that discharge calculations were particularly sensitive to wind speeds.

3.2. Techniques to identify water origins

3.2.1. Hydrochemistry

Bivariate plots, ternary diagrams, and specialised plots are often used to classify water types as a first step in the hydrochemical analysis of spring systems. Widely applied approaches include bivariate plots (e.g., Grobe and Machel, 2002), Schoeller diagrams (e.g., Bajjali et al., 1997), Piper plots (e.g., Brugger et al., 2005; Crossey et al., 2009; Alçiçek et al., 2016), ternary diagrams (e.g., Duchi et al., 1995; Apollaro et al., 2012) and Langelier-Ludwig diagrams (e.g., Brombach et al., 2000; Frondini et al., 2009). Piper plots are a graphical procedure for visualising water chemistry and have been applied in studies of spring systems to identify contributing groundwater endmembers to spring discharge (e.g., Brugger et al., 2005; Crossey et al., 2009; Alçiçek et al., 2016). Duchi et al. (1995) used a ternary diagram with analytes of HCO_3, SO_4 and Cl to classify water samples as groundwater (high HCO_3), mature water (high Cl) or steam heated acidic waters (high SO_4). They found that the spring waters plotted towards the HCO_3 apex of the diagram, suggesting groundwater from a carbonate-source aquifer. Langelier-Ludwig diagrams (rectangular diagrams based on the percent of cations from Na + K and Mg + Ca, and the percent of anions from HCO_3 + CO_3 and SO_4 + Cl) have been used in spring source-water studies to identify endmember water-types, geochemical reactions, and mixing (e.g., Frondini et al., 2009; Brogi et al., 2012). For example, Frondini et al. (2009) used a Langelier-Ludwig diagram to analyse hydrochemistry from springs and geothermal carbonate and metamorphic formations, finding four distinct water groups reflecting the geology and geochemistry of the source aquifers. These groups were tightly clustered, suggesting the sources were hydraulically isolated, and there was minimal mixing between sources.

The minerals present in spring discharge have been extensively used to characterise the subsurface geology and potential source aquifers (e.g., Brombach et al., 2000; Brugger et al., 2005; Frondini et al., 2009). Mineral speciation and saturation indices can be calculated using geochemical modelling software (e.g., PHREEQC, SOLMINEQ-88, Geochemists Workbench) and as they are dependent on temperature, these geochemical processes and water-rock interactions have been used to estimate the temperature in the source aquifer (e.g., Gemici and Tarcan, 2002) using a variety of techniques referred to as geothermometry (see Section 3.3).

3.2.2. Isotopes and age tracers

The stable isotopes of water (^{18}O, ^{17}O, ^{16}O and ^{2}H, ^{1}H), have been used to trace the origin of spring water and provide information on the climatic and environmental conditions at the time of recharge (Alçiçek et al., 2016). Comparing the stable isotopes of water with the local meteoric water line can provide insights into how evaporation and transpiration have influenced water composition and the seasonality of recharge (Appello and Postma, 2010). Stable isotopes of water have been used extensively to investigate the recharge elevation (e.g., Amoruso et al., 2011), the seasonality or age of spring source waters (e.g., Ingebritsen et al., 1992; Grobe and Machel, 2002; Alçiçek et al., 2016) and evaporation and/or transpiration (e.g., Duchi et al., 1995; Brusca et al., 2001; Brugger et al., 2005; Della Porta, 2015).

Age tracer techniques utilise the known rates of radioactive decay of isotopes to determine groundwater age. By comparing the activity in a water sample with the initial activity (e.g., that in the atmosphere) it is possible to infer the age of the water (Kazemi et al., 2006; Bethke and Johnson, 2008). By examining age of spring discharge, it is possible to assess the vulnerability to impacts such as contamination and/or groundwater drawdown (Kazemi et al., 2006; Bethke and Johnson, 2008).

Tritium (^{3}H), a tracer that can be used to distinguish the presence of modern waters aged <50 years old, has been used in studies of fault-controlled springs (e.g., Heinicke and Koch, 2000; Demlie et al., 2008; Alçiçek et al., 2016) to distinguish old deep-derived water from shallow younger waters. Radon-222 (^{222}Rn), is another short-lived (half-life of 3.82 days) radioactive tracer that has been used to indicate the rapid ascent of water from a deep reservoir in spring discharge (e.g., Brugger et al., 2005) and to identify the contribution of ^{222}Rn to water during flow through fractures or faults (Choubey et al., 2000). Changes in ^{222}Rn concentrations have also been observed due to stress regimes before earthquake events, which has been used to provide information on the stress regimes and activity of faults beneath springs (Kuo et al., 2006).

Other useful tracer techniques are based on isotopes of the carbon atom and their relative ratios in a water sample. The analysis of δ^{13}C can be applied to CO_2 gases (e.g., Cartwright et al., 2002; Battani et al., 2010), CH_4 gases and carbonate minerals such as travertine (e.g., Brogi et al., 2012; De Filippis and Billi, 2012; Alçiçek et al., 2016). Battani et al. (2010) used the δ^{13}C of bubbling CO_2 in spring discharge to assess the source of water to the springs and they found δ^{13}C was similar to typical values for the mantle indicating a reasonable contribution (likely ~40%) from a deeper source. Often the δ^{13}C values can vary within an aquifer unit, which makes it difficult to select a representative value for the aquifer. δ^{13}C signatures from biological sources have been found in spring discharge to assist in the determination of the source of spring water. For example, Brugger et al. (2005) found δ^{13}C in dissolved inorganic carbon ranged from −12.3 to −8.7‰ indicating a biological source, likely C-4 plants.

The δ^{13}C of CO_2 of travertine deposits surrounding springs has also been used to investigate the source of water contributing to spring discharge. For example, Brogi et al. (2012) studied δ^{13}C values in travertine surrounding springs and found values of between 1.6 and − 2.5‰, indicating a mix between hydrothermal fluids ($\delta^{13}C \geq 0$) and shallow waters ($\delta^{13}C < -4$). The benefit of examining travertine deposits rather than water from the springs or aquifer directly, is that samples can be collected without the need to install invasive infrastructure (e.g., wells), and the deposits can potentially provide a historical record of δ^{13}C. Similarly, radiocarbon (^{14}C) has been used to calculate the age of old travertine deposits using an initial activity based on the ratio of the ^{14}C activity in recent travertine deposits and atmospheric CO_2 (Mas-Pla et al., 1992).

Noble gases are produced in the crust (e.g., ^{4}He, ^{40}Ar), the mantle (e.g., ^{3}He) or the atmosphere (e.g., ^{20}Ne, ^{36}Ar) and have been used in studies of springs to assess the contributions to spring discharge from recent recharge and old deeper groundwater (Gilfillan et al., 2011). The ^{3}He/^{4}He ratio has been used widely in fault-controlled spring studies to assess the contributions of gases from the mantle and/or crust to spring source waters (e.g., Hoke et al., 2000; Haszeldine et al., 2005; Crossey et al., 2006; Crossey et al., 2009). In contrast to ^{3}He and ^{4}He, ^{20}Ne is primarily produced in the atmosphere and can be used to assess the atmospheric contribution to a sample (Gilfillan et al., 2011). For example, Chen et al. (2006) examined ^{4}He/^{20}Ne in spring water samples to assess the relative contribution of fluids containing crustal gases (^{4}He) and atmospheric gases (^{20}Ne). They observed high ratios in spring water relative to the atmosphere, indicating the addition of ^{4}He from a deep source, suggesting water may ascend via a fault.

^{40}Ar/^{36}Ar ratios have been measured in springs emanating from faults (e.g., Bräuer et al., 2011; Gilfillan et al., 2011), to assess the contribution to spring water from gases from the mantle (^{40}Ar/^{36}Ar ratio = ~40,000; Marty and Dauphas (2003)) and the atmosphere (^{40}Ar/^{36}Ar ratio = 295.5; Marty (1995)). For example, Gilfillan et al. (2011) observed ^{40}Ar/^{36}Ar ratios from spring samples ranging from 1369 to 1687, indicating a contribution of ^{40}Ar from the mantle. Crossey et al. (2006, 2009) compared ^{40}Ar/^{36}Ar from spring samples with the concentrations of other noble gases (e.g., ^{3}He) as different noble gases have distinct sources (i.e., the mantle, the crust, the atmosphere, etc.).

3.2.3. *Temperature and geothermometers*

The rate of groundwater ascent and contribution from deep aquifers to spring discharge can be estimated from spring water temperatures (Apollaro et al., 2012; Held et al., 2018). Typically, the temperature of groundwater increases with depth at a rate of 1 °C per 20–40 m (Anderson, 2005). In cases where springs source water from deep geological units, the spring discharge temperature may be elevated relative to ambient temperatures (Kresic, 2010; Wolaver et al., 2020). The temperature of spring source-water is related to a variety of factors including the source depth, the rate of ascent, the thermal conductivity of the geological media and the ambient surface temperatures (Blackwell, 1978; Brugger et al., 2005). The temperatures of spring discharge and aquifers can be measured directly using temperature sensors (e.g., Fairley and Hinds, 2004) or estimated based on chemical or isotopic indicators, called 'geothermometers' (e.g., Sakai and Matsubaya, 1974; Fournier, 1981; Giggenbach, 1988; Kharaka and Mariner, 1989; Arnorrson, 2000).

Geothermometers reflect geochemical reactions that occurred under equilibrium conditions and the rate of these reactions can be slow relative to the rate of groundwater flow (Fournier, 1981; Giggenbach, 1988). The use of geothermometers may better capture the temperature in the spring source aquifer than direct temperature measurements, as discharging waters can quickly equilibrate to ambient groundwater or surface temperatures, especially where the rate of ascent is slow. Once spring discharge samples have been collected, chemicals or isotopes can be considered to assess the temperature in the source aquifer (Fournier, 1981; Giggenbach, 1988). Geothermometry has been extensively applied to studies of fault-controlled springs to estimate the temperature in the source aquifer (e.g., Ingebritsen et al., 1992; Duchi et al., 1995; Bajjali et al., 1997; Brombach et al., 2000; Goff et al., 2000; Gemici and Tarcan, 2002; Brugger et al., 2005; Apollaro et al., 2012). Each geothermometer has a specific temperature range over which it is valid. The width of these temperature ranges vary between geothermometers, which means geothermometers with a large range can be used to approximately estimate the temperature, which subsequently can be refined using geothermometers with a narrower temperature range. For example, in a study of the Paralana hot springs (South Australia), Brugger et al. (2005) used the saturation indices of quartz and chalcedony to estimate temperatures and refined these estimates using the saturation indices of other minerals with narrower temperature ranges (e.g., illite, montmorillonite, K-feldspar, muscovite). Table 2 shows studies of fault-controlled spring systems where geothermometers were applied and the temperature range over which they are suitable.

3.3. *Geophysical investigation techniques to determine fault structure and properties*

Geophysical techniques are a non-intrusive approach that have been used to assess subsurface hydrogeological processes (Revil et al., 2012; Inverarity et al., 2016; Banks et al., 2019). Both faults and springs have unique physical properties that are discernible using geophysical techniques. For example, the fault core may have a vastly greater density than the surrounding protolith, resulting in gravity anomalies in the vicinity of faults (Hochstein and Nixon, 1979). While springs can feature resistive zones due to fluid and gases in permeable conduits (Inverarity et al., 2016).

A common first phase in hydrogeological investigations is to identify the locations of faults in large, poorly understood regions. Seismic surveys can assist by locating faults in regions up-to several kilometres in extent (Brogi et al., 2012). Similarly, magnetic and gravitational

Table 2
Geothermometers and the temperature range over which they are applicable. Note X is used to symbolise the concentration of the mineral when the chemical formula is too long (e.g., for Quartz), nsl denotes geothermometers with no steam loss and wsl denotes those with steam loss.

Geothermometer	Equation	Range	Case studies
Quartz (nsl)	$T(^\circ C) = \frac{1309}{5.19 - log\,X} - 273.15$	0–250 °C	Duchi et al. (1995); Bajjali et al. (1997); Brugger et al. (2005)
Quartz (wsl)	$T(^\circ C) = \frac{1522}{5.75 - log\,X} - 273.15$	0–250 °C	Fournier and Rowe (1966); Ingebritsen et al. (1992); Duchi et al. (1995)
Chalcedony	$T(^\circ C) = \frac{1032}{4.69 - log\,X} - 273.15$	0–250 °C	Duchi et al. (1995); Bajjali et al. (1997); Brugger et al. (2005)
a-Cristobalite	$T(^\circ C) = \frac{781}{4.51 - log\,X} - 273.15$	0–250 °C	Duchi et al. (1995)
Amorphous silica	$T(^\circ C) = \frac{731}{4.52 - log\,X} - 273.15$	0–250 °C	Duchi et al. (1995)
Na/K (Fournier)	$T(^\circ C) = \frac{1217}{log\,(Na/K) + 1.483} - 273.15$	>150 °C	Duchi et al. (1995); Brombach et al. (2000)
Na/K (Truesdell)	$T(^\circ C) = \frac{855.6}{log\,(Na/K) + 0.8573} - 273.15$	>150 °C	Duchi et al. (1995)
Na-K-Ca	$T(^\circ C) = \frac{1647}{log(Na/K) + \beta\left(log\left(\sqrt{(Ca)}/Na\right) + 2.06\right) + 247} - 273.15$	<100 °C, $\beta = 4/3$; >100 °C, $\beta = 1/3$	Ingebritsen et al. (1992); Duchi et al. (1995)
$\Delta^{18}O(SO_4 - H_2O)$	$a = \frac{1000 + \delta^{18}O(HSO_4)}{1000 + \delta^{18}O(H_2O)}$; $T(^\circ C) = \pm\frac{1200\sqrt{2}\sqrt{1000\,ln(a) + 4.1}}{1000\,ln(a) + 4.1} - 273.15$	>0 °C	Ingebritsen et al. (1992); Bajjali et al. (1997)
P_{CO_2}	$T(^\circ C) = (logP_{CO_2} + 3.78)\,0.0168^{-1}$	100–350 °C	Gemici and Tarcan (2002)

anomalies can be used to identify the location of faults using field measurements, airborne surveys or remote sensing products (Hochstein and Nixon, 1979; Ingebritsen et al., 1992; Finn and Morgan, 2002). Another secondary source of information is the location of springs themselves, as the geographical location of springs may indicate the fault location, which can be particularly clear when springs are aligned along a fault trace (e.g., Brogi et al., 2012). Together, these techniques provide a useful approach to identify the locations of faults for further study, particularly in data-poor areas where little subsurface information is available.

Once fault locations are identified, studying the structure (i.e., the core and damage zone) and properties (e.g., permeability, saturation) of the fault is often of interest. Electrical resistivity tomography can be applied to characterise fracture networks in the damage zone of a fault (Byrdina et al., 2009; Carbonel et al., 2013). For example, Byrdina et al. (2009) used electrical resistivity tomography transects to image faults in the area surrounding the Syabru-Bensi springs (Nepal) and concluded that resistive zones observed beneath springs were the result of fractures acting as conduits for the flow of water and gas. Applying multiple geophysical techniques in combination can provide complementary information. For example, Inverarity et al. (2016) conducted a study using self-potential, magnetotellurics and time-domain electromagnetics to image four mound springs in the Great Artesian Basin. Transects across the spring sites revealed an increase in self potential beneath the spring vents (which was hypothesised to represent upwards groundwater flow through a fault), while magnetotellurics and time-domain electromagnetics were used to image the geological structure and faults existing beneath the springs. Thus, the results from the three geophysical methods applied by Inverarity et al. (2016) were combined to create a conceptual model of flow through faults to each of the springs.

4. Numerical modelling

4.1. Fault model types and associated flow assumptions

Although analytical solutions exist for evaluating groundwater flow and solute transport within faults (e.g., Robinson and Werner, 2017), hydrological modelling of field-scale fault-controlled spring systems has thus far required the implementation of numerical methods (e.g., Folch and Mas-Pla, 2008; Magri et al., 2010; Yager et al., 2013). The representation of faults within numerical models depends on the intended use of the model. Types of groundwater models that include fault-controlled spring systems can be subdivided into: (1) Regional-scale, groundwater management models (e.g., Brunetti et al., 2013; OGIA, 2019; OGIA, 2020), and (2) Local-scale, process-investigation models (e.g., López and Smith, 1995; Abbo et al., 2003; Sebben and Werner, 2016a). Both scales of fault-analysis face limitations. For example, the simulation of the fine-scale processes known to control the flow through faults is difficult at the resolution of regional-scale models, particularly if solute transport is considered (Weatherill et al., 2008; Sebben and Werner, 2016b). On the other hand, groundwater management issues that require representation of the flow through faults, such as the impacts of pumping, mining and climate variability in faulted aquifers, typically require consideration of large scales, and therefore, process-investigation models may have limited capacity to inform management decision making.

The main features of faults, described in Section 2.1, are represented to varying degrees in previous modelling studies, often due to limits imposed by model discretisation and associated model run times. Typically, there are three different approaches to the representation of faults in mathematical models, consistent with the categorisation suggested by Medici et al. (2021) for fracture flow in carbonate-rock aquifers, as: (1) cases where the fault core and damage zone may be integrated into a single unit or treated separately, but both are represented as equivalent porous media using macro-scale hydraulic properties (e.g., Bense and Person, 2006; Magri et al., 2010); (2) the fault core and damage zone are integrated into a single unit, and treated as a discrete conduit, whereby flow within the fault can be considered as Darcian (e.g., Poulet et al., 2021) or non-Darcian (e.g., Liu et al., 2017). The latter applies when fluxes are sufficiently high to violate the linearity assumptions of Darcian flow; (3) the fault core and damage zone are integrated into a single unit and represented as a network of discrete fractures (e.g., Huang et al., 2019). Caine et al. (1996) refers to categories (2) and (3) as 'localised conduit' and 'distributed conduit' representations, respectively.

The flow of groundwater through faults is often presumed to occur in a similar manner to flow through fractures (e.g., Caine and Forster, 1999), which is far more widely studied than flow through faults. Fracture flow may be Darcian or non-Darcian, depending on whether discharge is linearly or non-linearly related (respectively) to the head gradient (e.g., Reimann et al., 2011). Typically, the transition between Darcian and non-Darcian flow (which is typically associated with laminar and turbulent conditions) in fractures is predicted from the Reynolds number (R_e), as given by Li et al. (2022) for a single fracture:

$$R_e = \frac{2bq}{2v} \tag{5}$$

where $2b$ is the characteristic length for rock fractures, typically assumed to be the fracture aperture [L], q is the specific discharge [L T^{-1}], and ν is the kinematic viscosity [L^2 T^{-1}]. According to Quinn et al. (2020), there is disagreement about the critical Reynolds number representing the change of flow regime within fractures, although they reported that this is generally found to be <20. Li et al. (2022) suggest an R_e value of about 0.9 as the upper limit for Darcian flow in fractures. They found that open fractures of aperture greater than 2.5×10^{-4} m involved non-Darcian flow, whereas the flow within smaller fractures could be treated as Darcian.

Where faults are treated as a fracture or network of fractures, the equivalent hydraulic conductivity of the fracture (K_f [L T^{-1}]) is commonly adopted in models. K_f is related to the fracture aperture via the cubic law, as (Witherspoon et al., 1980):

$$K_f = \frac{(2b)^2 \rho g}{12\mu} \tag{6}$$

where ρ is fluid density [M L^{-3}], g is acceleration of gravity [L T^{-2}], and μ is the dynamic fluid viscosity [M L^{-1} T^{-1}]. Sebben and Werner (2016a, 2016b) used this approach in their analyses of solute transport in single fractures within otherwise permeable aquifers.

4.1.1. *Equivalent porous media*

The most common approach for regional- and local-scale numerical investigations (i.e., scales larger than a few 10s of metres) commonly adopt the representation of faults described above as Category (1), i.e., the equivalent porous media approach for the fault core and damage zone (e.g., Bense and Person, 2006; Magri et al., 2010). In representing the fault core and damage zone as equivalent porous media, small-scale flow processes expected in the fractures of the damage zone are neglected.

The porous media properties assigned to the core and damage zones, when these zones are explicitly represented in numerical models, vary over several orders of magnitude across modelling case studies. For example, Taillefer et al. (2017) used an equivalent porous media for the damage zone, with permeability four orders of magnitude greater than the core zone. Magri et al. (2010, 2012) also adopted a large permeability ratio between the two zones in their finite-element models, although the numerical value of the ratio is not given (i.e., the isotropic hydraulic conductivity of the core zone is reported as ~0 m/year, with an isotropic value of 32 m/year attributed to the damage zone). These core-damage zone contrasts in permeability exceed the average permeability ratio between the two zones obtained by Scibek (2020) and Forster and Evans (1991) (i.e., two orders of magnitude difference; Section 2.1).

When adopting the equivalent porous media approach and treating the core and damage zone as a single unit, faults may be assigned an anisotropic hydraulic conductivity, where the hydraulic conductivity parallel to the fault plane is greater than the one perpendicular to it (e.g., López and Smith, 1996; Bense et al., 2003; Bense et al., 2008). Other cases adopt isotropic hydraulic properties and neglect the enhanced permeability parallel to the fault or the reduced permeability perpendicular to the fault. For example, Marshall et al. (2020) neglected the damage zone and represented the fault as a barrier to flow, with low permeability (relative to the protolith) assigned to the fault. López and Smith (1995) and Folch and Mas-Pla (2008) adopted higher permeability (relative to the protolith) for the fault to represent its tendency to transmit flow along the fault axis. Scanlon et al. (2003) used the Horizontal-Flow Barrier (HFB) package of MODFLOW (Hsieh and Freckleton, 1993) to represent faults implicitly as isotropic, low-permeability features (the HFB package cannot simulate anisotropic features) in simulations of the Barton Springs Edwards Aquifer (USA).

McCallum et al. (2018) included the modified conductance approach or "Manzocchi method" (e.g., Manzocchi et al., 1999) as a variation to the equivalent porous media approach. In the Manzocchi method, fault properties are represented by adopting "transmissivity multipliers", which are functions that modify the flow terms at the model cells where faults are located, rather than explicit representation of faults and their conductance properties. While the Manzocchi method is not commonly applied in groundwater flow studies, it is widely applied in the petroleum industry, as discussed by Turnadge et al. (2018). Application examples of the Manzocchi method can be found in Manzocchi et al. (2010), Michie et al. (2018), Wilson et al. (2020), and Islam and Manzocchi (2021), among others.

McCallum et al. (2018) undertook a comparison between the Manzocchi method and the equivalent porous media. Their numerical modelling results demonstrated that in cases where a fault acts as a barrier to flow, either method to represent the fault can be adopted. However, in cases where the fault acted as a conduit to flow, there was poor agreement between the two methods of representing faults.

4.1.2. *Discrete conduits*

Caine and Forster (1999) suggested that strike-slip faults (Fig. 2c, d) may be treated as localised, discrete conduits, representing flow within the space between adjacent slipped walls of the fault. Grant (2020) advised that the fault core may be converted to a conduit for fluid movement if, prior to faulting, the protolith was over-consolidated, causing dilation and enhanced fracturing of the core. For example, Coates et al. (1994) suggested that Moosy Brook Spring (USA) is an example of a fault-controlled spring caused by a localised conduit-type fault, where spring discharge between 189 and 227 L/min was observed.

The simulation of faults as discrete conduits requires the application of 'hybrid models' (Reimann et al., 2011), wherein one-dimensional features can be embedded into n-dimensional models (e.g., Shoemaker et al., 2008; Sebben and Werner, 2016a, 2016b; Poulet et al., 2021). When flow through discrete apertures is Darcian, the cubic law applies (Eq. (6)), whereas non-Darcian flow requires application of nonlinear, pipe flow equations, such as the Forchheimer and Darcy-Weisbach equations (e.g., Shoemaker et al., 2008; Qian et al., 2015). The choice of approach depends on R_e (Eq. (5)). Both laminar and turbulent flow can be simulated using common groundwater flow codes, such as the Conduit Flow Process (CFP) of MODFLOW-2005 (Shoemaker et al., 2008) or the conduit flow model capability of FEFLOW (Diersch, 2014). Both codes allow conduits to be embedded into the porous matrix.

Fang and Zhu (2018) reported that the adoption of the cubic law and the assumption of Darcian flow to simulate large fractures leads to overestimates of groundwater flow rates. Similarly, Reimann et al. (2011) found that the assumption of laminar flow within conduits overestimated groundwater discharge via springs. More generally, Scanlon et al. (2003) concluded that the validity of a groundwater model to estimate flow rates is limited if laminar flow is assumed in a faulted system. However, groundwater numerical investigations rarely adopt non-Darcian flow to represent faults (e.g., Liu et al., 2017; Xue et al., 2019). Rather, non-Darcian flow is more frequently applied for the study of karst conduits (e.g., Saller et al., 2013; Reimann et al., 2011; Kavousi et al., 2020; Zheng et al., 2021), which have considerably larger apertures than fractures.

4.1.3. Discrete fracture networks

The representation of faults using fracture networks allows for the analysis of local-scale processes that arise within the complex geological structures of faults, including localised permeability distributions (e.g., Caine and Forster, 1999). However, there are few examples of these in the published literature (e.g., Herbert, 1996; Caine and Forster, 1999; Huang et al., 2019; Volatili et al., 2019). Numerical models adopting discrete fracture networks (not necessarily related to faults) often apply stochastic techniques (e.g., de Dreuzy et al., 2012; Li et al., 2020) to explore the uncertainty that arises from the lack of sufficient field data to characterise fracture networks (Herbert, 1996; Medici et al., 2021). The stochastic representation of discrete fracture networks represents the most complex approach to the simulation of faults (Turnadge et al., 2016) and requires the largest computational burden (McCallum et al., 2018). Attempts to capture the physical realism of fracture networks using simpler, more-efficient representations have been made by Romano et al. (2017, 2020), who provides examples of the conversion from discrete fracture networks to equivalent porous media, allowing for more efficient simulation of large-scale fractured systems.

4.1.4. Numerical modelling case studies of fault-controlled springs

Despite the significant number of studies relying on numerical modelling to understand groundwater flow systems affected by faults (e.g., Bense et al., 2013), the numerical simulation of fault-controlled springs is scarce. Table 3 lists the study objectives, model characteristics, and conceptualisations for nine modelling case studies found in the published literature.

Table 3 shows that in the context of groundwater flow, the equivalent porous media approach is the most widely used to represent the influence of faults, whereas the adoption of a specified head is the most common approach to treat fault-controlled springs in models. MODFLOW and FEFLOW are the most commonly applied codes adopted in studying fault-controlled spring systems. Only one regional-scale study (that used FEFLOW), undertaken by Brunetti et al. (2013), was apparent in the literature, using the earlier definition of regional-scale (Section 4.1).

5. Management

Due to the high levels of ecological endemism, cultural significance and heritage values associated with many springs, their protection is a critical priority for environmental and natural resource management (Hatton and Evans, 1998; McMorran, 2008; Kresic, 2010; Brake et al., 2019). However, effective spring management, i.e., to achieve ecological and other objectives, presents multiple, substantial challenges. These include the high sensitivity of many spring environments and their ecosystems to disturbances, which requires a precautionary approach to avoid potentially irreversible damage (e.g., Kresic, 2010). The loss of many significant spring complexes worldwide over the past century (e.g., Fensham et al., 2016b; Silcock et al., 2020) highlights their vulnerability to human pressures.

Human pressures on springs can lead to serious environmental degradation and/or the extinction of rare or endangered ecosystems (Ponder, 1986; Fensham et al., 2010) due to changes in the flow rate, wetland area or water chemistry. Management regimes aimed at protecting springs were generally broadly applicable to both fault-controlled springs and other spring types, rather than being

Table 3
Examples of numerical modelling case studies of fault-controlled springs.

Reference	Objective	Scale	Approach/ model	Fault and spring conceptualisation
López and Smith (1995)	Fault-controlled thermal springs in hypothetical mountainous landscape	Local	Finite-element (3D)/ Galerkin numerical method	*Fault*: Homogeneous, isotropic equivalent porous medium of uniform width *Spring*: Constant specified head (equal to the land surface)
López and Smith (1996)	Fault-controlled thermal springs in hypothetic mountainous landscape	Local	Finite-element (3D)/ Galerkin numerical method	*Fault*: Heterogeneous, anisotropic equivalent porous medium of uniform width *Spring*: Constant specified head (equal to the land surface)
Abbo et al. (2003)	Fault-controlled onshore and offshore springs at Lake Kinneret, Israel	Local	Finite-difference (3D)/ MODFLOW-M3TDMS	*Fault*: Homogeneous, anisotropic equivalent porous medium of uniform width *Spring*: Time-dependent specified head
Folch and Mas-Pla (2008)	Surface-groundwater interaction through faults in Selva basin, Catalunya, Spain	Local	Finite-difference (2D)/ MODFLOW	*Fault*: Homogeneous, isotropic equivalent porous medium of uniform width *Spring (stream)*: Constant specified head
Magri et al. (2010)	Fault-controlled thermal springs in Aegean region, western Turkey	Local	Finite-element (2D)/ FEFLOW	*Fault*: Explicit representation of the core and damage zone as homogeneous, isotropic equivalent porous medium of uniform width *Spring*: Constant specified head (equal to the land surface)
Magri et al. (2012)	Seawater circulation in fault-controlled thermal springs in Aegean region, western Turkey	Local	Finite-element (2D)/ FEFLOW	*Fault*: Explicit representation of the core and damage zone as homogeneous, isotropic equivalent porous medium of uniform width *Spring*: Constant specified head (equal to the land surface)
Brunetti et al. (2013)	Fault-controlled thermal springs in Tivoli, Italy	Regional	Finite-element (3D)/ FEFLOW	*Fault*: Homogeneous, isotropic equivalent porous medium of uniform width *Spring*: Constant specified head (equal to the land surface)
Yager et al. (2013)	Fault-controlled springs in a karst aquifer in	Local	Finite-difference (3D)/ MODFLOW	*Fault*: Homogeneous, anisotropic equivalent porous

(continued on next page)

Table 3 (*continued*)

Reference	Objective	Scale	Approach/ model	Fault and spring conceptualisation
	Shenandoah Valley, USA			medium of uniform width *Spring*: Head-dependent flow boundary
Üner and Dogan (2021)	Fault-controlled thermal springs in Western Anatolia, Turkey	Local	Finite-volume (2D)/ANSYS FLUENT	*Fault:* Explicit representation of the core and damage zone as homogeneous, isotropic equivalent porous medium of uniform width *Spring*: Recharge boundary condition

specifically focused on fault-controlled springs. These regimes often involved the use of drawdown trigger levels, which define maximum allowable drawdown thresholds that can be used to instigate changes to activities that modify water levels in an aquifer (Currell, 2016; Doody et al., 2017). Such approaches may be attractive due to their apparent simplicity and ease of application (e.g., Werner et al., 2011). However, Currell (2016) pointed out several potential pitfalls, particularly if triggers are not complemented with additional monitoring and compliance criteria (e.g., a combination of water level, flow, and ecological-based indicators). Additionally, groundwater head and flow patterns in the vicinity of faults are often complicated and may change dramatically over relatively short distances (e.g., on either side of a fault and/or between overlying aquifers in a faulted sequence; Bense and Van Balen, 2004). It may not be immediately obvious where the most appropriate locations and depths are to monitor groundwater levels that drive spring discharge, and/or what the appropriate threshold levels are to achieve certain management objectives. Identifying the relationships between changes in aquifer hydraulic head and spring discharge rates can be difficult as spring discharge rates are dependent on the fault conductance (see Section 2.2), which is difficult to accurately measure. Nevertheless, establishing relationships between water level patterns, spring discharge and the associated habitat characteristics and functions supporting sensitive species have been shown to be important for effectively managing these systems (Eamus et al., 2006; Fensham et al., 2010). Detailed field investigations are especially important in fault-controlled spring systems as faulting and other geological heterogeneity can make the discharge pathways, and thus appropriate monitoring indicators difficult to establish (e.g., Wu et al., 2011).

Currell (2016) and Noorduijn et al. (2018) demonstrated that a reliance on trigger-level-based management systems may fail to consider reductions in spring discharge that are not necessarily apparent from monitoring drawdown. For example, observation wells that are situated at or near the spring location may not show drawdown from human activities until significant time-lags have passed, after which the impacts arising from groundwater extraction may be permanent (Alley et al., 2002). This was illustrated by Bredehoeft and Durbin (2009) who used a threshold for spring discharge as a trigger for stopping pumping. In their simulation, the management action was taken at a 10% reduction in spring discharge. However, even with management action, spring discharge continued to decline for ~25 years to a maximum reduction of discharge of ~18%, and it took a further ~100years for the spring discharge to recover to above the 10% flow reduction threshold.

Many studies aimed at managing groundwater-dependent ecosystems have identified the importance of baseline and ongoing assessments that integrate knowledge from remote sensing, field-based monitoring, modelling and expert knowledge (Eamus et al., 2006; Humphreys, 2009; Doody et al., 2017). In addition to data obtained using traditional scientific measurement and sampling techniques, information about long-term hydrological and ecological functioning and variability of springs can be gained from historical records, indigenous knowledge, and archaeological evidence (Florek, 1993; Fensham et al., 2016a; Brake et al., 2019; Silcock et al., 2020).

6. Future challenges and research opportunities

Despite extensive bodies of research on faults and springs separately, there remains significant challenges and knowledge gaps to be addressed in each phase of hydrogeological investigations of fault-controlled spring systems. The key challenges and research opportunities are discussed below.

6.1. Hydrogeological processes

Characterising the relationships between spring discharge rates and ecosystem functioning (including the associated vulnerability of these ecosystems to changes in spring discharge rates) is a critical area for future research. In addition to surface discharge, near-surface discharge (i.e., subterranean leakage to the near-surface) is an often-overlooked contribution of springs to ecosystems that can occur in the area surrounding a fault-controlled spring. Near-surface discharge can occur via lateral leakage from the subsurface structures (e.g., faults) beneath springs regardless of whether the spring actively discharges to the surface or not. For example, in a study of Francis Swamp (Australia), Lewis et al. (2013) observed low surface temperatures (relative to ambient conditions) in areas with and without active spring vents. This suggested subsurface seepage may be occurring in these areas. This type of near-surface discharge has been acknowledged as critical for certain groundwater-dependent ecosystems (see type 3 GDEs in Eamus et al. (2006)) and warrants further investigation as it may be as (if not more) sensitive to water level changes than surface discharge.

The hydrogeological processes relating to springs that emanate from faults remain poorly understood, limiting the ability to effectively manage these systems. In particular, future studies into the relationship between fault type (e.g., Fig. 2) and spring occurrence will provide much needed understanding on the functioning of fault-controlled spring systems. Future research would benefit from combined laboratory and in situ studies of fault permeability (e.g., packer tests or pumping tests; see Bense et al. (2013) for additional approaches) to provide insights into permeability ratios between measurements taken along the fault trace where springs occur and where springs are absent. Additionally, knowledge and datasets from other disciplines (e.g., structural geology, petroleum, mining) could be translated into the field of hydrogeology to improve the understanding of fault properties and behaviour.

Measurements of spring discharge provide a rare opportunity to directly observe groundwater fluxes, something that is otherwise extremely difficult in hydrogeology. Direct spring discharge measurements provide useful information that has been used to characterise groundwater flow conditions and constrain numerical models (e.g., Manga, 1997; Saar and Manga, 2004; Martínez-Santos et al., 2014). Technology is not a limitation for monitoring spring discharge rates, as proven techniques can be applied to monitor spring discharge rates (see Section 3.1). In contrast to typical groundwater measurements, spring discharge rates can be measured without installing wells, substantially reducing the cost of measurements. Despite a variety of methods being available (direct measurements, Darcy's law, chemical tracers and remote sensing; see Section 3.1), spring discharge measurements are not a routine part of water resource monitoring regimes. The availability of daily or sub-daily spring discharge estimates could provide significant benefits to management. Ideally, spring discharge time series could be viewed in the same light as stream and well hydrographs, which are routinely monitored.

As discussed in section 2.2, tectonic activity often influences fault behaviour (e.g., by opening new fractures or clearing mineral precipitates), which can have dramatic impacts upon spring discharge rates and water properties. Despite the potential for earthquakes to impact fault-controlled spring systems, these impacts are rarely considered in practice. Thus, the management of fault-controlled spring systems would benefit from increased collaboration between water managers and seismologists.

6.2. Field investigation techniques

Much can be learnt about fault-controlled spring systems from surface conditions. Previous studies have demonstrated the use of travertine structures (e.g., Brogi and Capezzuoli, 2009; Love et al., 2013b; Priestley et al., 2018), wetland area (e.g., Lewis et al., 2013) and fossilised pollen and diatoms (e.g., Ashley et al., 2004) to assess the spring discharge rates and historical variability. However, there is scope for this work to be expanded and for the consideration of additional surface features. For example, the hydrobiids discussed by Ponder and Colgan (2002) can be used as an indicator of spring discharge permanence, due to their limited tolerance to dry conditions. Additionally, indigenous knowledge, paintings and artefacts provide an underutilised source of information to construct a historic record of spring locations (Fensham et al., 2016b).

Characterising whether a fault acts as a conduit or barrier to flow requires detailed investigations into the geological properties of the fault. Relationships based on the relative proportions of core and damage zone (see Section 2.2) are a good starting point to determine whether a fault will act as a conduit or barrier to flow. However, detailed field studies will invariably be required to properly characterise the fault behaviour and properties. As springs often have high ecological and cultural values, invasive techniques (e.g., trenching or drill holes) may not be appropriate. This means future studies of fault-controlled spring systems should consider non-invasive techniques to investigate these systems. Geophysics can provide a non-invasive approach to characterise subsurface geology and to identify areas of vertical flow. For example, Inverarity et al. (2016) found self-potential can be helpful to identify the locations of vertical flow beneath springs, while magnetotellurics and time-domain electromagnetics can be used to identify faults and other high conductivity pathways. Hydraulic tomography using artificial stimuli (e.g., pumping tests) and natural stimuli (e.g., changes in river stage, lightning, earthquakes, barometric pressure changes) have been applied to characterise faults and fractures over both local and basin scales (e.g., Yeh and Lee, 2007; Yeh et al., 2008; Zha et al., 2016). The further use of geophysics and application of hydraulic tomography techniques to assess the subsurface characteristics of fault-controlled spring systems will provide a much-improved understanding of these systems.

Understanding the relationship between source aquifers and spring discharge is important to assess the vulnerability of springs to external stresses (Boy-Roura et al., 2013; Davis et al., 2017). Identifying the source aquifer and monitoring the relevant hydraulic head can be difficult if monitoring infrastructure is deemed a risk to ecologically significant ecosystems (e.g., Inverarity et al., 2016) or where large hydraulic head differences exist across a fault zone (e.g., Bense and Van Balen, 2004). Detailed understanding of fault-controlled spring systems can be obtained through the collection spring discharge hydrographs, hydrochemical time-series and the creation of a database of spring discharge and aquifer hydrographs. For example, Boy-Roura et al. (2013) collected nitrate concentration time-series from spring discharge to monitor the nitrate mass recharge rates. Similarly, spring discharge hydrograph databases have been created for karst systems (e.g., Olarinoye et al. (2020)) and could be extended to include non-karst fault-controlled spring systems.

Studies of karst systems have developed various tracer and hydrograph analysis techniques (e.g., Taylor and Greene, 2005; Goldscheider et al., 2008; Luhmann et al., 2012). Tracers have been used to identify flow directions, velocities and conduits between recharge and discharge areas, including springs (e.g., Taylor and Greene, 2005; Goldscheider et al., 2008; Luhmann et al., 2012). Examples of tracers given by Goldscheider et al. (2008) include dyes (e.g., uranine, eosin, pyranine), dissolved salts (e.g., sodium, potassium, bromide) and particles (e.g., fluorescent microspheres, bacteria, bacteriophages). Similarly, spring discharge hydrograph analysis is well developed for karst systems to provide information on aquifer properties and the response of spring discharge to external stresses (Taylor and Greene, 2005). For example, techniques are presented to estimate transmissivity from the recession of spring-discharge hydrographs (Taylor and Greene, 2005). Although not directly applied to fault-controlled springs, many of these techniques are relevant, and their translation would be a valuable future contribution.

The proportion of spring discharge contributed from potential source aquifers can be assessed through the comparison of spring water samples and wells cased in potential source aquifers. When water samples are available from potential source aquifers and springs, mixing models can be used to relate the concentrations of ions or isotopes to the proportion of water contributed to spring discharge from each aquifer. However, in data sparse areas where groundwater samples are not available, noble gases (e.g., ^{4}He, ^{40}Ar, ^{20}Ne) can provide an approach to assess the contribution from different sources to spring discharge. The concentrations of these gases are known in the atmosphere, the mantle, and in the crust (Gilfillan et al., 2011). Thus, analyses of noble gasses can be used to determine whether spring discharge shows evidence of being sourced from shallow aquifers or recent recharge (i.e., if the concentration is similar to that in the atmosphere), or if the sample is more consistent with a deeper source (i.e., if the concentration is similar to that in the mantle or the crust). Other isotopes can provide complementary information, for example, the stable isotopes of water in spring discharge can be used to infer recharge elevation, recharge seasonality and the amount of evapotranspiration. $\delta^{13}C$ in spring discharge can be used to assess the contribution of deep waters through a comparison with the concentrations in the mantle, the atmosphere, biological sources or the concentrations in potential source aquifers. Travertine structures can provide an alternate method of obtaining $\delta^{13}C$ from spring discharge. As these structures often reflect precipitation of minerals from spring discharge that has occurred over a long timescale, these deposits may provide a historic record of $\delta^{13}C$. In particular, a greater focus on the development of strategies to characterise springs primarily using analytes that can be obtained without the use of invasive monitoring infrastructure will assist in the management of fault-spring systems.

Temperature has been used to identify spring vents (e.g., Lewis et al., 2013), characterise aquifer permeability fields (e.g., Saar, 2011), estimate the depth of spring source-waters with geothermometry (e.g., Fournier, 1981; Kharaka and Mariner, 1989) and calculate spring discharge using a heat flux approach (e.g., Haselwimmer et al., 2013). Although not demonstrated in the reviewed case studies, newer geothermometry techniques are available (see Arnorrson (2000)), and the application of these techniques to fault-controlled springs would represent a valuable future contribution. Furthermore, the use of heat as a tracer to quantify spring discharge remains largely underutilised, a point that has been made about the use of heat as a tracer in hydrogeology more generally (Kurylyk and Irvine, 2019). Benefits of the use of heat as a tracer to quantify fluid flows include the availability of robust, low-cost sensors (Anderson, 2005; Irvine et al., 2017; Kurylyk et al., 2019) and the fact that temperature-based methods can be used to produce time series estimates of fluid flows (Irvine et al., 2020). Temperature-time series approaches can be used to estimate spring discharge using temperature sensor pairs (e.g., Hatch et al., 2006; Keery et al., 2007), or using other signal processing techniques that allow for multiple frequencies (aside from simple diurnal) and for two or more depths (e.g., Vandersteen et al., 2015). Several software packages are available to facilitate the application of these methods (e.g., Irvine et al., 2015; Vandersteen et al., 2015; Ford et al., 2021). Active heat tracer methods provide an alternative approach to quantify discharge whereby an artificial heat source is used to estimate groundwater flux (e.g., Lewandowski et al., 2011; Banks et al., 2018).

6.3. Numerical modelling

Given the widespread use of numerical models in groundwater management, significant benefits can come from improved numerical representation of fault-controlled springs. Although faults are typically composed of complex fracture networks, the extensive body of literature on modelling of fractured rock systems has not been translated into guidance on fault simulation. McCallum et al. (2018) identified that the type of numerical approach is important when faults act as conduits to flow. However, the comparison undertaken by McCallum et al. (2018) did not include the treatment of faults as fracture networks. A host of opportunities to further investigate the optimal numerical techniques to treat fault-derived springs remains. For example, the new unstructured grid version of MODFLOW (Panday et al., 2017) provides new capabilities to better represent faults in equivalent porous media models without significantly increasing the computational burden (McCallum et al., 2021). However, further investigations are required to determine appropriate modelling approaches to represent fault-controlled springs, including further investigation into the use of discrete conduits and discrete fracture networks.

Regional-scale models impose a significant computational challenge, especially if fault-related flow process are simulated. The applicability of numerical permeameters for the upscaling of fault hydraulic properties (e.g., Lupton et al., 2019) should be further investigated to improve the computational performance of faulted groundwater systems. Formal uncertainty analysis of groundwater flow systems affected by faults is also lacking in the current published literature.

6.4. Management of fault-controlled springs

Given their ecological and spiritual importance, the management of springs emanating from faults the management of these fault-controlled spring systems will benefit from the adoption of a structured management approach (e.g., adaptive management) with pre-defined mitigation strategies. These mitigation strategies should consider whether the impacts are reversible and the time scales of impacts (Thomann et al., 2020). When impacts are irreversible or reversible only over significant periods of time (e.g., centuries), the need for monitoring protocols for early detection of impacts becomes increasingly important. Numerical modelling can be an important tool to inform managers of the effectiveness of proposed mitigation strategies.

Management regimes should to identify: (1) the source aquifer(s) and major discharge pathway(s); (2) the spring geomorphic threshold(s) required to maintain discharge to the surface; (3) the relationship(s) between water level patterns in the source aquifer(s) and flow rates at the springs; (4) the ecological thresholds (e.g., spring discharge rates) required to sustain habitat for a particular species and/or ecological communities; and (5) the stakeholder perspectives on the significance and value of the spring(s). A comprehensive understanding of the hydrogeological functioning of springs is essential for the effective and science-based management of these systems. Hence, studies that integrate spring ecosystem responses within hydrological models, to assess ecosystem changes due to development pressures, are a critical area for future research. This is especially important for projects that may irreversibly compromise the ecological and/or cultural values of a system (Thomann et al., 2020).

Further to these recommendations, the use of comprehensive post audits of management plans could consider a range of factors including the choice and efficacy of mitigation measures, and the relationship between the use of prescribed management strategies and positive or negative management outcomes. Detailed post audits can help to retrospectively identify strategies that were effective (or ineffective) for the management of fault-controlled spring systems and encourage effective management by learning from past management experiences.

7. Conclusions

This review of fault-controlled springs revealed fundamental shortcomings in the present understanding of these systems. Characteristics of fault-controlled spring systems that remain poorly understood include the translation of source-aquifer hydraulic head to spring discharge rates, the fault structure and hydraulic properties (and their representation in models), and the impact of fault activity on spring discharge rates. A critical barrier to the characterisation of many fault-controlled spring systems is the need to protect spring expression features (e.g., calcareous mound structures) and accompanying wetlands, which often have high cultural and ecological values, from invasive methods of investigation (e.g., drilling). Studies of fault-controlled springs have typically focussed on one specific component of the system (e.g., the spring, the fault, or groundwater-dependent ecosystems) rather than the broader system and the interdependencies between components. Thus, a greater emphasis is needed on the analysis of interactions between faults and springs. This will allow spring measurements to be used in evaluating fault properties, amongst other benefits of considering faults and springs as connected, interdependent systems. This will also help to identify the sensitivity of fault-controlled spring systems to natural and anthropogenic forcings; a critical requirement of spring and spring-dependent ecosystem management. Finally, we recommend the establishment of several well-characterized field examples within both natural and modified hydrogeological settings to help elucidate critical functions and to advance the current understanding of fault-controlled spring systems.

Declaration of Competing Interest

None.

Acknowledgements

Robin Keegan-Treloar is supported by the Australian Government Research Training Program. Dylan Irvine, Adrian Werner, S. Cristina Solórzano-Rivas, Matthew Currell and Eddie Banks are supported by an Australian Research Council Linkage Project (project number LP190100713). We thank the anonymous reviewers whose comments helped improve the paper.

References

Abbo, H., Shavit, U., Markel, D., Rimmer, A., 2003. A numerical study on the influence of fractured regions on lake/ groundwater interaction; the Lake Kinneret (Sea of Galilee) case. J. Hydrol. 283, 225–243. https://doi.org/10.1016/S0022-1694(03)00273-7.

Alçiçek, H., Bülbül, A., Alçiçek, M.C., 2016. Hydrogeochemistry of the thermal waters from the Yenice Geothermal Field (Denizli Basin, Southwestern Anatolia, Turkey). J. Volcanol. Geotherm. Res. 309, 118–138. https://doi.org/10.1016/j.jvolgeores.2015.10.025.

Alley, W.M., Healy, R.W., LaBaugh, J.W., Reilly, T.E., 2002. Flow and storage in groundwater systems. Science (80-.) 296, 1985–1990. https://doi.org/10.1126/science.1067123.

Amoruso, A., Crescentini, L., Petitta, M., Rusi, S., Tallini, M., 2011. Impact of the 6 April 2009 L'Aquila earthquake on groundwater flow in the Gran Sasso carbonate aquifer, Central Italy. Hydrol. Process. 25, 1754–1764. https://doi.org/10.1002/hyp.7933.

Anderson, M.P., 2005. Heat as a ground water tracer. Ground Water 43, 951–968. https://doi.org/10.1111/j.1745-6584.2005.00052.x.

Apollaro, C., Dotsika, E., Marini, L., Barca, D., Bloise, A., De Rosa, N., Doveri, M., Lelli, M., Muto, F., 2012. Chemical and isotopic characterization of the thermomineral water of Terme Sibarite springs (Northern Calabria, Italy). Geochem. J. 46, 117–129. https://doi.org/10.2343/geochemj.1.0166.

Appello, C., Postma, D., 2010. Geochemistry, Groundwater and Pollution, 2nd ed. A.A. Balkema Publishers, Leiden, Netherlands.

Arnorrson, S., 2000. Isotopic and chemical techniques in geothermal exploration, development and use. In: Sampling Methods, Data Handling and Interpretation. Vienna.

Ashley, G.M., Mworia, J.M., Muasya, A.M., Owen, R.B., Driese, S.G., Hover, V.C., Renaut, R.W., Goman, M.F., Mathai, S., Blatt, S.H., 2004. Sedimentation and recent history of a freshwater wetland in a semi-arid environment: Loboi Swamp, Kenya, East Africa. Sedimentology 51, 1301–1321. https://doi.org/10.1111/j.1365-3091.2004.00671.x.

Bajjali, W., Clark, I.D., Fritz, P., 1997. The artesian thermal groundwaters of northern Jordan: Insights into their recharge history and age. J. Hydrol. 192, 355–382. https://doi.org/10.1016/S0022-1694(96)03082-X.
Banks, E.W., Shanafield, M.A., Noorduijn, S., McCallum, J., Lewandowski, J., Batelaan, O., 2018. Active heat pulse sensing of 3-D-flow fields in streambeds. Hydrol. Earth Syst. Sci. 22, 1917–1929. https://doi.org/10.5194/hess-22-1917-2018.
Banks, E.W., Hatch, M., Smith, S., Underschultz, J., Lamontagne, S., Suckow, A., Mallants, D., 2019. Multi-tracer and hydrogeophysical investigation of the hydraulic connectivity between coal seam gas formations, shallow groundwater and stream network in a faulted sedimentary basin. J. Hydrol. 578, 124132 https://doi.org/10.1016/j.jhydrol.2019.124132.
Battani, A., Deville, E., Faure, J.L., Jeandel, E., Noirez, S., Tocqué, E., Benoît, Y., Schmitz, J., Parlouar, D., Sarda, P., Gal, F., le Pierres, K., Brach, M., Braibant, G., Beny, C., Pokryszka, Z., Charmoille, A., Bentivegna, G., Pironon, J., de Donato, P., Garnier, C., Cailteau, C., Barrès, O., Radilla, G., Bauer, A., 2010. Geochemical study of natural CO2 emissions in the French Massif Central: How to predict origin, processes and evolution of CO2 leakage. Oil Gas Sci. Technol. 65, 615–633. https://doi.org/10.2516/ogst/2009052.
Bense, V.F., Person, M.A., 2006. Faults as conduit-barrier systems to fluid flow in siliciclastic sedimentary aquifers. Water Resour. Res. 42 https://doi.org/10.1029/2005WR004480.
Bense, V.F., Van Balen, R., 2004. The effect of fault relay and clay smearing on groundwater flow patterns in the Lower Rhine Embayment. Basin Res. 16, 397–411. https://doi.org/10.1111/j.1365-2117.2004.00238.x.
Bense, V.F., Van Balen, R.T., De Vries, J.J., 2003. The impact of faults on the hydrogeological conditions in the Roer Valley Rift System: An overview. Geol. en Mijnbouw/Netherlands J. Geosci. 82, 41–54. https://doi.org/10.1017/S0016774600022782.
Bense, V.F., Person, M.A., Chaudhary, K., You, Y., Cremer, N., Simon, S., 2008. Thermal anomalies indicate preferential flow along faults in unconsolidated sedimentary aquifers. Geophys. Res. Lett. 35 https://doi.org/10.1029/2008GL036017.
Bense, V.F., Gleeson, T., Loveless, S.E., Bour, O., Scibek, J., 2013. Fault zone hydrogeology. Earth Sci. Rev. 127, 171–192. https://doi.org/10.1016/j.earscirev.2013.09.008.
Bethke, C.M., Johnson, T.M., 2008. Groundwater age and groundwater age dating. Annu. Rev. Earth Planet. Sci. 36, 121–152. https://doi.org/10.1146/annurev.earth.36.031207.124210.
Bignall, G., Browne, P., 1994. Surface hydrothermal alteration and evolution of the Te Kopia Thermal Area, New Zealand. Geothermics 23, 645–658. https://doi.org/10.1016/0375-6505(94)90023-X.
Blackwell, D.D., 1978. Heat flow and energy loss in the Western United States. Mem. Geol. Soc. Am. 152, 175–208. https://doi.org/10.1130/MEM152-p175.
Bogan, M.T., Noriega-Felix, N., Vidal-Aguilar, S.L., Findley, L.T., Lytle, D.A., Gutiérrez-Ruacho, O.G., Alvarado-Castro, J.A., Varela-Romero, A., 2014. Biogeography and conservation of aquatic fauna in spring-fed tropical canyons of the southern Sonoran Desert, Mexico. Biodivers. Conserv. 23, 2705–2748. https://doi.org/10.1007/s10531-014-0745-z.
Bonada, N., Rieradevall, M., Prat, N., 2007. Macroinvertebrate community structure and biological traits related to flow permanence in a Mediterranean river network. Hydrobiologia 589, 91–106. https://doi.org/10.1007/s10750-007-0723-5.
Boy-Roura, M., Menció, A., Mas-Pla, J., 2013. Temporal analysis of spring water data to assess nitrate inputs to groundwater in an agricultural area (Osona, NE Spain). Sci. Total Environ. 452–453, 433–445. https://doi.org/10.1016/j.scitotenv.2013.02.065.
Brake, L., Harris, C., Jensen, A., Keppel, M., Lewis, M., Lewis, S., 2019. Great Artesian Basin Springs: a Plan for the Future. In: Evidence-Based Methodologies for Managing Risks to Spring Values.
Bräuer, K., Kämpf, H., Koch, U., Strauch, G., 2011. Monthly monitoring of gas and isotope compositions in the free gas phase at degassing locations close to the Nový Kostel focal zone in the western Eger Rift, Czech Republic. Chem. Geol. 290, 163–176. https://doi.org/10.1016/j.chemgeo.2011.09.012.
Bredehoeft, J., Durbin, T., 2009. Ground water development - The time to full capture problem. Ground Water 47, 506–514. https://doi.org/10.1111/j.1745-6584.2008.00538.x.
Brehme, M., Blöcher, G., Cacace, M., Kamah, Y., Sauter, M., Zimmermann, G., 2016. Permeability distribution in the Lahendong geothermal field: A blind fault captured by thermal–hydraulic simulation. Environ. Earth Sci. 75 https://doi.org/10.1007/s12665-016-5878-9.
Brogi, A., Capezzuoli, E., 2009. Travertine deposition and faulting: The fault-related travertine fissure-ridge at Terme S. Giovanni, Rapolano Terme (Italy). Int. J. Earth Sci. 98, 931–947. https://doi.org/10.1007/s00531-007-0290-z.
Brogi, A., Capezzuoli, E., Buracchi, E., Branca, M., 2012. Tectonic control on travertine and calcareous tufa deposition in a low-temperature geothermal system (Sarteano, Central Italy). J. Geol. Soc. Lond. 169, 461–476. https://doi.org/10.1144/0016-76492011-137.
Brombach, T., Marini, L., Hunziker, J.C., 2000. Geochemistry of the thermal springs and fumaroles of Basse-Terre Island, Guadeloupe, Lesser Antilles. Bull. Volcanol. 61, 477–490. https://doi.org/10.1007/PL00008913.
Brugger, J., Long, N., McPhail, D.C., Plimer, I., 2005. An active amagmatic hydrothermal system: The Paralana hot springs, Northern Flinders Ranges, South Australia. Chem. Geol. 222, 35–64. https://doi.org/10.1016/j.chemgeo.2005.06.007.
Brunetti, E., Jones, J.P., Petitta, M., Rudolph, D.L., 2013. Assessing the impact of large-scale dewatering on fault-controlled aquifer systems: A case study in the Acque Albule basin (Tivoli, central Italy). Hydrogeol. J. 21, 401–423. https://doi.org/10.1007/s10040-012-0918-3.
Brusca, L., Aiuppa, A., D'Alessandro, W., Parello, F., Allard, P., Michel, A., 2001. Geochemical mapping of magmatic gas-water-rock interactions in the aquifer of Mount Etna volcano. J. Volcanol. Geotherm. Res. 108, 199–218. https://doi.org/10.1016/S0377-0273(00)00286-9.
Bryan, K., 1919. Classification of springs. J. Geol. 27, 522–561.
Byrdina, S., Revil, A., Pant, S.R., Koirala, B.P., Shrestha, P.L., Tiwari, D.R., Gautam, U.P., Shrestha, K., Sapkota, S.N., Contraires, S., Perrier, F., 2009. Dipolar self-potential anomaly associated with carbon dioxide and radon flux at Syabru-Bensi hot springs in central Nepal. J. Geophys. Res. Solid Earth 114, 1–14. https://doi.org/10.1029/2008JB006154.
Caine, J.S., Forster, C.B., 1999. Fault zone architecture and fluid flow: insights from field data and numerical modeling. Am. Geophys. Union 101–127. https://doi.org/10.1029/GM113p0101.
Caine, Jonathan, S., Evans, James, P., Forster, Craig, B., 1996. Fault zone architecture and permeability structure. Geology 24, 1025–1028. https://doi.org/10.1130/0091-7613(1996)024<1025:FZAAPS>2.3.CO;2.
Carbonel, D., Gutiérrez, F., Linares, R., Roqué, C., Zarroca, M., McCalpin, J., Guerrero, J., Rodríguez, V., 2013. Differentiating between gravitational and tectonic faults by means of geomorphological mapping, trenching and geophysical surveys. The case of the Zenzano Fault (Iberian Chain, N Spain). Geomorphology 189, 93–108. https://doi.org/10.1016/j.geomorph.2013.01.020.
Cartwright, I., Weaver, T., Tweed, S., Ahearne, D., Cooper, M., Czapnik, K., Tranter, J., 2002. Stable isotope geochemistry of cold CO2-bearing mineral spring waters, Daylesford, Victoria, Australia: Sources of gas and water and links with waning volcanism. Chem. Geol. 185, 71–91. https://doi.org/10.1016/S0009-2541(01)00397-7.
Carvalho Dill, A.M.M., Stigter, T.Y., Brito, R., Chícharo, M.A., Chícharo, L., 2014. The combined use of radio frequency-electromagnetic surveys and chemical and biological analyses to study the role of groundwater discharge into the Guadiana estuary. Ecohydrology 7, 291–300. https://doi.org/10.1002/eco.1345.
Celico, F., Petrella, E., Celico, P., 2006. Hydrogeological behaviour of some fault zones in a carbonate aquifer of Southern Italy: an experimentally based model. Terra Nova 18, 308–313. https://doi.org/10.1111/j.1365-3121.2006.00694.x.
Chen, J., Zhao, X., Sheng, X., Dong, H., Rao, W., Su, Z., 2006. Formation mechanisms of megadunes and lakes in the Badain Jaran Desert, Inner Mongolia. Chin. Sci. Bull. 51, 3026–3034. https://doi.org/10.1007/s11434-006-2196-8.
Choubey, V.M., Bartarya, S.K., Ramola, R.C., 2000. Radon in Himalayan springs: a geohydrological control. Environ. Geol. 39, 523–530. https://doi.org/10.1007/s002540050463.
Coates, D.R., Timofeeff, N.P., Caine, J.S., Davis, W.D., 1994. Hydrogeology of the Northern Shawangunk Mountains. Consulting Report Prepared for Mohonk Preserve. Inc., Ulster County, New York, p. 81.
Cox, S.C., Rutter, H.K., Sims, A., Manga, M., Weir, J.J., Ezzy, T., White, P.A., Horton, T. W., Scott, D., 2012. Hydrological effects of the M w 7.1 Darfield (Canterbury) earthquake, 4 September 2010, New Zealand. New Zeal. J. Geol. Geophys. 55, 231–247. https://doi.org/10.1080/00288306.2012.680474.
Cox, S.C., Menzies, C.D., Sutherland, R., Denys, P.H., Chamberlain, C., Teagle, D.A.H., 2015. Changes in hot spring temperature and hydrogeology of the Alpine Fault hanging wall, New Zealand, induced by distal South Island earthquakes. Geofluids 15, 216–239. https://doi.org/10.1111/gfl.12093.
Criss, R.E., 2010. A Darcian model for the flow of Big Spring and the hydraulic head in the Ozark aquifer, Missouri, USA. Acta Carsol. 39, 379–387. https://doi.org/10.3986/ac.v39i2.106.
Crossey, L.J., Fischer, T.P., Patchett, P.J., Karlstrom, K.E., Hilton, D.R., Newell, D.L., Huntoon, P., Reynolds, A.C., de Leeuw, G.A.M., 2006. Dissected hydrologic system at the Grand Canyon: Interaction between deeply derived fluids and plateau aquifer waters in modern springs and travertine. Geology 34, 25–28. https://doi.org/10.1130/G22057.1.
Crossey, L.J., Karlstrom, K.E., Springer, A.E., Newell, D., Hilton, D.R., Fischer, T., 2009. Degassing of mantle-derived CO2 and He from springs in the southern Colorado Plateau region - Neotectonic connections and implications for groundwater systems. Bull. Geol. Soc. Am. 121, 1034–1053. https://doi.org/10.1130/B26394.1.
Curewitz, D., Karson, J.A., 1997. Structural settings of hydrothermal outflow: Fracture permeability maintained by fault propagation and interaction. J. Volcanol. Geotherm. Res. 79, 149–168. https://doi.org/10.1016/S0377-0273(97)00027-9.
Currell, M.J., 2016. Drawdown "Triggers": A Misguided Strategy for Protecting Groundwater-Fed Streams and Springs. Groundwater 54, 619–622. https://doi.org/10.1111/gwat.12425.
Currell, M.J., Werner, A.D., McGrath, C., Webb, J.A., Berkman, M., 2017. Problems with the application of hydrogeological science to regulation of Australian mining projects: Carmichael Mine and Doongmabulla Springs. J. Hydrol. 548, 674–682. https://doi.org/10.1016/j.jhydrol.2017.03.031.
Davis, J.A., Kerezsy, A., Nicol, S., 2017. Springs: Conserving perennial water is critical in arid landscapes. Biol. Conserv. 211, 30–35. https://doi.org/10.1016/j.biocon.2016.12.036.
de Dreuzy, J.R., Méheust, Y., Pichot, G., 2012. Influence of fracture scale heterogeneity on the flow properties of three-dimensional discrete fracture networks (DFN). J. Geophys. Res. B Solid Earth 117, 1–21. https://doi.org/10.1029/2012JB009461.
De Filippis, L., Billi, A., 2012. Morphotectonics of fissure ridge travertines from geothermal areas of Mammoth Hot Springs (Wyoming) and Bridgeport (California). Tectonophysics 548–549, 34–48. https://doi.org/10.1016/j.tecto.2012.04.017.
De Filippis, L., Faccenna, C., Billi, A., Anzalone, E., Brilli, M., Özkul, M., Soligo, M., Tuccimei, P., Villa, I.M., 2012. Growth of fissure ridge travertines from geothermal springs of Denizli Basin, western Turkey. Bull. Geol. Soc. Am. 124, 1629–1645. https://doi.org/10.1130/B30606.1.

Deane, D., Harding, C., Aldridge, K., Goodman, A., Gehrig, S., Nicol, J., Brookes, J., 2017. Predicted risks of groundwater decline in seasonal wetland plant communities depend on basin morphology. Wetl. Ecol. Manag. 1–14 https://doi.org/10.1007/s11273-017-9578-3.

Della Porta, G., 2015. Carbonate build-ups in lacustrine, hydrothermal and fluvial settings: comparing depositional geometry, fabric types and geochemical signature. Geol. Soc. Spec. Publ. 418, 17–68. https://doi.org/10.1144/sp418.4.

Demlie, M., Wohnlich, S., Ayenew, T., 2008. Major ion hydrochemistry and environmental isotope signatures as a tool in assessing groundwater occurrence and its dynamics in a fractured volcanic aquifer system located within a heavily urbanized catchment, central Ethiopia. J. Hydrol. 353, 175–188. https://doi.org/10.1016/j.jhydrol.2008.02.009.

Diersch, H.-J.G., 2014. FEFLOW: finite element modeling of flow, mass and heat transport in porous and fractured media. In: FEFLOW: Finite Element Modeling of Flow, Mass and Heat Transport in Porous and Fractured Media, p. 996. https://doi.org/10.1007/978-3-642-38739-5.

Doody, T.M., Hancock, P.J., Pritchard, J.L., 2017. Information Guidelines Explanatory Note: Assessing groundwater-dependent ecosystems. In: Report prepared for the Independent Expert Scientific Committee on Coal Seam Gas and Large Coal Mining Development through the Department of the Environment and Energy, C.

Duchi, V., Minissale, A., Vaselli, O., Ancillotti, M., 1995. Hydrogeochemistry of the Campania region in southern Italy. J. Volcanol. Geotherm. Res. 67, 313–328. https://doi.org/10.1016/0377-0273(94)00109-T.

Durner, W., 1994. Hydraulic conductivity estimation for soils with heterogeneous pore structure. Water Resour. Res. 30, 211–223. https://doi.org/10.1029/93WR02676.

Eamus, D., Froend, R., Loomes, R., Hose, G., Murray, B., 2006. A functional methodology for determining the groundwater regime needed to maintain the health of groundwater-dependent vegetation. Aust. J. Bot. 54, 97. https://doi.org/10.1071/BT05031.

Ellis, A.J., Wilson, S.H., 1955. Heat from the Wairakei-Taupo Thermal Region Calculated from the Chloride Output. New Zeal. J, Sci, p. 36.

Erman, A., Erman, D.C., 1995. Spring Permanence, Trichoptera Species Richness, and the Role of Drought. J. Kansas Entomol. Soc. 68, 50–64.

Fairley, J.P., Hinds, J.J., 2004. Rapid transport pathways for geothermal fluids in an active Great Basin fault zone. Geology 32, 825–828. https://doi.org/10.1130/G20617.1.

Falcone, R.A., Carucci, V., Falgiani, A., Manetta, M., Parisse, B., Petitta, M., Rusi, S., Spizzico, M., Tallini, M., 2012. Changes on groundwater flow and hydrochemistry of the Gran Sasso carbonate aquifer after 2009 L'Aquila earthquake. Ital. J. Geosci. 131, 459–474. https://doi.org/10.3301/IJG.2011.34.

Fang, H., Zhu, J., 2018. Simulation of groundwater exchange between an unconfined aquifer and a discrete fracture network with laminar and turbulent flows. J. Hydrol. 562, 468–476. https://doi.org/10.1016/j.jhydrol.2018.05.022.

Fatchen, T., 2001. Vegetated wetland area as an index of mound spring flows. In: 4th Mound Spring Researchers Forum. National Parks and Wildlife, Adelaide, South Australia, pp. 5–8.

Faulds, J.E., Varga, R.J., 1998. The role of accommodation zones and transfer zones in the regional segmentation of extended terranes. Spec. Pap. Geol. Soc. Am. 323, 1–45. https://doi.org/10.1130/0-8137-2323-X.1.

Faulds, J.E., Olson, E.L., Harlan, S.S., McIntosh, W.C., 2002. Miocene extension and fault-related folding in the Highland Range, southern Nevada: A three-dimensional perspective. J. Struct. Geol. 24, 861–886. https://doi.org/10.1016/S0191-8141(01)00116-X.

Faulds, J., Coolbaugh, M., Bouchot, V., Moeck, I., Oğuz, K., Cedex, O., 2008. Characterizing structural controls of geothermal reservoirs in the Great Basin, USA, and Western Turkey: developing successful exploration strategies in extended terranes. World C 25–29.

Felton, G.K., Currens, J.C., 1994. Peak flow rate and recession-curve characteristics of a karst spring in the Inner Bluegrass, central Kentucky. J. Hydrol. 162, 99–118. https://doi.org/10.1016/0022-1694(94)90006-X.

Fensham, R.J., Fairfax, R.J., 2003. Spring wetlands of the Great Artesian Basin, Queensland, Australia. Wetlands Ecol. Manag. 11, 343–362.

Fensham, R., Ponder, W., Fairfax, R.J., 2010. The Community of Native Species Dependent on Natural Discharge of Groundwater from the Great Artesian Basin.

Fensham, R., Silcock, J., Laffineur, B., MacDermott, H., 2016a. Lake Eyre Basin Springs Assessment Project: Hydrogeology, cultural history and biological values of springs in the Barcaldine, Springvale and Flinders River supergroups. Galilee Basin springs and Tertiary springs of western Queensland, Brisbane.

Fensham, R.J., Silcock, J.L., Powell, O., Habermehl, M.A., 2016b. In search of lost springs: a protocol for locating active and inactive springs. Groundwater 54, 374–383. https://doi.org/10.1111/gwat.12375.

Finn, C.A., Morgan, L.A., 2002. High-resolution aeromagnetic mapping of volcanic terrain, Yellowstone National Park. J. Volcanol. Geotherm. Res. 115, 207–231. https://doi.org/10.1016/S0377-0273(01)00317-1.

Florek, S., 1993. Archaeology of the Mound Spring Campsites Near Lake Eyre in. South Australia.

Folch, A., Mas-Pla, J., 2008. Hydrogeological interactions between fault zones and alluvial aquifers in regional flow systems. Hydrol. Process. 22, 3476–3487. https://doi.org/10.1002/hyp.6956.

Ford, R.G., Lien, B.K., Acree, S.D., Ross, R.R., 2021. Spreadsheet tools for quantifying seepage flux across the GW-SW interface. Water Resour. Res. 57 https://doi.org/10.1029/2019WR026232.

Forster, C.B., Evans, J.P., 1991. Hydrogeology of thrust faults and crystalline thrust sheets: Results of combined field and modeling studies. Geophys. Res. Lett. 18, 979–982. https://doi.org/10.1029/91GL00950.

Fournier, R.O., 1981. Application of water geochemistry to geothermal exploration and reservoir engineering. Geotherm. Syst. Princ. Case Hist. 109–143.

Fournier, R.O., 1989. Geochemistry and Yellowstone National. Annu. Rev. Earth Planet. Sci. 17, 13–53.

Fournier, R.O.O., Rowe, J.J., 1966. Estimation of underground temperatures from the silica content of water from hot springs and wet-steam wells. Am. J. Sci. 264, 685–697. https://doi.org/10.2475/ajs.264.9.685.

Fournier, R.O., White, D.E., Truesdell, A.H., 1976. Convective heat flow in Yellowstone National Park. In: Proceedings of the 2nd UN Symposium on the Development and Use of Geothermal Resources, San Francisco, pp. 731–739.

Friedman, I., Norton, D.R., 2007. Is Yellowstone Losing Its Steam. Integr. Geosci. Stud. Gt. Yellowstone Area Volcanic. Hydrothermal Tecton. Process. Yellowstone Ecosyst. 1717, 271–298.

Frondini, F., Caliro, S., Cardellini, C., Chiodini, G., Morgantini, N., 2009. Carbon dioxide degassing and thermal energy release in the Monte Amiata volcanic-geothermal area (Italy). Appl. Geochem. 24, 860–875. https://doi.org/10.1016/j.apgeochem.2009.01.010.

Gemici, Ü., Tarcan, G., 2002. Hydrogeochemistry of the Simav geothermal field, western Anatolia, Turkey. J. Volcanol. Geotherm. Res. 116, 215–233. https://doi.org/10.1016/S0377-0273(02)00217-2.

Gentry, W.M., Burbey, T.J., 2004. Characterization of ground water flow from spring discharge in a crystalline rock environment. J. Am. Water Resour. Assoc. 40, 1205–1217. https://doi.org/10.1111/j.1752-1688.2004.tb01580.x.

Giggenbach, W.F., 1988. Geothermal solute equilibria. Derivation of Na-K-Mg-Ca geoindicators. Geochim. Cosmochim. Acta 52, 2749–2765. https://doi.org/10.1016/0016-7037(88)90143-3.

Gilfillan, S.M.V., Wilkinson, M., Haszeldine, R.S., Shipton, Z.K., Nelson, S.T., Poreda, R. J., 2011. He and Ne as tracers of natural CO2 migration up a fault from a deep reservoir. Int. J. Greenh. Gas Control 5, 1507–1516. https://doi.org/10.1016/j.ijggc.2011.08.008.

Goff, F., Shevenell, L., 1987. Travertine deposits of Soda Dam, New Mexico, and their implications for the age and evolution of the Valles caldera hydrothermal system (USA). Geol. Soc. Am. Bull. 99, 292–302. https://doi.org/10.1130/0016-7606(1987)99<292:TDOSDN>2.0.CO;2.

Goff, F., McMurtry, G.M., Counce, D., Simac, J.A., Roldán-Manzo, A.R., Hilton, D.R., 2000. Contrasting hydrothermal activity at Sierra Negra and Alcedo volcanoes, Galapagos Archipelago. Ecuador. Bull. Volcanol. 62, 34–52. https://doi.org/10.1007/s004450050289.

Goldscheider, N., Meiman, J., Pronk, M., Smart, C., 2008. Tracer tests in karst hydrogeology and speleology. Int. J. Speleol. 37, 27–40. https://doi.org/10.5038/1827-806X.37.1.3.

Grant, N.T., 2020. Stochastic modelling of fault gouge zones: implications for fault seal analysis. Geol. Soc. Lond., Spec. Publ. 496 (1), 163–197.

Grobe, M., Machel, H.G., 2002. Saline groundwater in the Münsterland Cretaceous Basin, Germany: Clues to its origin and evolution. Mar. Pet. Geol. 19, 307–322. https://doi.org/10.1016/S0264-8172(02)00019-3.

Gudmundsson, A., 2000. Active fault zones and groundwater flow. Geophys. Res. Lett. 27, 2993–2996. https://doi.org/10.1029/1999GL011266.

Hancock, P.L., Chalmers, R.M.L., Altunel, E., Çakir, Z., 1999. Travitonics: Using travertines in active fault studies. J. Struct. Geol. 21, 903–916. https://doi.org/10.1016/S0191-8141(99)00061-9.

Haselwimmer, C., Prakash, A., Holdmann, G., 2013. Quantifying the heat flux and outflow rate of hot springs using airborne thermal imagery: case study from Pilgrim Hot Springs, Alaska. Remote Sens. Environ. 136, 37–46. https://doi.org/10.1016/j.rse.2013.04.008.

Haszeldine, R.S., Quinn, O., England, G., Wilkinson, M., Shipton, Z.K., Evans, J.P., Heath, J., Crossey, L., Ballentine, C.J., Graham, C.M., 2005. Natural geochemical analogues for carbon dioxide storage in deep geological porous reservoirs, a United Kingdom perspective. Oil Gas Sci. Technol. 60, 33–49. https://doi.org/10.2516/ogst:2005004.

Hatch, C.E., Fisher, A.T., Revenaugh, J.S., Constantz, J., Ruehl, C., 2006. Quantifying surface water-groundwater interactions using time series analysis of streambed thermal records: method development. Water Resour. Res. 42, 1–14. https://doi.org/10.1029/2005WR004787.

Hatton, T., Evans, R., 1998. Dependence of Ecosystems on Groundwater and its Significance to Australia. L. Water Resour. 12 (98), 77.

Heasler, H.P., Jaworowski, C., Foley, D., 2009. Geothermal systems and monitoring hydrothermal features. Geol. Monit. 105–140.

Heinicke, J., Koch, U., 2000. Slug flow - A possible explanation for hydrogeochemical earthquake precursors at Bad Brambach, Germany. Pure Appl. Geophys. 157, 1621–1641. https://doi.org/10.1007/pl00001053.

Held, S., Schill, E., Schneider, J., Nitschke, F., Morata, D., Neumann, T., Kohl, T., 2018. Geochemical characterization of the geothermal system at Villarrica volcano, Southern Chile; Part 1: impacts of lithology on the geothermal reservoir. Geothermics 74, 226–239. https://doi.org/10.1016/j.geothermics.2018.03.004.

Henchiri, M., Ben Ahmed, W., Brogi, A., Alçiçek, M.C., Benassi, R., 2017. Evolution of pleistocene travertine depositional system from terraced slope to fissure-ridge in a mixed travertine-alluvial succession (Jebel El Mida, Gafsa, Southern Tunisia). Geodin. Acta 29, 20–41. https://doi.org/10.1080/09853111.2016.1265398.

Herbert, A.W., 1996. Modelling Approaches for Discrete Fracture Network Flow Analysis, pp. 213–229. https://doi.org/10.1016/S0165-1250(96)80027-7.

Hochstein, M.P., Nixon, I.M., 1979. Geophysical study of the Hauraki depression, North Island, New Zealand. New Zeal. J. Geol. Geophys. 22, 1–19. https://doi.org/10.1080/00288306.1979.10422550.

Hoke, L., Poreda, R., Reay, A., Weaver, S.D., 2000. The subcontinental mantle beneath southern New Zealand, characterised by helium isotopes in intraplate basalts and

gas-rich springs. Geochim. Cosmochim. Acta 64, 2489–2507. https://doi.org/10.1016/S0016-7037(00)00346-X.
Hsieh, P.A., Freckleton, J.R., 1993. Documentation of a computer program to simulate horizontal-flow barriers using the U.S. Geological Survey's modular three-dimensional finite-difference ground-water flow model. In: Open-File Report 92-477. California, USA.
Huang, H., Chen, Z., Wang, T., Xiang, C., Zhang, L., Zhou, G., Sun, B., Wang, Y., 2019. Nitrate distribution and dynamics as indicators to characterize karst groundwater flow in a mined mineral deposit in southwestern China. Hydrogeol. J. 27, 2077–2089. https://doi.org/10.1007/s10040-019-01987-0.
Humphreys, W.F., 2009. Hydrogeology and groundwater ecology: Does each inform the other? Hydrogeol. J. 17, 5–21. https://doi.org/10.1007/s10040-008-0349-3.
Hynes, H., 1970. The Ecology of Running Waters. University of Toronto Press.
Ingebritsen, S.E., Sherrod, D.R., Mariner, R.H., 1992. Rates and patterns of groundwater flow in the Cascade Range Volcanic Arc, and the effect on subsurface temperatures. J. Geophys. Res. 97, 4599. https://doi.org/10.1029/91JB03064.
Ingebritsen, S.E., Galloway, D.L., Colvard, E.M., Sorey, M.L., Mariner, R.H., 2001. Time-variation of hydrothermal discharge at selected sites in the Western United States: implications for monitoring. J. Volcanol. Geotherm. Res. 111, 1–23. https://doi.org/10.1016/S0377-0273(01)00207-4.
Inverarity, K., Heinson, G., Hatch, M., 2016. Groundwater flow underneath mound spring tufas from geophysical surveys in the southwestern Great Artesian Basin, Australia. Aust. J. Earth Sci. 63, 857–872. https://doi.org/10.1080/08120099.2016.1261942.
Irvine, D.J., Lautz, L.K., Briggs, M.A., Gordon, R.P., McKenzie, J.M., 2015. Experimental evaluation of the applicability of phase, amplitude, and combined methods to determine water flux and thermal diffusivity from temperature time series using VFLUX 2. J. Hydrol. 531, 728–737. https://doi.org/10.1016/j.jhydrol.2015.10.054.
Irvine, D.J., Briggs, M.A., Lautz, L.K., Gordon, R.P., McKenzie, J.M., Cartwright, I., 2017. Using diurnal temperature signals to infer vertical groundwater-surface water exchange. Groundwater 55 (1), 10–26. https://doi.org/10.1111/gwat.12459.
Irvine, D.J., Kurylyk, B.L., Briggs, M.A., 2020. Quantitative guidance for efficient vertical flow measurements at the sediment–water interface using temperature–depth profiles. Hydrol. Process. 34, 649–661. https://doi.org/10.1002/hyp.13614.
Islam, M.S., Manzocchi, T., 2021. A novel flow-based geometrical upscaling method for representing fault zones with two-phase fault rock properties into a dynamic reservoir model. Sci. Rep. 11 (1) https://doi.org/10.1038/s41598-021-99024-2.
Jewell, P.W., Rahn, T.A., Bowman, J.R., 1994. Hydrology and chemistry of thermal waters near wells, Nevada. Ground Water 32, 657–665. https://doi.org/10.1111/j.1745-6584.1994.tb00902.x.
Karaisaoğlu, S., Orhan, H., 2018. Sedimentology and geochemistry of the Kavakköy Travertine (Konya, central Turkey). Carbonates Evaporites 33, 783–800. https://doi.org/10.1007/s13146-018-0436-z.
Kavousi, A., Reimann, T., Liedl, R., Raeisi, E., 2020. Karst aquifer characterization by inverse application of MODFLOW-2005 CFPv2 discrete-continuum flow and transport model. J. Hydrol. 587, 124922 https://doi.org/10.1016/j.jhydrol.2020.124922.
Kazemi, G.A., Lehr, J.H., Perrochet, P., 2006. Groundwater Age. John Wiley & Sons.
Keegan-Treloar, R., Werner, A.D., Irvine, D.J., Banks, E.W., 2021. Application of Indicator Kriging to hydraulic head data to test alternative conceptual models for spring source aquifers. J. Hydrol. 601, 126808 https://doi.org/10.1016/j.jhydrol.2021.126808.
Keery, J., Binley, A., Crook, N., Smith, J.W.N., 2007. Temporal and spatial variability of groundwater-surface water fluxes: development and application of an analytical method using temperature time series. J. Hydrol. 336, 1–16. https://doi.org/10.1016/j.jhydrol.2006.12.003.
Keppel, M.N., Clarke, J.D.A., Halihan, T., Love, A.J., Werner, A.D., 2011. Mound springs in the arid Lake Eyre South region of South Australia: A new depositional tufa model and its controls. Sediment. Geol. 240, 55–70. https://doi.org/10.1016/j.sedgeo.2011.08.001.
Kharaka, Y.K., Mariner, R.H., 1989. Chemical geothermometers and their application to formation waters from sedimentary basins. In: Thermal History of Sedimentary Basins. Springer New York, New York, NY, pp. 99–117. https://doi.org/10.1007/978-1-4612-3492-0_6.
King, C.Y., Basler, D., Presser, T.S., Evans, W.C., White, L.D., Minissale, A., 1994. In search of earthquake-related hydrologic and chemical changes along Hayward Fault. Appl. Geochem. 9, 83–91. https://doi.org/10.1016/0883-2927(94)90055-8.
Kresic, N., 2010. Types and classifications of springs. In: Groundwater Hydrology of Springs. Elsevier Inc, pp. 31–85. https://doi.org/10.1016/B978-1-85617-502-9.00002-5.
Kuo, T., Fan, K., Kuochen, H., Han, Y., Chu, H., Lee, Y., 2006. Anomalous decrease in groundwater radon before the Taiwan M6.8 Chengkung earthquake. J. Environ. Radioact. 88, 101–106. https://doi.org/10.1016/j.jenvrad.2006.01.005.
Kurylyk, B.L., Irvine, D.J., 2019. Heat: an overlooked tool in the practicing hydrogeologist's toolbox. Groundwater 57 (4), 517–524. https://doi.org/10.1111/gwat.12910.
Kurylyk, B.L., Irvine, D.J., Bense, V.F., 2019. Theory, tools, and multidisciplinary applications for tracing groundwater fluxes from temperature profiles. Wiley Interdiscip. Rev. Water 6 (1). https://doi.org/10.1002/wat2.1329.
La Rosa, A., Pagli, C., Keir, D., Sani, F., Corti, G., Wang, H., Possee, D., 2019. Observing oblique slip during rift linkage in Northern Afar. Geophys. Res. Lett. 46, 10782–10790. https://doi.org/10.1029/2019GL084801.
Lewandowski, J., Angermann, L., Nützmann, G., Fleckenstein, J.H., 2011. A heat pulse technique for the determination of small-scale flow directions and flow velocities in the streambed of sand-bed streams. Hydrol. Process. 25, 3244–3255. https://doi.org/10.1002/hyp.8062.
Lewis, M., White, D., Gotch, T., 2013. Allocating Water and Maintaining Springs in the Great Artesian Basin: Spatial Survey and Remote Sensing of Artesian Springs of the Western Great Artesian Basin. Canberra.
Li, X., Li, D., Xu, Y., Feng, X., 2020. A DFN based 3D numerical approach for modeling coupled groundwater flow and solute transport in fractured rock mass. Int. J. Heat Mass Transf. 149 https://doi.org/10.1016/j.ijheatmasstransfer.2019.119179.
Li, Y., Werner, A.D., Wen, A., Zhu, Q., 2022. Solute transport in permeable porous media containing a preferential flow feature: Investigation of non-Darcian flow effects. J. Hydrol. 604 https://doi.org/10.1016/j.jhydrol.2021.127210.
Liu, N., Pan, L., Cheng, J., 2017. Numerical modeling of CO2 and brine leakage through open fracture in a fault zone: open channel flow or darcy flow. Geofluids 2017. https://doi.org/10.1155/2017/9035032.
López, D.L., Smith, L., 1995. Fluid flow in fault zones: analysis of the interplay of convective circulation and topographically driven groundwater flow. Water Resour. Res. 31, 1489–1503. https://doi.org/10.1029/95WR00422.
López, D.L., Smith, L., 1996. Fluid flow in fault zones: influence of hydraulic anisotropy and heterogeneity on the fluid flow and heat transfer regime. Water Resour. Res. 32, 3227–3235. https://doi.org/10.1029/96WR02101.
Love, A., Shand, P., Crossey, L., Harrington, G., Rousseau-Gueutin, P., 2013a. Allocating Water and Maintaining Springs in the Great Artesian Basin: Groundwater Discharge of the Western Great Artesian Basin. Canberra.
Love, A.J., Shand, P., Karlstrom, K., Crossey, L., Rousseau-Gueutin, P., Priestley, S., Wholing, D., Fulton, S., Keppel, M., 2013b. Geochemistry and travertine dating provide new insights into the hydrogeology of the great Artesian Basin, South Australia. Proc. Earth Planet. Sci. 7, 521–524. https://doi.org/10.1016/j.proeps.2013.03.065.
Luhmann, A.J., Covington, M.D., Alexander, S.C., Chai, S.Y., Schwartz, B.F., Groten, J.T., Alexander, E.C., 2012. Comparing conservative and nonconservative tracers in karst and using them to estimate flow path geometry. J. Hydrol. 448–449, 201–211. https://doi.org/10.1016/j.jhydrol.2012.04.044.
Lupton, N., Janardhanan, S., Connell, L.D., Pickett, T., 2019. Improving groundwater models to better represent coal seam gas extraction impacts in the Namoi region. In: CSIRO Report Number EP193251. CSIRO, Canberra.
Magri, F., Akar, T., Gemici, U., Pekdeger, A., 2010. Deep geothermal groundwater flow in the Seferihisar-Balçova area, Turkey: results from transient numerical simulations of coupled fluid flow and heat transport processes. Geofluids 10, 388–405. https://doi.org/10.1111/j.1468-8123.2009.00267.x.
Magri, F., Akar, T., Gemici, U., Pekdeger, A., 2012. Numerical investigations of fault-induced seawater circulation in the Seferihisar-Balçova Geothermal system, western Turkey. Hydrogeol. J. 20, 103–118. https://doi.org/10.1007/s10040-011-0797-z.
Manga, M., 1997. A model for discharge in spring-dominated streams and implications for the transmissivity and recharge of quaternary volcanics in the Oregon Cascades. Water Resour. Res. 33, 1813–1822. https://doi.org/10.1029/97WR01339.
Manga, M., 1999. On the timescales characterizing groundwater discharge at springs. J. Hydrol. 219, 56–69. https://doi.org/10.1016/S0022-1694(99)00044-X.
Manzocchi, T., Walsh, J.J., Nell, P., Yielding, G., 1999. Fault transmissibility multipliers for flow simulation models. Pet. Geosci. 5, 53–63. https://doi.org/10.1144/petgeo.5.1.53.
Manzocchi, T., Childs, C., Walsh, J.J., 2010. Faults and fault properties in hydrocarbon flow models. Geofluids 10 (1-2), 94–113. https://doi.org/10.1111/j.1468-8123.2010.00283.x.
Mariner, R.H., Presser, T.S., Evans, W.C., Pringle, M.K.W., 1990. Discharge rates of fluid and heat by thermal springs of the Cascade Range, Washington, Oregon, and northern California. J. Geophys. Res. 95, 19517–19531. https://doi.org/10.1029/JB095iB12p19517.
Marshall, S.K., Cook, P.G., Konikow, L.F., Simmons, C.T., Dogramaci, S., 2020. Conjoint use of hydraulic head and groundwater age data to detect hydrogeologic barriers. Hydrogeol. J. 28, 1003–1019. https://doi.org/10.1007/s10040-019-02095-9.
Martínez-Santos, P., Díaz-Alcaide, S., Castaño-Castaño, S., Hernández-Espriú, A., 2014. Modelling discharge through artesian springs based on a high-resolution piezometric network. Hydrol. Process. 28, 2251–2261. https://doi.org/10.1002/hyp.9760.
Marty, B., 1995. Nitrogen content of the mantle inferred from N2–Ar correlation in oceanic basalts. Nature 377, 326–329. https://doi.org/10.1038/377326a0.
Marty, B., Dauphas, N., 2003. The nitrogen record for crust-mantle interaction and mantle convection from Archean to Present. Earth Planet. Sci. Lett. 206, 397–410. https://doi.org/10.1016/S0012-821X(02)01108-1.
Mas-Pla, J., Trilla, J., Valls, M.L., 1992. Radiocarbon dating of travertines precipitated from freshwater. Radiocarbon 34, 677–685. https://doi.org/10.1017/S0033822200063967.
Mathon, B.R., Schoonen, M.A., Riccardi, A.L., Borda, M.J., 2015. Measuring flow rates and characterizing flow regimes in hot springs. Appl. Geochem. 62, 234–246. https://doi.org/10.1016/j.apgeochem.2015.04.007.
McCallum, J., Simmons, C., Mallants, D., Batelaan, O., 2018. Simulating the Groundwater Flow Dynamics of Fault Zones: A Comparison of Methods for Representing Fault Properties and a Regional Implementation.
McCallum, J.L., Noorduijn, S.L., Simmons, C.T., 2021. Including vertical fault structures in layered groundwater flow models. Groundwater 59 (6), 799–807. https://doi.org/10.1111/gwat.13120.
McMorran, C., 2008. Understanding the "heritage" in heritage tourism: ideological tool or economic tool for a Japanese hot springs resort? Tour. Geogr. 10, 334–354. https://doi.org/10.1080/14616680802236329.
Medici, G., Smeraglia, L., Torabi, A., Botter, C., 2021. Review of modeling approaches to groundwater flow in deformed carbonate aquifers. Groundwater 59, 334–351. https://doi.org/10.1111/gwat.13069.
Meinzer, O.E., 1923. Outline of Ground-Water Hydrology, with Definitions.

Meyer, A., Meyer, E.I., 2000. Discharge regime and the effect of drying on macroinvertebrate communities in a temporary karst stream in East Westphalia (Germany). Aquat. Sci. 62, 216–231. https://doi.org/10.1007/PL00001333.
Michie, E.A.H., Yielding, G., Fisher, Q.J., 2018. Predicting Transmissibilities of Carbonate-hosted Fault Zones. https://doi.org/10.1144/SP459.9.
Mitchell, T.M., Faulkner, D.R., 2009. The nature and origin of off-fault damage surrounding strike-slip fault zones with a wide range of displacements: a field study from the Atacama fault system, northern Chile. J. Struct. Geol. 31, 802–816. https://doi.org/10.1016/j.jsg.2009.05.002.
Noorduijn, S.L., Cook, P.G., Simmons, C.T., Richardson, S.B., 2018. Protecting groundwater levels and ecosystems with simple management approaches. Hydrogeol. J. 27, 225–237. https://doi.org/10.1007/s10040-018-1849-4.
Norton, D.R., Friedman, I., 1985. Chloride flux out of Yellowstone National Park. J. Volcanol. Geotherm. Res. 26, 231–250. https://doi.org/10.1016/0377-0273(85)90058-7.
OGIA, 2019. Groundwater Modelling Report – Surat Cumulative Management Area. Brisbane.
OGIA, 2020. Hydrogeological Characterisation of Faults in the Surat Basin Assessing Fault-Induced Connectivity between the Walloon Coal Measures and Adjacent Aquifers.
Olarinoye, T., Gleeson, T., Marx, V., Seeger, S., Adinehvand, R., Allocca, V., Andreo, B., Apaéstegui, J., Apolit, C., Arfib, B., Auler, A., Barberá, J.A., Batiot-Guilhe, C., Bechtel, T., Binet, S., Bittner, D., Blatnik, M., Bolger, T., Brunet, P., Charlier, J.B., Chen, Z., Chiogna, G., Coxon, G., De Vita, P., Doummar, J., Epting, J., Fournier, M., Goldscheider, N., Gunn, J., Guo, F., Guyot, J.L., Howden, N., Huggenberger, P., Hunt, B., Jeannin, P.Y., Jiang, G., Jones, G., Jourde, H., Karmann, I., Koit, O., Kordilla, J., Labat, D., Ladouche, B., Liso, I.S., Liu, Z., Massei, N., Mazzilli, N., Mudarra, M., Parise, M., Pu, J., Ravbar, N., Sanchez, L.H., Santo, A., Sauter, M., Sivelle, V., Skoglund, R.Ø., Stevanovic, Z., Wood, C., Worthington, S., Hartmann, A., 2020. Global karst springs hydrograph dataset for research and management of the world's fastest-flowing groundwater. Sci. Data 7, 1–9. https://doi.org/10.1038/s41597-019-0346-5.
Panday, S., Langevin, C.D., Niswonger, R.G., Ibaraki, M., Hughes, J.D., 2017. MODFLOW-USG version 1.4.00: an unstructured grid version of MODFLOW for simulating groundwater flow and tightly coupled processes using a control volume finite-difference formulation: U.S. Geological Survey Software Release, 27 October 2017. https://doi.org/10.5066/F7R20ZFJ.
Ponder, W., 1986. Mound Springs of the Great Artesian Basin. Limnology in Australia.
Ponder, W., Colgan, D., 2002. What makes a narrow-range taxon? Insights from Australian freshwater snails. Invertebr. Syst. 16, 571–582.
Post, V.E.A., von Asmuth, J.R., 2013. Review: Hydraulic head measurements—new technologies, classic pitfalls. Hydrogeol. J. 21, 737–750. https://doi.org/10.1007/s10040-013-0969-0.
Poulet, T., Lesueur, M., Kelka, U., 2021. Dynamic modelling of overprinted low-permeability fault cores and surrounding damage zones as lower dimensional interfaces for multiphysics simulations. Comput. Geosci. 150 https://doi.org/10.1016/j.cageo.2021.104719.
Priestley, S.C., Karlstrom, K.E., Love, A.J., Crossey, L.J., Polyak, V.J., Asmerom, Y., Meredith, K.T., Crow, R., Keppel, M.N., Habermehl, M.A., 2018. Uranium series dating of Great Artesian Basin travertine deposits: Implications for palaeohydrogeology and palaeoclimate. Palaeogeogr. Palaeoclimatol. Palaeoecol. 490, 163–177. https://doi.org/10.1016/j.palaeo.2017.10.024.
Qian, J.Z., Wang, M., Zhang, Y., Yan, X.S., Zhao, W.D., 2015. Experimental study of the transition from non-Darcian to Darcy behavior for flow through a single fracture. J. Hydrodyn. 27, 679–688. https://doi.org/10.1016/S1001-6058(15)60530-3.
Quinn, P.M., Cherry, J.A., Parker, B.L., 2020. Relationship between the critical Reynolds number and aperture for flow through single fractures: evidence from published laboratory studies. J. Hydrol. 581, 124384 https://doi.org/10.1016/j.jhydrol.2019.124384.
Rau, G.C., Post, V.E.A., Shanafield, M., Krekeler, T., Banks, E.W., Blum, P., 2019. Error in hydraulic head and gradient time-series measurements: a quantitative appraisal. Hydrol. Earth Syst. Sci. 23, 3603–3629. https://doi.org/10.5194/hess-23-3603-2019.
Reimann, T., Rehrl, C., Shoemaker, W.B., Geyer, T., Birk, S., 2011. The significance of turbulent flow representation in single-continuum models. Water Resour. Res. 47, 1–15. https://doi.org/10.1029/2010WR010133.
Revil, A., Karaoulis, M., Johnson, T., Kemna, A., 2012. Review: some low-frequency electrical methods for subsurface characterization and monitoring in hydrogeology. Hydrogeol. J. 20, 617–658. https://doi.org/10.1007/s10040-011-0819-x.
Robinson, N.I., Werner, A.D., 2017. On concentrated solute sources in faulted aquifers. Adv. Water Resour. 104, 255–270. https://doi.org/10.1016/j.advwatres.2017.04.008.
Romano, V., De'Haven Hyman, J., Karra, S., Valocchi, A.J., Battaglia, M., Bigi, S., 2017. Numerical modeling of fluid flow in a fault zone: A case of study from Majella Mountain (Italy). Energy Procedia 125, 556–560. https://doi.org/10.1016/j.egypro.2017.08.191.
Romano, V., Bigi, S., Carnevale, F., De'Haven Hyman, J., Karra, S., Valocchi, A.J., Tartarello, M.C., Battaglia, M., 2020. Hydraulic characterization of a fault zone from fracture distribution. J. Struct. Geol. 135, 104036 https://doi.org/10.1016/j.jsg.2020.104036.
Rossini, R.A., Fensham, R.J., Stewart-Koster, B., Gotch, T., Kennard, M.J., 2018. Biogeographical patterns of endemic diversity and its conservation in Australia's artesian desert springs. Divers. Distrib. 24, 1199–1216. https://doi.org/10.1111/ddi.12757.
Rowland, J.C., Manga, M., Rose, T.P., 2008. The influence of poorly interconnected fault zone flow paths on spring geochemistry. Geofluids 8, 93–101. https://doi.org/10.1111/j.1468-8123.2008.00208.x.
Saar, M.O., 2011. Review: Geothermal heat as a tracer of large-scale groundwater flow and as a means to determine permeability fields. Hydrogeol. J. 19, 31–52. https://doi.org/10.1007/s10040-010-0657-2.
Saar, M.O., Manga, M., 2004. Depth dependence of permeability in the Oregon Cascades inferred from hydrogeologic, thermal, seismic, and magmatic modeling constraints. J. Geophys. Res. Solid Earth 109, 1–19. https://doi.org/10.1029/2003JB002855.
Sakai, H., Matsubaya, O., 1974. Isotopic geochemistry of the thermal waters of Japan and its bearing on the Kuroko ore solutions. Econ. Geol. 69, 974–991. https://doi.org/10.2113/gsecongeo.69.6.974.
Saller, S.P., Ronayne, M.J., Long, A.J., 2013. Comparison of a karst groundwater model with and without discrete conduit flow. Hydrogeol. J. 21, 1555–1566. https://doi.org/10.1007/s10040-013-1036-6.
Sato, T., Sakai, R., Furuya, K., Kodama, T., 2000. Coseismic spring flow changes associated with the 1995 Kobe Earthquake. Geophys. Res. Lett. 27, 1219–1222. https://doi.org/10.1029/1999GL011187.
Scanlon, B.R., Mace, R.E., Barrett, M.E., Smith, B., 2003. Can we simulate regional groundwater flow in a karst system using equivalent porous media models? Case study, Barton Springs Edwards aquifer, USA. J. Hydrol. 276, 137–158. https://doi.org/10.1016/S0022-1694(03)00064-7.
Scibek, J., 2020. Multidisciplinary database of permeability of fault zones and surrounding protolith rocks at world-wide sites. Sci. Data 7, 1–14. https://doi.org/10.1038/s41597-020-0435-5.
Scibek, J., Gleeson, T., McKenzie, J.M., 2016. The biases and trends in fault zone hydrogeology conceptual models: global compilation and categorical data analysis. Geofluids 16, 782–798. https://doi.org/10.1111/gfl.12188.
Sebben, M.L., Werner, A.D., 2016a. A modelling investigation of solute transport in permeable porous media containing a discrete preferential flow feature. Adv. Water Resour. 94, 307–317. https://doi.org/10.1016/j.advwatres.2016.05.022.
Sebben, M.L., Werner, A.D., 2016b. On the effects of preferential or barrier flow features on solute plumes in permeable porous media. Adv. Water Resour. 98, 32–46. https://doi.org/10.1016/j.advwatres.2016.10.011.
Segadelli, S., Filippini, M., Monti, A., Celico, F., Gargini, A., 2021. Estimation of recharge in mountain hard-rock aquifers based on discrete spring discharge monitoring during base-flow recession. Hydrogeol. J. 29, 949–961.
Shoemaker, W.B., Kuniansky, E.L., Birk, S., Bauer, S., Swain, E.D., 2008. Documentation of a Conduit Flow Process (CFP) for MODFLOW-2005 A product of the Ground-Water Resources Program. U.S. Geol. Surv. Techniques 50.
Silcock, J.L., Tischler, M.K., Fensham, R.J., 2020. Oases at the gates of hell: Hydrogeology, cultural history and ecology of the mulligan river springs, far western queensland. Proc. R. Soc. Queensl. 126, 91–108.
Smith, H., Wood, P.J., Gunn, J., 2003. The influence of habitat structure and flow permanence on invertebrate communities in karst spring systems. Hydrobiologia 510, 53–66. https://doi.org/10.1023/B:HYDR.0000008501.55798.20.
Springer, A.E., Stevens, L.E., 2009. Spheres of discharge of springs. Hydrogeol. J. 17, 83–93. https://doi.org/10.1007/s10040-008-0341-y.
Swanson, S.K., Bahr, J.M., 2004. Analytical and numerical models to explain steady rates of spring flow. Ground Water 42, 747–759. https://doi.org/10.1111/j.1745-6584.2004.tb02728.x.
Taillefer, A., Soliva, R., Guillou-Frottier, L., Le Goff, E., Martin, G., Seranne, M., 2017. Fault-related controls on upward hydrothermal flow: An integrated geological study of the têt fault system, Eastern Pyrénées (France). Geofluids 2017. https://doi.org/10.1155/2017/8190109.
Taylor, C.J., Greene, E., 2005. Hydrogeologic Characterization and Methods Used in the Investigation of Karst Hydrology. F. Tech. Estim. Water Fluxes Between Surf. Water Gr. Water, pp. 75–114.
Thomann, J.A., Werner, A.D., Irvine, D.J., Currell, M.J., 2020. Adaptive management in groundwater planning and development: a review of theory and applications. J. Hydrol. 586, 124871 https://doi.org/10.1016/j.jhydrol.2020.124871.
Torabi, A., Johannessen, M.U., Ellingsen, T.S.S., 2019. Fault core thickness: insights from siliciclastic and carbonate rocks. Geofluids 2019. https://doi.org/10.1155/2019/2918673.
Turnadge, C., Mallants, D., Peeters, L., 2016. Aquitard and fault simulation approaches for use in regional-scale assessments of coal seam gas extraction impacts. In: SPE Asia Pacific Oil & Gas Conference and Exhibition. SPE, Perth. https://doi.org/10.2118/182463-MS.
Turnadge, C., Mallants, D., Peeters, L., 2018. Overview of Aquitard and Geological Fault Simulation Approaches in Regional Scale Assessments of Coal Seam Gas Extraction Impacts, Prepared by the Commonwealth Scientific and Industrial Research Organisation (CSIRO), Canberra.
Üner, S., Dogan, D.D., 2021. An integrated geophysical, hydrological, thermal approach to finite volume modelling of fault-controlled geothermal fluid circulation in Gediz Graben. Geothermics 90. https://doi.org/10.1016/j.geothermics.2020.102004.
van der Kamp, G., 1995. The hydrogeology of springs in relation to the biodiversity of spring fauna: a review. J. Kansas Entomol. Soc. 68, 4–17.
Vandersteen, G., Schneidewind, U., Anibas, C., Schmidt, C., Seuntjens, P., Batelaan, O., 2015. Determining groundwater-surface water exchange from temperature-time series: combining a local polynomial method with a maximum likelihood estimator. Water Resour. Res. 51, 922–939. https://doi.org/10.1002/2014WR015994.
Volatili, T., Zambrano, M., Cilona, A., Huisman, B.A.H., Rustichelli, A., Giorgioni, M., Vittori, S., Tondi, E., 2019. From fracture analysis to flow simulations in fractured carbonates: the case study of the Roman Valley Quarry (Majella Mountain, Italy). Mar. Pet. Geol. 100, 95–110. https://doi.org/10.1016/j.marpetgeo.2018.10.040.

Weatherill, D., Graf, T., Simmons, C.T., Cook, P.G., Therrien, R., Reynolds, D.A., 2008. Discretizing the fracture-matrix interface to simulate solute transport. Ground Water 46, 606–615. https://doi.org/10.1111/j.1745-6584.2007.00430.x.

Werner, A.D., Alcoe, D.W., Ordens, C.M., Hutson, J.L., Ward, J.D., Simmons, C.T., 2011. Current practice and future challenges in coastal aquifer management: flux-based and trigger-level approaches with application to an australian case study. Water Resour. Manag. 25, 1831–1853. https://doi.org/10.1007/s11269-011-9777-2.

White, D.C., Lewis, M.M., 2011. A new approach to monitoring spatial distribution and dynamics of wetlands and associated flows of Australian Great Artesian Basin springs using QuickBird satellite imagery. J. Hydrol. 408, 140–152. https://doi.org/10.1016/j.jhydrol.2011.07.032.

White, D.C., Lewis, M.M., Green, G., Gotch, T.B., 2016. A generalizable NDVI-based wetland delineation indicator for remote monitoring of groundwater flows in the Australian Great Artesian Basin. Ecol. Indic. 60, 1309–1320. https://doi.org/10.1016/j.ecolind.2015.01.032.

Williams, A.F., Holmes, J.W., 1978. A novel method of estimating the discharge of water from mound springs of the Great Artesian Basin, central Australia. J. Hydrol. 38, 263–272. https://doi.org/10.1016/0022.

Wilson, P., Smith, S., Povey, D., Harris, S., 2020. Ranking and selecting fault models using flow-indicator fault properties and simple streamline simulations. Pet. Geosci. 27 (2) https://doi.org/10.1144/petgeo2020-017.

Witherspoon, P.A., Wang, J.S.Y., Iwai, K., Gale, J.E., 1980. Validity of Cubic Law for fluid flow in a deformable rock fracture. Water Resour. Res. 16, 1016–1024. https://doi.org/10.1029/WR016i006p01016.

Woith, H., Barbosa, S., Gajewski, C., Steinitz, G., Piatibratova, O., Malik, U., Zschau, J., 2011. Periodic and transient radon variations at the Tiberias hot spring, Israel during 2000-2005. Geochem. J. 45, 473–482. https://doi.org/10.2343/geochemj.1.0147.

Wolaver, B.D., Diehl, T.M., 2011. Control of regional structural styles and faulting on Northeast Mexico spring distribution. Environ. Earth Sci. 62, 1535–1549. https://doi.org/10.1007/s12665-010-0639-7.

Wolaver, B.D., Priestley, S.C., Crossey, L.J., Karlstrom, K.E., Love, A.J., 2020. Elucidating sources to aridland Dalhousie Springs in the Great Artesian Basin (Australia) to inform conservation. Hydrogeol. J. 28, 279–296. https://doi.org/10.1007/s10040-019-02072-2.

Wood, P.J., Gunn, J., Smith, H., Abas-Kutty, A., 2005. Flow permanence and macroinvertebrate community diversity within groundwater dominated headwater streams and springs. Hydrobiologia 545, 55–64. https://doi.org/10.1007/s10750-005-2213-y.

Wu, Q., Xing, L.T., Ye, C.H., Liu, Y.Z., 2011. The influences of coal mining on the large karst springs in North China. Environ. Earth Sci. 64, 1513–1523. https://doi.org/10.1007/s12665-009-0376-y.

Xue, Y., Liu, Y., Dang, F., Liu, J., Ma, Z., Zhu, L., Yang, H., 2019. Assessment of the nonlinear flow characteristic of water inrush based on the Brinkman and Forchheimer seepage model. Water 11, 855. https://doi.org/10.3390/w11040855.

Yager, R.M., Plummer, L.N., Kauffman, L.J., Doctor, D.H., Nelms, D.L., Schlosser, P., 2013. Comparison of age distributions estimated from environmental tracers by using binary-dilution and numerical models of fractured and folded karst: Shenandoah Valley of Virginia and West Virginia, USA. Hydrogeol. J. 21, 1193–1217. https://doi.org/10.1007/s10040-013-0997-9.

Yeh, T.C.J., Lee, C.H., 2007. Time to change the way we collect and analyze data for aquifer characterization. Ground Water 45, 116–118. https://doi.org/10.1111/j.1745-6584.2006.00292.x.

Yeh, T.C.J., Lee, C.H., Hsu, K.C., Illman, W.A., Barrash, W., Cai, X., Daniels, J., Sudicky, E., Wan, L., Li, G., Winter, C.L., 2008. A view toward the future of subsurface characterization: CAT scanning groundwater basins. Water Resour. Res. 44, 1–9. https://doi.org/10.1029/2007WR006375.

Zha, Y., Yeh, T.C.J., Illman, W.A., Tanaka, T., Bruines, P., Onoe, H., Saegusa, H., Mao, D., Takeuchi, S., Wen, J.C., 2016. An application of hydraulic tomography to a large-scale fractured granite site, Mizunami, Japan. Groundwater 54, 793–804. https://doi.org/10.1111/gwat.12421.

Zhang, Z., Chen, Xi, Chen, Xunhong, Shi, P., 2013. Quantifying time lag of epikarst-spring hydrograph response to rainfall using correlation and spectral analyses. Hydrogeol. J. 21, 1619–1631. https://doi.org/10.1007/s10040-013-1041-9.

Zheng, X., Yang, Z., Wang, S., Chen, Y.F., Hu, R., Zhao, X.J., Wu, X.L., Yang, X.L., 2021. Evaluation of hydrogeological impact of tunnel engineering in a karst aquifer by coupled discrete-continuum numerical simulations. J. Hydrol. 597, 125765 https://doi.org/10.1016/j.jhydrol.2020.125765.

Journal of Hydrology 601 (2021) 126808

Contents lists available at ScienceDirect

Journal of Hydrology

journal homepage: www.elsevier.com/locate/jhydrol

Research papers

Application of Indicator Kriging to hydraulic head data to test alternative conceptual models for spring source aquifers

Robin Keegan-Treloar[a,*], Adrian D. Werner[a], Dylan J. Irvine[b,a], Eddie W. Banks[a]

[a] College of Science and Engineering and National Centre for Groundwater Research and Training, Flinders University, Adelaide, Australia
[b] Research Institute for the Environment and Livelihoods, Charles Darwin University, Darwin, Australia

A R T I C L E I N F O

This manuscript was handled by Corrado Corradini, Editor-in-Chief

Keywords:
Conceptual model testing
Interpolation methods
Measurement uncertainty
Ordinary indicator co-kriging
Geostatistics
Hydraulic heads

A B S T R A C T

Hydraulic head distributions can inform spring source-water characterisation by determining whether aquifers meet the thresholds required to sustain spring flow. Assessing hydraulic head data can be challenging in areas where data are sparsely distributed and subject to variable measurement uncertainty. Geostatistical methods can be used to estimate hydraulic head values at unmeasured locations with quantitative uncertainty estimates. While these methods have been applied extensively for hydraulic head estimation in management contexts, no studies have used these approaches for spring source-water conceptual model testing. In this study, an investigation into the hydraulic head distribution was conducted through the application of Ordinary Indicator Co-Kriging. Interpolated hydraulic head estimates were used to quantitatively assess the plausibility of source-aquifer conceptual models for the Doongmabulla Springs Complex (DSC), Queensland, Australia. The results offer insights into the likelihood of alternative source aquifers having adequate head to support flow to eight springs within the DSC. Probabilities of adequate head to support the springs ranged from 0.03 to 0.12 for the Permian Formations, compared to $<$0.01 to 0.49 for the Triassic Formations. Analyses indicated that the Triassic Formations are more likely to have adequate hydraulic head to support spring flow. However, significant uncertainty exists in the conceptual model assessment due to hydraulic head measurement scarcity, particularly in the vicinity of the springs. These findings have important implications given that the Permian Formations will be dewatered by the operation of the nearby Carmichael coal mine. The techniques employed here can inform conceptual model uncertainties arising from the interpretation of sparsely distributed hydraulic head datasets, a major benefit over traditional interpolation methods.

1. Introduction

In hydrogeological investigations, the development of conceptual models requires the synthesis of uncertain observations and expert knowledge, leading to multiple plausible conceptual models (Oreskes et al., 1994; Neuman and Wierenga, 2003). When mathematically modelled, alternative conceptual models may provide vastly different estimates of hydrogeological behaviour, despite comparable consistency with field observations (Oreskes et al. 1994; Bredehoeft 2003; Neuman and Wierenga, 2003). This leads to non-uniqueness in the mathematical representations of hydrogeological systems. The importance of considering alternative conceptual models has been recognised (Neuman and Wierenga, 2003; Bredehoeft, 2005; Enemark et al., 2019); however, such conceptual models are rarely considered in practice (Bredehoeft, 2005). Failure to consider alternative conceptual models is problematic, as it can result in underestimation of the uncertainty of predictions (e.g., hydraulic heads, groundwater fluxes, solute concentrations) (Enemark et al., 2019). The importance of considering conceptual model uncertainty for decision making is well recognised in management frameworks, such as adaptive management (e.g., Williams et al., 2009; Thomann et al., 2020).

Hydraulic head is a measure of fluid potential that is used to determine groundwater flow patterns (Freeze and Cherry, 1979) and to inform conceptual model development (Neuman and Wierenga, 2003). Hydraulic head measurements are typically sparsely distributed and collected infrequently with varying precision (Post and von Asmuth, 2013; Rau et al., 2019). Expert knowledge and mathematical models are invariably needed to interpret hydraulic head data and predict hydraulic heads at unmeasured locations. Hydraulic head data may be analysed manually by contouring (e.g., Salama et al., 1996; Siegel, 2008), or

* Corresponding author.
E-mail address: robin.keegantreloar@flinders.edu.au (R. Keegan-Treloar).

https://doi.org/10.1016/j.jhydrol.2021.126808
Received 25 May 2021; Received in revised form 21 July 2021; Accepted 7 August 2021
Available online 16 August 2021
0022-1694/

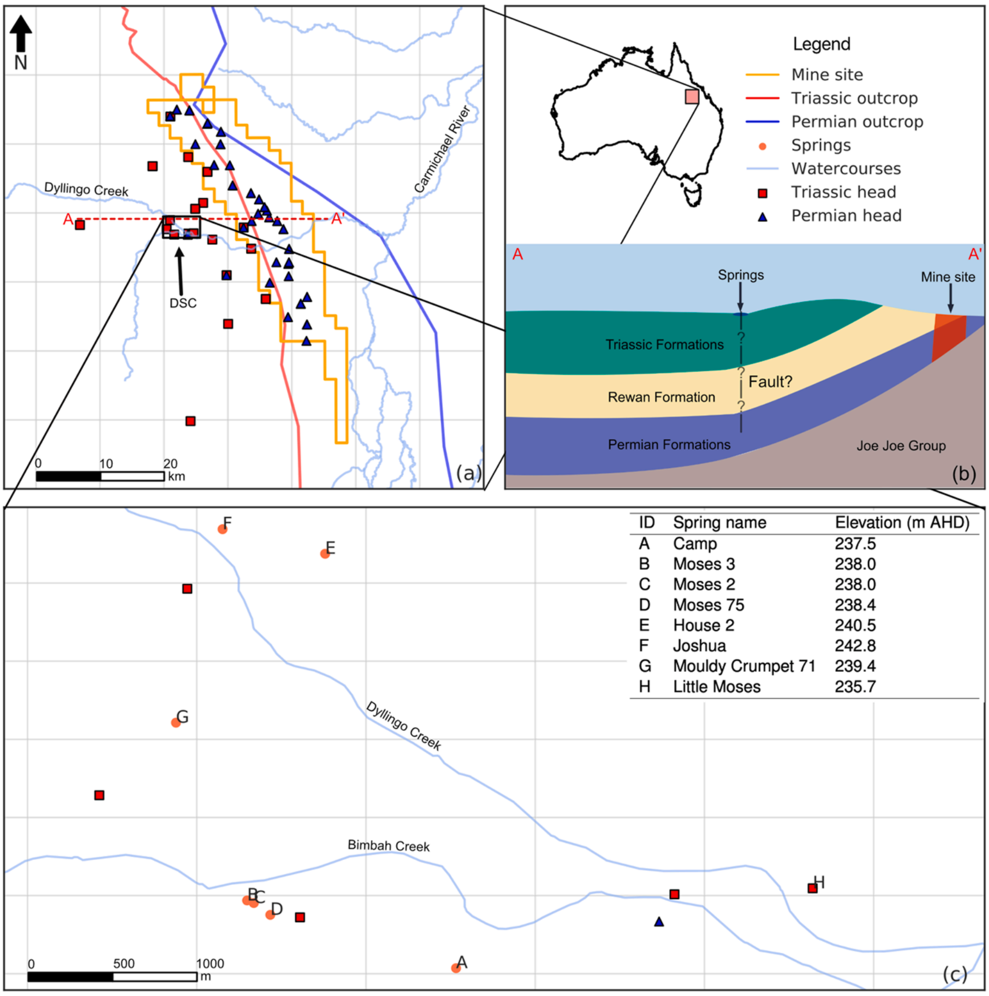

Fig. 1. Map of the study area, showing: (a) wells with hydraulic head measurements in the Permian and Triassic Formations and the formation extents, (b) a simplified conceptual diagram (not to scale) of the stratigraphy, and (c) the locations and SGT elevations of the eight DSC springs investigated in this study. The red line showing A-A′ in (a) is the approximate transect of (b). Spring elevations in (c) are relative to the Australian Height Datum (AHD), where 0 m AHD is approximately mean sea level. (For interpretation of the references to colour in this figure legend, the reader is referred to the web version of this article.)

through the use of automated mathematical approaches such as Kriging (e.g., Bastin and Gevers, 1985; Nikroo et al., 2010; Varouchakis and Hristopulos, 2013; Quay et al., 2020), or inverse distance weighted interpolation (e.g., Philip and Watson, 1986; Varouchakis and Hristopulos, 2013). By manually contouring hydraulic head data, hydrogeologists can include their understanding of the system into the interpretation (Kresic, 2006). For example, information on the subsurface hydrogeological features (e.g., faults or dykes), surface features (e.g., lakes or rivers), or physical properties (e.g., changes in hydraulic conductivity), may assist in the interpretation of regional flow directions, boundary effects (e.g., no-flow boundaries), and recharge/discharge stresses (Salama et al., 1996; Siegel, 2008). In contrast, automated techniques provide the ability to assess a wide range of alternative conceptual models through interpolation algorithms, which is generally infeasible with manual contouring. However, it is often challenging to include qualitative expert knowledge and understanding into automated analyses. Failure to consider expert knowledge and understanding can result in unrealistic interpretations of the hydraulic head (Salama et al., 1996; Siegel, 2008; Peeters et al., 2010). For example, in a case study of the Cuballing catchment, Western Australia, Salama et al. (1996) described hydraulic head predictions that intersect the surface elevation for unconfined aquifers.

Automated interpolation approaches applied to groundwater datasets include various forms of Kriging, which is used routinely to interpolate datasets in developing hydrogeological conceptual models. Journel (1983) developed a modified form of Kriging, Indicator Kriging (IK), whereby data are transformed to binary indicators of 1 for values less than or equal to a threshold value or 0 otherwise. The resulting indicators are termed 'indicator-transformed values'. The probability of a value less than or equal to the threshold value can be estimated at unmeasured locations by Kriging the indicator-transformed values. This process can be applied for a series of threshold values using Co-Kriging to estimate the conditional cumulative distribution function (CCDF) at unmeasured locations.

The IK technique makes no distribution assumptions and allows for a quantitative assessment of the uncertainty of predicted values at unmeasured locations (Journel, 1983). However, in cases of high measurement uncertainty, the use of a binary indicator transform (i.e., either 0 or 1) may be problematic as the measured values could plausibly be coded as either of the indicator values, leading to uncertainty in the indicator-transformed values. Furthermore, IK can result in predictions at unmeasured locations outside of the 0 to 1 bounds of probability (Journel, 1986). To address these limitations, Journel (1986) extended the technique to include expert knowledge in the form of constraints and prior probability distributions. The constraints ensure predictions lie within reasonable limits, while the prior probability distributions allow the inclusion of uncertain information based on observations or expert knowledge. In this way, IK provides the ability to overcome issues of unrealistic predictions and allows the user to include their qualitative expert knowledge into the modelling process.

In hydrogeology, IK has been widely applied to assess the probability of values of interest being above or below a chosen threshold based on a set of observations (e.g., Saito and Goovaerts, 2002; Liu et al., 2004; Lyon et al., 2006; Arslan, 2012; Anane et al., 2014; Chica-Olmo et al., 2014; Varouchakis et al., 2020). For example, IK has been used to compare contaminant concentrations with thresholds for remediation

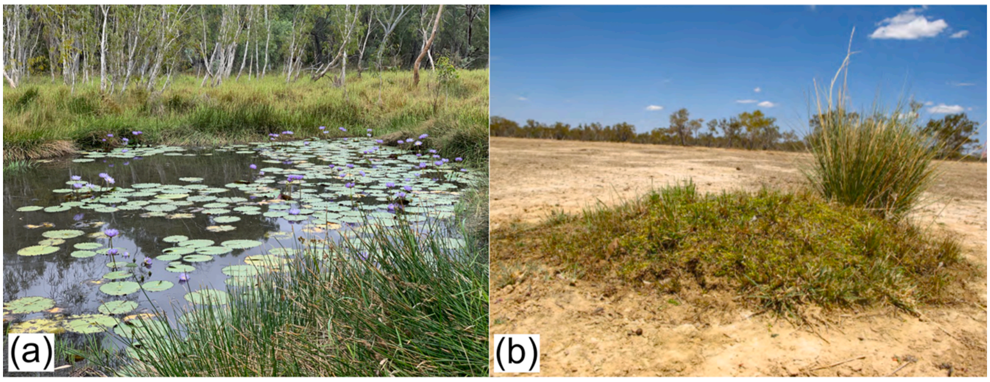

Fig. 2. (a) Little Moses, an outcrop spring at the DSC (Spring H; Fig. 1). (b) Mouldy Crumpet spring (Spring G; Fig. 1) at the DSC . reproduced with permission from Fensham et al. (2016)

(e.g., Saito and Goovaerts, 2002), to assess water quality parameters against guidelines for water use (e.g., Arslan, 2012; Anane et al., 2014; Chica-Olmo et al., 2014), and to evaluate the probability of saturated soil conditions (e.g., Lyon et al., 2006). IK has also been used to evaluate the probability of hydraulic heads dropping below a threshold value selected to avoid groundwater depletion (Varouchakis et al., 2020). Despite the widespread use of IK throughout the field of hydrogeology, we are unaware of any studies that have used IK to assess the probability of alternative aquifers having adequate hydraulic head to drive spring flow.

This study applies IK to hydraulic head data to assess the likelihood of alternative conceptual models relating to the source of discharge from a spring complex. The method evaluates the probability that an aquifer has adequate hydraulic head to meet a threshold required for spring flow. This threshold, referred to as the 'spring geomorphic threshold' (SGT), is defined as the topographical elevation in the vicinity of a spring vent that controls whether the spring will discharge to the surrounding landscape (Merrick, 2015; Currell et al., 2017).

The springs considered in this study are part of the ecologically and culturally significant Doongmabulla Springs Complex (DSC), located in Queensland, Australia (Fensham et al., 2016; Currell et al., 2017; Currell et al., 2020). The flow contribution to the DSC from underlying aquifers (i.e., the Triassic-aged and Permian-aged formations of the Galilee Basin) is disputed (Currell et al., 2017; Currell et al., 2020). Since the nearby Carmichael coal mine is expected to dewater the deeper Permian Formations to support mining activities (Currell et al., 2017; Currell et al., 2020), a better understanding of the water source to the DSC is essential for the ongoing conservation efforts.

2. Study area

The DSC is a collection of freshwater springs located in the Galilee Basin, Queensland, Australia (Fig. 1). The DSC provides water to an extensive wetland system, that is listed in the national directory of important wetlands in Australia (Environment Australia, 2001). These wetlands offer niche habitat for several endangered species and are culturally significant to the Wangan and Jagalingou people (Fensham et al., 2016; Currell et al., 2017).

The eight springs examined in this study (see Fig. 1c) were selected for being representative of the varying spring morphologies throughout the DSC. These springs were classified into two categories based on the spring morphology. The first category, discharge springs, are hypothesised to occur due to artesian discharge via vertical conduits in flatter areas (Fensham et al., 2016). In contrast, the second category, outcrop springs, are hypothesised to occur due to lateral discharge in areas of sloping topography, where the Triassic Formations outcrop (Fensham et al., 2016). The discharge springs show a variety of surface expressions; such as mounded vegetated areas with pooled water (e.g., springs B, C, D and E), a modified dam surrounding a spring vent (e.g., spring F), springs with discrete vents that discharge to wetland systems (e.g., Spring A), and small vegetated areas without visible pooled surface water (e.g., spring G, photograph shown in Fig. 2b). The outcrop spring examined in this study (spring H, photograph shown in Fig. 2a) did not have a visible discrete vent but rather a large pooled area (~100 m^2), which discharges to an extensive wetland system. The surface expression of the spring vent is important for characterising the SGTs, as they vary between springs surrounded by mounds or dams and those in flatter areas. In the case of discrete mound-form springs, the SGT is the minimum elevation of the mound over which spring water flows while, in flatter areas, with more diffuse springs, the SGT is simply the topographic elevation of the spring discharge point. The SGTs for the springs considered in this study were measured in May 2019 using a Trimble R10 Integrated GNSS System with a precision of 8 mm horizontal and 15 mm vertical (Trimble Navigation Limited, 2014).

The Triassic Formation aquifers (see Fig. 1b) consist of the Moolayember Formation, made up of sandstones and siltstones, the Clematis Formation, composed of siltstone, sandstone and mudstone, and the Dunda Beds, consisting of predominantly sandstone (AECOM, 2021). The Triassic Formations are separated from the Permian Formations by the Triassic-aged Rewan Formation (Fig. 1b), primarily composed of siltstone, fine-grained sandstone, clays and mudstone (AECOM, 2021). The Rewan Formation is considered a competent aquitard, at least in the areas where monitoring infrastructure has been installed (AECOM, 2021). The Permian Formations (Fig. 1b) consist of the Bandanna Formation, made up of lithic sandstone, siltstone, and coal seams, which overlies the Colinlea Sandstone, composed of quartz sandstone, conglomerate with minor shale, and coal seams (AECOM, 2021).

There are several proposed and active mining developments throughout the Galilee Basin that target the coal seams in the Permian Formations in areas where these formations outcrop along the edge of the basin. These developments include the currently under construction Carmichael coal mine, located approximately 8 km to the east of the DSC (Fig. 1a). The imminent mining operations will potentially dewater the Permian Formations that underlie the Triassic Rewan Formation aquitard (Fig. 1b) (Currell et al., 2017). The Triassic Formations, which outcrop to the west of the mine site, are unlikely to be impacted directly by the mine construction (Currell et al., 2017). However, it is currently unclear whether dewatering and associated reductions in hydraulic head in the Permian Formations will propagate through the Rewan Formation and impact the water levels in the Triassic Formations (Currell et al., 2017; CSIRO and Geoscience Australia, 2019). Furthermore, if the springs rely (even partially) on groundwater from the Permian Formations, mine-induced reductions in pressure could lead to the cessation of spring flow (Currell et al., 2017; Currell et al., 2020). Despite these concerns, the mine was approved (Currell et al., 2020).

Currently, there exist two conceptual models explaining the source of

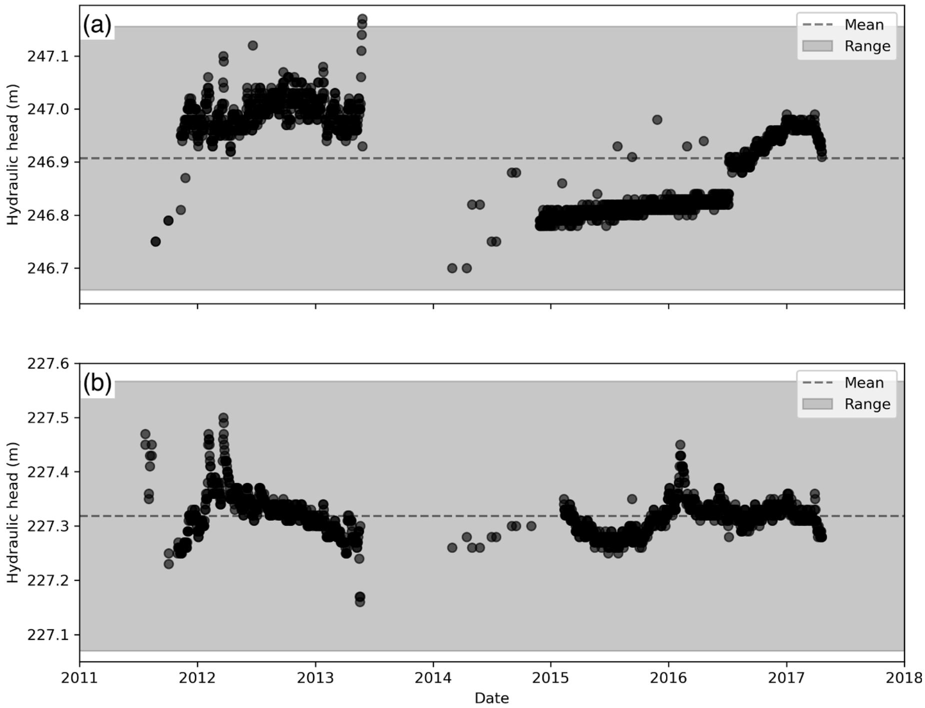

Fig. 3. Examples of hydraulic head time series with the mean (dashed line) and uncertainty ranges (grey shading) derived following the methods outlined in section 5.1. (a) shows well ID 158090_A in the Triassic Formations, while (b) shows well ID 158069_A in the Permian Formations.

water to the DSC (Currell et al., 2017). The first conceptualisation assumes that the Rewan Formation (see Fig. 1b) is a competent, laterally extensive aquitard comprised of sediments that do not allow significant vertical flow (Bradley, 2015). In this conceptual model, the DSC relies entirely on groundwater from the Triassic Formations (Bradley, 2015). The mine-induced drawdown in the Permian Formations will be less likely to impact the springs in this case (Bradley, 2015). The second conceptualisation proposes that the DSC may receive water, at least in part, from the Permian Formations via leakage or preferential flow (e.g., via faulting) through the Rewan Formation (Webb, 2015). In this case, the drawdown in the Permian Formations will more likely pose a significant threat to the long-term survival of the DSC (Webb, 2015). The outcomes of these previous studies highlight that further work is required to identify the potential risk of mine impacts on the springs.

3. Data sources

The data used in this study were collated from the Queensland Groundwater Database, the Department of State Development (2018) and the AECOM (2021) report. A total of 34 and 78 wells had available hydraulic head measurements in the Triassic and Permian Formations, respectively. Some of these wells featured extensive time-series of up to 10 years of daily measurements (6 and 39 in the Triassic and Permian, respectively), while others (28 and 39 in the Triassic and Permian, respectively) featured few (≤10) measurements. Fig. 3a displays the time-series data for well ID 158090_A in the Triassic Formations. The range of variability is relatively low (~0.6 m), indicating reasonably consistent hydraulic head conditions over the 7-year measurement period. Six wells in the Triassic Formations featured time-series data, and the temporal variability of these wells varied from ~1 m to ~0.2 m with an average range of ~0.4 m. The remaining 28 wells in the Triassic Formations featured few (≤10) or single measurements.

Fig. 3b shows hydraulic head time-series in well ID 158069_A in the Permian Formations. The period 2015 to mid-2017 displays a seasonal pattern with a range of 0.2 m. The hydraulic head values have a small range (~0.4 m), indicating that the groundwater conditions have remained relatively stable over the measurement period. In total, 39 wells in the Permian Formations had time-series data, and the range of measurements varied between <0.1 m and ~5 m with an average of ~1.9 m. The other 39 wells in the Permian Formations featured few (≤10) or single measurements. A table of the hydraulic head data available from each well in the Triassic and Permian Formations is provided as Supplementary Material 1.

4. Methods

The methodology aims to evaluate the likelihood that hypothesised spring source aquifers have sufficient hydraulic head to support discharge to eight springs in the DSC. This process can be separated into (i) assessing the uncertainty of the available hydraulic head measurements, (ii) transforming the hydraulic head data to indicator-transformed values relative to threshold values, (iii) characterising the semi-variance, and (iv) applying Ordinary Co-Kriging to make predictions at unmeasured locations.

4.1. Hydraulic head measurement uncertainty

Prior to the commencement of mine site dewatering in 2019, it was presumed that seasonal and random variations in head occur around a stationary mean value, and otherwise, the groundwater system was in a steady state. The steady-state assumption was reasonable, as there was limited groundwater abstraction in the area, and where multi-year records were available, the range was relatively small, on average approximately 0.4 and 1.9 m in the Triassic and Permian Formations, respectively (see Section 3). Where time-series data were available, the mean hydraulic head (denoted $\overline{h}(x)$) for each well was estimated as the arithmetic mean of pre-2019 records, except in the case of wells influenced by pumping or where only post-2019 records were available. In the case of pumping, the mean was estimated by discarding measurements that were believed to be influenced by pumping and estimating the mean. For wells that only featured post-2019 records, the earliest dated measurement was selected to represent the mean as this measurement was expected to be least impacted by mine site dewatering. In total, all Triassic wells and 73 Permian wells were estimated from the mean of pre-2019 records, while 3 Permian wells were interpreted to be influenced by pumping and 2 Permian wells featured only post-2019 records. Hydrographs and interpretations for each well are provided in Supplementary Material 2.

In this study, uncertainty is considered as a combination of accuracy and precision, whereby measurement precision is defined as the spread of measurements around the mean, and the measurement accuracy is the closeness of the mean to the true value (Post and von Asmuth, 2013). We consider explicitly the major factors expected to influence measurement uncertainty, including the temporal variability of hydraulic head measurements, the hydraulic head measurement technique, and the elevation survey method (Post and von Asmuth, 2013; Rau et al., 2019). Other sources of uncertainty are modelled implicitly using a nugget-effect parameter in the semi-variogram models (see Diggle et al., 1998).

The uncertainty due to the range of measurements above and below the mean was denoted as $\sigma_t(\boldsymbol{x})$, and where adequate data were available (i.e., >10 measurements), this was manually interpreted from hydrographs of the time-series data based on the range of measurements about the mean excluding clear outliers (e.g., measurements influenced by pumping). In cases with inadequate time-series (i.e., ≤10 measurements), values of 0.4 and 1.9 m were assigned based on the average of the ranges observed from time-series in the Triassic and Permian Formations, respectively. An additional 2 m of uncertainty was added to wells with single measurements (i.e., a total $\sigma_t(\boldsymbol{x})$ of 2.4 and 3.9 m for the Triassic and Permian, respectively) to reflect the uncertainty in groundwater levels following well construction and the lack of measurement repeatability.

Hydraulic head measurements were assigned an elevation survey uncertainty (denoted $\sigma_e(\boldsymbol{x})$), based on the elevation survey method detailed in the metadata. The reference elevation (e.g., top of casing) is the point from which water levels are measured at well locations and was presumed to be measured with three alternative levels of uncertainty: (1) high-precision survey ($\sigma_e(\boldsymbol{x}) = 0.04$ m; Garrido et al., 2011), (2) global positioning system ($\sigma_e(\boldsymbol{x}) = 1.8$ m; Wing and Frank, 2011), and (3) estimated elevation from Digital Elevation Model (DEM), for which $\sigma_e(\boldsymbol{x})$ was presumed to be 5 m, based on the average of the 'bare areas' and 'shrubland' scenarios described by Rexer and Hirt (2014). In the absence of a reported survey method, $\sigma_e(\boldsymbol{x})$ was set to 5 m, assuming the poorest precision method. These $\sigma_e(\boldsymbol{x})$ values were presumed to be normally distributed and were multiplied by 2 to construct intervals reflecting the range of plausible elevation values above and below the elevation measurement.

Measurement uncertainty arising from instrument error (denoted $\sigma_m(\boldsymbol{x})$) varies between measurement techniques, including dip meters, automated loggers, vibrating wire piezometers and drill stem tests (Rau et al., 2019). In the absence of detailed reporting on the instrument specification or data collection methods, a conservative approach was adopted by assigning measurements collected with dip meters, automated loggers or vibrating wire piezometers a value for $\sigma_m(\boldsymbol{x})$, consistent with the poorest precision method (i.e., dip meter with $\sigma_m(\boldsymbol{x}) = 8.4$ mm; Rau et al., 2019). These $\sigma_m(\boldsymbol{x})$ values were presumed to be normally distributed so were multiplied by 2 to construct intervals reflecting the range of plausible values around the measurement.

It was presumed that each of the considered sources of uncertainty (i.e., elevation survey method, water level measurement technique and temporal variability) were independent. Therefore, the range around the mean was estimated as:

$$\sigma_h(\boldsymbol{x}) = \sigma_t(\boldsymbol{x}) + \sigma_e(\boldsymbol{x}) + \sigma_m(\boldsymbol{x}) \tag{1}$$

4.2. Indicator transformation

The hydraulic head values for each well were converted to indicator-transformed values based on the probability of the measurement being less than or equal to a specified threshold value. A set of m hydraulic head threshold values were selected (denoted $\boldsymbol{a} = [a_1, \cdots, a_m]$) to discretise the range of plausible values at the spring locations. In our study, we defined 16 thresholds discretised with variable spacing starting with 7 SGT elevations (two springs shared the same threshold) and 9 equal p-quantiles from 0 to 1 derived from the empirical cumulative distribution function (ECDF) as described by Goovaerts (2009). Once the thresholds were defined, the probability of the hydraulic head measurement being less than or equal to a threshold value (denoted a_i) was estimated from the mean $\overline{h}(\boldsymbol{x})$ and range $\sigma_h(\boldsymbol{x})$ using the uniform cumulative distribution function (Grimmett and Stirzaker, 2020):

$$I(\boldsymbol{x}, a_i) = \begin{cases} 0, a_i < \overline{h}(\boldsymbol{x}) - \sigma_h(\boldsymbol{x})\Big/2 \\ \dfrac{a_i - \overline{(h}(\boldsymbol{x}) - \sigma_h(\boldsymbol{x})/2)}{\sigma_h(\boldsymbol{x})}, a_i \in \end{cases} \left[\overline{h}(\boldsymbol{x}) - \sigma_h(\boldsymbol{x})\Big/2, \overline{h}(\boldsymbol{x}) + \sigma_h(\boldsymbol{x})\Big/2\right] 1, a_i > \overline{h}(\boldsymbol{x}) + \sigma_h(\boldsymbol{x})\Big/2 \tag{2}$$

Where $I(\boldsymbol{x}, a_i)$ is the probability that a measurement is less than or equal to a_i.

4.3. Characterising the semi-variance

For Ordinary Co-Kriging, it is necessary to characterise the semi-variance of each variable and between each of the variables, which in the current study are indicator-transformed values. The experimental semi-variogram ($\gamma(\Delta x)$) consists of semi-variance values (γ) that are a function of distance between observation points, and is obtained from (Cressie, 1993):

$$\gamma(\Delta x) = \frac{1}{2|N(\Delta x)|} \sum_{N(\Delta x)} (I(\boldsymbol{x}_k, a_i) - I(\boldsymbol{x}_l, a_i))^2 \tag{3}$$

Here, $N(\Delta x)$ is a set of observation well pairs separated by Euclidean distance $||\boldsymbol{x}_k - \boldsymbol{x}_l|| = \Delta x$, $|N(\Delta x)|$ is the number of data pairs in $N(\Delta x)$, and $I(\boldsymbol{x}_k, a_i)$ and $I(\boldsymbol{x}_l, a_i)$ are the indicator-transformed hydraulic head values, for a threshold value a_i, at the locations $\boldsymbol{x}_k$ and $\boldsymbol{x}_l$, respectively. The semi-variogram is obtained by applying Eq. (3) to a set of values of Δx.

The semi-variance between variables (here, indicator-transformed hydraulic head values) can be assessed not only as a function of the distance between measurement sites (i.e., Eq. (3)) but also incorporating differences between values of $I(\boldsymbol{x}, a_i)$ that arise between elements of $\boldsymbol{a}$. This leads to a modified form of Eq. (3), whereby γ is calculated as a function of $I(\boldsymbol{x}, a_i)$ for alternate values within the vector $\boldsymbol{a}$ (i.e., a_i and a_j, where a_j is an alternate hydraulic head threshold value to a_i, both of which are elements of $\boldsymbol{a}$). This gives the experimental cross semi-variogram, $\gamma(\Delta x, a_{i,j})$, obtained as (Wackernagel, 1995):

$$\gamma(\Delta x, a_{i,j}) = \frac{1}{2|N(\Delta x)|} \sum_{N(\Delta x)} (I(\boldsymbol{x}_k, a_i) - I(\boldsymbol{x}_l, a_i))(I(\boldsymbol{x}_k, a_j) - I(\boldsymbol{x}_l, a_j)) \tag{4}$$

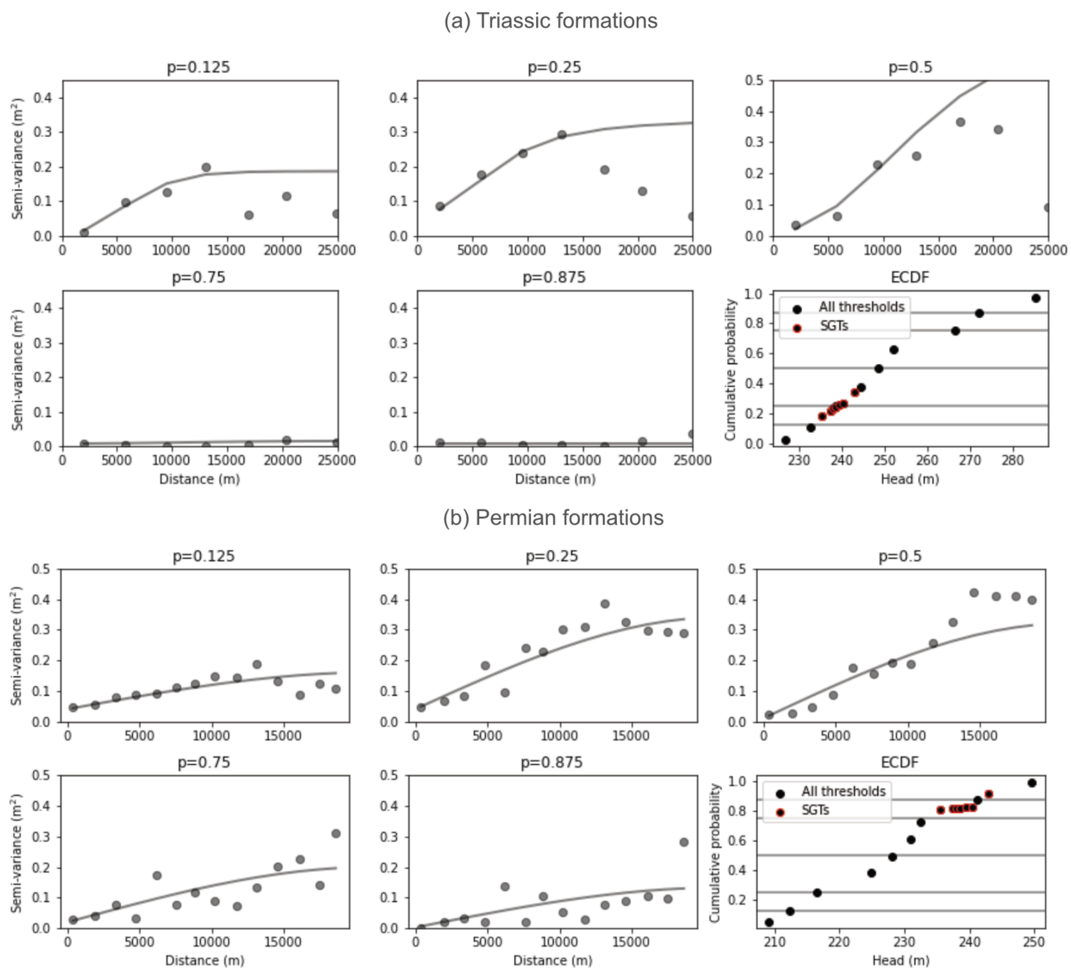

Fig. 4. The semi-variogram models for hydraulic head measurements in (a) the Triassic Formations and (b) the Permian Formations shown with the empirical cumulative distribution function (ECDF) signifying each threshold with the SGTs circled in red. (For interpretation of the references to colour in this figure legend, the reader is referred to the web version of this article.)

Here, a_{ij} refers to alternative hydraulic head threshold values a_i and a_j. Note that equation (4) reduces to equation (3) if $a_i = a_j$. In practice, Eqs. (3) and (4) are applied to bins of Δx values, thereby obtaining γ for a set of Δx bins.

The choice of the number of bins in the experimental semi-variogram is an essential consideration as there exists a trade-off between overly smooth semi-variance values (when using too few bins) and noisy semi-variance values (when using too many bins). In the current study, 9 bins of Δx values, ranging from 0 to 3787 m to 30,299–34,087 m, were adopted for the Triassic Formations, while 14 Δx bins (0–1398 m to 18,174, 19,572 m) were used for the Permian Formations. The number of Δx bins and maximum Δx values were selected to ensure that all bins contained a reasonable count of data pairs, albeit this was a subjective choice. This resulted in at least 22 data pairs in each Δx bin within the experimental semi-variograms for the Triassic Formations. In comparison, the experimental semi-variograms for the Permian Formations contained at least 103 data pairs. This difference in the count is due to the Permian Formations having 78 samples available compared with the Triassic Formations, which had 34 samples.

For Ordinary Co-Kriging, it is necessary to know γ at distances other than the discrete distances estimated with Eqs. (3) and (4) and for γ to be negative definite (Cressie, 1993). This is achieved by fitting empirical mathematical models to the relationships between semi-variance and distance for experimental semi-variograms and experimental cross semi-variograms. Commonly used models include the nugget, Gaussian, exponential, spherical, and Matérn models (Goovaerts, 1997). These semi-variogram models can be added together to construct more complex model structures (Goovaerts, 1997). For example, the nugget model characterises the discontinuity of the semi-variance at the origin (i.e., at or near a separation distance of zero), which can be included in a model structure (e.g., with the Gaussian model) to characterise the measurement error and micro-scale variability (Diggle et al., 1998).

In our study, isotropic semi-variogram models were used due to insufficient data to characterise anisotropy properly. The range was selected based on the range of the experimental semi-variogram of the indicator-transformed values for the median value. The median was used because the experimental semi-variogram is best defined when approximately half the data lies on either side of the threshold value (Journel, 1983). The fit of this range was visually assessed against the experimental semi-variograms at all other thresholds. Where the range was not appropriate for an experimental semi-variogram, an additional model structure was added to include the range of that experimental semi-variogram. Next, the sills and nuggets were modified to fit the experimental semi-variograms and experimental cross semi-variograms subject to a constraint of positive semi-definiteness (i.e., all eigenvalues are non-negative). In this study, the parameters of range, sill and nugget were estimated using weighted least-squares with weights proportional to $|N(\Delta x)|/\Delta x^2$ following Pebesma and Graeler (2020). When the condition of positive semi-definiteness is not met, it is necessary to apply a correction. In this study, we used the gstat package (Pebesma, 2004) in the R statistical language (Ihaka and Gentleman, 1996), which corrects for non-positive definite matrices by setting any negative eigenvalues to

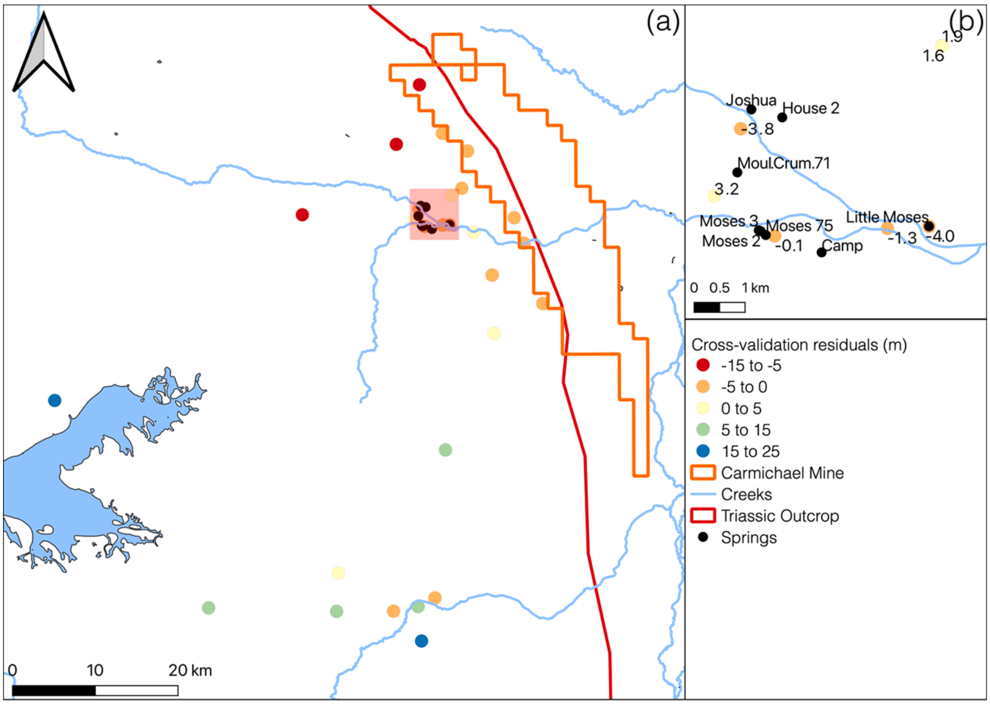

Fig. 5. Spatial distribution of residuals from leave-one-out cross-validation in the Triassic Formations with (a) showing a regional scale and (b) an inset map of the shaded red area in (a). (For interpretation of the references to colour in this figure legend, the reader is referred to the web version of this article.)

zero (Pebesma and Graeler, 2020).

The choice of semi-variogram models was qualitative based on the visual assessment of graphs of the fit of the semi-variogram models to the experimental semi-variance. We elected not to use leave-one-out cross-validation (LOO-CV) for semi-variogram model selection, as some of the semi-variogram models required the use of multiple nested model structures, which meant the number of possible model combinations increased substantially (e.g., 6 candidate models in a 2-model nested structure have 15 possible combinations). As such, the semi-variogram models were selected qualitatively based on the shape of the experimental semi-variance. LOO-CV was used as an exploratory technique to assess how well the chosen model represented the available data and identify the locations where the model performed poorly. The LOO-CV results were evaluated using summary statistics (i.e., mean error (ME), mean absolute error (MAE) and mean standardised squared residual (MSSR); see Goovaerts (2009) for details) and a spatial analysis of the residuals.

4.4. Predictions using Ordinary Co-Kriging

In applying Ordinary Co-Kriging to estimate the probability of hydraulic head values less than or equal to a set of threshold values, it is necessary to develop semi-variogram models of the indicator-transformed values for each threshold (see Section 4.3) and cross semi-variogram models between each the indicator-transformed values for each threshold (see Section 4.3). The indicator-transformed values for all thresholds at a well location $\boldsymbol{x}$ can be represented as:

$$\overline{\boldsymbol{I}}(\boldsymbol{x},\boldsymbol{a}) = [\, I(\boldsymbol{x},a_1) \quad \cdots \quad I(\boldsymbol{x},a_m) \,] \tag{5}$$

Given that a_1 is the first value in a set of m thresholds, and a_m is the last threshold in $\boldsymbol{a}$. The probabilities of hydraulic head values at unmeasured locations ($\boldsymbol{x}_*$) being less than or equal to the threshold values (denoted $\overline{\boldsymbol{I}}^*(\boldsymbol{x}_*,\boldsymbol{a})$) can be estimated using a linear combination of $\overline{\boldsymbol{I}}(\boldsymbol{x},\boldsymbol{a})$ for each of the n observation well locations (Myers, 1982):

$$\overline{\boldsymbol{I}}^*(\boldsymbol{x}_*,\boldsymbol{a}) = \sum_{j=1}^{n} \overline{\boldsymbol{I}}(\boldsymbol{x}_j,\boldsymbol{a})\boldsymbol{\lambda}_j \tag{6}$$

Here, $\boldsymbol{\lambda}_j$ is a matrix of weights, which are found by solving the equation (Myers, 1982):

$$\sum_{j=1}^{n} \overline{\boldsymbol{\gamma}}(\boldsymbol{x}_i - \boldsymbol{x}_j)\boldsymbol{\lambda}_j + \overline{\boldsymbol{\mu}} = \overline{\boldsymbol{\gamma}}(\boldsymbol{x}_i - \boldsymbol{x}_*) i = 1 \cdots n \tag{7}$$

subject to the constraint:

$$\sum_{j=1}^{n} \boldsymbol{\lambda}_j = \boldsymbol{I} \tag{8}$$

Where $\overline{\boldsymbol{\mu}}$ is an matrix of Lagrange parameters found by the solution of Eq. (7), $\overline{\boldsymbol{\gamma}}(\boldsymbol{x}_i - \boldsymbol{x}_j)$ is an matrix with the semi-variance between sites $\boldsymbol{x}_i$ and $\boldsymbol{x}_j$ given by the semi-variogram model for the indicator-transformed values for each threshold (as the diagonal elements) and the cross semi-variograms between indicator-transformed values for separate thresholds (as the off-diagonal elements), $\overline{\boldsymbol{\gamma}}(\boldsymbol{x}_i - \boldsymbol{x}_*)$ is an matrix with the semi-variance between the sites $\boldsymbol{x}_i$ and $\boldsymbol{x}_*$ and $\boldsymbol{I}$ is the identity matrix.

Once the probabilities of hydraulic head values less than or equal to each threshold were calculated, order-relation corrections were applied to ensure a valid CCDF. In this study, we corrected the CCDF using the average of the upwards and downwards corrections as described by Deutsch and Journel (1998). After order-relation corrections were applied, linear interpolation (see Deutsch and Journel, 1998) was used to interpolate between the threshold values examined in this study. Interpolation was used to allow for the prediction of hydraulic head values at selected probabilities (e.g., the median or quartiles) and of the probability of hydraulic heads less than or equal to specified threshold values (e.g., SGTs). Additionally, the mean was estimated from the CCDF using the procedure outlined by Goovaerts (2009).

5. Results and discussion

The following sections outline and discuss: (i) the semi-variogram models and cross-validation results, (ii) the regional hydraulic head distributions in the Triassic and Permian Formations, (iii) the likely hydraulic head values and associated uncertainties at the spring

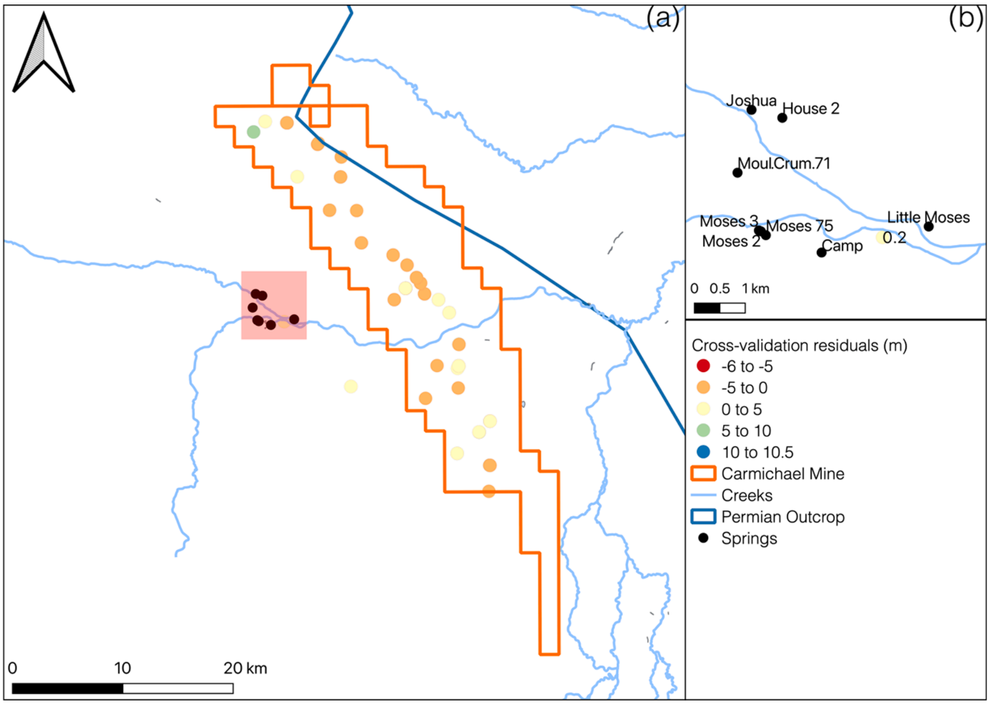

Fig. 6. Spatial distribution of residuals from leave-one-out cross-validation in the Permian Formations with (a) showing a regional scale and (b) an inset map of the shaded red area in (a). (For interpretation of the references to colour in this figure legend, the reader is referred to the web version of this article.)

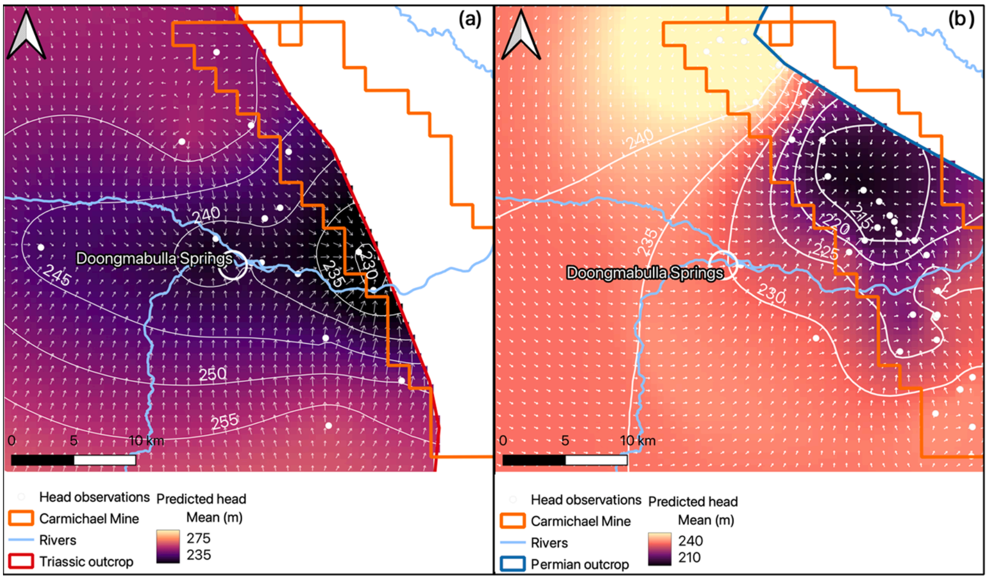

Fig. 7. Mean hydraulic head distributions in (a) the Triassic and (b) the Permian Formations.

locations, (iv) the CCDF for hydraulic heads in the Triassic and Permian Formations and the probabilities of hydraulic heads in each formation exceeding SGTs, (v) the likelihood of the alternate conceptual models for the source of water to the springs, and (vi) the uncertainties and future directions for this study.

5.1. Semi-variogram models and cross-validation

Sixteen threshold values were used, leading to 120 direct and cross experimental semi-variograms. Fig. 4 shows the semi-variogram models for 5 selected p-quantiles for the indicator transformed values in Triassic and Permian Formations. The 5 p-quantiles were chosen as representative values to show the fit of the semi-variogram models to the variety of semi-variance values derived from the experimental semi-variograms of the indicator transformed values for different thresholds. As shown in Fig. 4, the semi-variogram models in the Triassic Formations have a short range fit of 10,280 m for $p = 0.125$ and $p = 0.25$, which increases to 21,012 m for $p = 0.5$, meaning hydraulic head values became dissimilar over a shorter distance for $p = 0.125$ and $p = 0.25$ when compared with $p = 0.5$. This could be related to physical differences resulting in varying ranges for different p-quantiles or few measurements at extreme thresholds to populate semi-variograms (Journel, 1983). This meant it was necessary to use a nested model with a short range for the lower p-quantiles and a larger range for the

Table 1
The mean, median, quartiles, and interquartile range for the hydraulic head in the Triassic Formations at each spring location.

Spring ID (SGT in m)	Statistics				
	Mean (m)	Median (m)	Q1 (m)	Q3 (m)	Q3 – Q1 (m)
A (237.5)	236.4	236.8	234.5	238.5	3.9
B (238.0)	236.7	236.9	235.2	238.3	3.1
C (238.0)	236.6	236.9	235.2	238.3	3.2
D (238.4)	236.6	236.9	235.1	238.3	3.2
E (240.5)	237.3	237.3	235.4	239.0	3.6
F (242.8)	236.8	237.0	235.3	238.5	3.3
G (239.4)	236.8	237.0	235.5	238.4	2.9
H (235.7)	235.8	235.5	232.7	239.4	6.8

Table 2
The mean, median, quartiles, and interquartile range for the hydraulic head in the Permian Formations at each spring location.

Spring ID(SGT in m)	Statistics				
	Mean (m)	Median (m)	Q1 (m)	Q3 (m)	Q3 – Q1 (m)
A (237.5)	230.2	230.2	227.5	232.2	4.7
B (238.0)	230.9	230.6	228.0	232.5	4.5
C (238.0)	230.8	230.6	228.0	232.5	4.5
D (238.4)	230.8	230.6	227.9	232.5	4.5
E (240.5)	230.4	230.6	227.0	233.3	6.3
F (242.8)	231.1	230.9	227.4	233.9	6.6
G (239.4)	231.1	230.8	227.9	233.2	5.4
H (235.7)	228.5	229.1	226.3	231.6	5.3

Table 3
The probabilities of adequate hydraulic head to exceed SGTs for the springs in the Triassic and Permian Formations.

Spring ID (SGT in m)	Probabilities	
	Triassic	Permian
A (237.5)	0.40	0.06
B (238.0)	0.31	0.10
C (238.0)	0.31	0.09
D (238.4)	0.24	0.09
E (240.5)	0.11	0.08
F (242.8)	<0.01	0.03
G (239.4)	0.04	0.12
H (235.7)	0.49	0.04

higher p-quantiles. We selected the Gaussian model for the model structures as the shape of the semi-variance in the short-range (<10,000 m) had a shape similar to that of the Gaussian model. We used a three-model nested structure consisting of the nugget, the Gaussian with a range of 5140 m, and the Gaussian with a range of 10,506 m. The sills and nugget values were set using a linear model of coregionalization as described in Section 4.3. For example, the model structure for $p = 0.5$ consisted of a nugget of 0.02 m^2, a Gaussian with a range of 10506 m and a sill of 0.60 m^2 and a Gaussian with a range of 5140 m and a sill of 0.07 m^2. As there were 120 semi-variograms, the sill and nugget for each semi-variogram are provided in Supplementary Material 3. The semi-variance for $p = 0.75$ and $p = 0.875$ was low ($\sim$0 m^2) due to most measurements having a high probability ($\sim$1) of being less than these thresholds, leading to a consistent spatial distribution that yielded low semi-variance values. As the SGTs are located between $p = 0.125$ and $p = 0.5$, where the semi-variance is better defined, the low semi-variance values for the higher p-quantiles should not influence the SGT probability estimates.

The experimental semi-variance and semi-variogram models for 5 p-quantiles in the Permian Formations are shown in Fig. 4. The semi-variogram models exhibit a long range of 21,000 m, which is consistent between the semi-variance for the varying p-quantiles. A two-model nested structure was used comprising of the nugget and the spherical model with a range of 21,000 m. The sills and nuggets were fitted for each model using a linear model of coregionalization (see Section 4.3). For $p = 0.5$, the two-model structure consisted of a nugget of 0.01 m^2 and a spherical model with a range of 21,000 m and a sill of 0.31 m^2. The nugget and sill for each of the semi-variogram models are provided in Supplementary Material 4. The semi-variance for all of the shown p-quantiles were well defined, likely due to adequate samples to properly characterise the semi-variance, including at extreme p-quantiles (e.g., $p = 0.125$ or $p = 0.875$).

For the Triassic Formations, the model had a ME of 0.83 m, a MAE of 5.06 m and a MSSR of 0.66. The ME indicated a low model bias as the ME was close to 0, suggesting the model was not overly biased towards over or under-predicting values. The MAE of 5.06 m suggested the model did not perform well at all data points. Cross-validation predictions near the edge of the study area had higher residuals than predictions near the springs. This is expected given that the fundamental assumption of the model is that points closer together are more similar (i.e., have a lower semi-variance). Importantly, the residuals in the vicinity of the springs were lower (i.e., between 0 and −3.9 m), indicating good model performance in the area of interest (Fig. 5b). Additionally, the MSSR of 0.66 indicated that the prediction variance was larger than the squared residuals, suggesting the model over-estimated the prediction uncertainty, at least for the observation locations.

LOO-CV was conducted with the data for the Permian Formations. The results yielded a ME of −0.11 m, a MAE of 1.64 m, and a MSSR of 0.41. This indicated that the model for the Permian Formations had a low bias (i.e., the ME was close to 0) and had good predictive abilities, at least for the observation locations, as signified by the low MAE. The MSSR suggested that prediction variance was greater than the squared residuals, indicating that the model overestimated prediction uncertainty, at least for the observation locations. Spatially, the LOO-CV residuals in the Permian Formations suggested low errors (<5 m) throughout the study area (Fig. 6a). Most importantly, only one well was available near the spring locations, and the residual at this location was 0.3 m (Fig. 6b). This suggested that the model performed well in this area, despite few available measurements.

5.2. Regional hydraulic head distributions

The regional hydraulic head distributions can provide an indication of recharge areas, discharge areas and flow directions. Fig. 7 displays the mean hydraulic head distributions in the Triassic Formations (Fig. 7a) and the Permian formations (Fig. 7b). The mean hydraulic head distribution in the Triassic Formations suggests higher hydraulic heads (>250 m) to the north, south and west of the springs, with a lower head near the springs (230–240 m) and a continued decrease to the east. The lower hydraulic heads near the springs may indicate discharge occurring to the springs and/or the Carmichael River. This is consistent with the findings of Adani Mining (2013), who found that water in the Clematis Formation (a Triassic unit) flowed towards the DSC and Carmichael River. Furthermore, in both interpretations of the regional flow directions, the flow appears to continue to the east of the springs. As the formations outcrop to the east, it is plausible there may be flow from the

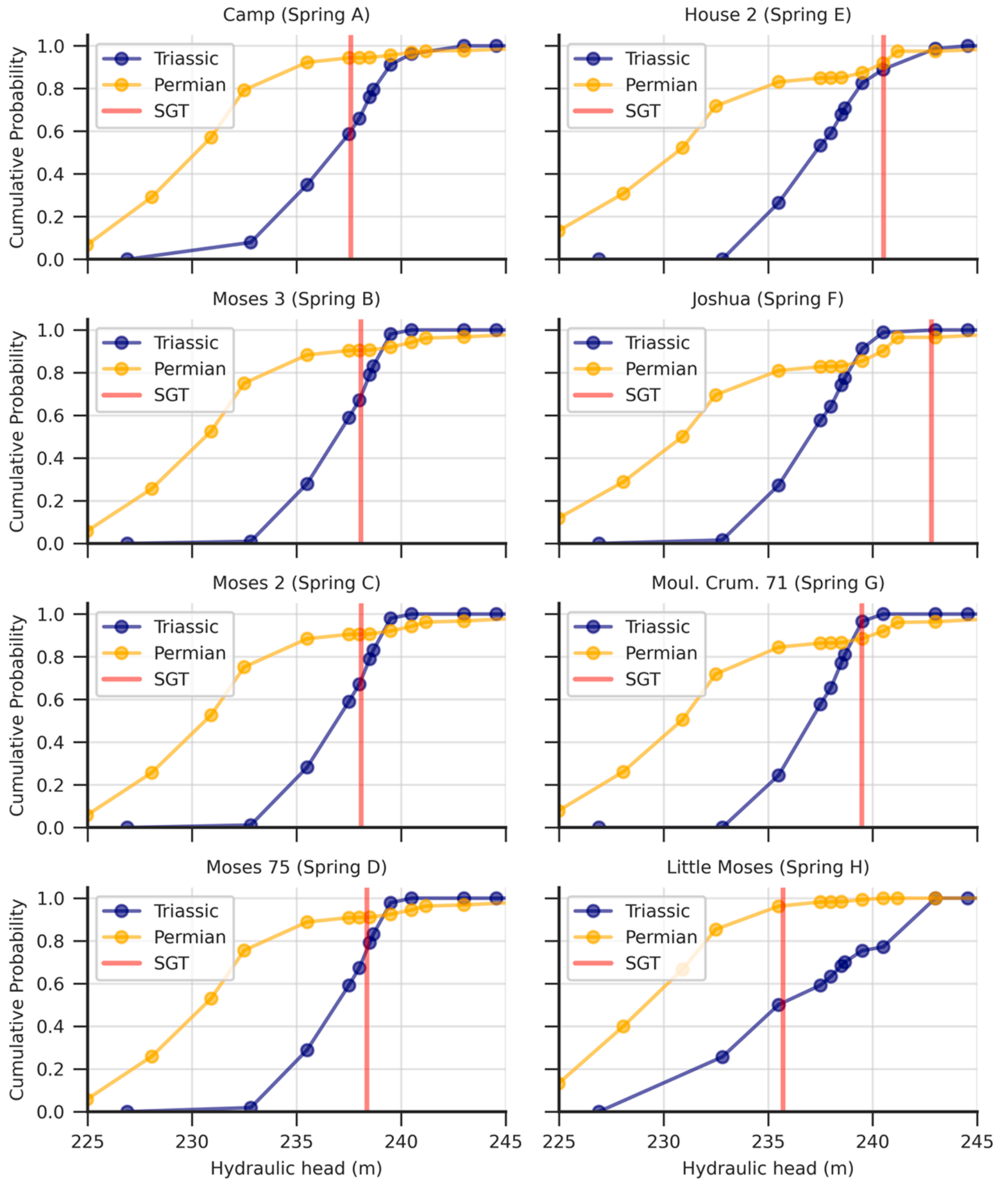

Fig. 8. Conditional cumulative distribution functions describing the probability of hydraulic head values less than hydraulic head thresholds for eight spring locations in the DSC. The red line indicates the spring geomorphic threshold (SGT) for each spring. See Fig. 1c for spring locations. (For interpretation of the references to colour in this figure legend, the reader is referred to the web version of this article.)

Triassic Formations to other formations beyond the Galilee Basin.

The mean predictions in the Permian Formations suggest higher hydraulic heads (230–240 m) to the north, south and west of the study area, which lowers to ~215 m in the mine area. Again, this is consistent with the flow directions interpreted by Adani Mining (2013) in the Colinlea Formation (a Permian unit). This pattern could indicate the presence of a discharge source in the mine site area. However, as no surface water bodies are observed, this may suggest discharge to another aquifer unit or groundwater extraction.

5.3. Hydraulic head estimates at spring locations

The CCDF for each spring was used to calculate statistics representing the likely hydraulic head values and associated uncertainties at the spring locations. These statistics consisted of the mean, median, first quartile (Q1), third quartile (Q3), and interquartile range (Q3 – Q1). Table 1 displays these statistics for the hydraulic head estimates in the Triassic Formations at each spring location. The mean hydraulic head estimates in the Triassic Formations range from 235.8 m at spring H to 237.3 m at spring E. The median is larger than the mean for all spring locations, except springs E and H, indicating that the CCDF is not symmetric and has a negative skew. The negative skew indicates a wider range of plausible values less than the mean compared to the range of values greater than the mean. The uncertainty in the mean estimate can be represented using the quartile values Q1 and Q3, which reflect the bounds about the mean within which there is a 0.5 probability of the true value residing. The lower quartile, Q1, ranges from 232.7 m at spring H to 235.5 m at spring G. While the upper quartile, Q3, ranges from 238.3 m at springs B, C and D to 239.4 m at spring H. The interquartile range, Q3–Q1, for estimates at the spring locations in the Triassic Formations ranges from 2.9 m to 6.8 m.

Table 2 displays the mean, median, quartiles and interquartile range in the Permian Formations at the spring locations. The mean hydraulic head estimates in the Permian Formations range from 228.5 m at spring

H to 231.1 m at springs F and G. The mean values are greater than the median for all springs, except for springs A, E and H. This suggests that the CCDF has a positive skew, indicating a larger range of plausible values greater than the median. The first quartile, Q1, ranges from 226.3 m at spring H to 228 m for springs B and C. While the third quartile, Q3, ranges from 231.6 m at spring H to 233.9 m at spring F. The interquartile ranges of Permian Formations range from 4.5 m for springs B, C and D to 6.6 m at spring F.

The mean values in the Permian Formations are less than the SGTs for all springs, while the mean values for these springs in the Triassic Formations are less than the SGTs for all springs except spring H. The SGTs are within the interquartile range for the hydraulic head in the Triassic Formations for springs A, B, C and H. In contrast, the SGTs at all spring locations are higher than Q3 for the hydraulic heads in the Permian Formations.

Tables 1 and 2 show that the estimated mean hydraulic head values are greater in the Triassic Formations than the Permian Formations for all springs. This difference between hydraulic head values in the Permian and Triassic Formations indicates the potential vertical direction of groundwater flow if hydraulic connectivity exists across the Rewan Formation aquitard. This hydraulic head difference has implications for interpreting the source aquifer for the DSC springs, and various scenarios can be developed whereby hydraulic head differences across the Rewan Formation influence conceptual model development. For example, it may be possible that connectivity exists across the Rewan Formation near the springs and the Permian Formations provide a source of water to the Triassic Formations, which in turn are a source of water to the DSC. In this case, that scenario appears unlikely as the hydraulic heads in the Triassic Formations appear higher than those in the Permian Formations, suggesting the potential for downwards flow.

5.4. Spring geomorphic threshold probabilities

The estimated probabilities (i.e., $\overline{\boldsymbol{I}}^{*}(\boldsymbol{x}_{*},\boldsymbol{a})$) that hydraulic heads at spring locations are less than or equal to thresholds (i.e., $\boldsymbol{a}$) are shown in Fig. 8, in the form of CCDFs. Probabilities range from 0 to 1. That is, probabilities for spring B of non-exceedance of 233 and 239 m are 0 and 1 (respectively) in the Triassic Formations, while corresponding non-exceedance probabilities for the Permian Formations are 0 and 1 for elevations of 220 and 245 m, respectively. Fig. 8 shows that the CCDF for Permian Formations changes more gradually than the CCDF for the Triassic Formations due to the larger range of hydraulic head values for the Permian Formations. This is a consequence of the greater uncertainty in Permian hydraulic head values (relative to Triassic hydraulic heads) at spring locations, as outlined in Section 5.2.

The estimates shown in Fig. 8 appear similar for some springs (e.g., Springs B, C and D) due to the close proximity of these locations (see Fig. 1c). For tabulated values of estimated probabilities, the reader is directed to Table A1 (for the Triassic Formations) and Table A2 (for the Permian Formations) in Appendix A. Tables A1 and A2 show that the majority of probabilities abide by order relations, with order-relation corrections applying predominantly to probabilities near the limits of 0 and 1. The order-relation deviations at extreme values are not unexpected, given the lack of data available to populate semi-variograms beyond the hydraulic head elevation limits, as discussed by Deutsch and Journel (1998).

CCDFs for the Triassic and Permian Formations can be used to assess the probability of each formation having adequate hydraulic head to exceed individual SGTs, referred to hereafter as 'SGT probabilities'. SGT probabilities are identified in Fig. 8 by the intersection of red lines (SGTs) and CCDF curves. The probabilities of the Triassic and Permian Formations having hydraulic heads exceeding the SGTs are given in Table 3. These were obtained by subtracting values of $\overline{\boldsymbol{I}}^{*}(\boldsymbol{x}_{*},\boldsymbol{a})$ from one. The probability that head in the Triassic Formations exceeds SGTs at the spring locations range from <0.01 to 0.49, while the probability that Permian Formation heads exceed SGTs ranges from 0.03 to 0.12. The results indicate that Triassic Formations have a moderate probability (≥0.24) of adequate hydraulic head to support the southern springs (A, B, C and D) and a south-eastern spring (H), but lower probabilities (≤0.11) of adequate hydraulic head to support the northern springs (E, F, G). Results also indicate a lower probability (≤0.12) that the Permian Formations have adequate head to exceed the SGTs of all springs. Notably, the Triassic Formations have a higher probability of hydraulic heads exceeding spring SGTs than the Permian Formations for all springs except springs F and G. Interestingly, the Triassic and Permian Formations both have low SGT probabilities for the springs E, F and G, possibly suggesting an alternate source aquifer or a missing component in our conceptual models.

5.5. The likelihood of alternate conceptual models

The likelihood of the alternate conceptual models for the source of water to the DSC can be considered based on the regional hydraulic head distributions (Section 5.2), likely hydraulic head values at spring locations (Section 5.3), and SGT probabilities (Section 5.4). The regional hydraulic head distributions in the Triassic Formations suggested higher head in the north, south and west of the study area reducing towards lower head near the springs and along the Carmichael river to the west (Fig. 7). This may suggest the occurrence of discharge (e.g., spring flow or baseflow to the river) from the Triassic Formations in this area. While, the hydraulic head distribution in the Permian Formations suggests higher heads to the north, south and west, lowering to a minimum in the mine site area (Fig. 8). As no surface water bodies are observed in this area, this pattern may indicate discharge occurring to another formation. These hydraulic head distributions suggest that the Triassic Formations display a pattern more consistent with discharge to the DSC than that observed in the Permian Formations.

The likely hydraulic head values at the spring locations indicate the potential vertical flow directions if connectivity existed across the Rewan Formation in these locations. The results suggest that the hydraulic head at the spring locations are likely higher in the Triassic Formations than in the Permian Formations (Table 1 and Table 2). This indicates that if connectivity existed in these locations, flow directions would likely be downwards from the Triassic to the Permian Formations, which implies it is unlikely that the Permian Formations could be contributing water to the Triassic Formations in this area.

The Triassic Formations have a higher probability than the Permian Formations of adequate hydraulic head to support spring flow to springs A, B, C, D, E and H. SGT probabilities for springs F and G were low for both formations suggesting inconclusive findings for these springs. Overall, the hydraulic head evidence interpreted from regional head distributions, potential vertical flow directions and SGT probabilities suggests that the Triassic Formations are more likely than the Permian Formations to provide a source of water to springs A, B, C, D, E and H, while results for spring F and G were inconclusive. Despite these findings, it remains plausible that the Permian Formations may indirectly support the springs by providing a source of water to the Triassic Formations via connectivity at a location away from the spring sites. Thus, although the Triassic Formations may present as the principal source of water at the spring locations (i.e., due to hydraulic heads exceeding the SGT and flow directions converging towards the DSC), the Permian Formations may nevertheless contribute indirectly to spring flow via leakage to, and pressurisation of, the Triassic Formations at another location. In this scenario, the Permian Formations may indirectly support spring flow even though Permian heads do not exceed Triassic heads at the spring locations.

Nevertheless, if connectivity exists across the Rewan Formation at a location, then drawdown in the Permian Formations due to mine site dewatering may impact the DSC. That is, if drawdown in the Permian Formations propagates through connections between the two formations, this will induce a net downward flux (relative to the natural, pre-mining conditions) regardless of the natural head gradient (and flow direction) across the Rewan Formation. The resulting drawdown could result in the reduction or cessation of flow from the DSC, even if the Permian Formations do not discharge either into the Triassic Formations or directly to the springs. Thus, for mining activities to potentially affect spring discharge, there need only to be connectivity between the Permian and Triassic Formations, close enough to the DSC that mining-induced drawdown in either formation can reach the springs.

5.6. Uncertainties and future directions

Conceptual models are often accepted or rejected based on their consistency with the observed data (Enemark et al., 2019). However, the consistency of a model with observed data does not ensure that the model is a valid representation of the system (Oreskes et al., 1994), and this consistency may change as new data becomes available (Enemark et al., 2019). In our case, both conceptual models are reasonably consistent with observations (see Section 5.1), but give a low probability of adequate head to support spring flow, particularly for springs F and G. This may be explained as either a type I error, where a valid conceptual model has not been considered, or a type II error, where an invalid conceptual model has been adopted (Neuman, 2003).

A plausible error type II error is that the conceptual models did not consider the vertical stratification of hydraulic head measurements within each formation. In this study, most of the available measurements, particularly in the Triassic Formations, were taken at shallow depths, making it difficult to characterise the vertical stratification of hydraulic heads within the formations. A recently drilled well (August 2020) in the Triassic Formation suggests an increase in the head with depth, and as the analysis in the Triassic Formations is based primarily on shallow measurements, it is plausible that it may underestimate the potential of the Triassic Formations to support spring flow. Similarly, vertical stratification of hydraulic heads within the Permian Formations may exist, which could influence modelling outcomes. However, there is a lack of measurements outside of the mine site to identify any vertical head stratification in the Permian Formations. Future studies should consider the vertical stratification within these formations and how this influences modelling outcomes, which would require the installation of piezometers to monitor the head at various depths in both the Permian and Triassic Formations.

Alternately, there could be a valid conceptual model being ignored (e.g., a conceptual model where the shallow Tertiary or deeper Joe Joe Formation that underlies the Permian Formation provide water to the spring), or there may be a lack of data to properly interrogate these conceptual models. Although there were more data points in the Permian Formations than the Triassic Formations (i.e., 78 and 34, respectively), these data were clustered in a region near the margin of the study area, with only a few measurements in the region near the springs (Fig. 1). The Kriging weights given by the solution of Eq. (7) take into account the redundancy of measurements, whereby measurements located close to one another may convey little additional information (Diggle et al., 1998). As such, many of the data points within localised data clusters were largely redundant and provided minimal additional information about the regional hydraulic head distribution. In contrast, the Triassic Formations had measurements over a wider spatial distribution and, therefore, less data redundancy than those of the Permian Formations (Fig. 1a). Furthermore, the Permian had only a single well (ID:190229_A) near the spring locations, which meant the findings in the Permian Formations at the spring locations were highly dependent on the quality of this measurement. This was a single measurement collected on the same day as drilling, without a reported survey method, and thus was assigned a mean of 229.86 m (i.e., the measured value) and a range of 222.9 to 236.8 m, based on the considered uncertainties. As demonstrated by the cross-validation map of residuals (Fig. 6), the inclusion of this well had little impact on the mean predictions as the predicted value at this well (when censoring the observation) was 229.57 m, which is within 0.3 m of the observed head value. However, the inclusion of this observation reduced the uncertainty of predictions substantially in the vicinity of the springs. This influenced the SGT probabilities for the Permian Formations by reducing the plausibility of adequate head to meet the SGTs.

The modelling of the impacts of mine induced drawdown on the DSC outlined in the environmental impact statement assumes that the source aquifer is the Triassic Formations and that adaptive management will be applied to mitigate impacts upon the springs (Adani Mining, 2013). However, studies by other investigators (e.g., Webb, 2015; Currell et al., 2017; CSIRO and Geoscience Australia, 2019; Werner et al., 2019; Currell et al., 2020) have suggested that there is substantial uncertainty in the source aquifer of the DSC and that the Permian conceptualisation remains plausible. The results of this study indicate that the Triassic conceptualisation is more likely than the Permian conceptualisation, although both conceptualisations remain plausible. Significant uncertainty exists in our assessment due to hydraulic head measurement scarcity in the vicinity of the springs and the analysis only considering a single data type (Neuman and Wierenga, 2003). Furthermore, the locations and degree of inter-aquifer connectivity across the Rewan Formation aquitard is a major source of uncertainty (CSIRO and Geoscience Australia, 2019), which will control how the drawdown in the Permian Formations will impact the DSC. Despite the remaining conceptual model uncertainties and the unsuitability of adaptive management to scenarios with time-delayed or irreversible impacts (Currell et al., 2017; Thomann et al., 2020), the mine has been approved. Future studies should aim to reduce the conceptual model uncertainty to identify potential impacts and mitigation strategies. This could be achieved through the installation of additional monitoring wells at various depths in the major formations as well as by analysing other data types, including hydrochemistry and geophysical surveys, and investigating the degree of inter-aquifer connectivity across the Rewan Formation aquitard at and away from the DSC.

6. Conclusions

Knowledge of hydraulic head distributions throughout aquifers can assist in hydrogeological conceptual model development and assessment. Ordinary Indicator Co-Kriging is a geostatistical interpolation technique that estimates hydraulic head values and their uncertainties at unmeasured locations. These hydraulic head estimates can be used to quantitatively assess the probability of hydraulic heads exceeding specified thresholds at unmeasured locations. Additionally, when expert knowledge is available for physical thresholds in the hydrogeological system (e.g., hydraulic head thresholds required for spring flow), the likelihood of conceptual models meeting these physical thresholds can be quantitatively assessed. This approach is widely applicable throughout hydrogeology in the assessment of conceptual models.

The application of the Ordinary Indicator Co-Kriging in conceptual model assessment was demonstrated using the hydraulic head data from the alternate hypothesised source aquifers of the DSC. The analysis indicated likelihoods ranging from <0.01 to 0.49 that the Triassic Formations have adequate hydraulic head to support flow to the DSC springs assessed here, while there was a lower likelihood (i.e., 0.03–0.12) that the springs could derive water from the deeper Permian Formations. These results suggest that the Triassic Formations have a higher likelihood of adequate hydraulic head than the Permian Formations. However, significant uncertainty exists in the conceptual model assessment due to hydraulic head measurement scarcity in the vicinity of the springs (particularly in the Permian Formations) and the analysis only considering a single data type. Furthermore, the locations and degree of inter-aquifer connectivity across the Rewan Formation aquitard is a major source of uncertainty, which will influence the likelihood of alternate conceptual models and control how the drawdown in the Permian Formations will impact the DSC. As such, we suggest that further studies are conducted to complement this research through the collection of additional hydraulic head measurements, analysis of other data types, including hydrochemistry and geophysical surveys, and further investigation into the degree of inter-aquifer connectivity across the Rewan Formation aquitard at and away from the DSC.

CRediT authorship contribution statement

Robin Keegan-Treloar: Conceptualization, Methodology, Software, Investigation, Data curation, Writing - original draft, Visualization. **Adrian D. Werner:** Conceptualization, Methodology, Writing - review & editing, Writing - original draft, Supervision, Funding acquisition. **Dylan J. Irvine:** Conceptualization, Methodology, Writing - original draft, Writing - review & editing, Supervision, Funding acquisition, Project administration. **Eddie W. Banks:** Conceptualization, Methodology, Writing - original draft, Writing - review & editing, Supervision, Funding acquisition.

Declaration of Competing Interest

The authors declare that they have no known competing financial interests or personal relationships that could have appeared to influence the work reported in this paper.

Acknowledgements

Robin Keegan-Treloar is supported by the Australian Government Research Training Program. Adrian Werner, Dylan Irvine, and Eddie Banks are supported by an Australian Research Council Linkage Project (project number LP190100713). We thank the editors and anonymous reviewers for their insightful suggestions, which contributed to the improvement of this manuscript.

Appendix A. Hydraulic head probabilities

Table A1
Probabilities of hydraulic head less than or equal to selected thresholds in the Triassic Formations at the locations of springs A to H. Values that have had order-relation corrections applied are followed by the original value in brackets.

Thresholds (m)	Spring ID (SGT in m)							
	A (237.5)	B (238.0)	C (238.0)	D (238.4)	E (240.5)	F (242.8)	G (239.4)	H (235.7)
226.9	0.0(−0.01)	0.0(−0.02)	0.0(−0.02)	0.0(−0.02)	0.0(−0.02)	0.0(−0.01)	0.0(−0.02)	0.0(0.02)
232.8	0.08	0.01	0.01	0.02	0.0(−0.01)	0.02	0.0(−0.02)	0.26
235.5	0.35	0.28	0.28	0.29	0.27	0.27	0.24	0.5
237.5	0.59	0.59	0.59	0.59	0.53	0.58	0.58	0.59
238	0.66	0.67	0.67	0.67	0.59	0.64	0.65	0.63
238.5	0.76	0.79	0.79	0.79	0.68	0.74	0.77	0.68
238.7	0.79	0.83	0.83	0.83	0.71	0.78	0.81	0.7
239.5	0.91	0.98	0.98	0.98	0.83	0.91	0.97	0.75
240.5	0.96	1.0(1.05)	1.0(1.05)	1.0(1.05)	0.89	0.99	1.0(1.05)	0.77
243	1	1	1	1	0.99	1.0(1.02)	1	1.0(1.01)
244.6	1.0(1.02)	1.0(0.99)	1.0(0.99)	1	1.0(1.04)	1.0(1.04)	1.0(0.99)	1.0(1.11)
248.7	1.0(1.01)	1.0(1.03)	1.0(1.02)	1.0(1.02)	1.0(0.94)	1.0(0.9)	1	1
252.1	1.0(0.99)	1.0(0.99)	1.0(0.99)	1.0(0.99)	1.0(0.96)	1.0(0.93)	1.0(0.98)	1.0(0.99)
266.4	1.0(0.96)	1.0(0.96)	1.0(0.96)	1.0(0.96)	1.0(0.96)	1.0(0.96)	1.0(0.96)	1.0(0.97)
272.2	1.0(0.93)	1.0(0.92)	1.0(0.93)	1.0(0.93)	1.0(0.95)	1.0(0.95)	1.0(0.93)	1.0(0.95)
285.4	1	1.0(1.01)	1.0(1.01)	1	1	1	1.0(1.01)	1

Table A2
Probabilities of hydraulic head less than or equal to selected thresholds in the Permian Formations at the locations of springs A to H. Values that have had order-relation corrections applied are followed by the original value in brackets.

Thresholds (m)	Spring ID (SGT in m)							
	A (237.5)	B (238.0)	C (238.0)	D (238.4)	E (240.5)	F (242.8)	G (239.4)	H (235.7)
209.2	0.0(0.01)	0.0(0.01)	0.0(0.01)	0	0.0(0.02)	0.0(0.01)	0.0(0.01)	0.0(0.02)
212.3	0.0(0.01)	0.0(0.01)	0.0(0.01)	0.0(0.01)	0.02(0.04)	0.0(0.03)	0.0(0.02)	0.03(0.04)
216.5	0.0(−0.02)	0.0(−0.03)	0.0(−0.03)	0.0(−0.03)	0.02(0.01)	0	0.0(−0.02)	0.03(0.01)
225	0.07	0.06	0.06	0.06	0.13	0.12	0.08	0.13
228.1	0.29	0.26	0.26	0.26	0.31	0.29	0.26	0.4
230.9	0.57	0.53	0.53	0.53	0.52	0.5	0.51	0.67
232.5	0.79	0.75	0.75	0.76	0.72	0.7	0.72	0.85
235.5	0.92	0.88	0.88	0.89	0.83	0.81	0.84	0.96
237.5	0.94	0.9	0.9	0.91	0.85	0.83	0.86	0.98
238	0.94	0.9	0.91	0.91	0.85	0.83	0.87	0.98
238.5	0.95	0.91	0.91	0.91	0.85	0.83	0.87	0.98
239.5	0.96	0.92	0.92	0.92	0.87	0.85	0.89	0.99
240.5	0.97	0.94	0.94	0.95	0.92	0.9	0.92	1
241.2	0.98	0.96	0.96	0.96	0.97(0.98)	0.97	0.96	1.0(1.01)
243	0.98	0.97	0.97	0.97	0.97	0.97(0.96)	0.96	1
249.6	1.0(0.99)	1.0(0.98)	1.0(0.98)	1.0(0.98)	1.0(0.96)	1.0(0.95)	1.0(0.96)	1

Appendix B. Supplementary data

Supplementary data to this article can be found online at https://doi.org/10.1016/j.jhydrol.2021.126808.

References

Adani Mining, 2013. Environmental Impact Statement (EIS) - Carmichael Coal Mine and Rail Project. Retrieved from: https://www.statedevelopment.qld.gov.au/coordinator-general/assessments-and-approvals/coordinated-projects/completed-projects/carmichael-coal-mine-and-rail-project/eis-documents.

AECOM, 2021. Groundwater Management and Monitoring Program - Carmichael Coal Project. Retrieved from: https://s3-ap-southeast-2.amazonaws.com/awsfiles-232340950/bravus/documents/gmmp_ccp_v11.a_25052021_final_appnd_web_upload.pdf.

Anane, M., Selmi, Y., Limam, A., Jedidi, N., Jellali, S., 2014. Does irrigation with reclaimed water significantly pollute shallow aquifer with nitrate and salinity? An assay in a perurban area in North Tunisia. Environ Monit Assess 186 (7), 4367–4390.

Arslan, H., 2012. Spatial and temporal mapping of groundwater salinity using ordinary kriging and indicator kriging: The case of Bafra Plain, Turkey. Agric. Water Manag. 113, 57–63.

Bastin, G., Gevers, M., 1985. Identification and optimal estimation of random fields from scattered point-wise data. Automatica 21 (2), 139–155.

Bradley, J.W., 2015. Adani Mining Pty Ltd vs. Land Services of Coast and Country Inc & Ors, 206 Further statement of evidence – geology and hydrogeology (groundwater conceptualisation). Retrieved from: http://envlaw.com.au/wp-content/uploads/carmichael8.pdf.

Bredehoeft, J., 2005. The conceptualisation model problem - Surprise. Hydrogeol. J. 13, 37–46. https://doi.org/10.1007/s10040-004-0430-5.

Bredehoeft, J.D., 2003. From Models to Performance Assessment: The Conceptualization Problem. Ground Water 41, 571–577. https://doi.org/10.1111/j.1745-6584.2003.tb02395.x.

Chica-Olmo, M., Luque-Espinar, J.A., Rodriguez-Galiano, V., Pardo-Igúzquiza, E., Chica-Rivas, L., 2014. Categorical Indicator Kriging for assessing the risk of groundwater nitrate pollution: The case of Vega de Granada aquifer (SE Spain). Sci. Total Environ. 470-471, 229–239.

Cressie, N.A.C., 1993. Statistics for Spatial Data, Technometrics, Wiley Series in Probability and Statistics. John Wiley & Sons, Inc., Hoboken, NJ, USA. https://doi.org/10.1002/9781119115151.

CSIRO, Geoscience Australia, 2019. Carmichael Coal Mine Advice on Groundwater Management and Monitoring and Groundwater Dependent Ecosystem Management plans to the Department of the Environment and Energy.

Currell, M.J., Irvine, D.J., Werner, A.D., McGrath, C., 2020. Science sidelined in approval of Australia's largest coal mine. Nat. Sustain. 3 (8), 644–649.

Currell, M.J., Werner, A.D., McGrath, C., Webb, J.A., Berkman, M., 2017. Problems with the application of hydrogeological science to regulation of Australian mining projects: Carmichael Mine and Doongmabulla Springs. J. Hydrol. 548, 674–682.

Deutsch, C.V., Journel, A.G., 1998. GSLIB: geostatistical software library and user's guide. Second edition.

Diggle, P.J., Tawn, J.A., Moyeed, R.A., 1998. Model-based geostatistics, J. R. Stat. Soc. Ser. C: Appl. Stat. https://doi.org/10.1111/1467-9876.00113.

Enemark, T., Peeters, L.J.M., Mallants, D., Batelaan, O., 2019. Hydrogeological conceptual model building and testing: A review. J. Hydrol. 569, 310–329.

Environment Australia, 2001. A Directory of Important Wetlands in Australia, Third Edition. Canberra.

Fensham, R., Silcock, J., Laffineur, B., MacDermott, H., 2016. Lake Eyre Basin Springs Assessment Project: Hydrogeology, cultural history and biological values of springs in the Barcaldine, Springvale and Flinders River supergroups. Galilee Basin springs and Tertiary springs of western Queensland, Brisbane. Retrieved from: https://www.publications.qld.gov.au/dataset/lake-eyre/resource/c5d1813b-73a4-4e05-aa86-39a8ed3045fb.

Freeze, A.R., Cherry, J.A., 1979. Groundwater. Prentice-Hall INC, Eaglewood Cliffs, New Jersey.

Garrido, Mª.S., Giménez, E., de Lacy, Mª.C., Gil, A.J., 2011. Surveying at the limits of local RTK networks: Test results from the perspective of high accuracy users. Int. J. Appl. Earth Obs. Geoinf. 13 (2), 256–264.

Goovaerts, P., 2009. AUTO-IK: A 2D indicator kriging program for the automated non-parametric modeling of local uncertainty in earth sciences. Comput. Geosci. 35 (6), 1255–1270.

Goovaerts, P., 1997. Geostatistics for Natural Resources Characterization. Oxford University Press.

Grimmett, G., Stirzaker, D., 2020. Probability and random processes. Oxford University Press.

Ihaka, R., Gentleman, R., 1996. R: A Language for Data Analysis and Graphics. J. Comput. Graph. Stat. 5, 299–314.

Journel, A.G., 1986. Constrained interpolation and qualitative information?The soft kriging approach. Math Geol 18 (3), 269–286.

Journel, A.G., 1983. Nonparametric estimation of spatial distributions. Math. Geol. 15 (3), 445–468.

Kresic, N., 2006. Hydrogeology and groundwater modeling. CRC Press.

Liu, C., Jang, C., Liao, C., 2004. Evaluation of arsenic contamination potential using indicator kriging in the Yun-Lin aquifer (Taiwan). Sci. Total Environ. 321 (1-3), 173–188.

Lyon, S.W., Lembo Jr., A.J., Walter, M.T., Steenhuis, T.S., 2006. Defining probability of saturation with indicator kriging on hard and soft data. Adv. Water Resour. 29 (2), 181–193.

Merrick, N., 2015. Land Services of Coast and Country Inc. v Adani Mining Pty Ltd. Expert Report to the Land Court by Dr Noel Patrick Merrick. Retrieved from: http://envlaw.com.au/wp-content/uploads/carmichael10.pdf.

Myers, D.E., 1982. Matrix formulation of co-kriging. Math. Geol. 14 (3), 249–257.

Neuman, S.P., 2003. Maximum likelihood Bayesian averaging of uncertain model predictions. Stochastic Environmental Research and Risk Assessment (SERRA) 17 (5), 291–305.

Neuman, S.P., Wierenga, P.J., 2003. A Comprehensive Strategy of Hydrogeologic Modeling and Uncertainty Analysis for Nuclear Facilities and Sites.

Nikroo, L., Kompani-Zare, M., Sepaskhah, A.R., Fallah Shamsi, S.R., 2010. Groundwater depth and elevation interpolation by kriging methods in Mohr Basin of Fars province in Iran. Environ Monit Assess 166 (1-4), 387–407.

Oreskes, N., Shrader-Frechette, K., Belitz, K., 1994. Verification, validation, and confirmation of numerical models in the earth sciences. Science 263 (5147), 641–646.

Pebesma, E.J., 2004. Multivariable geostatistics in S: the gstat package. Comput. Geosci. 30 (7), 683–691.

Pebesma, E.J., Graeler, B., 2020. Gstat User Manual.

Peeters, L., Fasbender, D., Batelaan, O., Dassargues, A., 2010. Bayesian data fusion for water table interpolation: Incorporating a hydrogeological conceptual model in kriging. Water Resour. Res. 46, 1–11. https://doi.org/10.1029/2009WR008353.

Philip, G.M., Watson, D.F., 1986. Automatic interpolation methods for mapping piezometric surfaces. Automatica 22 (6), 753–756.

Post, V.E.A., von Asmuth, J.R., 2013. Review: Hydraulic head measurements—new technologies, classic pitfallsRevue : Mesure du niveau piézométrique—nouvelles technologies, pièges classiquesRevisión: Medidas de carga hidráulica—nuevas tecnologías, trampas clásicasRevisão: Medição da carga hidráulica—novas tecnologias, armadilhas clássicas. Hydrogeol J. 21 (4), 737–750.

Quay, A., Hering, A.S., Mauter, M.S., 2020. Quantifying uncertainty in groundwater depth from sparse well data in the California Central Valley. Environ. Res. Lett. https://doi.org/10.1088/1748-9326/ab88fb.

Rau, G.C., Post, V.E.A., Shanafield, M., Krekeler, T., Banks, E.W., Blum, P., 2019. Error in hydraulic head and gradient time-series measurements: A quantitative appraisal. Hydrol. Earth Syst. Sci. 23, 3603–3629. https://doi.org/10.5194/hess-23-3603-2019.

Rexer, M., Hirt, C., 2014. Comparison of free high resolution digital elevation data sets (ASTER GDEM2, SRTM v2.1/v4.1) and validation against accurate heights from the Australian National Gravity Database. Aust. J. Earth Sci. 61 (2), 213–226.

Saito, H., Goovaerts, P., 2002. Accounting for measurement error in uncertainty modeling and decision-making using indicator kriging andp-field simulation: application to a dioxin contaminated site. Environmetrics 13 (5-6), 555–567.

Salama, R.B., Ye, L., Broun, J., 1996. Comparative study of methods of preparing hydraulic-head surfaces and the introduction of automated hydrogeological-GIS techniques. J. Hydrol. 185 (1-4), 115–136.

Siegel, D., 2008. Reductionist hydrogeology: ten fundamental principles. Hydrol. Process. 22 (25), 4967–4970.

The Department of State Development, 2018. China Stone Coal Project : Coordinator-General's evaluation report on the environmental impact statement. Retrieved from: https://www.statedevelopment.qld.gov.au/coordinator-general/assessments-and-approvals/coordinated-projects/completed-projects/china-stone-coal-project.

Thomann, J.A., Werner, A.D., Irvine, D.J., Currell, M.J., 2020. Adaptive management in groundwater planning and development: A review of theory and applications. J. Hydrol. 586, 124871. https://doi.org/10.1016/j.jhydrol.2020.124871.

Trimble Navigation Limited, 2014. Trimble R10 Datasheet.

Varouchakis, E.A., Theodoridou, P.G., Karatzas, G.P., 2020. Decision-Making Tool for Groundwater Level Spatial Distribution and Risk Assessment Using Geostatistics in R. J. Hazard. Toxic Radioact. Waste 24 (1), 04019031. https://doi.org/10.1061/(ASCE)HZ.2153-5515.0000464.

Varouchakis, E.A., Hristopulos, D.T., 2013. Comparison of stochastic and deterministic methods for mapping groundwater level spatial variability in sparsely monitored basins. Environ. Monit. Assess. 185 (1), 1–19.

Wackernagel, H., 1995. Geostatistics, in: Multivariate Geostatistics. Springer Berlin Heidelberg, Berlin, Heidelberg, pp. 74–81. https://doi.org/10.1007/978-3-662-03098-1_11.

Webb, J.A., 2015. Adani Mining Pty Ltd vs. Land Services of Coast and Country Inc & Ors, Expert report on groundwater impacts. Retrieved from: http://envlaw.com.au/wp-content/uploads/carmichael9.pdf.

Werner, A.D., Love, A.J., Irvine, D.J., Banks, E.W., Cartwright, I., Webb, J.A., Currell, M.J., 2019. Position Paper by Concerned Scientists - Deficiencies in the scientific assessment of the Carmichael Mine impacts to the Doongmabulla Springs. Retrieved from. https://dspace.flinders.edu.au/xmlui/handle/2328/39203?show=full.

Williams, B.K., Szaro, R.C., Shapiro, C.D., 2009. Adaptive management: The U.S. Department of the Interior technical guide. Washington, D.C.

Wing, M.G., Frank, J., 2011. Vertical measurement accuracy and reliability of mapping-grade GPS receivers. Comput. Electron. Agric. 78 (2), 188–194.

Journal of Hydrology 617 (2023) 128993

Contents lists available at ScienceDirect

Journal of Hydrology

journal homepage: www.elsevier.com/locate/jhydrol

Research papers

Identifying groundwater recharge and discharge zones using geostatistical simulation of hydraulic head and its derivatives

Robin Keegan-Treloar [a], Dylan J. Irvine [b,*,a], Adrian D. Werner [a], Eddie W. Banks [a]

[a] College of Science and Engineering and National Centre for Groundwater Research and Training, Flinders University, Adelaide, Australia
[b] Research Institute for the Environment and Livelihoods, Charles Darwin University, Darwin, Australia

ARTICLE INFO

Keywords:
Kriging
Hydrogeology Sequential Gaussian simulation
Galilee Basin
Hydraulic gradient

ABSTRACT

Identifying groundwater flow directions and the locations of recharge and discharge areas is critical for effective groundwater management. Groundwater flow directions, the concavity and the locations of extrema (i.e., minima and maxima) can be assessed using the first and second derivatives of the hydraulic head surface. We developed a geostatistical method to jointly simulate hydraulic head and its first and second derivatives using sequential Gaussian simulation. The derivative values were used to identify regional groundwater flow directions, and the second derivative test was used to probabilistically map the concavity and the locations of extrema in the hydraulic head surface. By comparing the mapped concavity and extrema to known features, it was possible to attribute areas of recharge and discharge to physical features of the system, such as rivers, lakes and geological outcrops. This was applied to Triassic aquifers in the Galilee Basin (Queensland, Australia) to delineate the likely recharge and discharge areas. This provided an objective assessment of likely recharge and discharge zones and their uncertainty, which is an important addition to a region where the hydrogeology has been the subject of much conjecture.

1. Introduction

Hydraulic head gradients are important in hydrogeological studies, as they are proportional to the rate of groundwater flow and control the flow directions, which provides critical information for understanding groundwater systems (Pardo-Igúzquiza and Chica-Olmo, 2004). However, hydraulic head measurements are typically sparsely distributed point measurements (Rau et al., 2019), which can make interpretation of hydraulic gradients challenging. To address these challenges, Philip and Kitanidis (1989) provided a modified form of Ordinary Kriging that allowed for the direct estimation of hydraulic head gradients from sparse hydraulic head observations. They applied their approach to estimate the regional groundwater flow directions in the Wolfcamp aquifer in northern Texas, USA. Pardo-Igúzquiza and Chica-Olmo (2004) further developed this approach, using Universal Kriging to account for a systematic trend in the mean. The benefits of geostatistical approaches over other techniques for mapping hydraulic head gradients (e.g., numerical modelling) include that they are generalisable, do not require specification of boundary conditions or geological properties, and can provide quantitative estimates of uncertainty. However, the results are dependent on the semi-variogram model and fitting a representative model can be challenging when working with small datasets (Goovaerts, 1997). Additionally, the grid resolution and number of realisations influence model run times, as can be the case with numerical modelling.

Developing conceptual models of groundwater systems, including by mapping groundwater flow directions and locations of recharge and discharge areas, is critical for effective groundwater management (Enemark et al., 2019; Thomann et al., 2020). The concavity (i.e., concave up or concave down) and the locations of extrema (i.e., minima, maxima or inflection points) in the hydraulic head surface (see Fig. 1) can be identified using information from the first and second derivatives of the inferred hydraulic head surface. Although previous work has used Kriging to estimate the first derivatives of hydraulic head surface (e.g., Philip and Kitanidis, 1989; Pardo-Igúzquiza and Chica-Olmo, 2004), no studies have used geostatistics to calculate higher-order derivatives and use these to map concavity and extrema in the hydraulic head surface. Herein, we extend the work of Philip and Kitanidis (1989) and Pardo-Igúzquiza and Chica-Olmo (2004), to simulate realisations of the first and second derivatives of the hydraulic head surface using sequential Gaussian simulation. We show how realisations of the derivatives of

* Corresponding author at: Research Institute for the Environment and Livelihoods, Charles Darwin University, Darwin, Australia.
E-mail address: dylan.irvine@cdu.edu.au (D.J. Irvine).

https://doi.org/10.1016/j.jhydrol.2022.128993
Received 23 August 2022; Received in revised form 5 December 2022; Accepted 12 December 2022
Available online 16 December 2022

hydraulic heads can be used to probabilistically map the locations of extrema and concavity of the hydraulic head surface, which can subsequently be compared with known surface features (e.g., rivers, lakes, geological outcrops) to identify plausible recharge and discharge areas. We apply the technique to sparsely distributed hydraulic head data from the Triassic aquifers of the Galilee Basin in Queensland, Australia. This provides an objective assessment of the likely recharge and discharge areas for the Triassic aquifers of the Galilee Basin, which is vital to inform the ongoing debate regarding the hydrogeology of the region (Currell et al., 2020). The approaches presented here represent a significant advancement in the use of hydraulic head data to map recharge and discharge areas.

2. Methods

2.1. Hydraulic head and derivative simulation

Consider the random function $\mathbf{Z}(\mathbf{u})$ observed at a set of coordinates $\mathbf{u}$ (e.g., $\mathbf{u}_1 = \{x_1, y_1\}$) of shape $n \times 2$. A single realisation of plausible values $(\mathbf{Z}^*(\mathbf{u}^*)_k)$ at a set of m unobserved locations $(\mathbf{u}^*)$ can be found using sequential Gaussian simulation (Goovaerts, 1997). Sequential Gaussian simulation is an iterative process where first a coordinate $(\mathbf{u}_i^*)$ is randomly selected from the set $\mathbf{u}^*$. Next, simple Kriging is used to estimate the mean (Cressie, 1990; Goovaerts, 1997):

$$\mathrm{Z}(\mathbf{u}_i^*) = \lambda^T \mathbf{Z}(\mathbf{u}) + (1_n - \lambda^T 1_n)\mu \tag{1}$$

Where $\lambda = \mathbf{C}(\mathbf{u}, \mathbf{u}_i^*)[\mathbf{C}(\mathbf{u}, \mathbf{u}) + I\sigma^2]^{-1}$, $\mathbf{C}(\mathbf{u}, \mathbf{u}_i^*)$ is the covariance between $\mathbf{u}$ and $\mathbf{u}_i^*$, $\mathbf{C}(\mathbf{u}, \mathbf{u})$ is the covariance between $\mathbf{u}$, 1_n is a vector of ones of length n, $\boldsymbol{\sigma}^2$ is a vector of the variance associated with each observation, and μ is a constant known mean. The $\boldsymbol{\sigma}^2$ term regularises the model to prioritise fitting higher quality measurements (i.e., low variance measurements) over those of lesser quality (i.e., high variance measurements). The variance of the hydraulic head timeseries available for each well can be assigned based on the measurement metadata (e.g., elevation survey method, water level measurement method; see Rau et al. (2019) and Post and von Asmuth (2013)) and the temporal variability in the hydrograph (see Keegan-Treloar et al. (2021)). Alternately, $\boldsymbol{\sigma}^2$ can be set to a constant value if all measurements have comparable error, or to 0 if the value is known exactly (e.g., from a computer simulation). μ can be chosen based on known values (e.g., if the function is known to converge towards a constant value), the arithmetic mean of the observation values, or the best linear unbiased estimate (Cressie, 1990; Goovaerts, 1997). The best linear unbiased estimate is defined as (Cressie, 1990):

$$\mu = \left(1_n(\mathbf{C}(\mathbf{u}, \mathbf{u}) + \boldsymbol{I\sigma}^2)^{-1}\right)^{\mathbf{T}} \frac{\mathbf{Z}(\mathbf{u})}{\left(1_n(\mathbf{C}(\mathbf{u}, \mathbf{u}) + \boldsymbol{I\sigma}^2)^{-1}\right)^{\mathbf{T}} 1_n} \tag{2}$$

The variance associated with estimates from Eq. (1) is calculated as (Cressie, 1990; Goovaerts, 1997):

$$\sigma^2(\mathbf{u}_i^*) = \mathbf{C}(\mathbf{u}_i^*, \mathbf{u}_i^*) - \lambda^T \mathbf{C}(\mathbf{u}, \mathbf{u}_i^*) \tag{3}$$

Once $\mathrm{Z}(\mathbf{u}_i^*)$ and $\sigma^2(\mathbf{u}_i^*)$ have been estimated, a value $\mathrm{Z}^*(\mathbf{u}_i^*)$ is randomly drawn from a normal distribution:

$$\mathrm{Z}^*(\mathbf{u}_i^*) = \mathrm{N}(\mathrm{Z}(\mathbf{u}_i^*), \sigma^2(\mathbf{u}_i^*)) \tag{4}$$

$\mathrm{Z}^*(\mathbf{u}_i^*)$ is then treated as an observed value by appending $\mathrm{Z}^*(\mathbf{u}_i^*)$ to $\mathbf{Z}(\mathbf{u})$, $\mathbf{u}_i^*$ to $\mathbf{u}$, and 0 to σ^2. Eq. (1), 3 and 4 are repeated until $\mathrm{Z}^*(\mathbf{u}_i^*)$ has been simulated for the m locations in $\mathbf{u}^*$. Note Eq. (2) is only applied on the first iteration to estimate a stationary value of μ from $\mathbf{Z}(\mathbf{u})$.

The term Kriging is a synonym for what is known as Gaussian processes in the machine learning community (Rasmussen and Williams, 2006). The derivative of a Gaussian process is itself a Gaussian process, and consequently, Gaussian processes can be used to estimate the derivatives of a function (Solak et al., 2003; Rasmussen and Williams, 2006; Duvenaud, 2014). Estimates of partial derivatives can be obtained by differentiating the covariance and mean functions, and Kriging as usual (Philip and Kitanidis, 1989; Pardo-Igúzquiza and Chica-Olmo, 2004; Duvenaud, 2014). As μ is assumed to be constant in Eq. (1), and the derivative of a constant value is 0, Eq. (1) simplifies to:

$$\bar{\mathbf{Z}}(\mathbf{u}^*) = \bar{\lambda}^{\mathbf{T}} \mathbf{Z}(\mathbf{u}) \tag{5}$$

Where a realisation of the partial derivatives is given by
$$\bar{\mathbf{Z}}(\mathbf{u}^*) = \left[\frac{\partial \mathbf{Z}(\mathbf{u}^*)}{\partial \mathbf{x}^*} \quad \frac{\partial \mathbf{Z}(\mathbf{u}^*)}{\partial \mathbf{y}^*} \quad \frac{\partial^2 \mathbf{Z}(\mathbf{u}^*)}{\partial \mathbf{x}^{*2}} \quad \frac{\partial^2 \mathbf{Z}(\mathbf{u}^*)}{\partial \mathbf{y}^{*2}} \quad \frac{\partial^2 \mathbf{Z}(\mathbf{u}^*)}{\partial \mathbf{x}^* \partial \mathbf{y}^*} \right]$$ and:

$$\bar{\lambda} = [\mathbf{C}(\mathbf{u}, \mathbf{u}) + I\boldsymbol{\sigma}^2]^{-1} \left[\frac{\partial \mathbf{C}(\mathbf{u}, \mathbf{u}^*)}{\partial \mathbf{x}^*} \quad \frac{\partial \mathbf{C}(\mathbf{u}, \mathbf{u}^*)}{\partial \mathbf{y}^*} \quad \frac{\partial^2 \mathbf{C}(\mathbf{u}, \mathbf{u}^*)}{\partial \mathbf{x}^{*2}} \quad \frac{\partial^2 \mathbf{C}(\mathbf{u}, \mathbf{u}^*)}{\partial \mathbf{y}^{*2}} \quad \frac{\partial^2 \mathbf{C}(\mathbf{u}, \mathbf{u}^*)}{\partial \mathbf{x}^* \partial \mathbf{y}^*} \right] \tag{6}$$

Where $\frac{\partial \mathbf{C}(\mathbf{u},\mathbf{u}^*)}{\partial \mathbf{x}^*}$ is the derivative of the covariance function with respect to $\mathbf{x}^*$, $\frac{\partial \mathbf{C}(\mathbf{u},\mathbf{u}^*)}{\partial \mathbf{y}^*}$ is the derivative of the covariance function with respect to $\mathbf{y}^*$, $\frac{\partial^2 \mathbf{C}(\mathbf{u},\mathbf{u}^*)}{\partial \mathbf{x}^{*2}}$ is the second derivative of the covariance function with respect to the $\mathbf{x}^*$, $\frac{\partial^2 \mathbf{C}(\mathbf{u},\mathbf{u}^*)}{\partial \mathbf{y}^{*2}}$ is the second derivative of the covariance function with respect to $\mathbf{y}^*$, and $\frac{\partial^2 \mathbf{C}(\mathbf{u},\mathbf{u}^*)}{\partial \mathbf{x}^* \partial \mathbf{y}^*}$ is the partial derivative of the covariance function with respect $\mathbf{x}^*$ and $\mathbf{y}^*$. Note that as the partial derivatives are conditioned solely on $\mathbf{Z}(\mathbf{u})$, the Kriging can be applied independently for each partial derivative (e.g., using $\bar{\lambda} = [\mathbf{C}(\mathbf{u}, \mathbf{u}) + \boldsymbol{I\sigma}]^{-1} \frac{\partial \mathbf{C}(\mathbf{u},\mathbf{u}^*)}{\partial \mathbf{x}^*}$ to estimate $\frac{\partial \mathbf{Z}(\mathbf{u}^*)}{\partial \mathbf{x}^*}$ with Eq. (5)), which may be necessary to preserve computer memory when working with large matrices. Any covariance function that is at least twice differentiable can be used. In this paper we provide the derivatives for the Gaussian covariance function (see Supporting Text S1).

2.2. Locating minima and maxima

Once a realisation of $\bar{\mathbf{Z}}(\mathbf{u}^*)$ is generated, extrema (i.e., minima and maxima in the hydraulic head surface) can be identified using the second derivative test (Stewart, 2010). The locations of critical points are identified by finding where $\frac{\partial \mathbf{Z}(\mathbf{u}^*)}{\partial x^*}$ and $\frac{\partial \mathbf{Z}(\mathbf{u}^*)}{\partial y^*}$ are equal to 0. As $\frac{\partial \mathbf{Z}(\mathbf{u}^*)}{\partial x^*}$ and $\frac{\partial \mathbf{Z}(\mathbf{u}^*)}{\partial y^*}$ are simulated at nodes and the zero values may be located between nodes, contouring (using linear interpolation) can be used to approximate the coordinates where $\frac{\partial \mathbf{Z}(\mathbf{u}^*)}{\partial x^*}$ and $\frac{\partial \mathbf{Z}(\mathbf{u}^*)}{\partial y^*}$ are equal to zero. This allows for the coordinates of the critical points to be approximated by finding the intersections of the zero contours for $\frac{\partial \mathbf{Z}(\mathbf{u}^*)}{\partial x^*}$ and $\frac{\partial \mathbf{Z}(\mathbf{u}^*)}{\partial y^*}$. Once these points are identified, the Hessian determinant $(\mathbf{H})$ can be used to determine the concavity of the critical points and to classify these as minima (concave up), maxima (concave down) or inflection points (a change of the concavity from concave up to concave down or vice-versa). $\mathbf{H}$ is calculated as:

$$\mathbf{H} = \frac{\partial^2 \mathbf{Z}(\mathbf{u}^*)}{\partial \mathbf{x}^{*2}} \frac{\partial^2 \mathbf{Z}(\mathbf{u}^*)}{\partial \mathbf{y}^{*2}} - \frac{\partial^2 \mathbf{Z}(\mathbf{u}^*)}{\partial \mathbf{x}^* \partial \mathbf{y}^*}^2 \tag{7}$$

If $\mathbf{H} > 0$, then the location can be classified as a minimum if $\frac{\partial^2 \mathbf{Z}(u^*)}{\partial x^{*2}} > 0$, or as a maximum if $\frac{\partial^2 \mathbf{Z}(\mathbf{u}^*)}{\partial \mathbf{x}^{*2}} < 0$. If $\mathbf{H} < 0$, the location is an inflection point. Values of $\mathbf{H} = 0$ indicate that there is insufficient information to classify the location as a minimum, maximum or inflection point.

2.3. Identifying boundary effects

The hydraulic head gradient perpendicular to the aquifer boundary can be indicative of flow into or out of the aquifer. The hydraulic head gradient perpendicular to an aquifer boundary can be assessed at nodes (in $\mathbf{u}^*$) closest to the boundary using $\frac{\partial \mathbf{Z}(\mathbf{u}^*)}{\partial \mathbf{x}^*}$, $\frac{\partial \mathbf{Z}(\mathbf{u}^*)}{\partial \mathbf{y}^*}$ and the angle (θ) projected perpendicular to the boundary. The resultant ($\mathbf{r}$) of the vectors $\frac{\partial \mathbf{Z}(\mathbf{u}^*)}{\partial \mathbf{x}^*}$ and $\frac{\partial \mathbf{Z}(\mathbf{u}^*)}{\partial \mathbf{y}^*}$ can be found using:

$$\mathbf{r} = \frac{\partial \mathbf{Z}(\mathbf{u}^*)}{\partial \mathbf{x}^*} \cos\theta + \frac{\partial \mathbf{Z}(\mathbf{u}^*)}{\partial \mathbf{y}^*} \sin\theta \tag{8}$$

Where $\mathbf{r} > 0$ represents flow towards the boundary and out of the aquifer, $\mathbf{r} < 0$ represents inflow into the aquifer from the boundary, and $\mathbf{r} = 0$ represents no flow across the boundary. Where the hydraulic head gradient across the boundary is steep, this may be indicative of either high groundwater inflow/outflow or low hydraulic conductivity of the aquifer material (according to Darcy's Law).

Values of θ can be identified using geometrically from a polygon of the aquifer boundary. First, all nodes within a specified buffer distance are selected, leading to k nodes denoted here as $\mathbf{u}_b^*$. Next, each node of $\mathbf{u}_b^*$ (given by $\mathbf{u}_b^* i = \{x_i^*, y_i^*\}$ (recalling $i = 1, \cdots, k$)) is projected orthogonally onto the nearest segment of the boundary polygon. The orthogonal projections onto each boundary segment are $\mathbf{x}_p = \mathbf{x}_1 + (\mathbf{x}_2 - \mathbf{x}_1)\mathbf{t}$ and $\mathbf{y}_p = \mathbf{y}_1 + (\mathbf{y}_2 - \mathbf{y}_1)\mathbf{t}$, where $\mathbf{t}$ is given by:

$$\mathbf{t} = \frac{(x_i^* - \mathbf{x}_1)(\mathbf{x}_2 - \mathbf{x}_1) + (y_i^* - \mathbf{y}_1)(\mathbf{y}_2 - \mathbf{y}_1)}{(\mathbf{x}_2 - \mathbf{x}_1)^2 + (\mathbf{y}_2 - \mathbf{y}_1)^2} \tag{9}$$

Where the coordinates ($\mathbf{x}_1$, $\mathbf{y}_1$, $\mathbf{x}_2$ and $\mathbf{y}_2$) are the vertices of each face of the boundary polygon.

The nearest boundary segment/s to each node can be identified using the condition $\mathbf{h} = \min(\mathbf{h})$, where $\mathbf{h} = \sqrt{(x_i^* - \mathbf{x_p})^2 + (y_i^* - \mathbf{y_p})^2}$ and the resulting projections, x_p and y_p, are calculated with the equations $x_p = x_i^* + \sum(\mathbf{x_p} - x_i^*)$ and $y_p = y_i^* + \sum(\mathbf{y_p} - y_i^*)$. The angle of $\mathbf{u}_b^* i$ projected on the boundary is obtained as $\theta_i = \mathrm{atan2}(y_p - y_i^*, x_p - x_i^*)$, where atan2 is a modified version of arctan, which handles special cases to ensure the resulting vector is oriented correctly with respect to the unit circle. This process is repeated for all nodes in $\mathbf{u}_b^*$, yielding $\theta = [\theta_1, \cdots, \theta_k]$.

3. Case study of the Galilee Basin, Australia

3.1. Study site and data description

We applied the method described above, in the Galilee Basin (Queensland, Australia), which is part of the Great Artesian Basin. The Galilee Basin outcrops to the east and is overlain by the Eromanga Basin to the west (Moya et al., 2016). The stratigraphy of the Galilee Basin is composed of Triassic-aged formations that overlie deeper Permian-aged formations. The aquifers of the Triassic and Permian-aged formations are composed mostly of sandstones separated by aquitards of siltstones and mudstones (Moya et al., 2016). The Permian-aged formations contain coal seams and are the target of proposed open-cut and underground mining, including the Carmichael Coal Mine (Fig. 2). Currell et al. (2020) and Keegan-Treloar et al. (2021) provide further details of the mine and surrounding hydrogeology. The shallower Triassic-aged formations have been hypothesised to provide a source of water to the culturally and ecologically significant Doongmabulla Springs Complex (Currell et al., 2020), amongst alternative possible source aquifers. Given the potential impacts of mining developments in the area, characterising the regional hydrogeology including the groundwater flow directions and the locations of likely recharge and discharge areas is of critical importance.

The Triassic formations have a good spatial distribution of hydraulic head data to the east where landholders target the upper formations for water supply, primarily for stock and domestic use (Fig. 2). However, fewer measurements are available to the west where the Galilee Basin is overlain by the Eromanga Basin and the Triassic formations are at substantial depth. In this study hydraulic head data were collated from the Queensland Groundwater Database (https://qldspatial.information.qld.gov.au/catalogue/), the Queensland Department of State Development (2018), and AECOM (2021). Hydrographs were plotted and a single value was selected as the representative steady-state water level for each well, following the approach used by Keegan-Treloar et al. (2021) (see Figures S1-S9). The steady-state assumption was assumed to

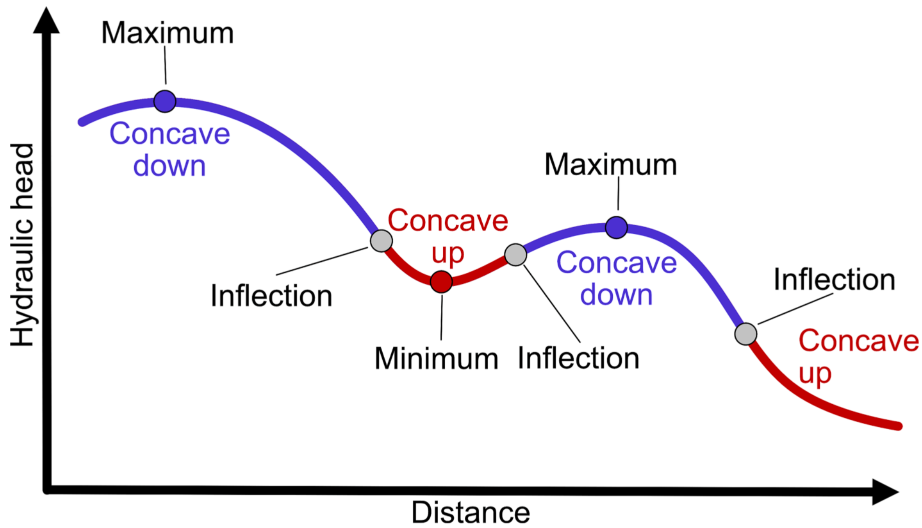

Fig. 1. Illustration of a 2D hydraulic head surface showing concave up areas (red) and concave down areas (blue) labelled with dots marking minimum, maximum and inflection points.

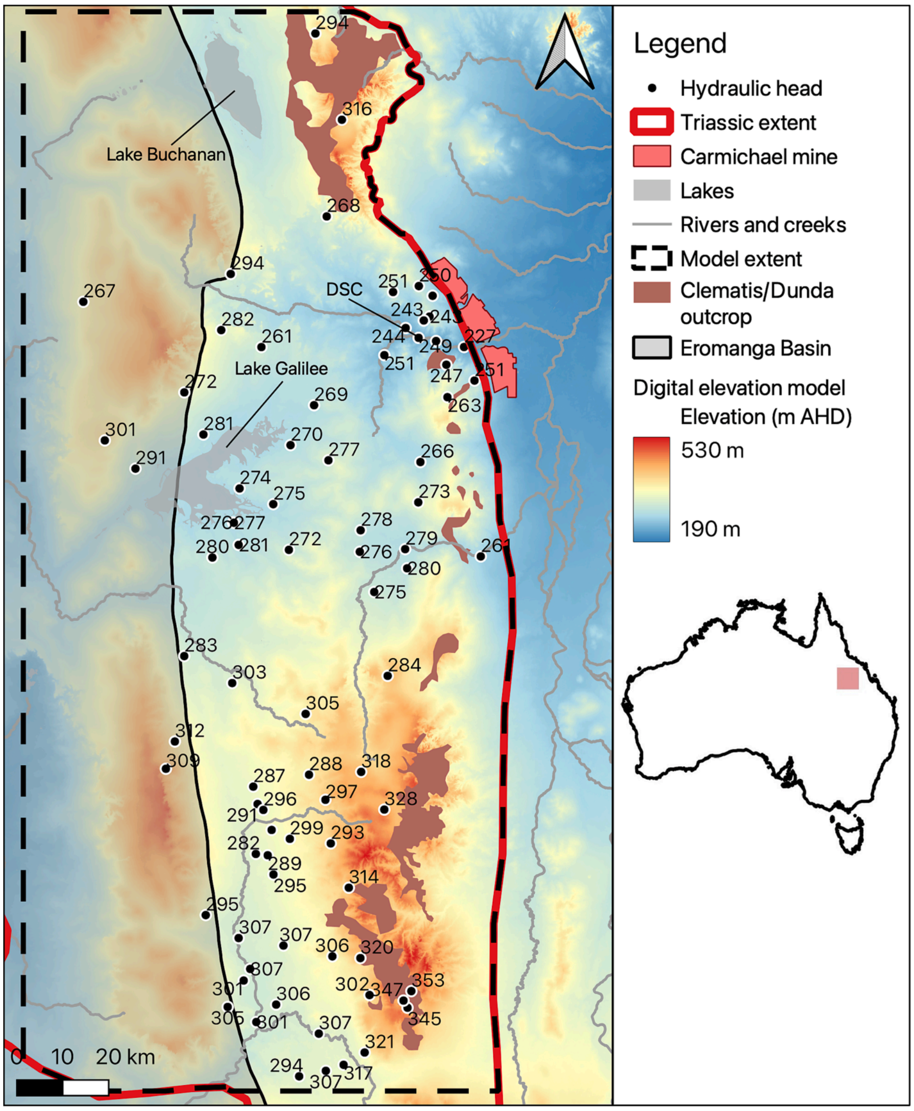

Fig. 2. Study area map that includes the Triassic extent (red line), Clematis/Dunda outcrop areas (brown, John Webb, pers. comm.), rivers, creeks and lakes (grey), the DSC (Doongmabulla Springs Complex), the Carmichael Mine (red areas), hydraulic head measurements in m AHD marked with the black circles, Eromanga Basin extent (grey shading with black outline) and the surface elevation in m AHD (blue to red colormap) from three second version of the Shuttle Radar Topographic Mission digital elevation model. The extent of the geostatistical model applied in this study is shown with the black dashed lines.

be reasonable as there was limited groundwater extraction (mainly just stock and domestic use) and at mine site dewatering had not yet impacted the Triassic formations. In total, there were 81 hydraulic head observations in the Triassic formations, ranging from 227.23 m to 352.66 m above the Australian Height Datum (see Table S1).

3.2. Hydraulic head and derivative simulation

The hydraulic head and derivative simulations of the Galilee Basin were run using Python, using libraries that come with a standard Anaconda installation. In the simulations, a regular grid ($\mathbf{u}^*$) was defined, with 1000 m intervals in the × and y directions. The 1000 m interval was selected to ensure reasonable model run times given the large extent of the study area (see Fig. 2). The global mean was calculated using the best linear unbiased estimate (Eq. (2)) and 100 realisations of hydraulic head and partial derivatives were generated. The minima, maxima and the concavity of the hydraulic head surface were mapped using the hydraulic head and partial derivatives realisations, and a polygon of the aquifer boundary was determined as per the methods described in Sections 2.2 and 2.3.

4. Results and discussion

4.1. Preliminary geostatistical data analysis

The D'Agostino and Pearson (1973) test was applied to the null hypothesis of the hydraulic head data being normally distributed and the null hypothesis could not be rejected using a significance level of 0.05 ($p = 0.89$, $k = 0.23$). The experimental semi-variance of the hydraulic head data was estimated using the gstat library (Pebesma, 2004) in R. A Gaussian semi-variogram model was then fitted to the experimental semi-variance by minimising the sum of the squared differences. Following Philip and Kitanidis (1989) and Pardo-Igúzquiza and Chica-Olmo (2004), the semi-variogram model was separated into a continuous model (the Gaussian semi-variogram model) and a discontinuous model (the nugget effect semi-variogram model). This was necessary, as the spatial variability must be continuous, including at the origin, for the derivatives to be calculated (Philip and Kitanidis, 1989). The continuous semi-variogram model was converted to a covariance model using the relationship that the semi-variogram is equal to the sill minus the covariance. The sill of the discontinuous model was used to parameterise σ^2, which regularises the Kriging model to avoid overfitting uncertain observations (see Eq. (1)) and essentially filters out the measurement error (see Philip and Kitanidis, 1989). The resulting semi-variogram

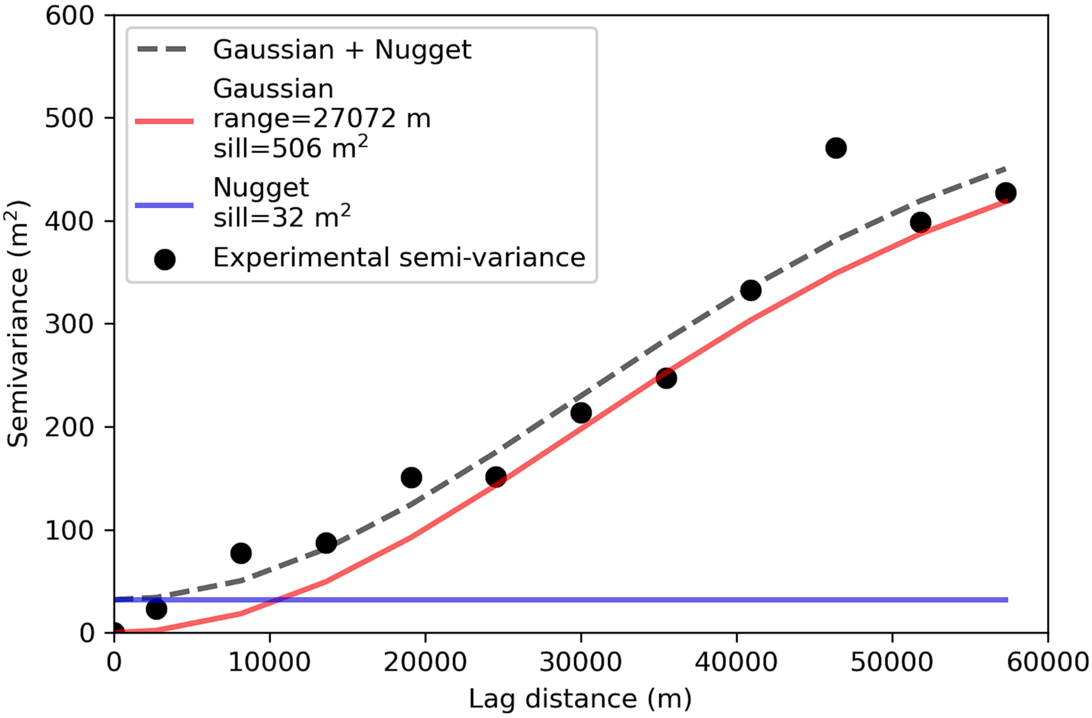

Fig. 3. The semi-variogram models in the Triassic formations showing the discontinuous nugget effect semi-variogram model (blue), the continuous Gaussian semi-variogram model (red) and the addition of the discontinuous and continuous semi-variogram models (black dashed line).

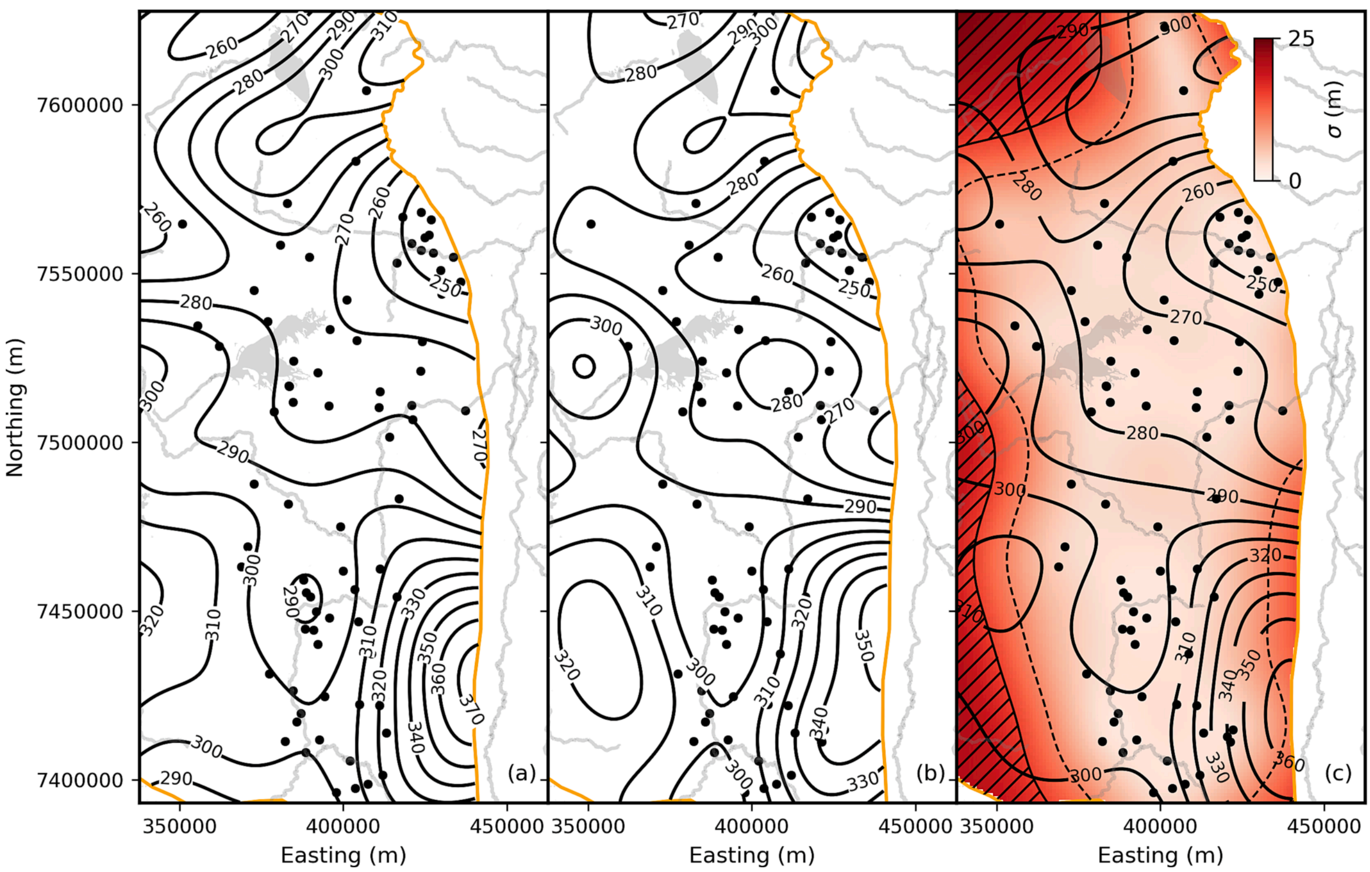

Fig. 4. (a) and (b) Hydraulic head contours (black lines) of realisations 1 and 2 (respectively), along with the location of hydraulic head observations (black dots). (c) Contours of the mean hydraulic head from all realisations (black lines), the standard deviation of all realisations (red heat map), and hydraulic head observation locations (black dots). The hashed area shows where $\sigma > 15$ m, while the dotted line shows $\sigma = 10$ m. Rivers, creeks and lakes are shaded grey in the background.

models (shown in Fig. 3) were composed of a nugget model with a sill of 32 m^2 and Gaussian model with a range of 27,072 m and a sill of 506 m^2.

4.2. Hydraulic head predictions

Following the preliminary geostatistical analysis, 100 realisations of hydraulic head and partial derivatives of hydraulic head were generated using sequential Gaussian simulation. The variability between realisations can be attributed to the values at model nodes being simulated sequentially by drawing from a normal distribution parametrised by the estimated mean and variance for a randomly selected node. This was followed by treating the simulated value as an observation that was included in the simulation of subsequent nodes (as described in Section 2.1). Fig. 4a and Fig. 4b show contours of hydraulic head for realisations 1 and 2, respectively. As shown, the realisations have the largest differences in the areas where there are few hydraulic observations and small differences near hydraulic head observations. This is expected, as the model is conditioned on the hydraulic head observations, such that predictions made close to observed data will closely match the observed values. Alternatively, the prediction uncertainty will increase further away from observations, leading to a larger range of plausible values. Fig. 4c shows the average hydraulic head of all realisations contoured over a heat map of the standard deviation of all realisations. As shown, the standard deviation is low (e.g., 0–5 m) close to observations and higher (up to 25 m) further away from the observations (i.e., in the north-west and south-west of the study area). We elected to hash out areas where the standard deviation was greater or equal to 15 m as predictions and inferences of extrema or concavity in these areas were highly uncertain. The contour where the standard deviation in the hydraulic head equals 10 m is also shown with a dotted line.

The average hydraulic head is higher to the north-east and south-east and lower in the central eastern area near the aquifer boundary (Fig. 4c). As water flows from high to low hydraulic head, it appears that recharge areas are in the north-eastern and south-eastern areas, while discharge occurs mainly in the central-eastern area, coinciding with the Doongmabulla Springs Complex and the Carmichael River (and the proposed site of the Carmichael Coal Mine; Fig. 2). There is also indication of boundary inflows in the south-west and outflows to the north-west, although these areas are highly uncertain ($\sigma \geq 10$ m). Note that the individual realisations (i.e., Fig. 4a and b) show substantial variability in flow direction (inferred as flow perpendicular to the hydraulic head contours) near and through the boundary relative to that shown in the averaged results (Fig. 4c). Similarly, the locations of likely recharge and discharge areas are variable between realisations (e.g., the recharge area in Fig. 4a is further east in Fig. 4b). As there is significant variability between realisations and it is unfeasible to examine all realisations in detail, an alternative approach is required to interpret the regional flow directions and likely recharge and discharge zones.

4.3. Minima and maxima in the hydraulic head surface

Extrema (minima, maxima and inflection points) in the hydraulic head surface were identified (see Section 2.2) and assigned to nodes within a 5000 m radius. This approach allows a comparison between realisations by counting the frequency of each grid node being proximal to an extremum. The buffer size of 5000 m was chosen after testing a wide range of values such that it created visible zones where extrema in hydraulics heads were obtained. Additionally, the component of flow

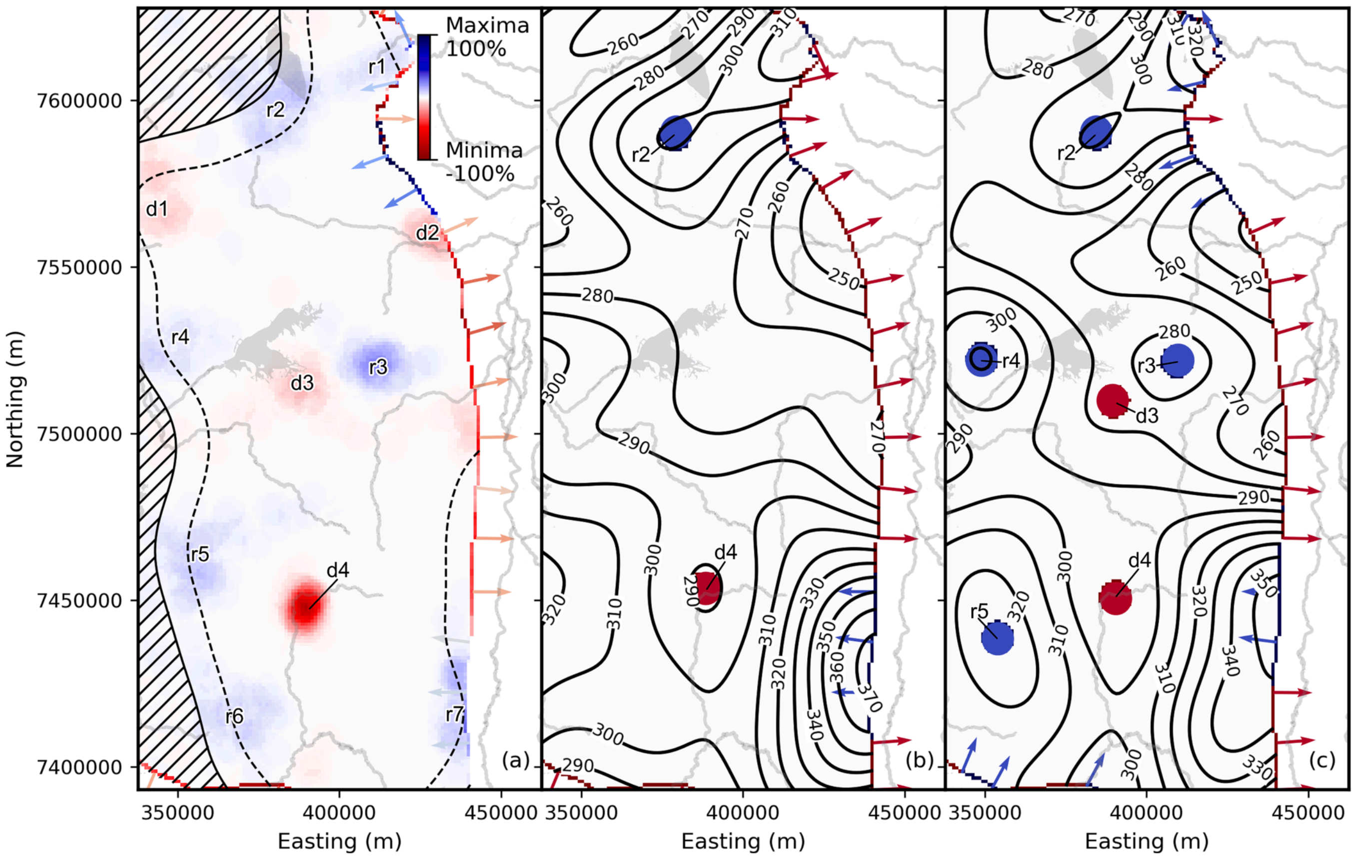

Fig. 5. (a) Relative percentage of realisations being minima (red) or maxima (blue). (b) and (c) show realisations of hydraulic head (black contours) with minima marked in red and maxima marked in blue. For visualisation, arrows (not to scale) have been added at the edge of the basin every 10 nodes of the grid to show whether the flow orthogonal to the boundary is out (minimum) or in (maximum), with the colour gradation in (a) representing the relative percentage of realisations where the edge node is a minimum or maximum. Minima and maxima have been labelled consecutively with the pretext "d" for discharge and "r" for recharge.

orthogonal to the boundary was used to classify boundary nodes as minima (flow out of the boundary), maxima (flow in through the boundary) or neither (flow is parallel to the boundary) as described in Section 2.3. These were discrete classifications (i.e., minima, maxima or neither) and did not consider the magnitude of the gradient both in and out of the boundary or the steepness of the surface around the minima or maxima.

Fig. 5b and c show realisations of hydraulic head with the locations of minima (red areas) and maxima (blue areas). The arrows are shown every 10 nodes along the boundary to indicate if flow is in (maxima) or out (minima). Some extrema occur frequently between realisations (e.g., r2 and d4 in Fig. 5b and Fig. 5c), while other extrema occur less frequently (e.g., r3, r4, r5 and d3 in Fig. 5c are not present in Fig. 5b). The flow directions orthogonal to the boundary suggest flow is out through most of the eastern boundary (red pixels and arrows, Fig. 5a-c). However, areas to the south in Fig. 5b and Fig. 5c and two areas to the north in Fig. 5c suggest inwards flows (blue pixels and arrows). All 100 realisations annotated with minima and maxima are provided online (https://doi.org/10.6084/m9.figshare.20225571.v1).

The summary of results represented in Fig. 5a shows the relative percentage of realisations (i.e., (total minimum – total maximum)/total realisations × 100 %) where each node is a minimum (red) or maximum (blue) from the 100 realisations. The relative percentage for each node is a continuous index (shown with the colour gradation between blue and red) ranging from −100 % (all realisations are minimum) to 100 % (all realisations are maximum) with an intermediate value of 0 %. As shown in Fig. 5a, seven maxima (r1 to r7) and four minima (d1 to d4) were identified from the analysis of the ensemble. The lighter shades of red or blue suggest zones are less common between analyses (e.g., r3 and d3) than those zones with darker shades of red or blue (e.g., d4).

Of these areas, r1 and r7 are likely recharge areas where the Triassic formation outcrops along the eastern margin of the basin and where groundwater recharge has been hypothesised to occur (Evans et al., 2018). There is also evidence of flow into the basin along the eastern edge to the north and south, near r1 and r7 as shown by the blue arrows. The maxima r2, r4, r5 and r6 lie beneath the Eromanga Basin (Fig. 2) and could represent areas of inter-aquifer connectivity where the Triassic formations obtain water from the Permian formations. This interpretation is in agreement with Moya et al. (2015) who found hydrochemical evidence of mixing between the Triassic and Permian aged units to the west where the Rewan formation (an aquitard separating the Triassic and Permian aquifers) is thin. The minima d4 may be a discharge area that forms a groundwater divide between flow from the hypothesised recharge areas to the south-west (r5 and r6) and the south-east (r7). This hypothesised discharge area (d4) is also located over a river, indicating the river may be gaining in this region. The geological and topographical causes of the r3 recharge area are less apparent. It is plausible that there may be unmapped outcrops of the Triassic units in the region of r3, as it is at a topographic high point (see Fig. 2).

The minimum d3 is located between r3 and r4, suggesting that it could be a sink for water from these hypothesised recharge areas. As d3 is located near Lake Galilee (i.e., see Fig. 2), it is plausible that this could represent surface discharge occurring from the Triassic units given the hypersaline condition of the lake. Similarly, the minimum d4 is located between recharge areas to the south-west (r5 and r6) and a recharge area to the south-east (r7) overlies a river. This suggests that the river may receive groundwater from the Triassic units in this area. The discharge area d2 is located over the Carmichael River and in a region that coincides with the Doongmabulla Springs Complex. This observation indicates that the Triassic units may be contributing groundwater to the river and/or springs in this area. Fig. 5a shows that there is also discharge along most of the eastern margin of the basin (red arrows). This suggests that discharge may be occurring along the edges of the basin possibly to geological formations beyond the Galilee Basin or to

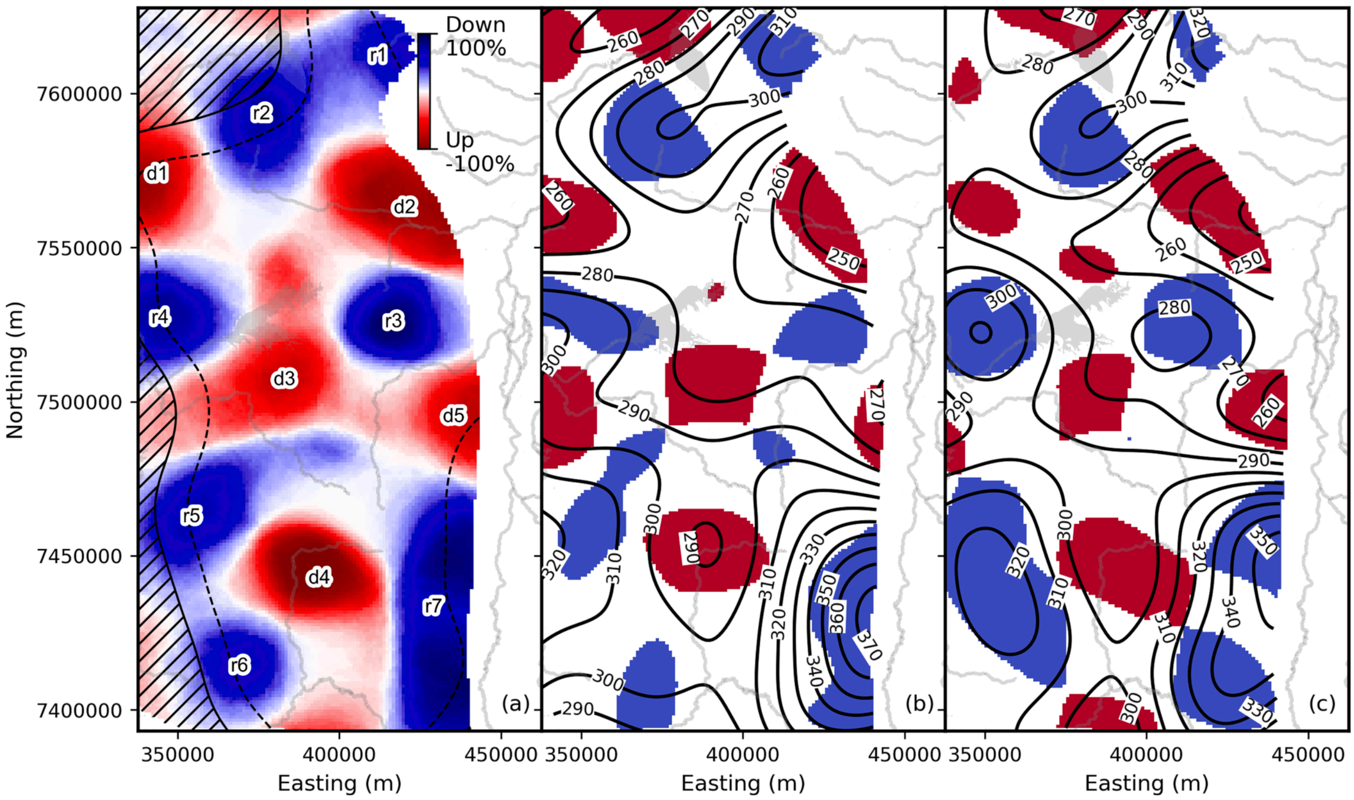

Fig. 6. (a) Relative percentage of realisations where each node is concave up or concave down. The hashed area shows where σ is 15 m or greater and the dotted line represents the $\sigma = 10$ m contour. (b) and (c) show the concavity of the hydraulic head surface for two realisations with blue areas concave up and red areas concave down. Concave up and concave down areas are labelled with the pretext "d" for discharge and "r" for recharge.

surface features. The cause of the minimum d1 is less apparent as the Triassic formations are at significant depth beneath the Eromanga Basin in this area.

4.4. Concavity of the hydraulic head surface

From a flow perspective, concave up areas can be interpreted as flow converging towards a low point, while concave down areas can be interpreted as flow dispersing away from a high point. In some cases, the concavity may be more informative than minima or maxima for identifying potential recharge or discharge areas or groundwater extraction. For example, if recharge is occurring over a large area, the concavity may be more informative of the recharge areas than the peak (maxima). Fig. 6b and c show two realisations of hydraulic head with the concave up and concave down areas marked in red and blue, respectively. As shown, the concave down areas are generally associated with high hydraulic head values, while the concave up areas are generally located near low hydraulic head values, as expected (see Fig. 1). All 100 realisations annotated with concavity are provided online (https://doi.org/10.6084/m9.figshare.20225796.v1).

Fig. 6a displays the relative percentage of realisations where each node was concave up or concave down (i.e., (total concave up – total concave down) / total realisations × 100 %). As shown, there are five concave up areas (d1-d5) and seven concave down areas (r1-r7). The concave down areas r1, r3 and r7 are located near the edge of the basin where the Triassic formations outcrop. It is plausible that these areas may be associated with inflow at the edge of outcrop areas that was identified by Evans et al. (2018). The concave down areas r4, r5 and r6

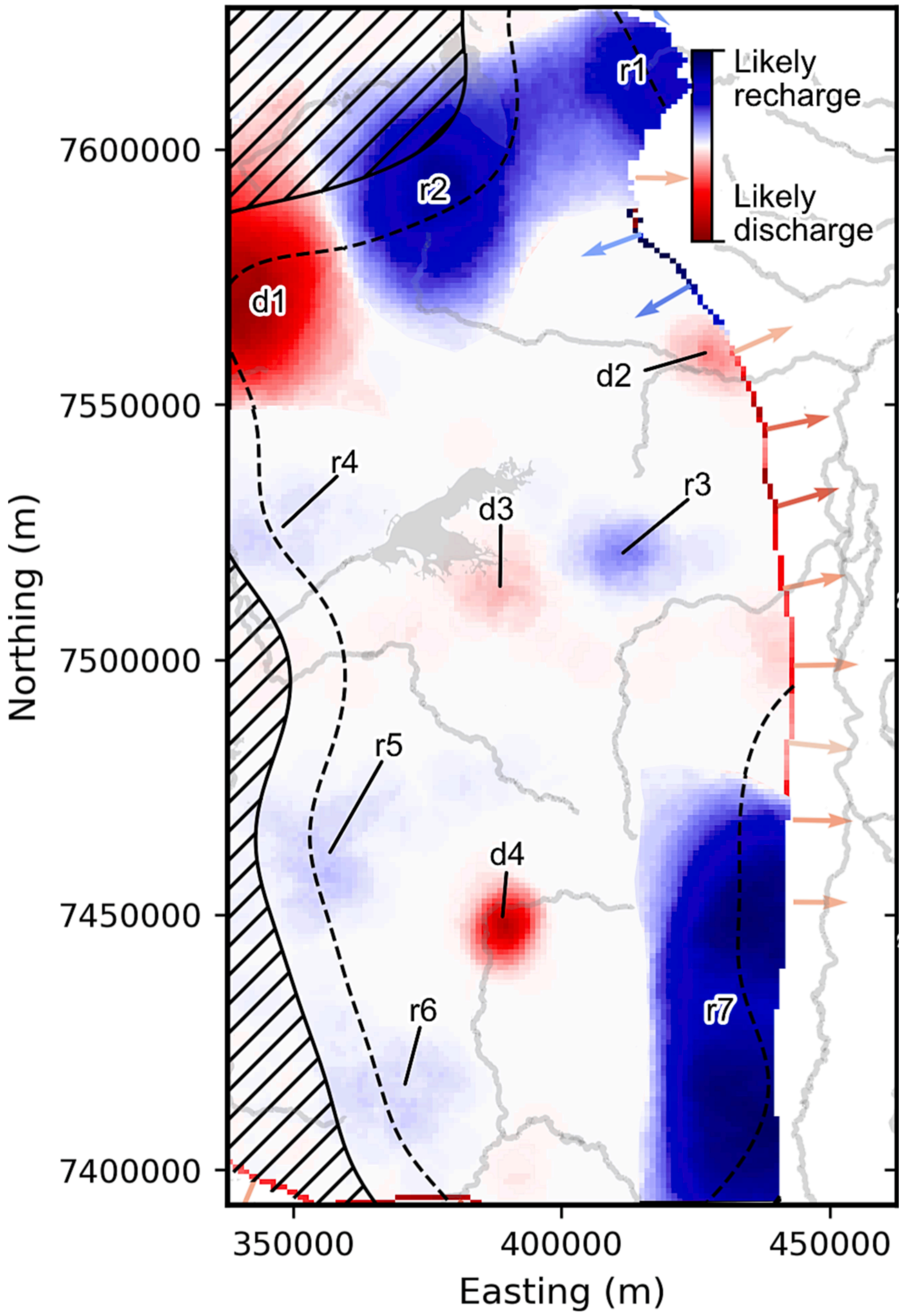

Fig. 7. Selected recharge (blue) and discharge areas (red) from the combined interpretation of the concavity and extrema in conjunction with the locations of rivers and lakes.

may reflect flow from the Permian formations due to a thinning of the Rewan formation aquitard in the area (Moya et al., 2015).

The concave up area d4 likely represents discharge to a river, which may act as a groundwater divide between the hypothesised recharge areas r5, r6, and r7. The concave up areas d2 and d5 along the eastern margin of the basin likely represent discharge out of the basin. In the case of d2, the concave up area could be representative of discharge to the Carmichael River and/or the Doongmabulla Springs Complex. The concave up area d3 is located near Lake Galilee and a river (Edie Creek), suggesting that the Triassic units may be contributing water to these surface features. The cause of the concave up area d1 is less obvious, as the Triassic formations are located at substantial depth beneath the Eromanga Basin in this area.

4.5. Combined analysis of minima, maxima and concavity

Expert knowledge of a study area can help to determine whether a hypothesised recharge or discharge area is likely to be discrete or diffuse. In areas where there are discrete surface features (e.g., rivers, creeks, wells, or springs), the use of extrema may be most informative of recharge or discharge areas, because these more likely coincide with easily recognisable recharge/discharge features within the landscape. Alternately, in areas where there are diffuse surface features (e.g., stands of vegetation, wetlands, exposed outcrop areas, etc.), then the use of concavity may be more informative to identify zones of recharge or discharge. This is notwithstanding that both localised and diffuse recharge/discharge are likely to create both extrema and concavity in the hydraulic head surface. Nevertheless, we suggest that concavity and extrema are interpreted in conjunction with knowledge of surface features to decide which is most appropriate to identify the causes and spatial extent of recharge and discharge.

The combined use of extrema and concavity were used to develop a recharge/discharge area map (Fig. 7). Recharge near the edge of the basin is expected to be diffuse infiltration from rainfall events where the Triassic formations are thin, weathered and exposed (Evans et al., 2018). In these regions, the concavity was selected as being representative of recharge areas r1 and r7. Similarly, area r2 is located near lake Buchanan, suggesting that the lake may act as a diffuse source of recharge to the underlying aquifers. The remaining hypothesised recharge areas are located at substantial depth beneath the Eromanga Basin far from known outcrop areas or lakes. The maxima were selected to represent these areas as these may represent isolated areas of connectivity between the Triassic and Permian formations (Moya et al., 2015). As d2, d3 and d4 are proximal to surface features (i.e., rivers, springs and lakes), the extrema approach was selected as representative of the discharge areas. The cause of d1 was less apparent as the Triassic formations were located at significant depth beneath the Eromanga Basin in this area. Therefore, it was assumed that d1 may be best represented using the concavity as it could represent discharge to other aquifers such as the Hutton Sandstone (Moya et al., 2015). Needless to say, these interpretations are preliminary and require further work to validate the nature of groundwater inflow/outflow within the regions of interest described above.

From a regional flow perspective, recharge appears to occur in the outcrop areas to the north-east and south-east (r1 and r7) and in the vicinity of Lake Buchanan (r2). There are also other plausible recharge areas (r3, r4, r5 and r6), although further investigation is required to determine the characteristics of these areas (e.g., inter-aquifer leakage, unmapped outcrops, etc.). There are plausible discharge areas near the Alice River to the south (d4), Lake Galilee (d3), and the Doongmabulla Springs Complex and the Carmichael River (d2). The area near the Carmichael Mine (see Fig. 2) appears to be a regional discharge point (see Fig. 7), and dewatering as part of the mining operation needs to account for influxes from both the Triassic and Permian units. There are important implications for the potential for mine-induced impacts to the Doongmabulla Springs Complex from this interpretation. If the Triassic system is the source of water to the springs and is connected to the mine area (as suggested here), then there is an elevated risk of drawdown propagating to the springs. This hypothesis warrants further analysis.

4.6. Uncertainties and future directions

A common criticism of Kriging techniques is that the resulting estimates are often unnaturally smooth, and not globally accurate, honouring neither the semi-variogram nor the measurement histogram (Caers, 2000; Yamamoto, 2005). So, while Kriging estimation may be locally accurate (i.e., provide the best estimates at individual prediction locations), the smoothness will result in an overestimation of lower values and an underestimation of higher values. Conditional simulations, such as sequential Gaussian simulation, honour both the semi-variogram model and the measurement histogram, guaranteeing global accuracy, albeit with a trade-off of decreased local accuracy (Caers, 2000). Thus, sequential Gaussian methods can better capture the spatial transitions between extreme values, although simulated values at individual prediction locations may be less optimum than those produced by Kriging (Goovaerts, 1997). In this study, Gaussian simulation was used in preference to Kriging, as global accuracy (i.e., an accurate transition between extreme values) was more important than local accuracy (i.e., the best estimates at each prediction location). The trade-off between poorer local accuracy and better global accuracy means that simulated hydraulic head and hydraulic gradients may have been less optimal than those produced using Kriging at individual prediction sites. Future studies should consider whether local or global accuracy is most important to the phenomenon of interest and choose a simulation or Kriging method accordingly.

Choosing between concavity and extrema for the identification of recharge/discharge areas is challenging when the data are sparse. Data sparsity issues were demonstrated in this study by different realisations inferring recharge and discharge at the same location. Secondary sources of information, such as the locations of surface features (e.g., rivers, lakes, springs, swamps), can provide critical information on whether a recharge/discharge feature is likely diffuse or discrete. Thus, this secondary information can assist the selection of the appropriate method (extrema vs concavity). However, this is a binary solution (i.e., either choosing the concavity or extrema for recharge/discharge locations), and rather there may be a spectrum between the two. Instead, the recharge source may encompass an area around the maximum that does not cover the entirety of the concave down area. Thus, in future studies, there may be a need to delineate an area encompassing the extrema to represent the likely recharge/discharge areas. This could be aided by considering additional datasets such as hydrochemistry or age tracers.

The analyses conducted here categorised features in the hydraulic head surface as recharge, discharge or neither, without consideration of the magnitude of the recharge/discharge rates. The impacts of this approach are that a small feature (e.g., mild concavity) received the same weighting as a larger feature (e.g., steep concavity) in the analysis. This simple categorisation of features was selected to make it straightforward to compare a single variable (i.e., recharge, discharge or neither) rather than two variables (i.e., recharge, discharge or neither and the varying magnitude of each). It may be possible to infer the magnitude of recharge/discharge features, at least within individual realisations. For example, by assessing the magnitude of the second derivatives for concavity/extrema and or of the first derivatives along the boundaries. However, the interplay between hydraulic conductivity and recharge, in creating head gradients, would need to be considered. Therefore, future studies could extend the method proposed here to include the magnitude of recharge/discharge features for individual realisations.

The coefficient of variation (i.e., standard deviation/mean) of all realisations was lowest for the hydraulic head values, increased with the first derivative and was highest for the second derivative (see Figure S10). This was expected given that a small change in the hydraulic head values may result in large changes in the first derivatives and possibly even the reversal of flow directions, leading to large coefficients of variability between realisations. Similarly, as the second derivative captures the change in the first derivative, the second derivative will have a higher coefficient of variability between realisations than the first derivative. This leads to a pattern where the coefficient of variation is lowest for the function values and increases with the order of the derivative. This emphasises the potential benefits of including derivative information within the modelling process. Hydraulic gradient observations can be included as a secondary variable in co-Kriging, and as the simulated first derivatives are more uncertain than the hydraulic head values themselves, the information value of gradient observations are higher than that of regular hydraulic head observations. Expert knowledge of the locations of recharge or discharge features could be encoded by adding nodes at the feature locations, setting the first derivatives at these locations to zero (as the first derivative equals 0 for minima and maxima), and co-Kriging these data with available hydraulic head observations. For example, if a river is known to be losing or gaining along a reach, nodes could be added with a first derivative value of zero and this could be co-Kriged with hydraulic head observations to reduce the uncertainty. Supporting Text S2 provides details on how the Kriging equations can be modified to include first derivative observations.

5. Conclusions

We developed a geostatistical method to model the concavity and locations of extrema in the hydraulic head surface. The new method extends previous work by using sequential Gaussian simulation to jointly simulate hydraulic head and the partial derivatives of the hydraulic head surface to identify the concavity and locations of extrema in the hydraulic head surface. The resultant maps of extrema and concavity can be interpreted with maps of known surface features to attribute the variation in the hydraulic head surface to recharge or discharge from known features such as geological outcrops, rivers, and lakes.

This was applied to the Galilee Basin to map the regional flow directions and the concavity and extrema of the hydraulic head surface. Likely recharge and discharge areas were identified by comparing maps of concavity and extrema with known features to attribute variations in the hydraulic head surface to recharge or discharge processes. These findings have important implications for the Galilee Basin, as they provide evidence suggesting recharge is likely to occur predominantly in the north-east and south-east where the Triassic formations outcrop, while discharge is apparent near several rivers, lakes and the Doongmabulla Springs Complex. Notably, this indicates that the Triassic formations may provide a source of water to the Carmichael River and the Doongmabulla Springs Complex, which has important implications given the potential for dewatering at the nearby Carmichael Coal Mine to impact hydraulic head in the Triassic formations, and potentially, discharge from the Doongmabulla Springs Complex.

The sequential Gaussian approach presented here is easy to apply, computationally efficient and requires only commonly available hydraulic head data. We facilitate the application of the technique through a worked example available online (https://doi.org/10.5281/zenodo.6655359). The approach can be extended to include derivative observations, which due to the higher uncertainty in derivative values relative to hydraulic head values, are of higher information value than hydraulic head observations. The inclusion of first derivative observations is particularly attractive as expert knowledge of recharge/discharge features (e.g., rivers, springs) can be encoded by setting the first derivative values to zero at the feature locations, and co-Kriging to constrain the analysis. Simulating the concavity and locations of extrema in the hydraulic head surface represents a substantial advancement in the geostatistical analysis of hydraulic head data sets by informing the locations of recharge and discharge areas and offering objective interpretation of recharge and discharge processes.

CRediT authorship contribution statement

Robin Keegan-Treloar: Conceptualization, Data curation, Formal analysis, Methodology, Software, Visualization, Writing – original draft. **Dylan J. Irvine:** Conceptualization, Funding acquisition, Supervision, Writing – original draft, Writing – review & editing. **Adrian D. Werner:** Conceptualization, Funding acquisition, Supervision, Writing – review & editing. **Eddie W. Banks:** Conceptualization, Funding acquisition, Supervision, Writing – review & editing.

Declaration of Competing Interest

The authors declare that they have no known competing financial interests or personal relationships that could have appeared to influence the work reported in this paper.

Data availability

Data included in supporting information + code available as an online resource

Acknowledgements

Robin Keegan-Treloar is supported by the Australian Government Research Training Program. Adrian Werner, Dylan Irvine, and Eddie Banks are supported by an Australian Research Council Linkage Project (project number LP190100713). The hydraulic head data used to conduct the analyses is available in the Supporting Material 2. A Python script to conduct the analysis is available at https://zenodo.org/record/6655391#.Y4fFinZByF4.

Appendix A. Supplementary data

Supplementary data to this article can be found online at https://doi.org/10.1016/j.jhydrol.2022.128993.

References

AECOM, 2021. Groundwater Management and Monitoring Program - Carmichael Coal Project. Retrieved from: https://s3-ap-southeast-2.amazonaws.com/awsfiles-232340950/bravus/documents/gmmp_ccp_v11.a_25052021_final_appnd_web_upload.pdf.

Caers, J., 2000. Adding local accuracy to direct sequential simulation. Math. Geol. 32, 815–850. https://doi.org/10.1023/A:1007596423578.

Cressie, N., 1990. The origins of kriging. Math. Geol. 22, 239–252. https://doi.org/10.1007/BF00889887.

Currell, M.J., Irvine, D.J., Werner, A.D., McGrath, C., 2020. Science sidelined in approval of Australia's largest coal mine. Nat. Sustain. 3, 644–649. https://doi.org/10.1016/j.jhydrol.2017.03.031.

D'Agostino, R., Pearson, E.S., 1973. Tests for departure from normality. Biometrika 60, 613. https://doi.org/10.2307/2335012.

Duvenaud, D.K., 2014. Automatic Model Construction with Gaussian Processes.

Enemark, T., Peeters, L.J., Mallants, D., Batelaan, O., 2019. Hydrogeological conceptual model building and testing: a review. J. Hydrol. 569, 310–329. https://doi.org/10.1016/j.jhydrol.2018.12.007.

Evans, T., Pavey, C., Cassel, R., Ransley, T., Sparrow, A., Kellett, J., Galinec, V., Dehelean, A., Bell, J., Caruana, L., Kilgour, P., 2018. Conceptual modelling for the Galilee subregion. Product 2.3 for the Galilee subregion from the Lake Eyre Basin Bioregional Assessment. In: Department of the Environment and Energy, Bureau of Meteorology. CSIRO and Geoscience Australia, Australia.

Goovaerts, P., 1997. Geostatistics for Natural Resources Characterization. Oxford University Press.

Keegan-Treloar, R., Werner, A.D., Irvine, D.J., Banks, E.W., 2021. Application of Indicator Kriging to hydraulic head data to test alternative conceptual models for spring source aquifers. J. Hydrol. 601, 126808 https://doi.org/10.1016/j.jhydrol.2021.126808.

Moya, C.E., Raiber, M., Taulis, M., Cox, M.E., 2015. Hydrochemical evolution and groundwater flow processes in the Galilee and Eromanga basins, Great Artesian Basin, Australia: a multivariate statistical approach. Sci. Total Environ. 508, 411–426. https://doi.org/10.1016/j.scitotenv.2014.11.099.

Moya, C.E., Raiber, M., Taulis, M., Cox, M.E., 2016. Using environmental isotopes and dissolved methane concentrations to constrain hydrochemical processes and inter-aquifer mixing in the Galilee and Eromanga Basins, Great Artesian Basin, Australia. J. Hydrol. 539, 304–318. https://doi.org/10.1016/j.jhydrol.2016.05.016.

Pardo-Igúzquiza, E., Chica-Olmo, M., 2004. Estimation of gradients from sparse data by universal kriging. Water Resour. Res. 40, 1–17. https://doi.org/10.1029/2004WR003081.

Pebesma, E.J., 2004. Multivariable geostatistics in S: the gstat package. Comput. Geosci. 30, 683–691. https://doi.org/10.1016/j.cageo.2004.03.012.

Philip, R.D., Kitanidis, P.K., 1989. Geostatistical estimation of hydraulic head gradients. Ground Water 27, 855–865. https://doi.org/10.1111/j.1745-6584.1989.tb01049.x.

Rasmussen, C., Williams, K., 2006. Gaussian Processes for Machine Learning. MIT Press.

Rau, G.C., Post, V.E.A., Shanafield, M., Krekeler, T., Banks, E.W., Blum, P., 2019. Error in hydraulic head and gradient time-series measurements: a quantitative appraisal. Hydrol. Earth Syst. Sci. 23, 3603–3629. https://doi.org/10.5194/hess-23-3603-2019.

Solak, E., Murray-Smith, R., Leithead, W.E., Leith, D.J., Rasmussen, C.E., 2003. Derivative observations in Gaussian Process Models of Dynamic Systems. Adv. Neural Inf. Process Syst.

Stewart, J. 2010. Multivariable Calculus, 7th ed.

Thomann, J.A., Werner, A.D., Irvine, D.J., Currell, M.J., 2020. Adaptive management in groundwater planning and development: A review of theory and applications. J. Hydrol. 586, 124871 https://doi.org/10.1016/j.jhydrol.2020.124871.

Yamamoto, J.K., 2005. Correcting the smoothing effect of ordinary kriging estimates. Math. Geol. 37, 69–94. https://doi.org/10.1007/s11004-005-8748-7.

Appendix F. Conference abstracts

Investigating the source waters of the Doongmabulla Spring Complex (484)

Robin K. Keegan-Treloar [1], Adrian D. Werner [1], Eddie W. Banks [1], Dylan J. Irvine [1]

1. Flinders University, Bedford Park, SA, Australia

The Doongmabulla Springs Complex (DSC) is a collection of permanent freshwater springs that provide water to approximately 160 wetlands, which are ecologically significant and provide niche habitat for several threatened species (Fensham et al. 2016). Currently, the source of water to the DSC is uncertain, and with proposed developments within the vicinity of the springs, it is essential that the source waters of the DSC are properly examined. Alternative conceptual models have been presented for the source of the springs, and there is conjecture as to the contributions from the Triassic Clematis Formation and deeper Permian sediments; these being separated by the Triassic Rewan Formation, a regional aquitard that represents the base of the Great Artesian Basin (Habermehl and Lau 1997; CSIRO and Geoscience Australia 2019). This presentation describes efforts to collate available hydrochemical data and supplement this with additional measurements from a field sampling campaign to address knowledge gaps in the existing hydrochemistry dataset for the DSC and nearby sedimentary units. Statistical analyses, including Principal Components Analysis (PCA) and K-Nearest Neighbours Clustering (KNN), were applied to hydrochemical data for the DSC and the aquifers of the region. PCA suggested an overlap between the hydrochemical signatures of the water types of the region's aquifers and the DSC. Hydrochemical overlap can be indicative of inter-aquifer mixing, which may suggest connectivity between the Triassic and Permian aquifers. KNN, a supervised classification technique, provided an insight into the most likely source aquifer of individual springs of the DSC. These preliminary results shine new light on the statistical association between individual DSC springs and groundwater in Triassic and Permian aquifers. These findings highlight the importance of continued investigation of alternative conceptual models for the source of discharge to the DSC.

1. CSIRO and Geoscience Australia (2019) Advice on Groundwater Management and Monitoring and Groundwater Dependent Ecosystem Management plans to the Department of the Environment and Energy. February, 2019, 63pp. http://www.environment.gov.au/system/files/pages/cb8a9e41-eba5-47a4-8b72-154d0a5a6956/files/csiro-geoscience-australia-final-advice.pdf
2. Fensham, R.J., Silcock, J.L., Laffineur, B., MacDermott, H.J. (2016) Lake Eyre Basin Springs Assessment Project: Hydrogeology, cultural history and biological values of springs in the Barcaldine, Springvale and Flinders River supergroups, Galilee Basin springs and Tertiary springs of western Queensland. Report to Office of Water Science, Department of Science, Information Technology and Innovation, Brisbane. https://publications.qld.gov.au/dataset/11c1af89-93b9-497a-b99f-2ec6c7a8d339/resource/c5d1813b-73a4-4e05-aa86-39a8ed3045fb/download/lebsa-hchb-report-springs-wst-qld.pdf
3. Habermehl, M. A. and Lau, J. E. (1997) Hydrogeology of the Great Artesian Basin, Australia (map at scale 1: 2,500,000), Australian Geological Survey Organisation, Canberra.

Geostatistical simulation of mounds and troughs in the hydraulic head surface to inform the mapping of recharge and discharge areas

Robin Keegan-Treloar[1]
Dylan Irvine[2], Adrian Werner[1] and Eddie Banks[1]
[1] Flinders University
[2] Charles Darwin University

Identifying groundwater flow directions and the locations of recharge and discharge areas is essential for effective groundwater management. Using hydraulic head data, we developed a novel geostatistical method to stochastically map mounds and troughs in the hydraulic head surface. Where possible, the mapped mounds and troughs were compared with surface structures (e.g., outcrops, springs, rivers and lakes) to attribute these mounds or troughs to recharge or discharge from the surface structures. This was applied to Triassic-aged aquifers in the Galilee Basin (Queensland, Australia) to identify the likely recharge and discharge areas. Likely recharge and discharge areas were compared with hydrogeochemical signatures from groundwater wells and their variations along inferred groundwater flow paths to assess the agreement between processes identified with hydrochemistry and those identified with the geostatistical hydraulics-based technique. The technique presented here provided an objective assessment of likely recharge and discharge zones and their uncertainty, which is an important addition to a region where the hydrogeology has been the subject of much conjecture.